UNIVERSIDADE DE LISBOA

INSTITUTO SUPERIOR TÉCNICO

Fire behaviour of concrete structures reinforced with GFRP bars

Inês Cruz Mina Rosa

Supervisor: **Doctor João Pedro Laje da Costa Firmo**

Co-Supervisors: **Doctor João Pedro Ramôa Ribeiro Correia**

Doctor Mário Rui Tiago Arruda

Thesis approved in public session to obtain the PhD Degree in Civil Engineering

Jury final classification: **Pass with Distinction and Honour**

2022

UNIVERSIDADE DE LISBOA

INSTITUTO SUPERIOR TÉCNICO

Fire behaviour of concrete structures reinforced with GFRP bars

Inês Cruz Mina Rosa

Supervisor: **Doctor João Pedro Laje da Costa Firmo**
Co-Supervisors: **Doctor João Pedro Ramôa Ribeiro Correia**
Doctor Mário Rui Tiago Arruda

Thesis approved in public session to obtain the PhD Degree in Civil Engineering

Jury final classification: **Pass with Distinction and Honour**

Jury

Chairperson: Doctor Eduardo Nuno Brito Santos Júlio, Instituto Superior Técnico, Universidade de Lisboa

Members of the Committee:

Doctor Luke Bisby, School of Engineering, The University of Edinburgh, United Kingdom
Doctor João Carlos de Oliveira Fernandes de Almeida, Instituto Superior Técnico, Universidade de Lisboa
Doctor Hamzeh Hajiloo, Carleton University, Canada
Doctor João Pedro Laje da Costa Firmo, Instituto Superior Técnico, Universidade de Lisboa

Funding Institutions

Fundação para a Ciência e a Tecnologia (SFRH/BD/129681/2017)
Fundação para a Ciência e a Tecnologia (PTDC/ECM/1882/2014)

2022

Abstract

The use of glass fibre reinforced polymer (GFRP) bars is becoming increasingly considered for reinforced concrete (RC) structures exposed to relatively harsh environments, where fire is not typically a primary design requirement. On the other hand, the adoption of GFRP reinforcement in buildings is still not common and this is mainly due to concerns and lack of information and guidance regarding fire design. However, and despite the relevance of the subject, few studies have comprehensively investigated the consequences of the severe degradation with temperature of the bars' mechanical properties and bond to concrete on the fire endurance of GFRP-RC structural members.

This thesis aimed at enhancing the knowledge about the aforementioned subjects, by presenting a comprehensive study about the fire behaviour of RC structures comprising GFRP bars. The research was conducted into three complementary strands, comprising: (i) an extensive experimental campaign performed at different scales of analysis, including the characterization of the bars' mechanical properties over a wide range of temperatures, their bond behaviour with concrete at elevated temperatures, and the fire resistance of GFRP-RC slabs; (ii) the numerical modelling of the GFRP-concrete bond and the fire behaviour of the GFRP-RC slabs; and (iii) the drafting of fire design recommendations. Different types of GFRP reinforcement were tested, presenting different surface finishes (sand coated and different types of rib profiles), diameters and geometries (straight and 90º bent bars).

The first stage of the study comprised investigations about the tensile properties and bond behaviour of the GFRP bars at elevated temperatures. First, steady-state tensile tests were performed to determine the bars' tensile modulus and strength up to 715 ºC. Next, pull-out tests between GFRP bars and concrete were conducted at temperatures up to 300 ºC. Local bond laws describing the GFRP-concrete interaction at elevated temperatures were then numerically calibrated using the experimental data. These laws were later implemented in three dimensional (3D) finite element (FE) models, duly validated with the results of the bond tests, in order to perform parametric studies that allowed proposing design oriented anchorage lengths for straight and 90º bent GFRP bars as a function of temperature, envisaging their use in RC beams and slabs.

One of the main contributions of the thesis was the development of an in-depth study about the fire performance of GFRP-RC slabs. In a first stage, fire resistance tests were performed in loaded GFRP-RC slab strips subjected to the ISO 834 standard fire curve. A total of 21 slab strips comprising different materials and detailing configurations were tested to evaluate the influence of the following parameters on their fire behaviour: (i) concrete cover thickness; (ii) presence of straight- or 90º bent tension lap splices directly exposed to fire with different overlap lengths; (iii) presence of "cold" anchorage zones;

(iv) type of GFRP bars (*i.e.*, with different surface finishes and diameters), and (v) concrete strength. In a second stage, 3D FE models were developed to simulate the thermomechanical fire behaviour of the GFRP-RC slab strips and to assess in further detail the fire behaviour of GFRP-RC flexural members, particularly with respect to lap splices and anchorage zones. The temperature-dependent thermophysical and mechanical properties of the bars and concrete were implemented in the models, and the GFRP-concrete interaction was modelled through the local bond laws (independently) calibrated for different temperatures. Based on the experimental and numerical results obtained, fire design recommendations were drafted, including: (i) critical temperatures to be considered for the GFRP reinforcement, and (ii) positions and lengths for their end anchors and overlapped lap-splices.

Overall, the research developed in this thesis proved that in spite of the high vulnerability of GFRP bars to elevated temperatures, GFRP-RC slabs can endure over 3 hours of fire exposure with considerably lower concrete covers than those recommended in existing FRP-RC design codes, provided that the bars remain well anchored in cool zones of the structure. If this requirement is fulfilled, failure is governed by the tensile strength of the bars at very high temperatures, well above their glass transition temperature (T_g). Moreover, it was shown that the progressive and severe bond degradation of the GFRP bars with temperature must be considered in the design of both cold anchorage zones and lap splices, aiming to prevent premature debonding failures when the bars' temperature increases above their T_g. In this regard, the adoption of bent bars was proven to be beneficial to decrease the cold end anchorage lengths, as well as to significantly improve the bond behaviour in splicing zones. The results obtained in this study may therefore contribute to improve existing design guidelines for FRP-RC structures, which currently provide insufficient and overconservative recommendations for their fire design – ultimately, the findings of this study will also promote a safer, and more economic and sustainable use of FRP reinforcement in civil engineering applications.

Keywords: reinforced concrete; glass fibre reinforced polymer (GFRP) bars; bond behaviour; fire performance; experimental tests; numerical modelling.

Resumo

A utilização de varões de polímero reforçado com fibras de vidro (GFRP) em estruturas de betão armado (BA) tem vindo a aumentar, sobretudo em ambientes agressivos. Nestas aplicações, a resistência ao fogo não é tipicamente um requisito de desempenho. Por outro lado, a adoção de varões de GFRP em edifícios ainda é pouco comum e isso deve-se, sobretudo, às preocupações e à falta de informação e recomendações de dimensionamento relativas à segurança em situação de incêndio. Contudo, e apesar da relevância do tema, a literatura ainda carece de estudos aprofundados sobre os efeitos que a degradação das propriedades mecânicas e da aderência dos varões de GFRP ao betão com a temperatura têm na resistência ao fogo de elementos estruturais de BA que incorporam este tipo de armadura.

Esta tese teve como principal objetivo aprofundar o conhecimento neste tema, investigando com detalhe o comportamento ao fogo de estruturas de BA incorporando armaduras em GFRP. O estudo foi efetuado em três vertentes complementares, incluindo: (i) uma extensa campanha experimental realizada a diferentes escalas de análise, incluindo a caracterização das propriedades mecânicas dos varões numa ampla gama de temperaturas, o seu comportamento de aderência ao betão a temperatura elevada, e a resistência ao fogo de lajes de BA; (ii) a modelação numérica da aderência betão-GFRP a temperatura elevada e do comportamento ao fogo de lajes; e (iii) a elaboração de recomendações de dimensionamento ao fogo. Foram testados diferentes tipos de varões de GFRP, apresentando diferentes acabamentos superficiais (revestidos a areia e com diferentes tipos de nervuras), diâmetros e geometrias (retos e dobrados a 90º).

Numa primeira fase, foi estudado o comportamento à tração e a aderência ao betão dos varões de GFRP a temperaturas elevadas. Para o efeito, realizaram-se ensaios de tração em regime estacionário para determinar a resistência e o módulo de elasticidade em tração dos varões a temperaturas até 715 ºC e, em seguida, ensaios de arrancamento de varões de GFRP, embebidos em cilindros de betão, a temperaturas até 300 ºC. Os resultados experimentais obtidos foram por sua vez utilizados para calibrar numericamente leis locais de aderência que definem a interação GFRP-betão a temperaturas elevadas. As leis foram implementadas em modelos de elementos finitos tridimensionais (3D), devidamente validados com base nos resultados dos ensaios de arrancamento, com o objetivo de efetuar estudos paramétricos – estes permitiram propor comprimentos de ancoragem, em função da temperatura, para varões de GFRP retos e dobrados a 90º, perspetivando a sua utilização em vigas e lajes de betão armado.

Uma das principais contribuições da tese foi o desenvolvimento de um estudo aprofundado sobre o desempenho ao fogo de lajes de betão armadas com varões de GFRP. Numa primeira fase, foram realizados ensaios de resistência ao fogo em faixas de laje sujeitas simultaneamente a um carregamento

de serviço e expostas à curva de incêndio padrão da norma ISO 834. Foram testadas um total de 21 faixas de laje com diferentes materiais e esquemas de pormenorização de armaduras, com o objetivo de avaliar a influência dos seguintes parâmetros no seu comportamento ao fogo: (i) espessura de recobrimento; (ii) presença de emendas, diretamente expostas ao fogo, com extremidades retas ou dobradas a 90º e diferentes comprimentos de sobreposição; (iii) presença de zonas de ancoragem "frias"; (iv) tipo de varão de GFRP (*i.e.*, com diferentes acabamentos superficiais e diâmetros); e (v) resistência do betão. Numa segunda fase, foram desenvolvidos modelos de elementos finitos 3D para simular o comportamento termomecânico das faixas de laje e avaliar em detalhe o desempenho ao fogo de elementos estruturais de BA com armaduras em GFRP, com particular incidência nas zonas de emendas e ancoragem. As propriedades termofísicas e mecânicas dos varões e do betão, dependentes da temperatura, foram implementadas nos modelos e a interação GFRP-betão foi modelada através das leis locais de aderência que foram calibradas, de forma independente, para diferentes temperaturas. Com base nos resultados experimentais e numéricos obtidos, foram propostas recomendações de dimensionamento ao fogo, incluindo (i) temperaturas críticas, e (ii) o posicionamento, geometria e comprimento dos varões em zonas de extremidade e de emenda.

A investigação desenvolvida no âmbito desta tese mostrou que, apesar da grande vulnerabilidade dos varões de GFRP a temperaturas elevadas, as lajes de betão incorporando este tipo de armaduras podem atingir resistências ao fogo superiores a 3 horas com espessuras de recobrimento consideravelmente inferiores àquelas atualmente recomendadas em guias de dimensionamento, desde que os varões sejam ancorados em zonas frias da estrutura. Se este requisito for cumprido, a rotura é determinada pela resistência à tração dos varões a temperaturas muito elevadas, consideravelmente superiores à sua temperatura de transição vítrea (T_g). Para além disso, mostrou-se que a degradação severa e progressiva da aderência entre os varões de GFRP e o betão com a temperatura deve ser considerada no dimensionamento das emendas e zonas "frias" de ancoragem, como forma de prevenir roturas prematuras por perda de aderência quando a temperatura dos varões excede a T_g. Neste contexto, a adoção de varões dobrados mostrou-se benéfica para diminuir o comprimento de ancoragem em zonas "frias", assim como para melhorar significativamente o comportamento de aderência em zonas de emenda. Deste modo, os resultados obtidos neste estudo podem contribuir para melhorar as recomendações de dimensionamento ao fogo para estruturas de BA com armaduras em FRP, que, atualmente, fornecem recomendações insuficientes e excessivamente conservativas no que se refere à segurança em situação de incêndio – em última análise, as conclusões deste estudo irão também promover o uso mais seguro, sustentável e económico de varões de FRP em aplicações de Engenharia Civil.

Palavras-chave: Betão armado; varões de polímero reforçado com fibras de vidro (GFRP); comportamento de aderência; comportamento ao fogo; ensaios experimentais; modelação numérica.

Acknowledgments

During the course of my doctoral research I was fortunate to receive the support of so many kind-hearted, generous and amazingly talented people without whom the development of my thesis would not have been possible. A simple thank you is hardly enough to truly express how grateful I am for all of those that directly and indirectly were part of this remarkable journey. The following paragraphs are dedicated to them.

I wish first to express my deepest and most sincere gratitude to my scientific supervisors Dr. João Pedro Firmo and Professor João Ramôa Correia. No words will ever suffice to show how much I admire them and how much they impacted the success of this journey. I am beyond grateful for their ever constant support, availability, understanding and encouragement during every step of my PhD thesis. Their incomparable dedication to their students, outstanding and unmatched personal qualities, and extraordinary wisdom will always be a true inspiration and role model in every aspect of my personal and professional life. Thank you for your kindness, generosity and friendship. Thank you for giving me the confidence to believe in myself, to not be afraid of challenging myself and to always aspire to do better.

I would also like to thank my co-supervisor Dr. Mário Arruda for his great support, encouragement, valuable advises and expert guidance during the course of my research, particularly with respect to the numerical investigations. I extend my deep gratitude to Dr. António Duarte for his invaluable support, willingness to help and exceptional contribution to the numerical simulation of the fire resistance tests.

The present research was funded by the *Portuguese National Foundation for Science and Technology* (FCT) through a doctoral scholarship (SFRP/BD/129681/2017) and the *FireComposit*e project (PTDC/ECM/1882/ 2014), whose financial support is greatly acknowledged. I would also like to thank my research centre *Civil Engineering Research and Innovation for Sustainability* (CERIS) and to the *Department of Civil Engineering, Architecture and Georesources (*DECivil*)* of *Instituto Superior Técnico* (IST) for providing the facilities and conditions needed for the development of my research.

I am very grateful for the support of the industrial partners who generously provided the materials needed to conduct my experimental investigations, namely: *Owens Corning* and *Schöck*, for supplying the GFRP bars; *Secil* and *Unibetão*, for providing the concrete; and Sika, for supplying the bi-component resin.

I would also like to thank Dr. Susana Bravo from the *National Laboratory of Civil Engineering* (LNEC) for her assistance in the dynamic mechanical analysis (DMA). The help of Dr. Everton Santos from the *Chemical Engineering Department* of IST with the thermogravimetric (TGA) and differential scanning

calorimetry (DSC) tests is also greatly appreciated. The accomplishment of parts of my experimental campaign is the result of a teamwork carried out with the collaboration of several Master students, to whom I also thank.

I am grateful to the laboratory technicians Mr. Fernando Alves, Mr. Jorge Pontes, Mr. Fernando Costa and Mr. Francisco Almeida for their help and companionship during the development of my experimental campaign. My heartfelt gratitude goes especially to Mr. Fernando Alves, who has been accompanying my academic journey since I was a Master student and with whom I shared countless hours in the laboratory. It is mostly thanks to him that my experimental work was possible to be accomplished. His technical expertise and problem solving skills never fail to amaze me, and neither does his kind heart and joyful spirit.

I would like to deeply thank the following colleagues and friends at IST, some of which are very close to my heart, namely Adriana Azevedo, André Castelo, António Duarte, Cinthia Maia, David Martins, Eloísa Castilho, Filipe Aparício, Francisco Nunes, Inês Teotónio, João Lazzari, João Pacheco, João Sousa, José Gonilha, Lourenço Fernandes, Marina Santos, Mário Garrido, Mário Sá, Mateus Hofman, Md Abu Toyob Shahid, Miguel Proença, Pedro Kantor, Pietro Mazzuca, Rodrigo Morais, Tiago Morgado and Wallace Maia. Thank you for your friendship, for your many words of encouragement, helpful suggestions and your extraordinary help during the experimental campaign. More importantly, thank you for so many joyful moments spent together, I will cherish them forever.

I could have never accomplished so much without the unconditional friendship, support, love and affection of my closest friends, whom I treasure as my second family. Thank you Adriana, Ana, Carlos, Catarina, Duarte, Gonçalo, Inês, João, Marta, Pietro, Rodrigo and Tiago, for believing in me, for being an endless source of happiness, kindness and encouragement, and for always being present in the happiest and hardest of times. I am lucky to have you in my life.

Lastly, no words will ever be enough to thank my parents Ana Bela and Fernando, my sister Pipa, my brother Diogo, my aunts Eulália and Cândida, and my grandparents, especially my late grandmother Elvira, for everything they have done to allow me to be where I am today. Your affection, understanding, encouragement and tireless support gave me the motivation to pursue my goals and the strength to overcome so many obstacles along the way. I am happy to have made you proud.

Table of contents

List of figures

List of tables

Notation

Roman lower case

c_p	Specific heat
d	Nominal (core) diameter; distance from the extreme fibre of the cold design compression zone to the extreme fibre of the cold design tension zone of the structural section
e	Flow potential eccentricity; anchor tube thickness
f	Fibres
f_{b0}	Initial equibiaxial compressive yield stress
f_{c0}	Initial uniaxial compressive yield stress
f_{cm}	Average cylinder compressive strength of concrete
$f_{cm,cube}$	Average cube compressive strength of concrete
f_{ctm}	Average splitting tensile strength of concrete
f_f	Tensile strength of GFRP
h_c	Convection coefficient
k'	Parameter obtained through curve fitting
l_b	Development length of bar
l_{splice}	Splice length
l_t	Tail length
m	Matrix
r	Bend radius
s	Slip
s_1	Parameter numerically derived
s_m	Slip at maximum bond stress
s_{pl}	Plastic slip
t	Time

x	Position along embedment length

Roman capital

A	Anchorage length
B	Parameter obtained through curve fitting; bent bar
C	Concrete cover thickness; parameter obtained through curve fitting
D	Damage; diameter; equivalent diameter; deflection limit
E	Elastic modulus; experimental
E'	Storage modulus
E''	Loss modulus
E_{cm}	Average modulus of elasticity of concrete
E_{exp}	Tensile modulus experimentally determined
E_f	Tensile modulus of GFRP bar; tensile modulus of fibres
E_L	Tensile modulus in longitudinal direction
E_m	Tensile modulus of polymeric matrix
E_S	Tensile modulus of steel
E_T	Tensile modulus in transverse direction
F	Applied force
G	Shear modulus
G_f	Fracture energy
G_{LT}	In-plane (or longitudinal) shear modulus
G_{TT}	Transverse shear modulus
K	Tangential contact stiffness
K_c	Ratio of the second stress invariant on the tensile meridian to that on the compressive meridian
$K_{F\text{-}s}$	Bond stiffness (slope of load *vs.* slip curve)
$K_{\tau\text{-}s}$	Bond stiffness (slope of bond stress *vs.* slip curve)

L	Clear span between supports; longitudinal direction; anchor length
L_b	Embedment length
LS	Lap-splice
N	Numerical
P	Mechanical property
P_r	Property value after glass transition, before decomposition
P_u	Property value at ambient temperature
S	Central length in slabs' span; straight bar
T	Temperature; thermocouple label; transverse direction
T_d	Decomposition temperature
T_g	Glass transition temperature
$T_{g,mech}$	Parameter obtained by fitting a hyperbolic tangent function to the experimental data
$T_{g,onset}$	Glass transition temperature obtained based on the onset decay of the storage modulus curve
$T_{ISO\ 834}$	Temperature defined in the ISO 834 fire curve
T_{target}	Target temperature
U_3	Longitudinal displacement field

Greek symbols

α	Thermal expansion coefficient; parameter numerically derived
α'	Parameter numerically derived
α_c	Thermal expansion coefficient of concrete
α_f	Thermal expansion coefficient of GFRP
δ	Phase angle (DMA experiments)
ε_c	Emissivity of concrete
λ	Thermal conductivity
μ	Viscosity

υ_c	Poisson's ratio of concrete
υ_f	Poisson's ratio of fibres
υ_m	Poisson's ratio of matrix
υ_{LT}	Longitudinal Poisson's ratio
υ_S	Poisson's ratio of steel
υ_{TT}	Transverse Poisson's ratio
$\upsilon_{SC\ bar}$	Poissons' ratio of SC bar
$\upsilon_{RB\ bar}$	Poissons' ratio of RB bar
$\upsilon_{RBP\ bar}$	Poissons' ratio of RBP bar
ρ	Density
ρ_i	Reinforcement ratio
ρ_{min}	Minimum reinforcement ratio
Φ	Rebar diameter; external diameter of anchor tube
ψ	Dilation angle
τ	Bond stress; average bond stress
τ_b	Bond strength
τ_m	Maximum bond stress
τ'_m	Local bond strength in bent section of bar

Acronyms

3D	Three-dimensional
ACI	American Concrete Institute
ASTM	American Society for Testing and Materials
BFRP	Basalt fibre reinforced polymer
CDP	Concrete Damaged Plasticity
CFRP	Carbon fibre reinforced polymer
CNR	National Research Council

CSA	Canadian Standard Association
CTE	Coefficient of thermal expansion
DMA	Dynamic mechanical analysis
DSC	Differential scanning calorimetry
EC	Eurocode
FCT	Fundação para a Ciência e a Tecnologia (Portuguese National Foundation for Science and Technology)
FE	Finite element
FEM	Finite elements method
Fib	International Federation for Structural Concrete (*Fédération Internationale du Béton*)
FRP	Fibre reinforced polymer
GFRP	Glass fibre reinforced polymer
ISI	Institute for Scientific Information
ISO	International Organization for Standardization
IST	Instituto Superior Técnico
LERM	Laboratório de Estruturas e Resistência de Materiais (Structures and Strength of Materials Laboratory)
LNEC	Laboratório Nacional de Engenharia Civil (Portuguese National Laboratory of Civil Engineering)
MAPE	Mean absolute percentage error
NSM	Near-surface mounted
PEMAG	Plastic magnitude field
RB	Ribbed bar
RBP	Ribbed bar
RC	Reinforced concrete
SC	Sand coated bar
SCI	Science citation index
TGA	Thermogravimetric analysis

Part I

Introduction and state-of-the-art review

Chapter 1

Introduction

1.1. Context and motivation

In recent years, the use of glass fibre reinforced polymer (GFRP) bars has grown significantly, mostly as internal reinforcement of bridge decks, as they provide an innovative solution to address the stringent durability requirements of reinforced concrete (RC) structures subjected to severe environmental conditions [1–5]. Since GFRP reinforcing bars do not corrode, they potentially enable the adoption of lower concrete cover thicknesses and the design of more durable constructions with lower maintenance demands throughout their service life; furthermore, nowadays, GFRP bars are already commercialized as a cost-competitive alternative to stainless steel bars [6].

Research in the area of GFRP-RC structural members has now advanced to a point where various design codes are available [6–10]; however, these codes provide very limited fire design guidelines comparing to those existing for conventional steel-RC, narrowing the use of FRP reinforcement mostly to structures that do not require fire safety verifications [6–8]. Indeed, the concerns about the behaviour of GFRP rebars at elevated temperatures, namely the severe degradation of their mechanical properties and of their bond to concrete, as well as the above-mentioned lack of guidance regarding fire design, are currently the major obstacles towards the widespread use of these materials in buildings, where the fire accidental action has to be considered in design.

Although FRP bars are very susceptible to elevated temperatures, it has been proven that their adoption in buildings is feasible [11,12]. Indeed, several studies have shown that GFRP-RC beams and slabs can attain significant fire endurances (in some cases well above 90 min) if appropriate constructive provisions are guaranteed (*e.g.* [11–14]). According to existing FRP-RC codes, this includes anchoring the rebars in cooler zones of the structure where bond is less degraded in case of fire and adopting appropriate concrete cover thicknesses to delay the degradation of the rebars' mechanical properties and bond to concrete during the exposure to heat. However, only very general recommendations are provided in existing codes; more detailed provisions about the design of the "cold anchorage length" of the rebars are needed, as well as clear definitions of how "appropriate" concrete cover thicknesses should be derived.

Recently, several studies have drawn the attention to other constructive details not yet covered by current design codes that can significantly affect the fire resistance of FRP-RC flexural members. Despite the

limited research performed in elements with spliced reinforcement, it has been shown that the location and geometry of tension lap splices are also critical details to be considered in fire design [15–21]. In cases where the splicing zones were directly exposed to fire, the use of straight bars and splice lengths designed for ambient temperature conditions was proven to be insufficient to attain fire endurances above 60 min. In fact, the severe loss of bond between GFRP rebars and concrete that occurs for temperatures near the glass transition temperature (T_g) of the rebars led, in some cases, to premature debonding failures in the splices after less than 20 min of fire exposure. In beam applications, a few studies have shown that the adoption of bent bars in tension lap splices can prevent such premature failures, significantly improving the beams' fire endurance. Yet, there is still very scarce information concerning the bond behaviour of bent FRP reinforcement under high temperatures and, to the best of the author's knowledge, no studies have investigated the performance of bent-end lap splices in GFRP-RC slabs exposed to fire. It has however been demonstrated, through a limited number of studies, that bent reinforcement can be adopted in the ends of FRP-RC beams and slabs to shorten the protected end anchorage length.

Until recently, research performed on the bond behaviour of GFRP bars in concrete at elevated temperatures was relatively scarce and constitutive bond laws describing such behaviour were inexistent. Consequently, very few studies were able to relate the structural response of GFRP-RC members during fire with the progressive degradation of the GFRP-concrete bond with the temperature increase. Due to the lack of temperature-dependent bond laws for GFRP bars, most numerical simulations of the thermomechanical behaviour of GFRP-RC elements have considered a perfect bond between the rebars and the surrounding concrete. Although this simplification is deemed acceptable in specific conditions, it can also lead to inaccurate predictions of the members' fire resistance, especially when failure is governed by the loss of bond at elevated temperatures, which is typically the case of insufficiently insulated anchorage zones or splicing zones. This largely explains why, despite the relevance of these aspects and due to the aforementioned reasons, no numerical studies were performed so far comprising structural members with spliced FRP reinforcement exposed to fire.

On the other hand, it has been shown that if continuous bars are adopted between supports and proper insulation is provided in the anchorage zones, the failure of GFRP-RC members is likely to occur due to the tensile rupture of the rebars along the heated span for considerably higher temperatures than those causing the loss of bond with concrete (*i.e.* above T_g); in fact, studies have reported that the rebars' temperature can increase up to 650 ºC, hence well beyond their decomposition temperature, before failing. Under these circumstances, quantifying the degradation of the rebars' mechanical properties at elevated temperatures is necessary in order to predict fire resistance (collapse). However, the experimental results available about the tensile properties of GFRP bars at elevated temperatures still do not cover a sufficiently wide range of temperatures likely to be attained during a fire incident. In fact, very few data have been reported for temperatures above the decomposition temperature of the

polymeric resin, and the reduction of the tensile strength and modulus of GFRP bars above 400 ºC still remains largely unknown.

Despite the meaningful research breakthroughs achieved in the last two decades with respect to the fire behaviour of GFRP reinforcement and GFRP-RC members, the current knowledge is founded on a very limited number of studies which, besides comprising a narrow range of bars and detailing parameters, do not yet provide a comprehensive approach to the subject. Moreover, the accuracy of existing numerical models in simulating the thermomechanical behaviour of GFRP-RC structural members is largely affected by the numerous simplifications adopted by authors to overcome the lack of data regarding both the mechanical and bond properties of GFRP bars at elevated temperature. The development of more comprehensive fire design recommendations is therefore pending on additional experiments and, especially, on the development of accurate simulation tools, allowing to extend the limited range of geometries and constructive details that have been studied experimentally to the present day. This thesis aims at contributing to bridge the above-mentioned gaps in knowledge.

1.2. Objectives and methodology

The overarching objectives of the present thesis were two-fold: (i) to improve the knowledge about the fire behaviour of concrete slabs reinforced with GFRP bars, and (ii) to propose guidelines for fire design, complementing the (limited) recommendations available in existing FRP-RC building codes. The thorough assessment of the structural response of RC members during a fire incident requires a solid understanding of the behaviour at elevated temperature of both the reinforcement and concrete, as well as of their composite action – the rebar-concrete bond behaviour. This thesis was developed based on this reasoning, providing a comprehensive assessment comprising experimental, numerical and analytical methodologies in the following three complementary domains, each representative of a different scale of analysis:

- Thermophysical and mechanical characterization of GFRP bars at elevated temperature;
- Bond behaviour of GFRP bars in concrete at elevated temperature;
- Fire behaviour of GFRP-reinforced concrete slabs strips.

This research considered five types of GFRP bars provided by two manufacturers (*Owens Corning* and *Schöck*) with different constituent materials, diameters, geometries (straight and 90º bent) and surface finishes (sand coated and ribbed), hence exhibiting distinct thermophysical, mechanical and bond properties at both ambient and elevated temperature. In view of these differences, the behaviour of each bar was investigated and compared in all three domains (*i.e.* at the material, interaction with concrete and structural level). Given the wide variety of bars currently available in the construction market, the

aim was therefore to assess how different bars perform at elevated temperature and how this should be considered in future FRP-RC design guidelines.

Regarding the first domain, concerning the characterization of the thermophysical and mechanical properties of the GFRP bars at elevated temperature, the following objectives were defined:

- To characterize the constitution (fibre content) and thermophysical properties (glass transition and decomposition temperatures) of the GFRP bars;
- To quantify their tensile strength and modulus degradation at elevated temperature;
- To propose analytical formulae describing the variation of the GFRP bars' tensile properties with temperature, considering the results obtained in present study and those available in the literature.

To achieve the aforementioned goals, several standard characterization tests were conducted to the GFRP bars at IST (namely differential scanning calorimetry tests, thermogravimetric analyses and calcination tests) and at the *National Laboratory of Civil Engineering* (LNEC) (specifically dynamic mechanical analyses). Next, an extensive campaign of 117 steady-state tensile tests were performed to four types of straight GFRP bars (different materials and diameters) over a large temperature range between 20 ºC (ambient temperature) and 715 ºC, thereby covering the entire glass transition and decomposition of the polymeric resin. The tensile tests were conducted at the *Structures and Strength of Materials Laboratory* (LERM) of IST and allowed quantifying the reduction of both the tensile strength and modulus of the GFRP bars over the referred temperature interval. These results were benchmarked with those available in the literature for other types of GFRP reinforcement and jointly used to propose analytical expressions, obtained based on curve fitting procedures, to describe the degradation of the tensile properties of GFRP bars as a function of temperature.

In the scope of the second domain, concerning the bond behaviour of GFRP bars in concrete at elevated temperature, the following objectives were drawn:

- To compare the bond strength and stiffness degradation with temperature of GFRP bars with different surface finishes (sand coated *vs.* two types of rib profiles), diameters, geometries (straight *vs.* 90º bent) and embedment lengths to concrete (5 *vs.* 9 times the bar diameter);
- To assess the accuracy of empirical models described in the literature for modelling the degradation of the bond strength of GFRP bars with temperature;
- To calibrate temperature-dependent local bond stress *vs.* slip laws for different types of GFRP bars;
- To numerically simulate the bond behaviour of GFRP bars in concrete at elevated temperature;

- To propose development lengths for straight bars with different surface finishes (sand coated and ribbed), as well as development and tail lengths for bent bars as a function of temperature.

To attain the above-mentioned objectives, a large series of 121 pull-out tests were performed to different types of GFRP bars; the bars were embedded in concrete cylinders and tested at different elevated temperatures, under steady-state conditions, from 20 ºC up to 300 ºC (*i.e.*, including temperatures above glass transition but below the resin decomposition). The variation of the bond strength of the bars with temperature obtained in this study was compared with results from the literature; together, these data were used to perform an analytical study to demonstrate the adequacy of the empirical models of Gibson *et al.* [22] and Correia *et al.* [23] in simulating the GFRP-concrete average bond strength reduction with temperature. Using the load *vs.* slip curves obtained from the pull-out tests, local bond laws were calibrated for straight bars with different surface finishes and diameters at different temperatures (up to 300 ºC); the parameters defining such laws were obtained through a numerical procedure that used a *MatLab* code, initially developed by researchers from the University of Minho and later upgraded in IST. The calibrated local bond laws and properties of the GFRP and concrete as a function of temperature were in turn implemented in tridimensional (3D) finite elements (FE) models (developed using the commercial software *ABAQUS Standard*) to simulate the pull-out tests. Firstly, the 3D-FE models were duly validated with experimental results, and then they were used to perform parametric studies with the aim of optimizing the development lengths required to anchor GFRP bars with different surface finishes and geometries under elevated temperatures.

Regarding the third domain, the assessment of the fire behaviour of GFRP-reinforced concrete slabs strips, the study aimed to attain the following objectives:

- To understand in further depth the thermal and thermomechanical behaviour of GFRP-RC slabs during a fire by relating the structural response with the progressive degradation of the bars' tensile and bond properties with temperature;
- To assess the influence of the following parameters on the slabs' fire resistance behaviour: (i) presence of straight or 90º bent tension lap splices directly exposed to fire with different overlap lengths; (ii) presence of cold anchorage zones; (iii) type of reinforcement (material and surface finish); (iv) bar diameter; (v) concrete cover thickness (2.5 *vs.* 3.5 cm), and (vi) concrete strength;
- To develop FE models able to simulate the fire behaviour of GFRP-RC slab strips in which the progressive degradation of the GFRP-concrete bond with increasing temperature is explicitly modelled, allowing to accurately simulate failure of structural members due to the loss of the GFRP bars-concrete interaction;

- To conduct a numerical investigation about the structural effectiveness of the GFRP reinforcement under fire exposure, with particular focus on the efficacy of the anchorage zones and on the influence of lap splicing along the span.

In order to achieve these objectives, the experimental programme consisted of fire resistance tests on 21 GFRP-RC slab strips with continuous and spliced reinforcement (comprising different materials and detailing configurations, as mentioned above), which were simultaneously loaded in bending and heated from the bottom face according to the ISO 834 standard fire curve [24]; these fire resistance tests were conducted in the intermediate scale furnace of LERM at IST. Additionally, 19 flexural tests were performed to identical slabs (adopting a similar loading configuration to that of the fire resistance tests) to evaluate their flexural response (up to failure) under ambient temperature conditions. Regarding the numerical study, 3D FE models were developed in *ABAQUS Standard* to simulate the fire response of five slab strips with sand coated bars. The thermophysical and mechanical properties as a function of temperature of the GFRP bars and concrete were implemented in the FE models, and the GFRP-concrete interaction was modelled by means of previously calibrated local bond laws for different temperatures.

The research presented in this PhD thesis was developed in the framework of the project *Fire Behaviour of Reinforced Concrete Structures with FRP Composites – FireComposite* (project PTDC/ECM/1882/2014), funded by the *Portuguese Nacional Foundation for Science and Technology* (FCT). The project was promoted in a partnership between Instituto Superior Técnico (IST) and University of Minho (UM). This project aimed at investigating the fire behaviour of reinforced concrete members incorporating FRP materials for two different civil engineering structural applications: (i) new construction with FRP reinforcement, the scope of the present thesis, and (ii) strengthening with advanced FRP systems, a topic that is being addressed in an ongoing PhD Thesis [25]. It should also be noted that part of the research developed in this thesis was carried out with the collaboration of four Master students, whose dissertations ([26–29]) are duly referenced in the corresponding chapters.

1.3. Main scientific contributions and publications

The research developed in this thesis provided relevant scientific contributions regarding the mechanical and bond behaviour of GFRP reinforcement under elevated temperatures and the fire performance of GFRP-reinforced concrete structural members. These contributions, further detailed in the following paragraphs, are considered relevant to the scientific community as they significantly enhanced the existing knowledge in the above-mentioned topics. By doing so, the findings of this study may therefore contribute to the improvement of current design recommendations for FRP-RC structures and thus promote the widespread use of GFRP reinforcement in structures subjected to elevated service temperatures (*e.g.* bridge decks in warm climates) and/or likely to be subjected to fire (*e.g.* buildings).

The research developed in this thesis provided a wealth of new experimental, analytical and numerical results which were scarce (or inexistent) in the literature when the thesis was initiated. The extensive campaign of tensile tests performed allowed to extend the existing database of results regarding the tensile strength and modulus of GFRP bars (well-documented in the literature up to 400 ºC) to temperatures up to 715 ºC. The results now available comprise a wider range of temperatures likely to be attained during a fire event and were needed to improve the precision of numerical models simulating the thermomechanical behaviour of GFRP-RC members exposed to fire, essential to define critical temperatures for the GFRP material. Unlike most studies available in the literature, the bars' T_g and decomposition temperature (T_d) were appropriately defined (through standard procedures), therefore allowing to relate the reduction of the tensile properties of the bars with the thermal decomposition processes undergone by their constituent materials (particularly the polymeric resin); it is worth referring that these thermophysical properties of the bars, although important, are typically not provided in the manufacturers' catalogues. In the framework of the aforementioned experiments, the following SCI[1] journal paper was published:

1. Rosa, I.C., Firmo, J.P., Correia, J.R. (2022). *Experimental study of the tensile behaviour of GFRP reinforcing bars at elevated temperatures.* Construction and Building Materials, Vol. 324. pp. 126676.

With respect to the bond behaviour at elevated temperatures, the experiments conducted in the frame of this thesis allowed to quantify the bond strength and stiffness degradation with temperature (up to 300 ºC) of GFRP bars with different surface finishes, diameters, geometries and embedment lengths in concrete. The numerical calibration of temperature-dependent local bond laws for different GFRP bars, describing their pre- and post-peak bond stress *vs.* slip response, is one of the most relevant research contributions. These laws are needed to accurately simulate the behaviour at elevated temperature and under fire exposure of GFRP-RC members – so far, the laws proposed in previous studies had only described the pre-peak stage or were obtained based on the residual behaviour after exposure to elevated temperature. The numerical simulations of the bond behaviour, by means of FE models explicitly considering the above-mentioned laws, allowed to more precisely model the (relatively complex) GFRP-concrete interaction at elevated temperatures, especially concerning the behaviour of bent FRP reinforcement, which, up to this work, had not yet been simulated at high temperatures. Another output of this thesis with practical relevance was the definition of development lengths required to anchor straight and bent GFRP bars in RC beams and slabs as a function of temperature – this is a very useful result for the purpose of designing GFRP anchorages, which was also not available in the literature. The investigations concerning the bond behaviour of GFRP bars at elevated temperature resulted in the following three publications in SCI journals:

[1] SCI stands for the Science Citation Index, defined by the Institute for Scientific Information (ISI).

2. Rosa, I.C., Firmo, J.P., Correia, J.R., Barros, J.A.O. (2018). *Bond behaviour of sand coated GFRP bars to concrete at elevated temperature – Definition of bond vs. slip relations,* Composites Part B, Vol. 160, pp. 329-340.
3. Rosa, I.C., Firmo, J.P., Correia, J.R., Mazzuca, P. (2021). *Influence of elevated temperatures on the bond behaviour of ribbed GFRP bars in concrete.* Cement and Concrete Composites, Vol. 122, pp. 104119.
4. Rosa, I.C., Arruda, M.R.T, Firmo, J.P., Correia, J.R. (2022). *Bond behaviour of straight and bent GFRP bars at elevated temperature: pull-out tests and numerical simulations.* Journal of Composites for Construction, Vol. 26, Issue 3, pp. 04022028.

Together with the formerly described contributions, this thesis provided an in-depth understanding of the fire behaviour of RC slabs comprising GFRP reinforcement and delivered new insights about the importance of several constructive details to the fire resistance of these structural members, most of which are not yet covered by current FRP-RC building codes. In this regard, the thesis provided recommendations concerning (i) the appropriate location and length of tension lap-splices and end anchors, (ii) the potential of using bent reinforcement in the ends of splicing bars to improve the slabs' fire resistance, and (iii) the possibility of adopting lower concrete cover thicknesses than those currently prescribed in design guidelines, namely the Canadian design code [8], without compromising the fire endurance, thus leading to more economic (and sustainable) designs. The study developed herein also presented preliminary investigations on the influence of the bar diameter and concrete strength on the fire behaviour of GFRP-RC slabs, which might serve as basis for future research.

The thesis presents an approach for simulating the fire behaviour of GFRP-RC members with continuous or spliced reinforcement that considers (i) the explicit modelling of the bond behaviour of the bars through local bond laws calibrated as a function of temperature, and (ii) the degradation of the tensile properties of the bars up to 715 ºC, defined according to experimental data. To the best of the author's knowledge, only one study ([30]) had modelled the GFRP-concrete interaction through calibrated bond laws; however, unlike the ones considered in this thesis, those laws were not derived from bond tests performed on the same bars used in the fire tests and the variation of the tensile properties of the bars considered for temperature above 500 ºC lacked experimental validation. The numerical methodology adopted in the present thesis thereby contributed to a significant improvement in the accuracy of FE models to simulate the thermomechanical behaviour of RC structural members comprising FRP reinforcement, particularly with respect to the anchorage zones and lap splices. The experimental and numerical studies performed on the fire behaviour of GFRP-RC slabs strips resulted in the following three publications in SCI journals:

5. Rosa, I.C., Santos, P., Firmo, J.P., Correia, J.R. (2020). *Fire behaviour of concrete slab strips reinforced with sand-coated GFRP bars.* Composite Structures, 244, 112270.

6. Rosa, I.C., Firmo, J.P., Correia, J.R.. *Fire behaviour of GFRP-reinforced concrete slab strips – effect of straight and 90º bent tension lap splices*. Submitted for publication in the Engineering Structures journal (revision requested in March 2022).
7. Duarte, A.P.C., Rosa, I.C., Arruda, M.R.T., Firmo, J.P., Correia, J.R.. *Three-dimensional finite element modelling of the thermomechanical response of GFRP-reinforced concrete slab strips subjected to fire.* Journal of Composites for Construction, Vol. 26, Issue 5, 04022044.

Finally, grounded on the solid knowledge obtained in the field, this thesis presents a comprehensive state-of-the-art review on the fire performance of GFRP-reinforced concrete structural members, encompassing the mechanical and bond behaviour of GFRP reinforcement at elevated temperatures and providing an overview of existing guidelines for the fire design of FRP-RC structures. It is worth noting that the main findings of this thesis are included in this review, allowing to frame the novelty and importance of the results obtained herein with those currently available in the literature. This literature review resulted in the following SCI paper:

8. Rosa, I.C., Firmo, J.P., Correia, J.R. *State-of-the-art review on the fire behaviour of FRP-RC members.* Under preparation – to be submitted in June 2022.

In addition to the aforementioned 8 publications in SCI international journals, the research developed within the scope of this PhD thesis was also published in 10 international conference papers [31–40] and 7 national conference papers [41–47].

1.4. Outline of the document

The present thesis document is organized into eight chapters, which were grouped in the following five parts:

- Part I – Introduction and state-of-the-art review (Chapters 1 and 2);
- Part II – Properties of GFRP bars at elevated temperature (Chapter 3);
- Part III – Bond behaviour of GFRP bars in concrete at elevated temperature (Chapters 4 and 5);
- Part IV – Fire behaviour of GFRP-reinforced concrete slab strips (Chapter 6 and 7);
- Part V – Conclusions and future developments (Chapter 8).

The thesis document was prepared based on the 8 international journal papers cited in the previous section. However, the original content of the papers was slightly edited in order to provide an interconnected discussion of the different subjects addressed in this study, while removing unnecessary

repetitions and maintaining the outline of a standard thesis. Table 1.1 summarizes the general organization of the thesis and the corresponding SCI journal papers included in each chapter.

Table 1.1. General outline of the thesis, including the SCI journal papers associated with each chapter.

Thesis parts	Chapters	Journal papers [1]
I	1. Introduction	-
	2. State-of-the-art review	8
II	3. Thermophysical and mechanical properties of GFRP bars at elevated temperature	1
III	4. Pull-out tests on GFRP bars embedded in concrete at elevated temperature	2, 3, 4
	5. Numerical modelling of the bond behaviour of GFRP bars at elevated temperature	2, 3, 4
III	6. Fire resistance tests in GFRP-reinforced concrete slab strips	5, 6
	7. Numerical modelling of the fire behaviour of GFRP-reinforced concrete slab strips	7
IV	8. Conclusions and recommendations for future research	-

[1] Numbering defined in Section 1.3.

The first and present chapter introduces the thesis subject, describing the context and motivation behind this research, its main objectives, the methodology adopted and lastly the main scientific contributions.

Chapter 2 presents a state-of-the-art review on the fire behaviour of FRP-reinforced concrete structural members. First, the thermophysical and mechanical behaviour of GFRP bars at elevated temperature is addressed, and thereafter the influence of elevated temperatures on the bond interaction between the bars and concrete is examined. Next, the available experimental and numerical studies on the fire performance of FRP-RC flexural members are reviewed. Finally, the existing FRP-RC fire design guidance is presented and discussed in light of the most recent research breakthroughs on the subject.

The experimental characterization of the GFRP bars used in this study is presented in Chapter 3. It begins with the description of the standard thermophysical characterization tests performed to the GFRP material. The second part of this chapter presents the tensile tests performed to the bars at elevated temperatures, comprising the description of the test series and experimental procedures, the discussion of the results obtained and their comparison with those available in the literature; at the end of the chapter, analytical expressions proposed to describe the variation of the tensile strength and modulus of the bars as a function of temperature are presented.

Chapter 4 concerns the experimental studies on the bond behaviour of GFRP bars in concrete. Firstly, the test programme and procedure used in the pull-out tests are detailed, and in the following subsections

the results obtained for different types of GFRP bars are presented. In the final part of the chapter, the results are compared to those available in the literature and the conclusions of an analytical study carried out to describe the variation of the bond strength with temperature are drawn.

Further studies about the GFRP-concrete interaction at elevated temperature are presented in Chapter 5, in this case through a numerical approach. In this regard, the first part of the chapter addresses the numerical calibration of temperature-dependent bond stress *vs.* slip constitutive relationships for different temperatures and types of bars. Then, the accuracy of these relationships to numerically simulate the pull-out tests is validated. The final part of the chapter presents the description of the numerical procedure and results of parametric studies, carried out to assess the influence of the bars' surface finish and geometry on their bond behaviour at elevated temperature.

The sixth chapter of the thesis addresses the intermediate-scale fire resistance tests performed to GFRP-RC slab strips. First, the test programme and procedure are detailed, including the flexural tests carried out at ambient temperature. Next, the results of the latter tests are examined, regarding both the mechanical response and failure modes of the slab strips. Finally, the results of the fire resistance tests are presented and discussed, namely with respect to the thermal behaviour, deflection response and failure modes.

Chapter 7 comprises the numerical simulation of the fire resistance tests on GFRP-RC slab strips described in the previous chapter. Firstly, a detailed description of the FE models and numerical procedure is provided. Subsequently, a comparison between the experimental and numerical responses is performed regarding both the thermal and thermomechanical behaviour of the slab strips during fire exposure. Finally, in the last part of the chapter, the numerical outputs obtained are analysed in further depth to investigate the structural efficiency of the GFRP reinforcement during fire exposure, with particular emphasis on the behaviour of the end anchorage zones of the bars and tension lap splices located in the fire exposed span.

The last chapter, Chapter 8, summarizes the main conclusions drawn from this research and proposes recommendations for future developments on subjects that, based on the experience gathered from this research, should be assessed to enable the safe use of GFRP reinforcement in structures where the fire action has to be considered in design.

Chapter 2

State-of-the-art review

2.1. Introduction

The durability and in-service performance of reinforced concrete (RC) structures are often compromised by the corrosion of steel reinforcement, which require frequent maintenance and costly repairs to guarantee the intended service life, especially in more aggressive environments. In this regard, different stakeholders of the construction sector have been promoting the design of more durable structures, through the adoption of materials with better performance against environmental degradation agents and with lower maintenance [1]. In this context, the use of glass fibre reinforced polymer (GFRP) bars as internal reinforcement of concrete structural members has grown in recent years, as they offer a non-corrodible and cost-competitive alternative to stainless steel reinforcement.

Among the different types of FRP bars available, GFRP bars are the ones more frequently used as they are the most inexpensive, namely compared to carbon-FRP (CFRP) bars, more often used in strengthening applications [48]. To date, GFRP rebars have been mainly used in the rehabilitation and construction of bridge decks, but also in barrier walls and ground slabs, where fire safety is not typically a primary design requirement. To a lesser extent, applications have also been made in industrial, medical and research facilities [49], as well as in parking garage slabs [50,51] and even in a four-storey residential building [52]. However, the potential for replacing steel with GFRP reinforcement in buildings remains largely unexploited, mostly owing to concerns and the limited fire design guidance available in FRP-RC codes [6–8].

The concerns about the possibility of GFRP-RC structural members fulfilling fire safety requirements for buildings applications result from the fact that the mechanical and bond properties of GFRP bars are very susceptible to degradation under exposure to elevated temperatures. Two main reasons explain the lack of design guidance in this respect: (i) the limited availability of comprehensive studies on the fire behaviour of GFRP reinforcement and GFRP-RC members; and (ii) the absence of material standards about the geometry, manufacturing process and properties of GFRP bars – this results in a large diversity of materials with different thermophysical, mechanical and bond properties at both ambient and elevated temperatures.

The most relevant state-of-the-art review about the fire performance of GFRP-RC structural members was published by Bisby *et al.* [53], now almost a decade ago, pursuing previous reviews on this topic [54–56]. Since then, the knowledge in this field has achieved significant progress, demonstrating that

GFRP-RC members are able to meet the fire safety requirements prescribed in building codes, provided that certain provisions are implemented. Furthermore, recent studies have shown that there are several critical aspects to the members' fire endurance that have not yet been addressed in a comprehensive manner in the literature and, consequently, were not susceptible to be incorporated in the latest versions of existing FRP-RC design codes.

This chapter presents an updated state-of-the-art review about the fire performance of GFRP-RC structural members, discussing the most important factors that govern fire resistance at different scales: (i) the GFRP material level, (ii) the bond of GFRP bars to concrete, and (iii) the structural fire behaviour of GFRP-reinforced concrete flexural members. Section 2.2 discusses the influence of elevated temperature on the thermal and mechanical properties of GFRP bars. Section 2.3 reviews their bond behaviour at elevated temperature, including experimental, analytical and numerical studies of the bars-concrete interaction at elevated temperatures. Section 2.4 discusses the fire behaviour of GFRP-RC flexural members, reviewing fire resistance tests and numerical analyses of their thermal and thermomechanical behaviour. Section 2.5 reviews existing codes for structural fire design of GFRP-RC members and provides an overview of aspects that, based the current state of knowledge, could be improved in future revisions of those codes. Finally, the main conclusions and recommendations for further research are summarized in Section 2.6.

2.2. Behaviour of GFRP rebars at elevated temperature

2.2.1. Thermal degradation of resins and fibres

GFRP bars are generally manufactured by pultrusion, comprising unidirectional fibre reinforcement (rovings) in the axial direction, embedded in a polymeric matrix. The matrix of GFRP bars is generally composed by an epoxy or vinylester thermosetting resin, and it may also include fillers and additives. The engineering properties of the bars depend on the type and volume fractions of resin and fibres, as well as on their interaction. Due to their organic nature, polymeric resins undergo significant thermal, chemical and physical changes under elevated temperatures, presenting stiffness and strength reductions, which also weakens their composite action with fibres [57]. Consequently, the mechanical properties of GFRP bars, as well as their bond to concrete, become severely deteriorated when the material is exposed to elevated temperatures. Being anisotropic materials, GFRP bars behave differently in the longitudinal and transverse directions, with longitudinal properties (fibres direction) being fibre-dominated, and transverse properties (orthogonal to the fibres) being matrix-dominated. Not only the bars present different properties at ambient temperature depending on the direction considered, but the resins and fibres themselves also experience different magnitudes of deterioration under elevated temperature, the former being more susceptible to temperature than the latter. As a consequence, the variation of the thermal and mechanical properties of

GFRP bars with temperature depends on whether they are fibre- or matrix-dominated, being largely affected by the properties of their constituent materials.

When GFRP bars are exposed to elevated temperature, relevant changes in the material occur when the glass transition temperature (T_g) and the decomposition temperature (T_d) of the polymeric matrix are approached and exceeded; the T_g marks the transition from a glassy/vitreous (hardened) state to a softened state. The T_g and T_d are relevant parameters to consider when selecting FRP bars for structural applications, as the glass transition and decomposition processes of the matrix are associated with a significant decrease of the bars' mechanical properties and of their bond to concrete. Thermoset resins used in GFRP bars (epoxy and vinylester) are greatly affected by the increase in temperature, typically presenting a T_g in the range of 93 ºC to 120 ºC [6] and a T_d between 250 ºC and 400 ºC [57]. Conversely, E-glass fibres (the ones most commonly used) are inorganic materials and therefore present higher stability under high temperatures, softening at ~830 ºC and melting at ~1070 ºC [57]. For this reason, the fibres are able to carry a significant portion of the (tensile) load even after the resin is fully decomposed.

The transition of polymers between a glassy to a softened state, and later to a decomposed state, is a gradual process that develops over a certain temperature range, yet the T_g and T_d of the bars (*i.e.* of the resin) are normally specified as a single reference value. Different testing techniques can be used to characterize the softening and decomposition reactions of FRP materials, thereby resulting in different values of T_g and T_d for the same material [57,58]. Dynamic mechanical analysis (DMA) or differential scanning calorimetry (DSC) are the most frequently used test methods to estimate the T_g. DMA provides different estimates of the T_g based on the onset decay of the storage modulus curve ($T_{g,onset}$), and on the peaks of the loss modulus and loss factor (also known as tangent delta) curves, which define respectively lower, intermediate and upper bounds of the T_g. Despite the lack of consensus, the $T_{g,onset}$ is often referred in the literature as the reference (conservative) value for the glass transition temperature, as recommended in ACI 440.1R-15 [6]. In case of DSC tests, the T_g is identified as the first notable shift in the baseline response of the heat flow *vs.* temperature curve. Thermogravimetric analysis (TGA) or DSC are the most common techniques to determine the T_d of the resin, being based, respectively, on the evolution with temperature of the mass loss or of the heat release/absorption of the polymer with temperature. The criteria to define the T_d is not clearly defined in test standards, however it is usually set as the middle temperature of the remaining mass curve. Both T_g and T_d are affected by the heating rate of the FRP sample – the temperature range over which the material decomposes increases with the heating rate, as glass transition and decomposition are kinetic processes [57]; these thermophysical properties are also influenced by the atmosphere (air or nitrogen) in which the tests are performed, as the decomposition reaction is accelerated in the presence of oxygen [57].

Unlike steel or concrete, the thermal and mechanical properties of GFRP bars are not yet standardized, and therefore can vary greatly among manufacturers according to the production technique, which may involve different constituents (types and volumetric proportions of resin and fibres), curing conditions,

geometries and surface finishes. In addition, the temperature effects on the properties of GFRP bars depend also on extrinsic parameters related with the exposure environment, and the heating and loading history (intensity and duration). The above-mentioned aspects explain the difficulty in generalizing the behaviour of GFRP bars at elevated temperature.

2.2.2. Thermal properties

Modelling the thermal response of GFRP-RC structural members exposed to fire requires knowing the variation with temperature of the thermal properties of both concrete and GFRP reinforcement, including their density, specific heat and thermal conductivity, and also the emissivity of concrete (that of the GFRP rebars is not relevant as they are embedded in concrete and therefore do not contribute to the heat transfer by radiation). Albeit the thermal properties of concrete as a function of temperature are well defined in building codes, fewer information and guidance is available for GFRP bars. Experimental data are however available for a variety of FRP laminates and plates, and FRP products used in the automotive and aerospace industries, based on which several authors (*e.g.* [59–62]) have proposed empirical models to describe the variation of the thermophysical properties of FRP materials with temperature.

2.2.2.1. Density

The fibres generally represent around 50 to 70% of the total volume of FRP bars [6] and, unlike the resin, they are chemically and physically stable under high temperatures; the reduction of the density of the material with temperature is therefore mostly due to the thermal decomposition of the matrix [1,6]. Thermogravimetric analysis conducted in [19,63–68] confirmed that the mass of GFRP bars presents minor changes until the decomposition of the resin begins (roughly around 250-400 ºC [57]), from which it is greatly reduced, as shown in Figure 2.1. During the decomposition of the resin, most of its mass is converted into volatiles, some of which flammable and toxic, while a small percentage is decomposed into char; this chemical reaction involves the release of heat, smoke and soot when it occurs in air [57] (in nitrogen, it is endothermic, as discussed ahead). According to Mouritz and Gibson [57], the percentage of resin mass converted into volatiles is 80-90% in epoxy, and 90-95% in vinylester and polyester resins. Therefore, given that the matrix is almost fully decomposed into volatiles, the remaining mass of the bars after the pyrolysis of the resin corresponds mainly to the fibres, whose density, strength and stiffness present high retention for fairly higher temperatures than the resin's T_d. It is worth noting that the degradation of the thermophysical properties of GFRP bars is a function of temperature and also of time [61]. Accordingly, the density, depends on the temperature and also on the heating rate, with faster heating (corresponding to a shorter heating time) resulting in lower decrease of density [69].

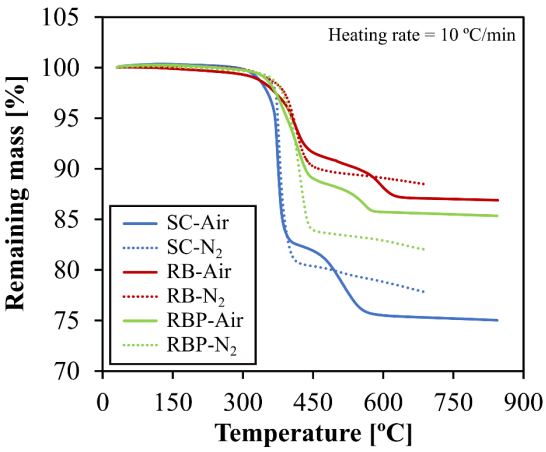

Figure 2.1. Remaining mass of different types of GFRP bars (one sand coated (SC) and two ribbed bars (RB and RBP)) as a function of temperature, obtained from TGA tests conducted in air and nitrogen (N_2) atmospheres (adapted from Rosa *et al.* [65], *cf.* Section 3.3).

2.2.2.2. Thermal conductivity

As for the mechanical properties, the thermal conductivity of GFRP bars is a directionally dependent material property. GFRP bars have very low thermal (and electrical) conductivity in comparison with steel, in both longitudinal and transverse directions, a characteristic they share with other types of FRP bars [1,57], except CFRP bars, which are highly conductive (thermally and electrically) in the fibres direction [1,57,66]. Hence, GFRP reinforcement normally has a minor contribution to the heat transfer within the RC structural member, owing to their low thermal conductivity and reduced geometric percentage in comparison with concrete [70,71].

To the best of the author's knowledge, there are no experimental data about the variation of the thermal conductivity of GFRP bars with temperature. The few results available for GFRP plates [69], CFRP bars [66] and CFRP plates/laminates [59,72–74] have however shown that the longitudinal and transverse thermal conductivities of FRP composites typically increase from ambient temperature up to temperatures near (but below) the matrix decomposition. According to Mouritz and Gibson [57], referring to the experimental study of Dimitrienko [69] in GFRP plates (see Figure 2.2), in the initial stages of heating, the thermal conductivity of FRP composites increases due to the increase in the conductivity of the matrix and fibres; however, when the decomposition of the matrix begins, the conductivity decreases considerably due to the formation of a porous char layer and afterwards, after the full pyrolysis of the matrix, the conductivity increases again as a result of the increasing conductivity of char and fibres with temperature [57,69]. Due the lack of experimental data, simplified models such as that proposed by Bai *et al.* [75] (depicted in Figure 2.2, derived based on the rule of mixtures) have been used to describe the variation of the thermal conductivity of GFRP bars in numerical simulations.

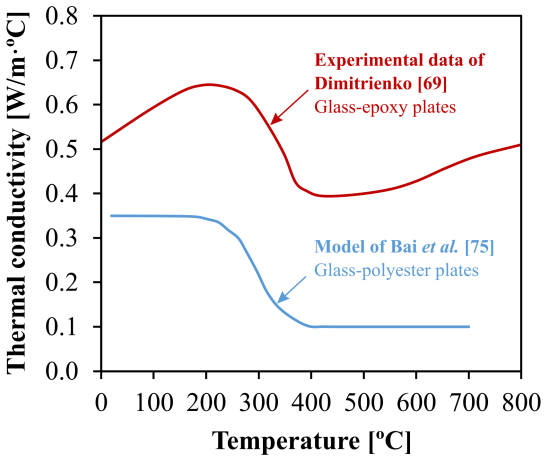

Figure 2.2. Through-thickness thermal conductivity of GFRP composites as a function of temperature: experimental data of Dimitrienko [69] and model proposed by Bai *et al.* [75].

2.2.2.3. Specific heat

The specific heat of FRP composites can be determined through DSC analysis and depends on the mass fraction and specific heat of the constituent materials, including the matrix, fibres and charred material [57,69]. Presently, not much information is available about the variation of the specific heat of FRP bars with temperature. The existing experimental data on CFRP bars and plates [59,66,72,73] indicates that similarly to the thermal conductivity, the specific heat of FRP composites also experiences a non-monotonic variation with temperature – when tested in nitrogen (within concrete, the environment is non-oxidative) it increases almost linearly when heated above ambient temperature, then presents a sharp peak near the onset of the matrix decomposition and an acute decrease afterwards due to the endothermic nature of resin decomposition [59,66]. Due to the absence of specific data for GFRP bars, the model proposed by Bai *et al.* [75] for GFRP plates (Figure 2.3, also derived using the rule of mixtures) has been used for numerical modelling purposes.

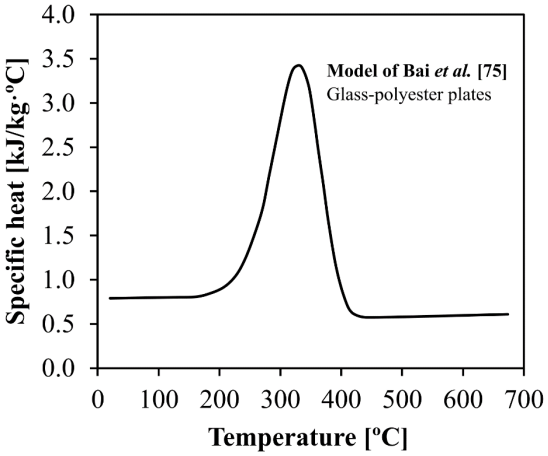

Figure 2.3. Model for the variation of the specific heat of GFRP-polyester plates as a function of temperature proposed by Bai *et al.* [75].

2.2.3. Mechanical properties

Due to the susceptibility of the GFRP reinforcement to elevated temperature, the degradation of its mechanical properties (namely strength) can be the governing phenomenon leading to the failure of GFRP-RC members exposed to fire. To accurately simulate the thermomechanical response of these members, and ultimately predict their fire resistance, it is required that both the thermal and mechanical behaviour of the bars and concrete (as well as the interaction between them) as a function of temperature is well defined. Regarding the mechanical behaviour, the most relevant properties respect to the materials' tensile modulus and strength and thermal expansion coefficient. As shown next, the tensile behaviour of GFRP bars at elevated temperature has been the object of considerable research, while little is still known about the influence of high temperatures on their compressive and shear properties, as well as on their longitudinal and transverse thermal expansion coefficients.

2.2.3.1. Thermal expansion coefficient

The anisotropy of FRP bars is also reflected on the different coefficients of thermal expansion (CTE) in the longitudinal and transverse directions: at ambient temperature, the longitudinal CTE is relatively low and governed by the properties of the fibres, while the transverse CTE is considerably higher than the former and predominantly controlled by the matrix. These coefficients depend on the type of fibre, resin and of their corresponding volumetric fractions [6,10]. The longitudinal CTE of GFRP bars is of the same order of magnitude of that of concrete (and steel) and, for fibre volume fractions ranging from 50% to 75%, it has been reported to range between 5 and 10 × 10^{-6}/ºC [6,10,76,77]; as reference, the (isotropic) CTE of concrete typically varies between 7.2 and 10.8 × 10^{-6}/ºC [6], depending on the aggregate type (higher in concrete with siliceous aggregates than with carbonate aggregates [78,79]).

The transverse CTE of GFRP bars is significantly higher than that in the longitudinal direction (hence greater than that of concrete) owing to the higher thermal expansivity of polymeric matrices in comparison to glass, carbon or basalt fibres [10]. According to current FRP-RC design guides [6,10], the transverse CTE of GFRP bars at ambient temperature typically varies between 21 and 23 × 10^{-6}/ºC, although values ranging from 23 to 56 × 10^{-6}/ºC have been reported in the literature [76,77,80–84]. Based on the experimental data available, the transverse CTE of GFRP bars can therefore be 4 to 8 times greater than that of concrete.

The differential thermal expansion between GFRP bars and concrete has raised concerns about the structural response of GFRP-RC members during fire, given that the significant increase in radial expansion of the bars can cause splitting cracks; ultimately, if the confining action of the concrete is insufficient, it can lead to spalling of the concrete cover. Under these circumstances, the bond between the bars and the concrete can be abruptly reduced and the bars become directly exposed to fire, resulting

in their (much) faster heating and degradation of mechanical properties. The effects of the (transverse) thermal incompatibility between concrete and GFRP bars on the cracking behaviour of concrete were investigated by several authors [76,80,81,85–89], yet available studies are limited to fairly moderate temperatures (up to 80 ºC), well below the relevant temperature range in a fire scenario. These studies confirmed that relatively wide bar spacings and minimum concrete covers should be adopted to reduce the potential of spalling due to rapid heating [80,87–89].

The only data available at temperatures more likely to be attained during a fire was obtained by Silverman [83], who measured the transverse thermal expansion of GFRP laminates with different types of resins in the range of 25 ºC to 400 ºC and found that the transverse CTE experienced a significant increase between 150 ºC and 200 ºC, which apparently coincided with the glass transition of the bars. This result indicates that the detrimental effects arising from thermal expansion of FRP bars could be a matter of concern at the maximum temperatures likely to be attained by the rebars during a fire. Regardless of the potential higher risk of spalling due to the high values of transverse CTE, the findings of fire resistance tests performed in GFRP-RC flexural members (*cf.* Section 2.4.1) have shown that, even with relatively low concrete covers (*e.g.* 2 times the bar diameter) these members are not necessarily more prone to spalling that those reinforced with steel bars [70,89–91].

2.2.3.2. Strength and elastic modulus

The greatest concern about the use of FRP reinforcement in buildings is related to the fact that, compared to steel, its strength and modulus (and bond to concrete, *cf.* Section 2.3) are more intensely reduced with the temperature increase [92], consequently affecting both the mechanical performance at elevated temperature (*i.e.,* during thermal exposure) and the (post-fire) residual mechanical performance of the bars. Over the past two decades, numerous studies have contributed with extensive data about the (longitudinal) tensile strength [15,19,63,65,69,77,93–107] and modulus [65,94–97,99,101,102,107] of various types of GFRP bars at elevated temperature – Table 2.1 presents a summary of those studies.

Figure 2.4 and Figure 2.5 present the data gathered from the literature concerning the normalized variation (with reference to ambient temperature) of the tensile strength and modulus of GFRP bars as a function of temperature. The results depicted in the figures have high scatter, particularly for temperatures between the bars' T_g and T_d, showing that the degradation rate of the mechanical properties of GFRP bars with temperature varies greatly among studies, mainly due the large diversity of materials considered. In other words, despite all GFRP bars experiencing a progressive reduction of their tensile properties with temperature, the magnitude of the degradation depends significantly on the type of resin, fibre ratio and thermophysical properties (T_g and T_d) of the bars.

Table 2.1. Summary of mechanical tests on GFRP rebars at elevated temperature.

Reference	Conditioning	Glass transition		T_d [ºC]	Measured properties	Temperature range [ºC]
		T_g [ºC]	Method			
AlAjarmeh *et al.* [111]	Bare bars	126	DSC	-	Compressive strength	23–140
Rosa *et al.* [65]	Bare bars	98–157	DMA (onset *E'*)	374–400	Tensile strength and modulus	20–715
Zhou *et al.* [102]	Bare bars	-	-	-	Tensile strength and modulus	20–400
Rozsypalova *et al.* [104]	Bare bars	110–120	-	-	Tensile strength	20–298
McIntyre [19]	Bare bars	59–86	DMA (onset *E'*)	390–408	Tensile strength	20–570
Najafabadi *et al.* [105]	Bars embedded in concrete	110	-	-	Tensile strength	25–800
Ashrafi *et al.* [106]	Bare bars	95	-	-	Tensile strength	15–300
Hajiloo *et al.* [107]	Bare bars	110–140	DSC/DMA (onset *E'*)	-	Tensile strength and modulus	25–500
Ashrafi *et al.* [93]	Bare bars	110	-	-	Tensile strength	25–450
McIntyre *et al.* [94]	Bare bars	59	DMA (onset *E'*)	391	Tensile strength and modulus	25–495
Wang and Zha [95]	Bare bars	-	-	-	Tensile strength and modulus	10–500
Robert and Benmokrane [63]	Bare bars	120	DSC	-	Tensile and transverse shear strengths	-100–325
Weber [15]	Bare bars	-	-	-	Tensile strength	20–500
Abbasi and Hogg [96]	Bare bars	-	-	-	Tensile strength and modulus	20–120
Wang and Kodur [97]	Bare bars	-	-	-	Tensile strength and modulus	20–500
Dimitrienko [98]	Bare bars	-	-	-	Tensile strength	20–300
Dimitrienko [69]	Bare bars	-	-	-	Tensile strength	20–400
Tanano *et al.* [99]	Bare bars	-	-	-	Tensile strength	20–350
Clarke [100]	Bare bars	-	-	-	Tensile strength	20–400
Kumahara *et al.* [101]	Bare bars	-	-	-	Tensile strength and modulus	20–400
Chaallal and Benmokrane [77]	Bare bars	-	-	-	Tensile strength	20–400

Note: Most of the studies listed above concern tests in steady-state conditions. Studies [19,107] performed tests in both steady- and transient-state regimes.

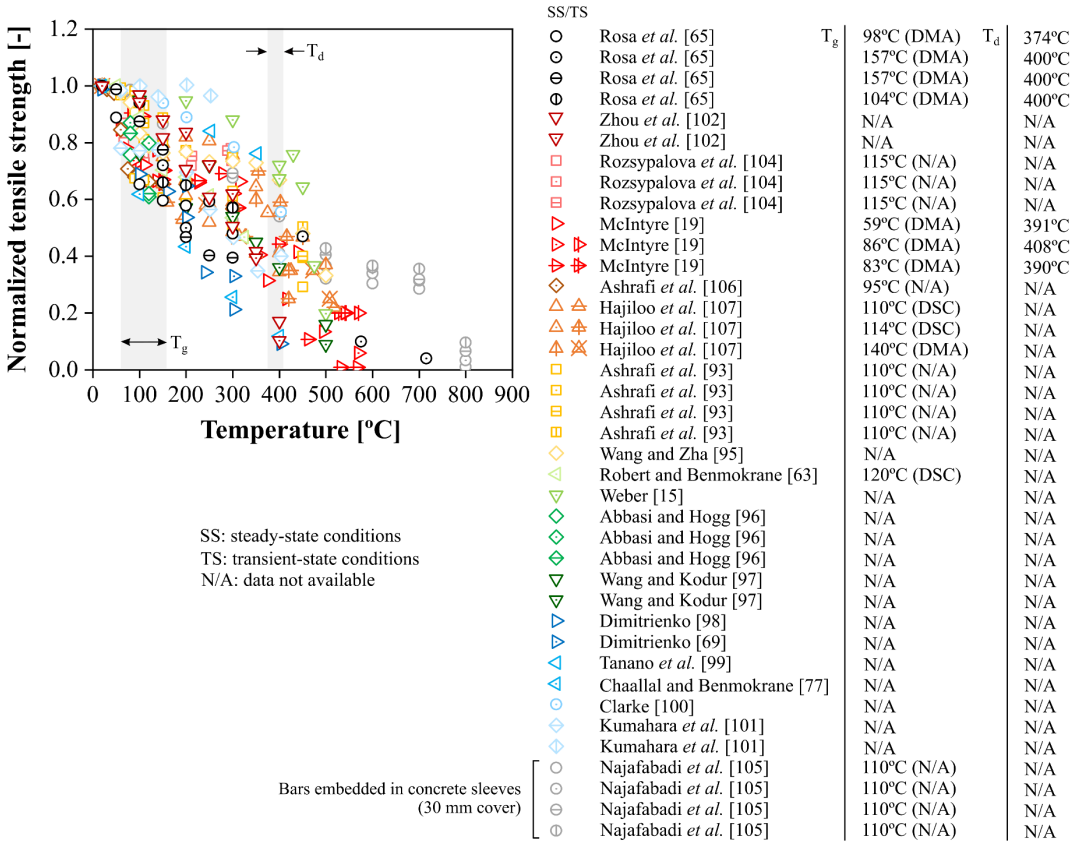

Figure 2.4. Normalized longitudinal tensile strength of GFRP bars as a function of temperature (average results).

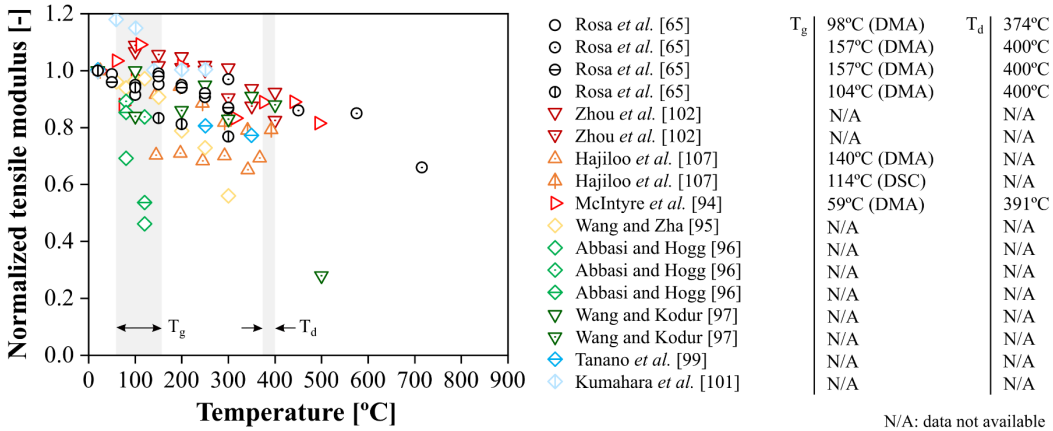

Figure 2.5. Normalized longitudinal tensile modulus of GFRP bars as a function of temperature (average results).

Tensile tests can be conducted according to two heating/loading procedures: (i) steady-state regime, in which the test specimen is loaded up to failure under constant temperature; or (ii) transient-state regime, in which temperature is gradually increased until failure of the specimen, while it is subjected to a sustained load. The determination of the tensile strength of GFRP bars (Figure 2.4) has been mostly accomplished through steady-state tensile tests; fewer studies, among them those of McIntyre [19] and Hajiloo *et al.* [107], also included transient-state regime tests, which are more representative of the thermomechanical conditions experienced by the reinforcement during exposure to fire. According to these tests and as depicted in Figure 2.4, steady-state tests typically provide slightly higher, thereby more conservative, reductions of the bars' strength with increasing temperatures, and therefore are suitable to be considered for design purposes. The results plotted in Figure 2.5 concerning the tensile modulus respect to steady-state regime tests.

As depicted in Figure 2.4, the tensile strength in the longitudinal direction of GFRP bars is relatively well characterized up to 500 ºC, with much less data being available for higher temperatures up to 800 ºC ([65,103,105]). Overall, previous studies have shown that the tensile strength typically presents a gradual two-step degradation with temperature, as exemplified in Figure 2.6 (see also Figure 2.8), each step relating to the different stages of the thermal degradation of the constituent materials. The first steep decrease of tensile strength occurs due to the softening of the resin, which reduces the matrix's ability to efficiently transfer stresses amongst the fibres. The data indicates that in the T_g range, the tensile capacity of the bars can be reduced up to almost 40% in comparison with the strength at ambient temperature [65]. This first stage is then followed by a much less pronounced strength reduction, which extends up to temperatures near the T_d. From the T_d onwards, a second severe strength reduction occurs, this time associated with the decomposition of the matrix and its combustion (if in the presence of oxygen). The severity of the degradation at each temperature naturally depends on the thermophysical properties of the bars (T_g and T_d), which are often unknown, preventing a deeper analysis of the results.

This is well demonstrated in Figure 2.4 which shows that the tensile strength of GFRP bars at 400 ºC (near T_d) can vary from around 30%, as reported in Weber [15], up to 90%, as obtained in Zhou *et al.* [102] and Dimitrienko *et al.* [69]; unfortunately, none of these studies reported the T_g or T_d of the rebars, preventing the assessment of the degrees of glass transition and decomposition. The (limited) data available for temperatures above 500 ºC, which exceed the typical values of T_d ([19,65,97,105]), show that the tensile strength of GFRP bars is further reduced, but is not negligible in several studies – this is due to the fact that glass fibres are able to retain a considerable fraction of their original tensile strength (and modulus) before their softening temperature is reached [57].

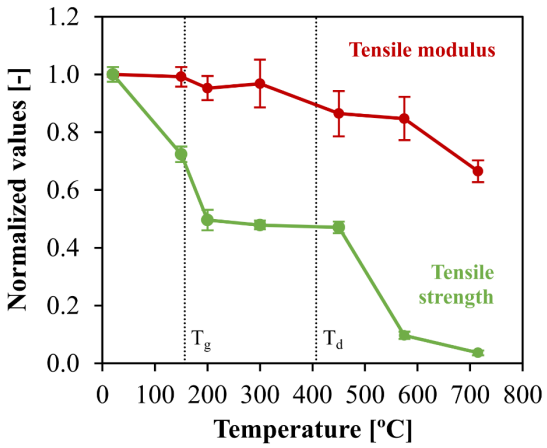

Figure 2.6. Normalized average tensile strength and modulus as a function of temperature (normalization with respect to ambient temperature; vertical lines mark the T_g and T_d of the bar) (adapted from Rosa *et al.* [65], *cf.* Section 3.4.3.3).

As observed in Figure 2.5, much less information is available about the variation with temperature of the tensile modulus of GFRP bars. Yet, the data show that the tensile modulus is much less degraded by elevated temperature that the tensile strength. This is due to the fact that despite both properties are fibre-dominated, the tensile modulus is mainly governed by the fibres, which, as mentioned, present greater stability under elevated temperatures than the matrix. However, besides the fibres, the tensile strength also relies on the integrity of the fibres-matrix interface, which in turn is more susceptible to thermal degradation. Indeed, according to most of the literature [65,94,95,97,99,101,102,107], the tensile modulus of GFRP bars is less affected than the tensile strength up to the resin T_d, for which it is typically reduced by less than 30% compared to ambient temperature; some outlier results were obtained in Abbasi and Hogg [96], indicating a harsher degradation of the bars' modulus at temperatures near the T_g, temperature at which other studies only reported minor reductions.

There is a relevant gap in knowledge about the variation of the tensile modulus of GFRP bars for temperatures above 400 ºC. The few results available for this temperature range ([65,97]) indicate that the steepest decrease in the tensile modulus occurs as a result of the softening of the glass fibres, thereby for temperatures considerably above the resin T_d. In the study of Wang and Kodur [97], the tensile modulus was drastically reduced by 12% at 400% and by 72% at 500 ºC. In Rosa *et al.* [65], the tensile modulus presented minor reductions (below 15%) up to 575 ºC, decreasing a little further to 34% at 715 ºC (temperature at which the bars retained only 4% of their ambient temperature strength). For the purpose of modelling, it seems reasonable to consider that the tensile modulus of GFRP bars is negligible after the softening of the fibres, given that, according to the tests of Dimitrienko [98], the strength and stiffness of glass fibres is reduced by about 20% at 600 ºC and 70% at 800 ºC, while marginal values were obtained at 1200 ºC.

Experimental investigations have also shown that the degradation of the mechanical properties of GFRP bars with temperature is not only affected by the temperature but also by the heating conditions and

exposure environment. On the one hand, Alsayed *et al.* [108] concluded that higher temperatures or longer periods of exposure to heat cause greater reductions of the residual tensile strength of GFRP bars (the same conclusion was obtained for example in GFRP laminates [109]). On the other hand, the presence of oxygen accelerates both the thermal decomposition of polymeric resins [57] (*cf.* Figure 2.1) and the softening of the glass fibres [110], which, together with the large quantity of heat released during the ignition and combustion of the matrix, can intensify the degradation of the mechanical properties of GFRP bars [57]. The majority of tensile tests reported in the literature were conducted in bare bars and therefore in an oxidative environment; however, this environment differs from that encountered in bars embedded in concrete, where the thermal decomposition occurs mainly in an inert atmosphere, hence, being solely driven by the action of heat. The few tensile tests performed on GFRP bars embedded in concrete demonstrated that both their tensile strength at elevated temperature [105] (*cf.* Figure 2.4) and their residual tensile strength and modulus [108] experience slightly lower reductions compared to those of bare bars tested in an oxidative environment.

As discussed above, the variation of the tensile properties of GFRP bars has been object of significant research, however, few studies have investigated the effects of elevated temperature on their compressive [111] and shear [63] properties. In AlAjarmeh *et al.* [111] (Figure 2.7a), the compressive strength of the GFRP bars (T_g of 126 ºC) at 140 ºC showed average reductions of 77% compared to ambient temperature. Robert and Benmokrane [63] on the other hand concluded that the shear behaviour of GFRP bars is more dependent on the fibre-matrix interface (therefore, it is more severely affected by the glass transition of the resin) than the tensile strength (which is governed by the fibres, hence less sensitive to the temperature increase). In this study (see Figure 2.7b), the transverse shear strength of the bars (T_g of 120 ºC) was reduced by 12% at 150 ºC, 72% at 250 ºC and 78% at 325 ºC; conversely, the bars retained nearly 50% of their ambient temperature tensile strength at 325 ºC.

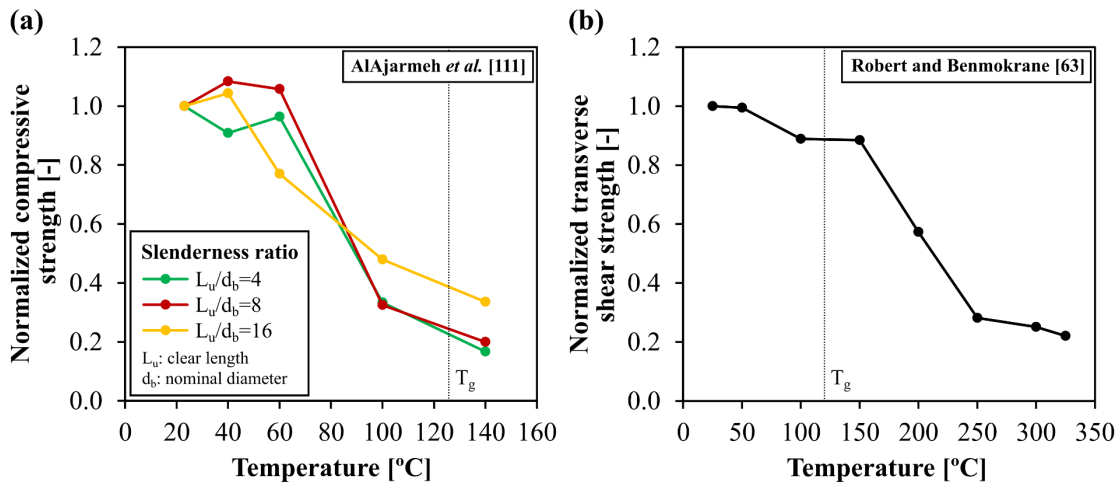

Figure 2.7. Normalized (a) compressive strength (AlAjarmeh *et al.* [111]) and (b) transverse shear strength (Robert and Benmokrane [63]) of GFRP bars as a function of temperature .

Lastly, it is worth mentioning that the residual properties of GFRP bars after being exposed to high temperatures have also been investigated in recent years (*e.g.* [67,92,102,108,112–114]), as this knowledge is needed to evaluate the remaining structural integrity of GFRP-RC structural members after fire exposure. Studies have shown that for temperatures below the resin decomposition, the residual tensile strength of GFRP bars is normally greater than the retained strength at elevated temperature [64,102,113]; yet, the higher the degree of decomposition of the matrix, the more similar the referred reductions are. The discussion of the residual behaviour of GFRP bars lies beyond the scope of the present state-of-art review and thesis and, for that purpose, interested readers are referred to the above-mentioned studies.

2.2.4. Prediction models for the tensile properties

Several analytical models have been proposed to predict the degradation of the tensile strength ([19,65,69,77,93,94,96,98,102,103,105,106,111,115–120]) and modulus ([65,93,96,102,116–120]) of GFRP bars as a function of temperature. Expressions have also been calibrated for the variation with temperature of the compressive and flexural strengths of GFRP bars [111] and also for the tensile strength of glass, carbon and aramid fibres [115]. The models available were empirically derived based on simple fitting procedures of sigmoidal [98,115] or polynomial functions to the experimental data, the latter including linear/multilinear regressions [65,93,96,116,117,119,120] and higher degree polynomials [65,102,118]; these analytical models were typically able to capture the general degradation trend of the bars' mechanical properties with temperature. In other studies [103,105,106], linear Bayesian regression analyses were conducted to propose degradation models for the tensile strength of GFRP bars, in which the influence of both the exposure temperature and the bar diameter were considered; the authors found that the effect of the bar diameter on the strength degradation was much less relevant than that of the temperature, although its contribution increased with temperature. A semi-empirical model (Figure 2.8, see following page) was proposed by McIntyre *et al.* [94] (later improved in [19]) that correlated well the two-step reduction of the bars' tensile strength (near the T_g and T_d) with the storage modulus and mass variations with temperature; however, the application of this model requires the referred thermophysical properties and their variation with temperature (needed as input in the model) to be known.

Apart from the following studies [103,105,106], in which the diameter was considered as a model variable, the analytical expressions proposed in the literature have been derived solely considering the exposure temperature of the bars. However, the degradation of the bars' properties with temperature is also affected by the thermophysical properties of their constituent materials (resin and fibres) and other factors, such as the resin's decomposition and combustion (if in the presence of oxygen), as well as the heating duration; therefore, these aspects would also need to be considered to improve the models' accuracy, especially if they are to be used for design purposes. Yet, this has not yet been possible, because the bars' T_g and T_d are often not reported in the literature, and the studies that provide this

information either do not specify the test method used to define those reference temperatures or adopted different test methods to determine them.

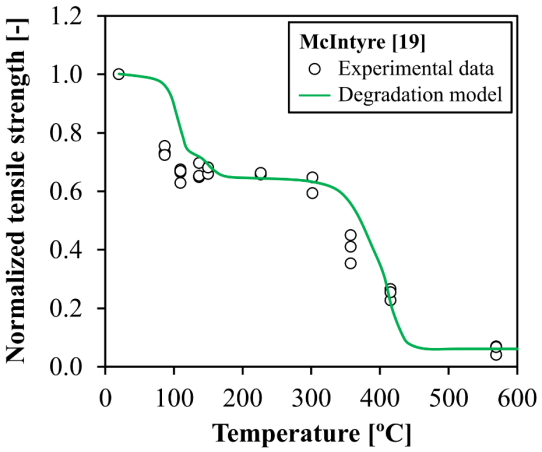

Figure 2.8. Normalized tensile strength of GFRP bar (compared to ambient temperature) as a function of temperature: experimental data and semi-empirical model proposed by McIntyre [19] (adapted from McIntyre [19]).

In the meantime, empirical/semi-empirical models are still of great usefulness, especially to be used as input data in numerical models that aim at simulating the thermomechanical behaviour of GFRP-RC members exposed to elevated temperature and fire. With this objective in mind, two empirical models were proposed to describe the average variation of the tensile strength and modulus of GFRP bars with temperature – they were based on the models proposed by Rosa *et al.* [65], yet they consider a more up-to-date database of results (three additional studies were included). To this end, the considered database featured the individual results (per specimen; otherwise, average results were considered) obtained from steady-state tensile tests performed on bare GFRP bars under short-term exposure to elevated temperature (*cf.* Table 2.1). The analytical expressions, plotted in Figure 2.9, were derived through a fitting procedure to the experimental results, aiming at the minimization of the mean square errors between the predicted and experimental values; second-order polynomial and linear functions were adopted to describe, respectively, the normalized variation of the tensile strength and modulus of GFRP bars with temperature (Equation (2.1) and Equation (2.2), respectively),

$$f(T) = 6.40 \times 10^{-7} \cdot T^2 - 1.84 \times 10^{-3} \cdot T + 1.04 \tag{2.1}$$

$$E(T) = 1.01 - 5.18 \times 10^{-4} \cdot T \tag{2.2}$$

where T is the absolute temperature in degrees Celsius, and $f(T)$ and $E(T)$ are the normalized tensile strength and modulus of the bars compared to ambient temperature, respectively. As depicted in Figure 2.9a, although Equation (2.1) is not able to describe the above-mentioned two-step degradation of the

tensile strength with temperature (due to the aforementioned reasons), it provides a reasonable agreement with the overall trend of available data. It is worth referring that the scatter of test data is quite significant, especially for the tensile modulus (Figure 2.9b).

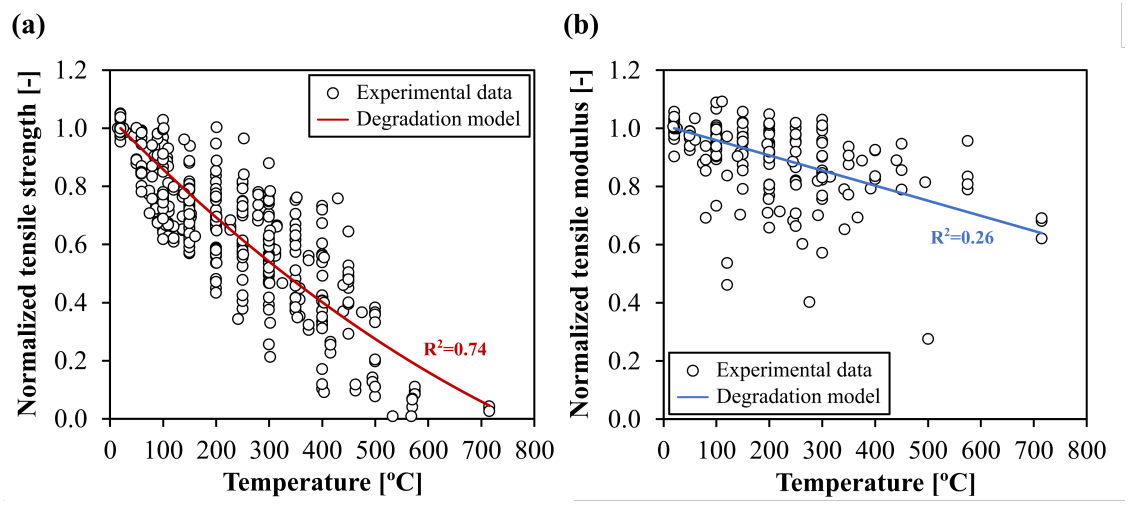

Figure 2.9. Normalized (a) tensile strength and (b) modulus of GFRP bars (compared to ambient temperature) as a function of temperature: experimental data and modelling curves.

2.2.5. Research needs

As discussed in previous sections, there is lack of information about the variation of the thermal properties of GFRP bars with temperature. Further research is also needed to investigate the influence of elevated temperatures on the mechanical properties of GFRP bars in both longitudinal and transverse directions – this need includes straight and especially bent bars (for which no data is presently available). The influence of the duration of exposure to heat and exposure environment on the mechanical behaviour of the bars also needs to be better understood and quantified. Future research should provide experimental data for a wider variety of bars and larger temperature ranges, especially for the upper range of temperatures likely to be attained in a fire. Lastly, it is essential to propose predictive models to estimate the degradation of the mechanical properties of the bars with temperature, which, in addition to the exposure temperature, also take into account their thermophysical properties (T_g and T_d), exposure environment and duration of heating, so that they could be incorporated in future versions of FRP-RC design guidelines/codes and avoid the need for testing.

2.3. Bond behaviour of GFRP rebars at elevated temperature

2.3.1. Parameters affecting bond at elevated temperature

As discussed in the previous section, the glass transition of the polymer matrix of GFRP reinforcement affects its ability to transfer stresses amongst the fibres, resulting in a reduction of the bars' strength and modulus, which are further degraded when the resin decomposes. In addition, as discussed below, the matrix also plays an important role on the stress transfer from the concrete to the glass fibres and, therefore, when it softens, a severe reduction also occurs in the bond between the bars and the concrete, affecting the bars' anchorage capacity during a fire. The consequences of the loss of bond at the GFRP-concrete interface when the bars are exposed to elevated temperatures are particularly deleterious in lap splices and anchorage zones of structural members, where premature debonding failures might occur if the bars' temperature approaches T_g. For this reason, the effects of elevated temperatures on the bond behaviour of GFRP bars need to be thoroughly investigated.

The bond behaviour of GFRP bars to concrete at elevated temperature was investigated in a relatively limited number of studies by means of direct pull-out tests, conducted in both steady-state [15,19,121–128] and transient-state regimes [19,126] – the main features of these studies are summarized in Table 2.2 (presented next in page 32). In direct pull-out tests (hereafter referred to simply as pull-out tests), an individual bar is pulled in tension while embedded in a concrete cube or cylinder; the adoption of these tests over pull-out bending tests has been preferred in the literature due their simpler execution, although the latter replicates more accurately the confinement/boundary conditions of the reinforcement in RC members in flexure. Figure 2.10 gathers the results available in the literature about the normalized (average) bond strength of GFRP bars as a function of temperature (normalization with respect to the values at ambient temperature). The results include bars from several manufacturers, hence with different surface finishes (mostly sand coated and ribbed), T_gs and diameters; the majority of the pull-out tests were performed in straight bars, with the exception of Rosa *et al.* [121], who tested 90º bent bars. The figure only includes results of pull-out failures, as reported in [123–126,128] (the remaining studies [15,19,122] reported failures due to splitting of concrete). It is worth mentioning that in the studies of Hajiloo *et al.* [126] and Mousavi *et al.* [122], tests were conducted in both steady-state and transient-state conditions, and very similar results were reported for the two conditions. Similarly, the results of the residual bond behaviour of GFRP bars after exposure to elevated temperature are also not presented [92,113,114,129–133]; yet, it is worth mentioning that, according to Hajiloo and Green [113], the residual bond strength of GFRP bars is higher than the retained bond strength at elevated temperature.

Table 2.2. Summary of bond tests on GFRP bars at elevated temperature.

Reference	Bar geometry	Surface finish	Glass transition		Temperature range [°C]	Bond law calibration method
			T_g [°C]	Method		
Rosa *et al.* [121]	90° bent	Ribbed	104	DMA (onset *E'*)	20–300	Numerical procedure (1)
Mousavi *et al.* [122]	Straight	Sand coated	118	DSC	25–300	-
Rosa *et al.* [123]	Straight	Ribbed	104–157	DMA (onset *E'*)	20–300	Numerical procedure (1)
Solyom *et al.* [124]	Straight	Ribbed	164	DMA (onset *E'*)	20–300	Curve fitting (only pre-peak) (2)
McIntyre [19]	Straight	Sand coated	83-86	DMA (onset *E'*)	20–159	-
Rosa *et al.* [125]	Straight	Sand coated	98	DMA (onset *E'*)	20–140	Numerical procedure (1)
Hajiloo *et al.* [126]	Straight	Ribbed; sand coated	110–140	DSC/ DMA (onset *E'*)	25–314	-
Weber [15]	Straight	Ribbed	-	-	20-220	-
Katz *et al.* [128]	Straight	Ribbed; sand coated; rough surface (3)	60-124	DSC	20-280	-

Note: Most of the studies listed above concern tests in steady-state conditions. Studies [19,126] include tests in both steady- and transient-state regimes.
(1) Local bond-slip laws.
(2) Average bond-slip laws (*i.e.*, considering a uniform stress distribution along the embedment length).
(3) Rough surface consisting of residues of hardened resin at the surface of the bar (older generation bar).

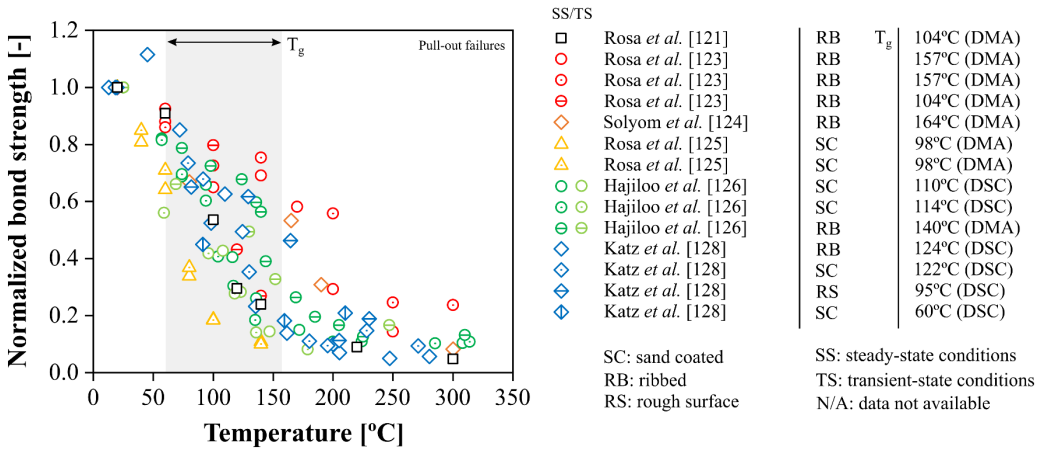

Figure 2.10. Normalized average bond strength of GFRP bars as a function of temperature (data respecting to short-term exposure to elevated temperature and failure by pull-out).

It has been widely demonstrated that the bond strength and stiffness of GFRP bars are more steeply reduced with the temperature increase than the tensile properties (*e.g.* [15,19,123,125]), due to the fact that the former are more matrix-dependent and, consequently, are more affected by resin softening. As shown in Katz *et al.* [128], the bond of GFRP bars to concrete is also more affected by elevated temperatures than that of steel bars. Indeed, previous studies have consistently shown that the bond strength of GFRP bars experiences a severe degradation at moderately elevated temperatures, namely when approaching the T_g, and that the degradation rate with temperature depends on a number of factors, the most dominant being the T_g and the surface finish of the bars [123], which both vary among manufacturers. This explains the large scatter of results depicted in Figure 2.10 in the range of temperatures comprising the bars' T_g. Indeed, while the bond strength of some bars can be reduced by over 75% at temperatures close to the T_g (*e.g.* [125,126,128]), others experience similar reduction levels only above 200 ºC (*e.g.* [19,124,126,128]). Regardless of this variability, experimental data has provided evidence that the GFRP-concrete bond is typically fully degraded even before the resin begins to decompose; as seen in Figure 2.10, the bond strength retention at around 200 ºC (below the usual bars' T_d) normally ranges between 5% and 25% of the bond strength at ambient temperature.

There are many parameters known to affect the bond of GFRP bars to concrete in normal (ambient) temperature conditions [134]; yet, concerning the behaviour at elevated temperature, significantly less information is available. According to Rosa *et al.* [123], the bond strength of bars with sand coating is typically more sensitive to elevated temperature than that of bars with ribs – while in sand coated bars most of the bond strength is lost below the T_g, ribbed bars normally experience more severe bond strength reductions after the resin softening. As explained in [123,126], this seems to be related with the fact that the bar core-sand coating interface is usually more affected by temperature than the sand coating-concrete interface. Note that the binding resin that embeds the sand particles is applied over the hardened core of the bars, therefore experiencing different curing conditions than the resin used in the

core; on the other hand, the ribs are typically grounded into the hardened bars and therefore are cured in the same manner.

Contrarily to the surface finish and T_g, the influence of the diameter [123,135], geometry (straight *vs.* 90º bent) [121] and embedment length [125] of GFRP bars on the degradation rate of their bond strength with temperature was found to be much less meaningful. These conclusions, drawn for the materials, test procedures and temperatures considered in above-mentioned studies, also agree with results obtained for bars with basalt (BFRP) [129] and carbon (CFRP) [136,137] fibres. The study of Li *et al.* [129] in BFRP bars also showed that similar overall bond strength reductions were obtained with the temperature increase irrespectively of the concrete strength (C30, C45 and C60 grades were compared up to 270 ºC).

Regardless of the foregoing discussion, the test data show that, for the same temperature, the bond strength increases with the increase in the concrete strength and thickness of the concrete cover [122,123,125,126,129,135], while it decreases with the bar diameter [123,135]; moreover, the maximum average bond stress increases with the increase in the embedment length [122,125]. Mousavi *et al.* [122] showed that increasing the embedment length from 4 to 22 times the bar diameter greatly enhances the anchorage capacity of the bars for temperatures up to 200 ºC; yet, for higher temperatures, the bond was so harshly damaged that the pull-out loads converged irrespectively of the embedment length considered. Regarding the geometry of the bars, Rosa *et al.* [121] compared the behaviour of straight and 90º bent bars at temperatures up to 300 ºC and concluded that while the bond strength of both bars was severely reduced near the T_g (reductions of 73-75% were obtained at 140 ºC), the anchorage capacity of the bent bars was between 30% and 90% higher than that of straight bars, considering both ambient and elevated temperatures. A different result was obtained in the study of Kiari *et al.* [137] using CFRP bars; here, the use of 90º bent bars did not provide a meaningful improvement in bond strength compared to straight bars, yet closed-loop bars provided pull-out loads 3.2 to 3.6 times higher than those obtained with straight and 90º bent bars.

Mousavi *et al.* [122] investigated the bond behaviour of GFRP bars under a gradient temperature along their embedment length to simulate the performance of the reinforcement at the unexposed zones of flexural GFRP-RC members. The results showed that as temperature increases, stresses are gradually transferred from the warmer zones near the loading section (where bond is more severely deteriorated) towards the cooler (less damaged) extremity of the bar, indicating that during a fire the effective anchoring length gradually migrates away from the more heated zones towards the unexposed zones of the member. This load transfer mechanism in GFRP-RC members was further assessed in Duarte *et al.* [40], by means of fire resistance tests and numerical modelling (*cf.* Sections 2.4.1.2.2 and 2.4.2.2).

2.3.2. Prediction models for bond strength

As with the thermal and mechanical properties, it is rather difficult to provide generalizations about the effects of temperature on the bond properties of GFRP bars. Predictive models of the bond strength reduction with temperature are however much needed to design anchorage zones and lap splices and, to date, they are not provided by FRP-RC design codes. Empirical and semi-empirical analytical models have however been proposed by researchers to describe the effects of short-term [19,115,120,125,138] and long-term [135] exposure to elevated temperature on the average bond strength of GFRP bars. These models were derived from non-linear regression analysis (curve fitting) of experimental results referring to various types of bars. Given that more recent data are available, new and updated empirical models are hence proposed here.

Figure 2.11 plots the normalized average bond strength of straight sand coated GFRP bars (in blue) and ribbed GFRP bars (in red) as a function of temperature; the results concern only short-term tests and pull-out failure modes [123–126,128]. Two different degradation trends with temperature are clearly identified in the figure according to the type of surface finish of the bars, showing that the bond strength decay of sand coated bars is steeper and occurs at lower temperatures compared to that of ribbed bars. For this reason, analytical expressions for each type of surface finish are proposed herein.

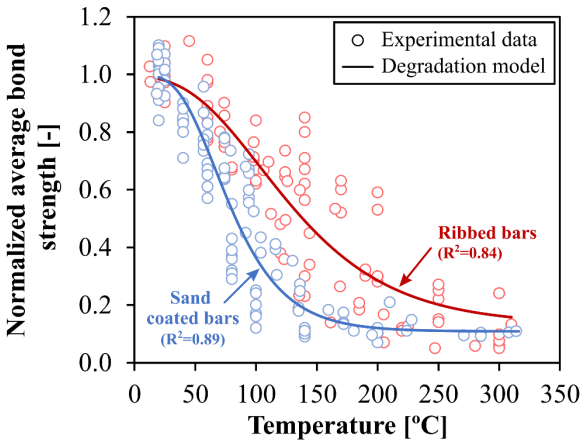

Figure 2.11. Normalized average bond strength of sand coated and ribbed GFRP bars (compared to ambient temperature) as a function of temperature: experimental data and modelling curves.

To this end, the relaxation model proposed by Correia *et al.* [23], which is based on the Gompertz statistical distribution, was considered to reproduce the reduction of the average bond strength of the bars with temperature. The model is expressed by Equation (2.3),

$$P(T) = P_r + (P_u - P_r) \times (1 - e^{Be^{C \times T}}) \tag{2.3}$$

where T is the temperature, and P_u and P_r are the values of the property (the average normalized bond strength) at, respectively, ambient temperature and after the glass transition of the resin (yet, prior to decomposition). The parameters B and C are obtained by fitting the theoretical curve to the experimental data, through minimization of the mean square errors between predicted and experimental results. For each type of surface finish, a set of parameters were calibrated (Table 2.3). The theoretical curves are plotted in Figure 2.11 – in spite of the relatively high scatter, the curves are able to capture the average degradation trend of the bars' average bond strength with increasing temperature.

Table 2.3. Defining parameters and mean absolute percentage error (MAPE) of the degradation models proposed for the average bond strength variation with temperature of sand coated and ribbed GFRP bars.

Model parameters	Sand coated bars	Ribbed bars
P_u [-]	1.00	1.00
P_r [-]	0.11	0.13
B [-]	-8.581	-5.708
C [-]	-0.032	-0.017
MAPE (%)	26	40

2.3.3. Modelling of the bond behaviour at elevated temperature

The bar-concrete interaction is typically expressed through bond-slip laws, which define the local bond stress along the embedment length of the bar as a function of the local slip. The most popular analytical models to describe the bond behaviour of FRP bars in concrete at ambient temperature conditions are: (i) the BPE model, originally proposed by Eligehausen *et al.* [139] to describe the bond between steel bars and concrete; (ii) the modified BPE model (mBPE), by Cosenza *et al.* [140], which proposes a modification of the post-peak branch of the BPE model; and (iii) the CMR model, also by Cosenza *et al.* [141], presenting an alternative to the pre-peak branch of the BPE model. These models have been broadly used in the literature to model the GFRP-concrete interaction at ambient temperature; however, to accurately simulate the thermomechanical response of GFRP-RC members during fire, models defining the GFRP bar-concrete interaction as a function of temperature are also needed.

Unlike steel bars, standardized temperature-dependent bond-slip laws are not yet available for GFRP reinforcement, due to the limited experimental data available, the complexity of modelling the GFRP-concrete interaction at elevated temperature and the non-standardized geometry and manufacturing techniques of GFRP bars. Accordingly, temperature-dependent bond-slip laws for GFRP bars are still scarce in the literature – to date, only Solyom *et al.* [124], Aslani *et al.* [120] and Rosa *et al.* [121,123,125] have proposed bond-slip laws for GFRP bars under short term exposure to elevated

temperature (*cf.* Table 2.2). Bond-slip laws have also been proposed to describe the bond behaviour of GFRP bars under long-term exposure to elevated temperature [127,135], as well as their residual behaviour after being heated and cooled down to ambient temperature [120,127,130,132].

Aslani *et al.* [120] calibrated the parameters of the mBPE model for three types of GFRP bars (sand coated, ribbed and with a rough surface) based on the experimental results obtained by Katz *et al.* [128] at temperatures up to 230 ºC. The bond laws considered the effects of concrete strength, cover thickness, bar diameter and embedment length in the maximum bond stress at ambient temperature, and were recently implemented in the numerical study of Duan *et al.* [142] (reviewed in Section 2.4.2.2). Solyom *et al.* [124] assessed the adequacy of the mBPE and CMR models to describe the pre-peak bond behaviour of a ribbed GFRP bar up to 300 ºC, concluding that the latter model was better suited for that purpose. In both studies, the models were calibrated through curve fitting to the experimental data, an approach that assumes a uniform distribution of tangential stresses along the bar' embedment length; however, the stresses at the bar-concrete interface actually decrease from the loaded extremity towards the free extremity of the bars. Although the simplifying assumption of uniform stresses might be reasonable for relatively short embedment lengths (as shown in the numerical study by Veljkovic *et al.* [143]), it is not necessarily accurate to describe the stress distribution over longer embedment lengths.

In this regard, a different approach was followed by Rosa *et al.* [123,125], who derived local bond-slip laws for sand coated bars [125] and three types of ribbed rebars [123] (including different rib geometries and core diameters) for temperatures up to 300 ºC. In these studies, the temperature-dependent local bond-slip laws (exemplified in Figure 2.12) were numerically calibrated based on the load-slip responses measured in pull-out tests, at both free and loaded ends of the bars. The numerical calibration procedure allowed considering the non-uniform stress distribution along the embedment length, as well as the

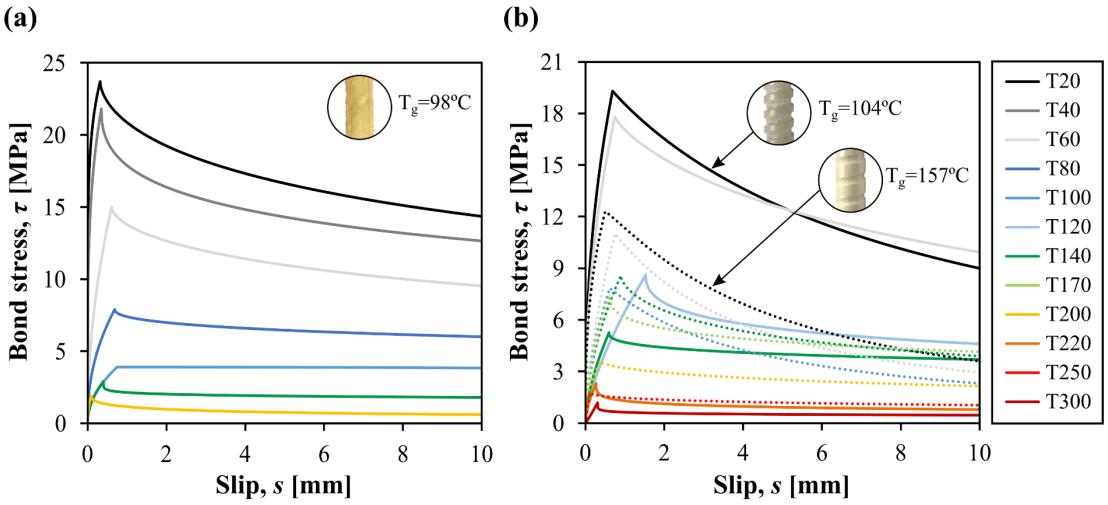

Figure 2.12. Temperature-dependent bond *vs.* slip laws for (a) sand coated and (b) ribbed GFRP bars (adapted from Rosa *et al.* [121], *cf.* Section 5.2).

degradation of the bars' tensile modulus with temperature. The bond constitutive relationships were defined according to Sena-Cruz [144], who considered the models proposed by Eligehausen *et al.* [139] and Stand and Aarre [145] to describe, respectively, the pre- and post-peak stages of the bond stress-slip response. The proposed bond-slip laws were implemented and validated in numerical models simulating pull-out tests (Rosa *et al.* [121]) and fire resistance tests on GFRP-RC slabs (*cf.* Duarte *et al.* [146] revised in Section 2.4.2.2).

In Rosa *et al.* [121] the bond-slip laws proposed in [123,125] were implemented in tridimensional (3D) solid finite element (FE) models with the aim of simulating the pull-out tests performed at elevated temperature in straight GFRP bars with different surface finishes [123,125] and 90º bent ribbed GFRP bars [121]. It was found that the bond laws (calibrated for straight bars) provided accurate predictions of the bond stress-slip response of the straight bars at ambient and elevated temperatures, as well as of 90º bent bars at ambient temperature. However, separate local bond-slip laws had to be calibrated through inverse numerical analysis for their bent development, to allow simulating the bond behaviour of the bent bars at elevated temperatures. This procedure implicitly considered the higher localized damage that occurs in the curved zones of the bars at elevated temperature, as a result of the combined effect of the softening state of the resin and of the crushing and shearing off of the ribs during pull-out. The validated 3D FE models were then used by Rosa *et al.* [121] to carry out design-oriented parametric analyses, aiming to investigate the influence of elevated temperatures on the anchorage capacity of straight bars with different surface finishes and development lengths, and of 90º bent ribbed bars with different tail and straight development lengths. From these parametric studies, development and tail lengths were proposed as a function of temperature, envisaging the use of GFRP reinforcement in beams and slabs; these lengths, defined according to Figure 2.13, are reproduced in Table 2.4. Based on the findings of this study, it was concluded that the development lengths designed for ambient temperature are insufficient to mobilize the bars' capacity at elevated temperatures; hence, significantly longer embedment lengths are required at higher temperatures to counteract the severe reduction of bond near the T_g. It was again demonstrated that the bars' constituent materials, T_g and surface finish need to be considered when designing GFRP anchorages, as these parameters affect the retention of both tensile and bond properties of the reinforcement at elevated temperatures. It was shown that the development length required to anchor straight bars can be considerably shortened by adopting bent extremities and sufficiently long tail lengths beyond the bend. Lastly, the results highlighted the great potential of using bent bars to improve the anchorage capacity of the reinforcement in anchorage zones and lap splices of concrete members – this possibility is also supported by the findings from fire resistance tests performed in GFRP-RC slabs by Nigro *et al.* [14] and Rosa *et al.* [90], reviewed in Sections 2.4.1.2.2 and 2.4.1.2.3, respectively.

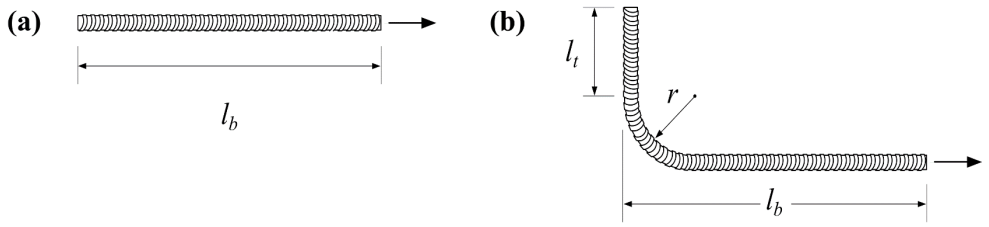

Figure 2.13. Schematic of development length (l_b) and tail length (t_l) of (a) straight and (b) bent bars (adapted from Rosa *et al.* [121], *cf.* Section 5.4).

Table 2.4. Development lengths proposed by Rosa *et al.* [121] for straight and 90º bent GFRP bars, given as function of the bar diameter (D) (*cf.* Section 5.4).

Structural member	T [ºC]	Straight bars	90º bent bars		
		Development length of straight bar (l_b)	Development length of bent bar (l_b) (1)	Optimal tail length (l_t)	Total anchorage length of bent bar (2)
Slabs and beams	20	17D	12D	3D	17D
	60	18D	13D	6D	21D
Beams	120	37D	25D	15D	42D
	140	47D	27D	20D	49D
Slabs	120	37D	30D	10D (3)	42D
	140	47D	38D	10D (3)	50D

(1) Development length of bent bar (see Figure 2.13).
(2) Total anchorage length corresponding to the sum of the tail, bent and straight anchorage lengths.
(3) Maximum tail length of 10D set due to slab thickness constraints.

2.3.4. Research needs

There is a broad consensus that the bond behaviour of GFRP bars at elevated temperature must be further investigated to consider more realistic confinement, heating and loading conditions than those simulated in direct pull-out tests, as well as to include a wider diversity of bars and different confinement conditions (concrete strength and cover thickness). The performance of bent bars was found to be promising regarding the improvement of the anchorage capacity of GFRP reinforcement; yet, further studies are needed to assess the behaviour of different bend configurations at elevated temperature. Efforts should also be made to develop models predicting the degradation of the bond strength with temperature, considering as variables the relevant parameters (*e.g.* T_g and surface finish of the bars). The accuracy of simulations of the thermomechanical behaviour of GFRP-RC members exposed to fire depends on the existence of such temperature-dependent constitutive bond laws for different types of GFRP bars, which are presently scarce in the literature.

2.4. Fire resistance of FRP-RC structural members

For many years, fire was regarded as a serious and unacceptable hazard to the structural safety of concrete members reinforced with FRP bars due to the absence of comprehensive research on the subject. Consequently, until the release of the first fire-design guidelines for FRP-RC members in the American ACI 440.1R-15 [6] and Canadian CAN/CSA S806-12 [8] codes, the use of FRP internal reinforcement was simply not recommended in structures with fire safety requirements. However, nowadays the fire behaviour of FRP-RC structural members is much better understood, thanks to the various experimental and numerical studies carried out on this matter. These studies provided evidence that despite the sensitivity of GFRP reinforcement to elevated temperature, GFRP-RC members can still fulfil the fire performance criteria established in building codes and even attain comparable fire resistance to that presented by steel-RC members. This section present a review of the current state of knowledge on the fire behaviour of GFRP-RC beams and slabs assessed by means of fire resistance tests (Section 2.4.1) and numerical analyses (Section 2.4.2).

2.4.1. Experimental assessment of the fire resistance of GFRP-RC flexural members

2.4.1.1. Fire performance requirements

The fire resistance of a structural member is the period of time during which it is able to perform its designed functions during a fire event, which may typically entail the following three criteria: (i) load bearing capacity (ability to withstand the applied load during fire without collapsing or presenting excessive deflections); (ii) integrity (ability to maintain its separating/barrier function, without passage of flames or gases through it), and (iii) insulation (capacity to present low temperatures at its unexposed surface). The fire resistance is typically evaluated by means of furnace tests, in which the structural member is subjected to a sustained service load while being exposed to fire according to a given heating curve, typically a standard fire curve. Fire resistance tests allow assessing both the thermal and thermomechanical responses of structural members during fire exposure, providing relevant data which are then used to calibrate numerical models. Fire resistance tests of concrete beams and slabs reinforced with GFRP bars performed to date are relatively limited in number, as attested by the short summary presented in Table 2.5. However, these tests have provided relevant insights about the thermal and mechanical performance of GFRP-RC members, clarifying some common misconceptions about this topic, which are addressed next.

Table 2.3. Summary of fire resistance tests on GFRP-reinforced concrete slabs and beams

Reference	Structural member	Concrete cover [mm]	Reinforcement continuity	Lap-splice geometry	Anchorage geometry	Heating curve	Fire resistance [min]
Rosa *et al.* [90]	Slabs	25; 35	Continuous; lap-spliced	Straight; 90º bent	Straight; 90º bent	ISO 834	19–221
Gurung *et al.* [21]	Beams	60	Lap-spliced	Straight	Straight	CAN/ULC-S101	51–62
Nour *et al.* [20]	Beams	60	Lap-spliced	Straight	Straight	CAN/ULC-S101	53–60
Rosa *et al.* [147]	Slabs	25; 35	Continuous; lap-spliced	Straight	Straight	ISO 834	12–158
Hajiloo *et al.* [11]	Slabs	40	Continuous	-	Straight	ASTM E119	≥180
McIntyre [19]	Beams	20	Continuous; lap-spliced	Straight	Straight	Non-standard	7–(>90)
Hajiloo *et al.* [12]	Slabs	60	Continuous	-	Straight	ASTM E119	<180
Carvelli *et al.* [16]	Beams	20	Continuous; lap-spliced	Straight; 90º bent	Straight	Localized fire (1)	-
Nigro *et al.* [14]	Slabs	32; 51	Continuous	-	Straight; 90º bent	ISO 834	60–(>180)
Nigro *et al.* [148]	Slabs	32; 51	Continuous	-	Straight	ISO 834	60–(>180)
Rafi *et al.* [149]	Beams	20	Continuous	-	Straight	ISO 834	50–(>60)
Weber [15]	Slabs	60	Lap-spliced	Straight	Straight	ISO 834	90
Abbasi *et al.* [13]	Beams	70	Continuous	-	90º bent	BS 476	94–128
Sadek *et al.* [91]	Beams	25	Continuous	-	Straight	ASTM E119	30-45
Kodur *et al.* [70]	Slabs	25; 38	Continuous	-	Straight	ASTM E119 (2)	-

(1) Tests performed under steady-state regime: imposed temperature of 230 ºC or 550 ºC along 1/5 of span, followed by loading until failure.

(2) Slabs were only subjected to their self-weigh to assess their thermal behaviour during fire exposure.

2.4.1.2. Parameters affecting fire resistance

For many years there was a biased perception that the fire resistance of GFRP-RC members was necessarily much lower than that of "comparable" steel-RC members, given the more severe degradation of the mechanical properties of GFRP bars and of their bond to concrete at elevated temperature, comparing to those experienced by steel bars [6]. However, recent studies showed that GFRP-RC members can not only fulfil the fire performance criteria defined in building codes but, under certain circumstances (described ahead), can even present comparable fire endurance to steel-RC members of equivalent ambient temperature strength [11,12,19,90].

Recent studies have demonstrated that GFRP-RC slabs [11,12,14,15,90,147,148] and beams [13,19,149] can endure from 60 min to well over 180 min of fire exposure with significantly lower concrete covers than those prescribed in standard CAN/CSA S806 [8], provided that: (i) the concrete cover thickness is adequate to delay the temperature increase of the rebars; (ii) continuous reinforcement is adopted between supports (*i.e.* splicing is avoided in spans susceptible to fire), and (iii) the rebars are well-anchored in cool zones of the structure to prevent them from attaining the bars' T_g, thus avoiding bond failures. These provisions, further elaborated ahead, are now becoming consensually recognized among researchers as key to the fire endurance of GFRP-RC members. Furthermore, it has been shown that the fire endurance also depends on several parameters related with the type of bar, the properties of concrete and the loading conditions, aspects that are also addressed next. However, as discussed in Section 2.5, all these issues are not yet sufficiently reflected (or not addressed at all) in existing design guidelines [6,8]; more research is still needed to further understand their impact in fire performance and, ultimately, to allow drafting more detailed fire design recommendations. It is worth mentioning that the post-fire (residual) behaviour of FRP-RC flexural members has also been investigated (*cf.* [19,112,113,150–152]), although limited information is currently available about this subject.

2.4.1.2.1. Concrete cover

According to the literature ([71,90,147,153]), the thermal behaviour of GFRP-RC structural members during fire can be considered similar to that of concrete members reinforced with steel bars, given the low contribution of GFRP rebars to the heat transfer in concrete members [70,71]. Conversely, the temperature increase of the concrete cross-section is mainly affected by the composition of the concrete mix, the type of aggregate, the moisture content, as well as the heating conditions [13]; these parameters are known to affect both the thermal and mechanical properties of concrete, as well as its propensity to spalling [78]. Regardless of the above-mentioned similarities, there are relevant differences between the thermomechanical response of conventional steel-RC and GFRP-RC members, which derive from the higher vulnerability to elevated temperatures of GFRP bars.

The fire endurance of RC structures is strongly affected by the concrete cover thickness, since concrete thermally insulates the reinforcement, ensuring that the temperature of the rebars remains below a given critical value for a certain period of time. Due to the lower thermal conductivity of GFRP bars, large thermal gradients are typically developed within the bars' cross-section during fire [71,147], as opposing to steel rebars, in which the distribution of temperature is rather uniform through their thickness [90,147]. However, although temperature increases at a slower rate in GFRP bars than in steel bars, the former are much more susceptible to the effects of temperature, which means that even moderately elevated temperatures can cause faster and more severe deterioration of their mechanical properties and bond to concrete. The adoption of appropriate concrete cover is therefore essential to delay the temperature increase of the GFRP reinforcement and thus allow the retention of such properties over longer periods during a fire event.

Presently, the Canadian guide CAN/CSA S806 [8] recommends relatively thick concrete cover thicknesses of 50 to 60 mm to ensure a 60 min fire resistance rating. Following these guidelines, a significant number of fire resistance tests can be found in the literature comprising covers ranging from 51 to 70 mm [12–15,20,21,148]. However, some authors [14,90,147,154] have shown that more efficient designs can be attained by adopting considerably lower concrete cover thicknesses than those proposed in [8], provided that the anchoring of continuous rebars is properly executed in cool zones of the structure (*cf.* Section 2.4.1.2.2). Hajiloo *et al.* [11] found that it is possible to decrease the concrete cover of GFRP-RC slabs from 60 mm [12] to 40 mm and still obtain fire endurances of 180 min. In the tests of Rosa *et al.* [90], the GFRP-RC slabs were able to withstand a standard fire exposure of up to 180 min with a thin cover thickness of 25 mm, while the adoption of a cover of 35 mm (still significantly lower than that prescribed in [8]) allowed delaying the failure instant to 221 min. In the study of Nigro *et al.* [14] it was concluded that slabs with concrete covers of 51 or 32 mm could both attain fire resistances of 180 min, provided that the anchoring conditions of the rebars were adequate to prevent their pull-out from the concrete at the ends of the slabs.

As referred in Section 2.2.3.1, a minimum cover should also be provided to control the thermal-induced cracking and to prevent spalling from occurring, because of the differences between the transverse thermal expansion coefficients of GFRP bars and concrete. According to Aiello [81], the occurrence of splitting cracks at elevated temperature depends on (i) the type of FRP reinforcement and concrete, (ii) the confining action provided by the transverse reinforcement and (iii) the geometry of the cross-section, including the spacing between rebars, as demonstrated in Gentry [86]. Due to the large number of factors affecting the occurrence of spalling at elevated temperatures, the definition of the minimum concrete cover thickness needed to prevent spalling can therefore be a cumbersome task and no design recommendations are available. However, it was shown that as long as the moisture content is sufficiently low, a cover thickness of 2 times the bar diameter may often be enough to prevent severe cracking and spalling from occurring [19,90,91,147].

2.4.1.2.2. Anchoring zones

One of the concerns regarding the fire resistance of GFRP-RC members is related with the bond performance of GFRP bars at elevated temperature, as it affects the members' deflection response, crack spacing and, ultimately, its load carrying capacity. The severe degradation of the GFRP-concrete bond with temperature is a gradual process that occurs from the onset of fire exposure, quickly evolving to the complete loss of interaction between the rebars and concrete even before the T_d of the resin is attained. The acute reduction of the bond strength and stiffness of the bars near their T_g is particularly worrying during a fire event, posing as a serious risk in zones where the load bearing capacity of the members relies on the anchorage capacity of the reinforcement, as is the case of anchorage zones and lap splices (*cf.* Section 2.4.1.2.3) – the detailing of such zones should therefore be one of the primary concerns in the fire design of GFRP-RC members.

Among the research conducted in this field, the studies of Hajiloo *et al.* [11,12] and Rosa *et al.* [90,147] are worth being highlighted for having comprehensively investigated the relation between the thermomechanical behaviour of GFRP-RC slabs exposed to fire and the progressive degradation of both bond and tensile properties of the rebars with temperature. In these studies, the temperature of the reinforcement was duly monitored along the fire exposed span of the slabs and the cold anchorage zones, allowing to trace the bond strength and tensile strength retentions of the rebars during fire exposure, which had been previously determined from tensile and pull-out tests performed on identical bars. For the range of cover thicknesses tested in these studies (25 to 60 mm, *cf.* Table 2.5), it was shown that the temperature of the rebars at the fire exposed zones generally attained the T_g within the first 20 to 60 min of fire exposure, indicating that the capacity of stress transfer between the GFRP rebars and concrete can be drastically reduced from the very early stages of fire. As an example, in the fire tests of slabs reinforced with continuous GFRP rebars (T_g of 104 ºC and T_d of 400ºC) and cover thickness of 25 mm by Rosa *et al.* [90], it was observed that the temperature of the rebars along their exposed length attained the T_g after just 20 min, quickly attaining 200 ºC (at midspan) after 30 min (Figure 2.14). As illustrated in Figure 2.15a, during this period, the bond strength (at midspan) decreased by around 80% compared to ambient temperature. The bond strength along the exposed length of the rebars was entirely loss within 60-90 min of fire exposure, as temperatures exceeded the T_d along most of the referred length; during that period, the tensile strength of the rebars along the exposed zone was much less reduced, with retention (compared to ambient temperature) ranging between 40% and 60%, as shown in Figure 2.15b.

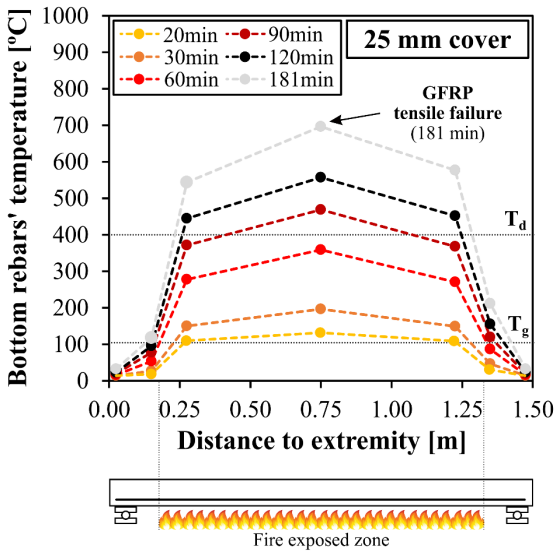

Figure 2.14. Temperature distribution along the fire exposed span and insulated extremity zones of a GFRP-RC slab (temperature measured in the bottom rebars); horizontal lines mark the bars' T_g and T_d (reproduced from Rosa *et al.* [90], *cf.* Section 6.5.1).

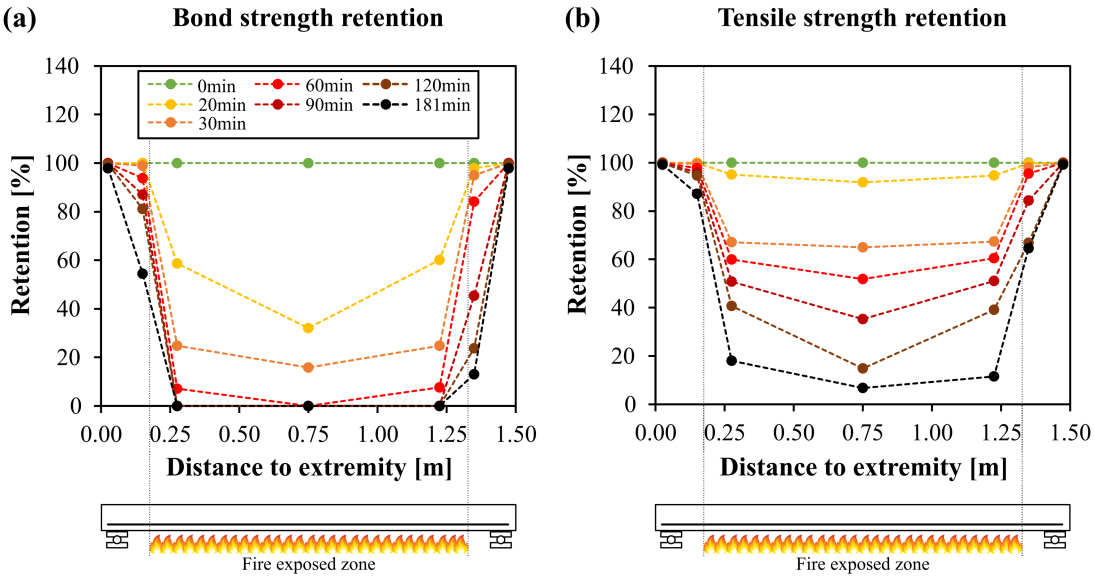

Figure 2.15. Variation of (a) bond strength and (b) tensile strength in the bottom rebars of a GFRP-RC slab (25 mm cover) for different periods of fire exposure (reproduced from Rosa *et al.* [90], *cf.* Section 6.5.2.1).

It was shown that when the temperature along the exposed length of the rebars approaches the T_d, the GFRP-concrete bond is fully deteriorated, yet the members are still able to carry the applied load due to the existence of cold anchoring zones. At this point, the load bearing capacity of the members becomes fully reliant on the rebars' (*i.e.,* on the glass fibres') strength and on the anchorage capacity of the reinforcement at their extremities: the bond stresses, once sustained along the exposed length, are transferred to the cold anchorage zones – this behaviour is described in the literature as a "cable" or "tied-arch" mechanism

[90,146,147,154–156]. For this mechanism to be effective, the temperature at the members' extremities should be low enough (typically, below T_g) to afford sufficient anchorage to the ends of the rebars, preventing them from slipping. As confirmed in the fire tests performed in [13,14,19,90,147,148], if such condition is fulfilled and continuous rebars are adopted between supports, the loss of bond in the heated span does not govern the members' fire endurance and the ultimate load bearing capacity will likely be limited by the tensile capacity of the reinforcement at very high temperatures.

The studies of McIntyre [19] and Abbasi and Hogg [13] in GFRP-RC beams, and those of Nigro *et al.* [14,148] (with due exceptions, addressed ahead) and Rosa *et al.* [90,147] in GFRP-RC slabs, are good examples where proper anchoring conditions were provided at the ends of the reinforcement. In the studies where temperatures in the anchorage zones were measured [19,90,147,148], it was verified that the rebars' extremities remained well below the T_g during the tests (*cf.* Figure 2.14), indicating that at least part of the anchoring zones remained nearly unaffected by temperature and, therefore, provided sufficient anchorage capacity up to the end of the fire tests (*cf.* Figure 2.15a). As shown next, since no slippage was observed at the ends of the rebars in those studies, it was possible to fully exploit the reinforcements' contribution to the members' strength through a cable behaviour, hence maximizing the fire endurance of the structural members.

McIntyre [19] conducted 16 non-standard fire tests on small-scale beams with concrete cover of 20 mm reinforced with different types of bars, including steel, CFRP and two different GFRP rebars. The beams were simultaneously subjected to a sustained load (corresponding to around 30-50% of their ultimate capacity at ambient temperature) and were heated along approximately one third of their span, while the remaining length was thermally insulated. For one of the types of GFRP rebars tested, the beams failed after 63 and 82 min due to tensile rupture of the reinforcement at temperatures above T_d. The other slabs with GFRP and CFRP rebars endured 90 min of fire exposure without failing (just as those reinforced with steel rebars), despite the rebars temperature significantly exceeded their T_d; in all cases, the extremities of the rebars were kept below the T_g, thus preventing bond failures in the anchorage zones.

The above-mentioned studies of Rosa *et al.* [90,147] included 9 fire resistance tests on slab strips reinforced with different continuous GFRP rebars and relatively thin concrete covers (25 and 35 mm). The test specimens were subjected to a sustained load corresponding to 70% of the ambient temperature design load (corresponding from 50 to 68% or their ambient temperature flexural strength). The cold anchoring length of 175 mm adopted in each rebar extremity was found to be adequate to maintain their temperature below T_g during the entire duration of the tests and thereby avoid premature bond failures. The fire resistance of the slabs ranged between 83 and 221 min (depending on the concrete cover, bar type and concrete strength) and it was ultimately governed by the tensile rupture of the reinforcement at midspan; at that zone, the maximum temperature of the rebars varied between 570 ºC and 713 ºC, hence considerably above the resin T_d. Similar conclusions and failure modes to those reported above were obtained in Abbasi and Hogg [13].

The abovementioned studies demonstrate that protecting the ends of the rebars from direct heat exposure is of the utmost importance to allow exploiting their load capacity at elevated temperature. However, there might be cases where the cold anchorage length provided is not sufficiently long (*i.e.* the ends of the rebars are not sufficiently distanced from the heat source) to prevent their temperature from approaching the T_g and therefore to avoid failures triggered by the loss of bond to concrete. This type of failure mode was reported in several studies conducted on GFRP-RC beams and slabs exposed to fire [11,12,14,17,64,148], as well as in members reinforced with CFRP bars (*e.g.* [155,156]).

The above-described failure mechanism caused by loss of bond was comprehensively investigated in the study by Hajiloo *et al.* [11,12], where the fire behaviour of slabs with continuous GFRP rebars was assessed and correlated with the degradation of the bond and tensile strength of the rebars with temperature (obtained in [107,126]). The slabs were 3900 mm in length and the unexposed anchorage length was 200 mm at each slab extremity. The slabs were designed considering two different concrete covers (60 mm in [12] and 40 mm in [11]) and were subjected to a sustained load corresponding to 45-55% of their ultimate flexural strength. All slabs endured 180 min of fire exposure, after which the tests were either interrupted or the load was increased, triggering the collapse shortly after. In the latter case, the authors concluded that failure was initiated by the bond degradation at the anchorage zones when the rebars' ends attained temperatures very close to the T_g, causing them to slip from the concrete; this caused large deflections in the slabs followed by the tensile rupture of the rebars at midspan. A very relevant contribution of the work of Hajiloo *et al.* [11] was the estimation of the increase in tensile stress of the GFRP reinforcement during fire exposure which is required to accurately estimate the remaining strength of the rebars at a given temperature and, therefore, to predict the fire resistance of a structural member. The authors were able to measure the strains in the main rebars during the first 20 min of fire and estimated that: (i) the increase in tensile stress of the rebars during that period, due to the thermal effects, was roughly 20% of the initial stress (prior to the onset of fire); and (ii) the increase in the tensile stress of the rebars during 180 min of fire exposure was conservatively estimated as 50% of that due to the sustained load.

Nigro *et al.* [14,148] investigated the influence of the length and geometry (straight [148] or 90º bent [14]) of cold anchorage zones in GFRP-RC slabs with different concrete covers. The slabs with shorter unexposed anchorage length and thinner concrete cover failed due to the rebars' pull-out at the anchorage zones, presenting fire resistances between 60 and 180 min depending on the load level (*cf.* Section 2.4.1.2.5). Yet, this failure mode was prevented when (i) the cold anchorage length and the concrete cover were increased, or (ii) when a shorter anchorage length was used but bent reinforcement was adopted; in both cases, the slabs endured the predefined limit of 180 min of fire exposure, before failing due to the tensile rupture of the reinforcement. Given that both the concrete cover and protected anchorage length were increased in one of the sets of slabs, the contribution of each parameter to the fire endurance increase could not be quantified. Nevertheless, the results allowed concluding that providing adequate anchoring conditions, either by protecting a sufficient length of the ends of the rebars from direct fire exposure or by

adopting bent rebars, can contribute to the enhancement of the rebars' anchorage capacity (as verified in Rosa *et al.* [121]) and thereby improve the members' fire resistance. It is worth highlighting that the adoption of bent bars has the advantage of enabling the reduction of the heat protected anchorage length of the rebars; yet, the shape of the bars needs to be customized (the bends are shaped prior to the curing process), which presently involves higher manufacturing costs compared to straight bars.

2.4.1.2.3. Lap splices

As far as the fire behaviour of GFRP-RC members is concerned, the detailing of lap splices has received little attention. The few research available, conducted in beams and slabs reinforced with spliced GFRP [15,16,19–21,90,147] or CFRP rebars [17,18] has however demonstrated that the presence of tension lap splices in zones of the structure exposed to heat can considerably reduce the members' fire endurance. Furthermore, they showed that both the location and geometry of the splices, including the length and shape, are also important details that need to be considered in design.

In previous studies, unlike real practice, the splices were intentionally tested in the most unfavourable configuration possible, namely they were positioned at the central span of the members (thus subjected to higher stresses) and directly exposed to fire. In these conditions, it was proven in [17–19,90,147] that the adoption of straight rebars and splice lengths designed for ambient temperature conditions is largely insufficient to achieve fire resistances above 60 min. These studies showed that in the worst cases, the severe loss of bond that happens between the rebars and concrete near the T_g can cause the premature debonding (slippage) of the spliced rebars, as illustrated in Figure 2.16, after less than just 20 min of fire exposure. This was observed in the study of McIntyre [19], where GFRP-RC and CFRP-RC beams with straight-end lap splices failed after 7-17 min of fire exposure, whilst the slabs with continuous rebars withstood fire during ~60 min to over 90 min. The temperature at the ends of the splices was measured (as in [19,20,90]), allowing to confirm that the temperature along the entire overlapped length was slightly above the T_g when the rebars slipped and the beams failed. The same failure mechanism was observed in Rosa *et al.* [90,147] and Kiari *et al.* [17,18], as described ahead.

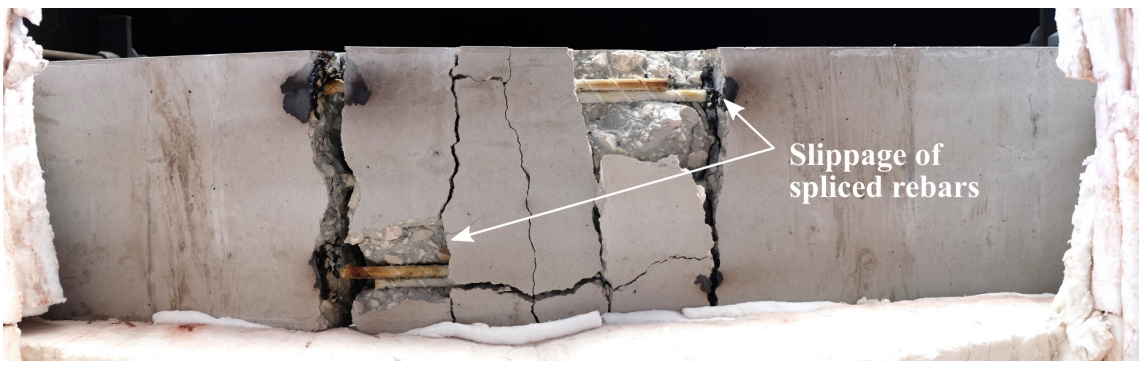

Figure 2.16. Failure of GFRP-RC slab due to the slippage of spliced rebars (bottom view; adapted from Rosa *et al.* [147], *cf.* Section 6.4.4).

There are however reports of studies where members reinforced with spliced GFRP rebars presented more satisfactory fire performance than those mentioned above, as was the case of the slab tested by Weber [15], which failed after 60 min of fire exposure, and the beams of Nour *et al.* [20] and Gurung *et al.* [21] that collapsed 90 min after the onset of fire; these members also failed due to the debonding of the spliced rebars shortly after the T_g was attained. These studies had in common the adoption of a thick concrete cover of 60 mm (as recommended in [8]), unlike the remaining studies from the literature, which comprised cover thicknesses below 35 mm (*cf.* Table 2.5). These results indicate that while it is possible to adopt small concrete covers in members with continuous rebars – as long as the rebars are well-anchored in cool zones of the structure – the same does not apply in members where splicing is performed along spans likely to be subjected to fire.

One solution to prevent premature debonding of the spliced rebars might be to extend the extremities of the splices towards cooler zones of the structure, as recommended for the end anchorage zones of the reinforcement [90,147]. Another answer to this concern might be the adoption of bent rebars at the extremities of lap splices as a mean to improve their bond performance at elevated temperature. As shown in Section 2.3.1, not much is known about the bond behaviour of bent GFRP rebars at elevated temperature (besides the study by Rosa *et al.* [121]) and, accordingly, few fire resistance tests were performed to date in FRP-RC members comprising lap splices with bent extremities. Yet, as discussed below, the studies that investigated the fire behaviour of FRP splices with extremities bent at 90º and 180º angles [16,90] or with closed loop geometries [17,18] have provided clear evidence of their (much) better fire performance compared to those with straight rebars, namely in significantly improving the rebars' anchorage capacity at elevated temperature.

Carvelli *et al.* [16] assessed the behaviour in steady-state regime of GFRP-RC beams with straight- and 180º bent-end splices. The aim of the study was to simulate a localized fire event at one of the splices' extremities; to that end, the temperature at the bottom of the beams was maintained constant at 230 ºC or 550 ºC during 90 min, after which they were monotonically loaded up to failure. It is worth noting that the described heating and loading conditions differ greatly from those simulated in fire resistance tests and therefore the results obtained cannot be extrapolated to a realistic fire scenario in a building. Regardless of this limitation, it was verified that the beams with straight-end splices failed due to the slippage of the spliced rebars and that their load capacity was reduced by 40% in comparison with the undamaged beam. On the other hand, the beams with continuous rebars and 180º bent-end splices both failed due to concrete crushing, with the reduction of load capacity being lower in the former (around 7%) than in the latter (around 36%) after being exposed to 550 ºC (the maximum temperature registered in the reinforcement was 400 ºC).

Kiari *et al.* [17,18] tested CFRP-RC beams with continuous rebars and beams with lap splices comprising straight-rebars or closed loops. In the first part of the study [17], the authors also tested different loop arrangements, comprising a single or two hoop overlaps in the fire exposed zone. All

beams with lap splices tested in [17] failed within the first 3 to 11 min of fire exposure: those with straight-end splices failed due to the slippage of the spliced rebars, while those with closed loop rebars presented premature shear failures of the concrete in the splicing region due to the insufficient splicing length considered. In the second part of the study [18], the loop overlapping length was significantly increased and shear reinforcement was also adopted in that zone to prevent premature shear failure and to allow exploiting the load carrying capacity of the CFRP looped rebars; here, beams with and without shear reinforcement were tested: the beams with closed loop splices failed due to the rupture of the CFRP rebars after 57 and 76 min of fire exposure, with longer fire resistance being attained in beams with stirrups. These beams actually endured longer that those previously tested in [17] with continuous reinforcement, which had failed prematurely (after 45-51 min) due the slippage of the rebars at the anchorage zones. The beams with straight-end splices presented the same failure mode as those tested in the first part of the study, *i.e.*, due to the loss of bond of the overlapped rebars when their temperature exceeded the T_g.

More recently, Rosa *et al.* [90,147] assessed the fire behaviour of GFRP-RC slab strips with tension lap splices comprising different (i) overlapping lengths, (i) surface finishes (sand coated [147] and two ribbed rebars [90]), and (iii) geometries (straight [90,147] and 90º bent [147]), some of which illustrated in Figure 2.17. In the slabs in which the development length designed for ambient temperature was adopted and straight rebars were used, the bond failure of the splices occurred after between 12 and 39 min of fire exposure, depending on the splice length, T_g and surface finish of the bars; as expected, the spliced rebars with lower T_g loss their bond to concrete sooner (at lower temperatures) than those with higher T_g. As shown in Figure 2.17, increasing the splice length from 1.0 to 1.3 times the development length designed for ambient temperature only provided a minor increase of 7 min in fire resistance, because the T_g was quickly attained in most of the fire exposed span from the very early stages of fire [90] (*cf.* Figure 2.11). It was concluded that irrespectively of the splice length, the failure of the slabs with straight-end splices was triggered when the ends of the rebars attained a temperature close to the T_g and for which the GFRP-concrete bond was known to be severely degraded; as comparison, the slabs with continuous reinforcement failed after 149 min [147] to 181 min [90] of fire exposure due to the rebars' rupture. However, a notable improvement in fire endurance was obtained by adopting bent rebars in the extremities of the splices, while also increasing the straight overlapping length to 1.3 times the development length designed at ambient temperature (*cf.* Figure 2.18a). This splice configuration significantly enhanced the fire resistance from 26 min (using straight rebars) to 75 min, as it allowed anchoring the reinforcement at a higher depth of the slab, where bond was degraded at a slower rate and, hence, remained less damaged. The bent bars ultimately slipped from the concrete when their extremities attained the T_g (*cf.* Figure 2.18b), which however occurred approximately 60 min after that temperature was reached in the lower section of the bend, as evidenced in Figure 2.18a.

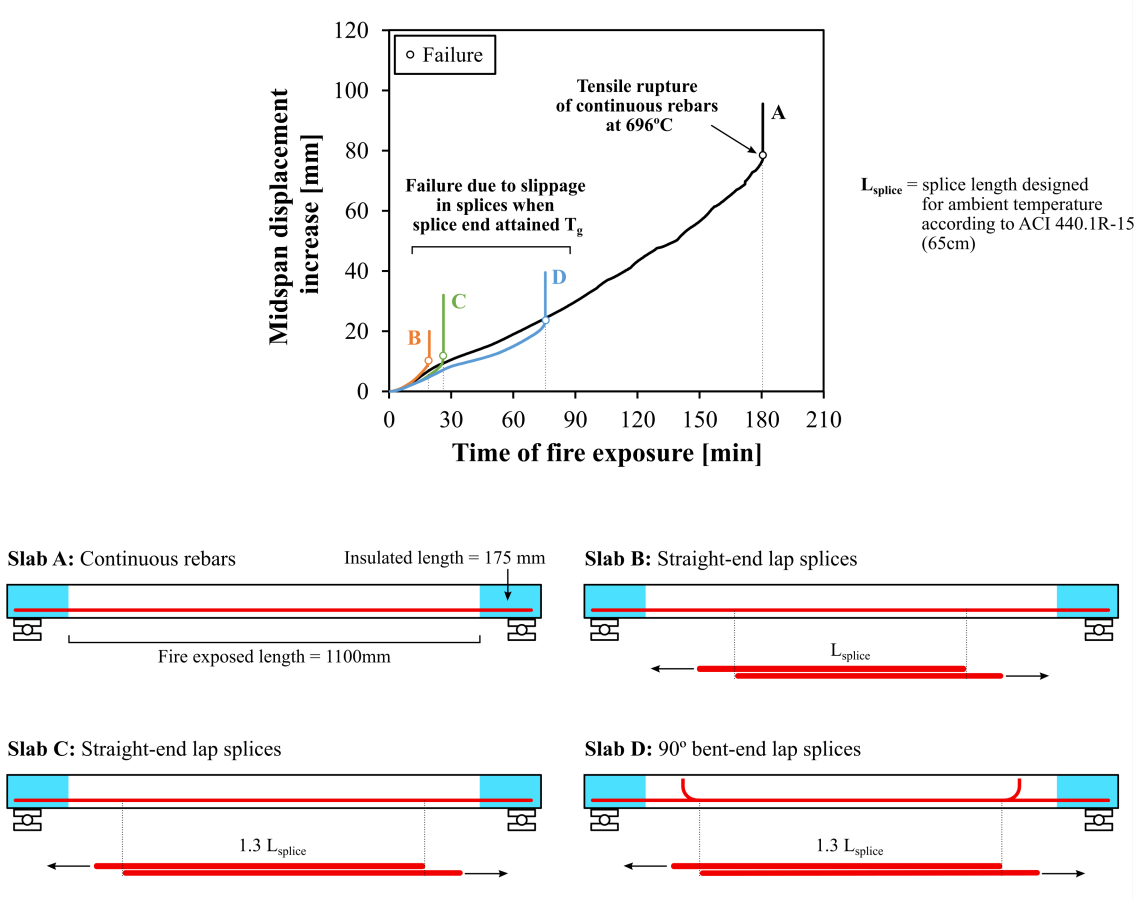

Figure 2.17. Evolution of midspan displacement increase during fire exposure – comparison of fire endurance of GFRP-RC slabs with continuous rebars (slab A), straight-end lap splices (slabs B and C) and 90º bent-end lap splices (slab D) (adapted from Rosa *et al.* [90], *cf.* Section 6.5.2.1 and Section 6.5.2.2).

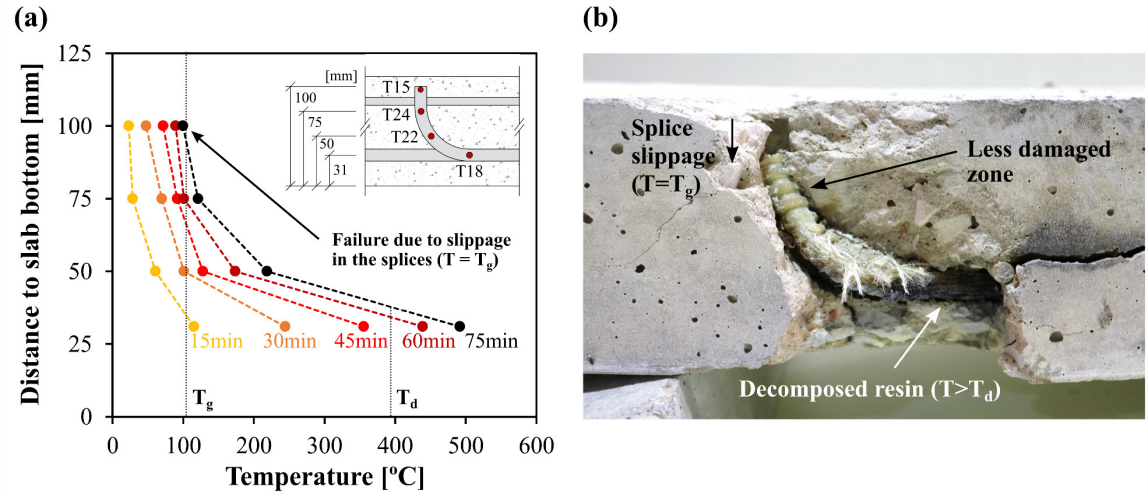

Figure 2.18. (a) Evolution of temperature along the bent extremities of lap splices directly exposed to fire; (b) failure of the slab due to the splices' debonding when temperature at the extremity attained the T_g (adapted from Rosa *et al.* [90], *cf.* Section 6.5.2.2).

2.4.1.2.4. Type of bar

As previously shown, the fire resistance of GFRP-RC structural members strongly depends on the concrete cover thickness adopted, on the concrete's ability to ensure good anchoring conditions to the reinforcement during fire and, ultimately, on the degradation of the GFRP bars' mechanical properties and of their bond to concrete at elevated temperature. In turn, such degradation largely depends on the material and geometrical characteristics of the bars, namely their T_g, T_d, surface finish and geometry; this allows concluding that the type of bar adopted markedly influences the deflection response and fire resistance of GFRP-RC members.

Researchers agree that in zones of the structure where the load bearing capacity relies on the GFRP-concrete bond, which include anchorage and splicing zones, the temperature of the reinforcement should be limited to its T_g, which is associated with a severe reduction of bond strength. Accordingly, it has been demonstrated that the lower the bars' T_g, the more prone structural members are to premature debonding failures [19,90]. On the other hand, if proper anchoring conditions are provided to the rebars, the fire endurance is governed by the tensile strength of the reinforcement at temperatures above the resin's T_d. However, in this regard, the definition of the critical temperature for the tensile strength of the rebars is not as straightforward as it is for the bond strength, mainly due to the lack of consensus on the criteria that should be considered to define such value (*cf.* Section 2.5.4) and also because of the large diversity of FRP bars available (affected differently by elevated temperature). Indeed, based on the available literature, it has been shown that the temperature at which the rebars' rupture can occur vary significantly (in the order of hundreds of degrees depending on the type of bar). As discussed in the following section, the rupture of the reinforcement can also be affected by localized heating effects to which they might be subjected to in widely cracked sections and, naturally, the stress level installed in the reinforcement (which depends on geometry, loading and support conditions).

A brief mention is also made to the conclusions obtained in Rosa *et al.* [90] with respect to the influence of the bar diameter on the fire resistance; the authors compared slabs with similar reinforcement ratios, but comprising rebars with different diameters (8 and 12 mm). It was observed that while the tensile rupture of the rebars occurred for nearly the same temperature, the slab with larger rebars endured around 30 min longer that the slab with smaller rebars. This result was partially attributed to the slower propagation of heat through the cross-section of the larger rebars, which, in turn, led to a slower reduction of their tensile properties with temperature. Unfortunately, no other studies are available in the literature to corroborate/refute these results, therefore further tests are needed to draw definitive conclusions with respect to the effect of the bar diameter in the members' fire endurance.

2.4.1.2.5. Concrete strength and load level

The effects of the composition and properties of concrete, as well as of the applied load on the fire resistance of GFRP-RC members have also been investigated. Kodur *et al.* [70] showed that from a thermal behaviour point of view, concrete members cast with carbonate aggregates perform better in fire that those with siliceous aggregates (due to the lower thermal conductivity of the former [157]). The effect of the load level on the fire performance of FRP-RC members was investigated in [14,20,21,148,149]. Gurung and Salem [21] tested two GFRP-RC beams with straight-end lap splices exposed to fire and subjected to 85% of the design load at ambient temperature, and compared the results with those obtained by Nour *et al.* [20] in two identical beams yet loaded to 40% of the design load. The authors found that varying the load level did not affect the fire resistance of the beams because the governing failure mechanism was the loss of bond between the spliced rebars and the concrete when the T_g was attained. Different conclusions were reported by Nigro *et al.* [14,148], who tested slabs with continuous GFRP reinforcement subjected to service loads corresponding to 10% (*i.e.* self-weight), 40% and 60% of the ultimate bearing capacity of the slabs designed for ambient temperature. They found that the slabs in which the rebars remained well-anchored at the extremity zones were able to endure fire for 180 min without collapsing, irrespectively of the load level. However, in the slabs that failed due to the pull-out of the rebars at the anchorage zones, the fire resistances was progressively reduced as the load level increased: the time to failure was 180, 120 and 60 min respectively when the slabs were loaded at 10%, 40% and 60% of the ultimate bearing capacity at ambient temperature.

Rafi *et al.* [149] found a relation between the load level and the propensity of GFRP-RC beams to spalling when exposed to fire. The authors tested beams subjected to their self-weight, or with an additional mechanical load corresponding to 11% or 22% of their ultimate bearing capacity at ambient temperature. Interestingly, the decrease in sustained load increased the severity of spalling: the unloaded beam presented massive spalling after 60 min of fire exposure, while the more heavily loaded slab did not show any concrete delamination. This result was justified by the pre-cracking effect of the concrete during the loading stage (hence prior to heating), as it facilitated the evaporation of the moisture present in the concrete and thereby reduced the propensity for spalling during heating. The conclusions obtained by Rafi *et al.* were confirmed by Bellakehal *et al.* [89], who demonstrated that the thermal-induced radial pressure at the bar-concrete interface, and consequently the propagation of radial cracks in the concrete, decreases with the increase in applied load.

A strong influence of the localized heating effects at cracked sections of the concrete members, and its relation with the concrete strength, on the fire resistance of GFRP-RC members was also reported by Sadek *et al.* [91] and Rosa *et al.* [147]. These studies found that members with lower concrete strengths presented shorter fire resistance than those with higher concrete strength. The explanation for these results was found to be the more extensive cracking pattern presented by members with lower concrete

strength; therefore, temperature of the bars increases more rapidly in widely cracked zones, consequently accelerating (locally) the degradation of their mechanical properties and triggering an earlier failure. As highlighted by Duarte *et al.* [146], the occurrence of wider cracks in the concrete also promotes an oxidative environment, in which the resin and the glass fibres are more rapidly degraded (compared to an inert environment). It is worth mentioning that the influence of cracking on the thermal field of concrete members was also investigated in recent years; however, there seems to be a lack of consensus, with some studies referring that the heat propagation tends to increase in the presence of cracks [158,159], others mentioning the opposite trend [160,161], and others stating that cracking does not have a meaningful influence in the heat propagation within concrete [162,163].

2.4.2. Numerical analysis of the fire resistance of GFRP-RC flexural members

2.4.2.1. Modelling of thermal behaviour

According to the author's best knowledge, the numerical study of Kodur and Baingo [164] was likely the first to model the thermal behaviour of FRP-RC structural members and is the basis of the concrete cover design abacus provided in the CAN/CSA-S806 standard [8]. Since then, several authors have used numerical tools to perform thermal analysis of GFRP-RC members subjected to fire with varying member thickness [153,164], concrete cover [14,71,116,146,153,164–167], type of aggregate [153,164] and moisture content [153,168]. Overall, the models were able to accurately predict the temperature distribution through the thickness of the heated span; to that end, the authors have emphasised the importance of properly defining the thermal properties of concrete, among which the specific heat [154,168] and the thermal conductivity [169], as they were shown to have a major influence on the predicted temperatures, and consequently on the deformations of RC members exposed to fire. Conversely, the presence of the reinforcement can usually be disregarded in heat transfer analyses given their low thermal conductivity and geometric percentage, and consequent low influence on the cross section's thermal behaviour [70,71]. Nigro *et al.* [71] assessed the influence of the presence of the rebars in thermal analysis and concluded that although this approach leads to more accurate temperature estimations, the relative differences obtained were very low, around 5 to 10%. Furthermore, as shown in [12,146,154], it is worth noting that special attention should be given to the definition of the thermal boundary conditions of the cold anchorage zones of GFRP-RC members, since the accuracy of temperature predictions in these zones is paramount for the design of the protected anchorage lengths.

2.4.2.2. Modelling of thermomechanical behaviour

Several FE models have been developed to assess the thermomechanical response of GFRP-RC slabs [30,142,146,154,168,170–173] and beams [165–167]. These models simulated the effects of standard

fire curves and imposed mechanical loadings by means of uncoupled procedures (the thermal analysis was decoupled from the mechanical analysis). The accuracy of the models in predicting the deflection response, failure mode and fire resistance of the members was proven to rely on the appropriate definition of the temperature-dependent mechanical properties of both concrete and GFRP bars.

The numerical models developed in [146,165–167] demonstrated that increasing the concrete cover thickness enhances the fire resistance of GFRP-RC structural members (Figure 2.19) by delaying the temperature rise in the reinforcement and thereby enabling the retention of strength, stiffness and bond properties of the GFRP rebars over longer periods of time; these results are in agreement with fire resistance tests performed by Rosa *et al.* [90,147]. Numerical studies also showed that the type of reinforcement affects the fire performance of RC structures [30,117,119,166,167]. The fire resistance of GFRP-RC members has been reported to be lower than that of equivalent steel-RC members, due to the higher susceptibility of GFRP rebars to elevated temperatures [117,166,167]; however, a different conclusion was obtained (experimentally) in Rosa *et al.* [90], since GFRP-RC slabs presented longer fire endurances (between 133 min to 181 min) to that of a comparable steel-RC slab (which failed after 114 min).

Yu and Kodur [166] and Hawileh and Naser [165] performed parametric studies about GFRP-RC beams exposed to standard and performance-based fire curves, showing that their fire behaviour is highly influenced by the type of exposure. Compared to a standard fire, a severe fire exposure involving steeper temperature increase and higher peak temperature was found to induce faster reinforcement degradation, resulting in lower fire resistance. Yu and Kodur [166] also assessed the increase in fire resistance of restrained FRP-RC beams against unrestrained beams: restrained beams endured fire 5 min to 25 min longer than simply supported beams when the boundary conditions of a typical beam-column connection or a shear wall constraint, respectively, were simulated; similar conclusions were obtained by Bilotta *et al.* [30].

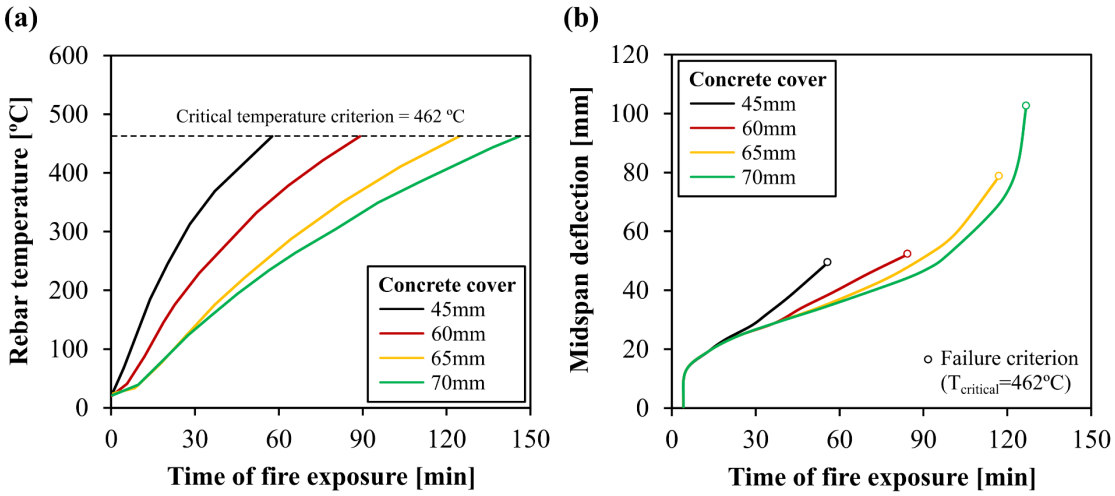

Figure 2.19. Influence of concrete cover on the (a) thermal and (b) deflection responses of GFRP-RC beams exposed to fire (numerical results; adapted from Hawileh and Naser [165]).

Numerical studies were also carried out to assess the influence of the sustained load level [154,167] and concrete strength [146] on the fire behaviour of GFRP-RC beams. The results indicated that the fire resistance decreases with the increase in load level, since the materials' ultimate strength (which is reduced with temperature) is attained earlier under higher loads. Rafi *et al.* [174] conducted parametric studies on CFRP-RC beams and concluded that the fire resistance decreases with the increase in concrete strength. This result was explained by the higher load levels (in fire) applied to beams with higher concrete strength – the higher load bearing capacity at ambient temperature (numerically estimated) resulted in a higher fire load level and, consequently, in an increased stress level on the FRP reinforcement. However, no experimental evidence was found in the literature to support these findings. On the other hand, fire resistance tests performed by Sadek *et al.* [91] and Rosa *et al.* [147] (the latter in thin GFRP-RC slabs strips under an identical sustained load) showed that members with higher concrete strength endured fire longer than those using a lower concrete grade; as discussed in Section 2.4.1.2.5, this was due to more extensive cracking observed in the latter members, which accelerated the thermal-induced degradation of the GFRP-concrete bond and tensile strength of the rebars. The slabs of Rosa *et al.* [147] were modelled by Duarte *et al.* [146], yet the FE models were not capable of simulating the localized heating effects of the reinforcement at cracked sections of the slabs, because the thermal analysis was uncoupled from the mechanical analysis, and therefore the results were not sensitive to the influence of concrete strength.

Until recently, temperature-dependent bond stress *vs.* slip laws were not available for GFRP reinforcement, which explains why only in very few of the abovementioned numerical studies the progressive degradation of bond with increasing temperatures was explicitly considered. In most studies, a perfect FRP-concrete bond was considered, which is only a reasonable (but not necessarily accurate) assumption when pull-out failure at the ends of the reinforcement is prevented, namely by assuring sufficiently long anchorages protected from direct fire exposure. This latter hypothesis was validated in

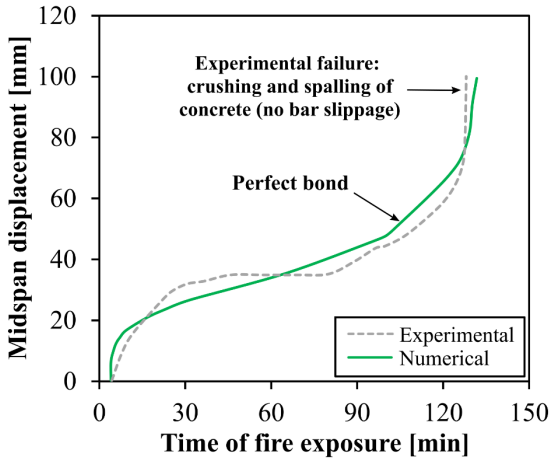

Figure 2.20. Numerical simulation of deflection response during fire exposure of a GFRP-RC beam assuming perfect bond between the bars and concrete (adapted from Hawileh and Naser [165]).

some numerical studies (*e.g.* [165,170,171]), which provided reasonably good agreements between measured and numerical deflection responses of FRP-RC flexural members where pull-out failures in the anchorage zones did not occur (Figure 2.20).

In the meantime, other authors [166,171] have considered alternative modelling approaches to the "perfect bond" simplification. In the study of Nigro *et al.* [171], perfect bond was only considered in the anchorage zones, while the bond interaction in the fire exposed span was neglected from the onset of exposure; however, overall, the numerical results presented some deviations from the measured deflections during thermal exposure. Yu and Kodur [166] developed a FE model to perform 2D heat transfer analysis of a beam's cross section and then trace the beam's mechanical behaviour based on moment-curvature relationships. The model took into account the strain resulting from the slip of the reinforcement as part of the total FRP strain; to that end, the temperature-dependent bond strength and stiffness obtained from pull-out tests at elevated temperature were considered. Even though the model was able to accurately predict the deflection evolution of two FRP-RC beams throughout most of the fire exposure, failure (due to slippage of the rebars in the anchorage zones) was indirectly estimated based on strength and deflection limit states criteria; in other words, failure was not explicitly simulated; in this regard, it is worth mentioning that failure in the test of one of the beams was triggered by the slippage of the rebars in the anchorage zones.

As previously discussed, the loss of bond at high temperature governs the fire endurance of FRP-RC when spliced reinforcement is used or if the anchorage zones at the ends of the members are not sufficiently insulated. In these cases, premature pull-out failure will likely occur prior to the tensile rupture of the rebars, and thus assuming a perfect bond leads to inaccurate and unsafe predictions of fire endurance. This research need was duly highlighted in the studies of Hajiloo *et al.* [154] and Rafi *et al.* [117], where FE models considering the perfect bond simplification were unable to simulate the loss of bond at the ends of the reinforcement; consequently, the deflection response and fire endurance deviated from those experimentally obtained. An accurate simulation of the aforementioned failures modes thus relies on explicitly considering temperature-dependent bond stress *vs.* slip laws, which was only recently implemented in [30,142,146,168].

The FE models developed by Bilotta *et al.* [30] aimed to simulate the fire resistance tests of GFRP-RC slabs that failed due to tensile rupture of the reinforcement or due to rebars' pull-out in the anchorage zones. Overall, the numerical deflections presented a good agreement with those experimentally measured; although the models were able to simulate failure due to the loss of bond in the end anchors, they were not able to predict the time to failure of some of the slabs. This might be due to the fact that the bond-slip laws implemented in the model were not derived from bond tests conducted on the same bars used in the experiments; instead, a theoretical bond model calibrated for ambient temperature was considered and then temperature-dependent reduction factors were applied to the maximum bond stress (those factors had been calibrated to consider the bond reduction with temperature for different bars).

Furthermore, the ability of the models to simulate the tensile rupture of the GFRP rebars was not demonstrated, because, although they sustained the fire exposure during at least 180 min before failing, the numerical deflections were only depicted up to 120 min. Veljkovic *et al.* [168] simulated the deflection response prior to failure of GFRP-RC slabs subjected to a maximum temperature of 210 ºC; the model provided good estimates of the midspan deflections by considering a bond damage evolution law that was calibrated in [143] from results of pull-out tests.

Duan *et al.* [142] simulated some of the slab tests conducted by Nigro *et al.* [14] and Hajiloo *et al.* [12] in which failure was initiated by the rebars' slippage at the anchorage zones. The GFRP-concrete interaction of the bars of Nigro *et al.* was uniquely defined according to the bond-slip model proposed by Aslani *et al.* [120]; in the study of Hajiloo *et al.*, the interfacial slip was also computed according to the model of Aslani *et al.*, yet the peak bond stress at each temperature was computed considering the decay of bond strength with temperature obtained from pull-out tests performed in identical bars ([126]). The numerical results were compared to those obtained in Hajiloo *et al.* [154] assuming perfect bond and allowed confirming that the latter approach led to significantly less accurate predictions of the deflection behaviour of the slabs, as depicted in Figure 2.21. Overall, the models were capable of predicting the bond failure at the anchorage zones, though the prediction of the moment of failure was far more accurate for the slab tested by Hajiloo *et al.*

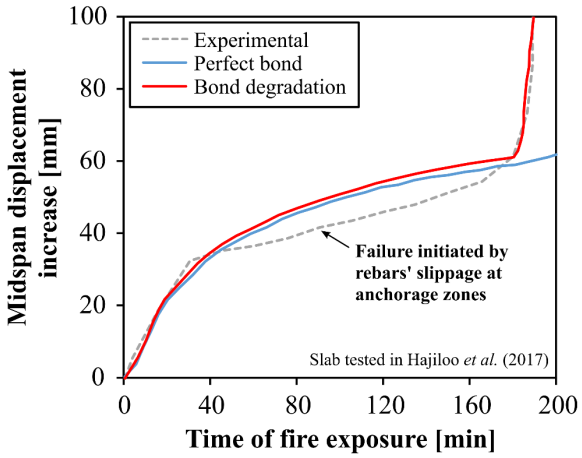

Figure 2.21. Numerical simulation of deflection response of the slab of Hajiloo *et al.* [12] during fire exposure considering both perfect bond approach and explicit modelling of bond degradation with temperature (adapted from Duan *et al.* [142]).

Duarte *et al.* [146] simulated the GFRP-RC slabs tested by Rosa *et al.* [147]; this is the only study found in the literature that besides modelling slabs with continuous rebars also simulated the fire behaviour of members with lap splices. To that end, the GFRP-concrete interaction at elevated temperature was modelled through local bond-slip laws calibrated in [125] based on pull-out tests conducted in identical bars. The FE models provided fairly good predictions of the thermomechanical behaviour of the slabs, including the simulation of the slippage of the spliced rebars and the tensile rupture of the continuous

rebars, though the predictions of the time to failure deviated slightly from the experimental results. Regardless of these deviations, the models were able to capture (i) the increase in fire resistance with the increase in the cover thickness, and (ii) the considerable reduction in the fire endurance due to the presence of lap splices directly exposed to fire.

2.4.3. Research needs

Substantial progress has been achieved in recent years about the understanding of the susceptibility of GFRP reinforcement to elevated temperature and the fire resistance of GFRP-RC members. However, further testing is still required, especially of full-scale beams and slabs comprising different detailing configurations and concrete covers. These experiments should aim at simulating realistic restraining conditions provided by adjacent structural members to validate the feasibility of the recommendations provided by researchers, namely those respecting to the location and geometry of anchoring zones and lap splices and to the adoption of thin cover thicknesses. Comprehensive investigations of the influence of the detailing of bent rebars in the aforementioned zones, as well as of the bar diameter, axial restraint and concrete strength on the fire endurance of GFRP-RC members should also be pursued. The findings of fire resistance tests should be complemented with numerical simulations of the thermomechanical behaviour of the members, if possible using fully coupled thermomechanical models to capture local effects caused by concrete cracking; the models should be able to explicitly model the degradation of GFRP-concrete bond with the increase in temperature in order to provide more accurate predictions of the deflection behaviour and failure modes, especially when the members' failure is triggered by rebars slippage.

2.5. Fire design guidance: available guidelines and prospects for future revisions

The research and use of FRP reinforcement in concrete structural members has expanded over the years in parallel with the continuous development of standard design codes [6–8,10,175] and design manuals (*e.g.* [1,176,177]); yet, only the American ACI 440.1R-15 [6] and Canadian CAN/CSA S806-12 [8] standards (and also its previous version [178]) provide fire design guidance. As described next, the available guidance comprises very general design recommendations, which are insufficient to guarantee that the fire resistance requirements defined in building codes are fulfilled. Apart from the design charts provided in [8] for the selection of the concrete cover thickness (*cf.* Section 2.5.3), no calculation models or design-oriented specifications are available. Moreover, the design provisions are very limited in scope and lack in providing detailed guidance with respect to several constructive aspects that recent studies have demonstrated to be key for the members' fire resistance, such as the detailing and location of anchorage zones and lap splices, or the effects of the concrete strength and bar type/finish. It should be

referred that the now outdated fib Bulletin 40 [10], published prior to the latest versions of the American and Canadian codes [6,8], does not advise the use of FRP rebars in buildings (as did the previous version of ACI 440.1R [179]); this is due to the limited knowledge on the topic at the time of its elaboration.

2.5.1. General fire design recommendations

ACI 440.1R-15 [6] is the guide that currently provides more recommendations with respect to the fire design of concrete members flexurally reinforced with FRP bars, though of very general scope. That document states that the fire resistance of FRP-RC members may be governed by the heat-induced degradation of the mechanical properties of the rebars and/or by the loss of the FRP-concrete bond. For these reasons, special consideration should be given to the type of FRP reinforcement adopted, since the degradation rate of the bars' properties with increasing temperature varies greatly depending on their thermophysical properties and geometrical features (including the surface finish). Likewise, this document recommends that the concrete cover thickness and type of aggregate should also be carefully selected, as they influence the temperature evolution of the reinforcement during fire exposure and, therefore, the retention of the bars' tensile strength and modulus and bond to concrete over time [6]. When assessing the fire endurance of FRP-RC members through fire resistance tests, ACI 440.1R-15 [6] advises against the use of the critical temperature approach to assess the fire resistance rating; instead, the fulfilment of the fire performance criteria defined in building codes (load bearing capacity, insulation and integrity) should explicitly be considered [6,8].

2.5.2. Cold anchorage zones and lap splices

The literature shows that the severe degradation of the FRP-concrete bond with increasing temperature can be detrimental to the members' fire endurance. In this regard, the exposure to elevated temperatures has been proven to be especially concerning in poorly insulated anchorage zones and in unprotected lap splices, where the attainment of T_g can trigger premature debonding failures. Appropriate design provisions on this matter are therefore needed for engineering practice; however, only general and theoretical recommendations are available in existing codes. For example, ACI 440.1R-15 [6] mentions that the reduction of the FRP bars' bond strength with increasing temperature should be accounted for in the design of FRP-RC members; however, design expressions or degradation models for the tensile and bond properties of the bars as a function of temperature are not provided. Yet, ACI 440.1R-15 [6] does provide an important recommendation with respect to the anchorage zones of the rebars, stating that they should be located in unexposed (*i.e.* cool) zones of the members, to ensure that the rebars' temperature is kept below their T_g in the event of a fire.

The knowledge about the fire behaviour of FRP-RC members has improved considerably in recent years, especially with respect to key details, such as the cold anchorage zones and lap splices, which has

allowed several authors to propose design provisions on these issues, which could be included in future versions of codes. These comprise protecting both the anchorage zones of the bars and lap splices from the high temperatures attained during a fire, preferably locating/extending them into cooler areas of the structure, such as connection zones with other structural elements or over partition walls [11,90,147]. It has been shown that the splice and cold anchorage lengths of the bars need to be longer than those designed for ambient temperature due to the severe reduction of the GFRP-concrete bond at elevated temperature [17–19,90,121,147]. The use of bent rebars is strongly encouraged as a practical and efficient method to improve the bars' anchorage capacity in cold anchorage zones [13,14,18] and lap splices [90,121]. The length and geometry of the rebars, regardless of being straight or (preferably) bent, should be designed to consider adequate development lengths (and also tail lengths in the case of bent rebars) for the temperatures expected to be attained in the structure and the stress level installed; they should also consider the type of surface finish and T_g of the rebars, as they govern the degradation rate of the bond strength with the temperature increase.

2.5.3. Concrete cover

The adoption of appropriate concrete cover is key to the fire endurance of FRP-RC members, as it should prevent the premature rupture of the reinforcement by maintaining its temperature below a certain critical value (*cf.* Section 2.5.3). CAN/CSA S806-12 [8] provides a set of design charts, derived from the parametric study of Kodur and Baingo [164], from which the concrete cover thickness can be designed based on the definition of a critical temperature of the GFRP bar. However, concerns were raised about the use of these charts since the critical temperature criterion for FRP bars is not unanimous. Although this temperature has been normally considered as the temperature at which the material loses 50% of its strength (as considered for steel rebars), this value remains unknown for a significant number of FRP bars and, due to the wide variety of FRP products available in the market, generalizations cannot be made based on existing data from other manufacturers. As a matter of fact, as shown in Section 2.2.3.2 (*cf.* Figure 2.4), the critical temperature of GFRP bars (defined as above) can vary greatly between 200 ºC and 450 ºC (as reference, for steel rebars, such temperature is reported to be 593 ºC [180]). On the other hand, as discussed in Section 2.4.1.2.1, some studies (*e.g.* [11,12,90,147]) have proven that this simplified method leads to overly conservative designs and that lower concrete covers thicknesses can be adopted if the reinforcement is well-anchored in cool zones of the structure; this aspect could be improved in future revisions of FRP-RC codes, to allow the design of more economical structures. Although the following aspects are not addressed in FRP-RC design codes, it is important to highlight that the concrete cover thickness should also be sufficiently thick to: (i) prevent heat-induced spalling, due to the effect of the transverse thermal expansion of the FRP reinforcement, and (ii) to enable sufficient bond strength in the cold anchorage zones of the bars during a fire, hence preventing bond splitting failures from occurring.

2.5.4. Critical temperatures

Critical temperatures for GFRP bars should be defined based on the degradation of their tensile and bond strengths with temperature as a way to prevent the loss of effectiveness of the reinforcement due to the exposure to elevated temperature; moreover, they should also consider the location and detailing of the reinforcement. In this regard, in zones where bond is vital to maintain the structural integrity of members during fire exposure, namely in anchorage zones and lap splices, the maximum allowable temperature should naturally be lower than along the remaining span, due to the more severe degradation of the bond properties with temperature compared to that experienced by the tensile properties.

In service conditions, ACI 440.1R-15 [6] recommends that the temperature of the reinforcement should be kept below its T_g to preserve its good bond performance; this temperature should be conservatively considered as the onset temperature of the glass transition, preferably obtained by DMA. In the case of a fire event, the standard states that if the anchorage zones of the rebars are protected from heat, the resin softening along the fire exposed zone of the reinforcement will not be determinant to the members' fire endurance and therefore temperatures are allowed to exceed the T_g in that zone; however, the threshold temperature with respect to the tensile strength degradation is not reported in this guide. Alternatively, as mentioned, CAN/CSA S806-12 [8] defines the critical temperature as the one corresponding to 50% of strength retention (compared to ambient temperature). However, some authors (*e.g.* [107]) have found that this criterion leads to a great strength reserve of the concrete member and, therefore, more efficient designs could be attained with alternative approaches. In this regard, Hajiloo *et al.* [107] proposed that the critical temperature could be defined based on a strength retention of 25%; this level of degradation is normally associated with temperatures near the resin T_d. No recommendations are currently available with respect to the effects of elevated temperature in lap splices; yet, according to existing research, the temperature of splicing zones should not exceed T_g in both service conditions and during fire.

2.6. Concluding remarks and recommendations for future research

This chapter presented a review of the knowledge and most recent developments about the fire behaviour of concrete members reinforced with GFRP bars, including the applicable fire design guidance. During the last two decades, remarkable progress and relevant insights were obtained about the fire performance of GFRP-RC structures. However, such progress is not yet reflected in existing design codes – fire design guidance is still limited to general principles and design rules are not yet provided. Updating and improving the existing fire design recommendations is therefore warranted.

The literature already comprises a wealth of data regarding the tensile and bond properties of GFRP bars at elevated temperatures; together with recently proposed temperature-dependent GFRP-concrete bond

stress *vs.* slip laws, such data have considerably improved the ability of FE models to accurately simulate the fire behaviour of GFRP-RC members. However, the effects of elevated temperature on the thermal and other mechanical properties of GFRP bars remain poorly understood, and the influence of relevant parameters, such as the thermal expansion coefficients, the bar geometry, the environment and duration of thermal exposure on the bars' mechanical performance are worth being more thoroughly investigated. This should improve the accuracy of numerical simulations and allow developing more reliable analytical models that can be used for design purposes.

The mechanical and bond behaviour of straight GFRP reinforcement under elevated temperature have been widely studied and their influence on the fire performance of GFRP-RC beams and slabs has been demonstrated by means of fire resistance tests and numerical simulations. These studies proved that the type of bar, the concrete cover thickness and the detailing of the anchorage and splicing zones are the most critical aspects for the fire resistance of FRP-RC members. It has also been shown that fire design must consider the severe degradation with temperature of the bars' mechanical properties and of their bond to concrete. A few recent studies have demonstrated that the use of bent FRP bars can significantly improve the reinforcements' anchorage capacity during fire exposure; yet, the efficacy of this detailing solution in anchorage zones and lap splices needs to be more thoroughly investigated. Further efforts should also be made to cover a wider range of bars and concrete member geometries and FRP detailing configurations – these efforts should comprise full-scale fire resistance tests (simulating realistic heating, loading and restraining conditions) and the development of robust numerical models, able to assess and validate the adequacy of design provisions suggested in several studies.

Part II

Properties of GFRP bars at elevated temperature

Chapter 3

Thermophysical and mechanical properties of GFRP bars at elevated temperature

3.1. Introduction and objectives

The state-of-the-art review presented in Chapter 2 showed that the severe reduction of the mechanical properties of GFRP bars at elevated temperatures has remarkable implications in the fire resistance of GFRP-reinforced concrete structural members. Indeed, in a significant number of studies, failure of GFRP-RC flexural members under fire exposure has been reported to be triggered by the tensile rupture of the GFRP rebars at temperatures well above the decomposition temperature (T_d) of the polymeric matrix (which is typically between 250 ºC and 400 ºC in thermosetting resins [57]). This was the case of the slabs tested in the present thesis (*cf.* Chapter 6) and also in [19,148], in which the collapse occurred due to the failure of the bottom reinforcement at temperatures (in the bars) between 500 ºC and 713 ºC.

Understanding and characterizing the behaviour of the GFRP reinforcement at very high temperatures is therefore needed in order to accurately predict the deflection behaviour, failure modes and fire resistance of GFRP-RC structural members exposed to fire. However, the existing data about the properties of GFRP bars at high temperatures does not yet cover a sufficiently wide range of temperatures likely to be attained in the GFRP reinforcement during fire exposure. Actually, the tensile properties of GFRP bars at elevated temperatures are relatively well documented in the literature, only up to 500 ºC ([15,19,63,69,93,95–101,106,107,181,182]), and with the exception of the few results provided in [94,97] at 500 ºC, the variation of the bars' tensile modulus for temperatures above 400 ºC remains largely unknown.

This chapter presents experimental and analytical investigations about the tensile behaviour of GFRP bars at elevated temperatures, aiming to fulfil the above-mentioned knowledge gaps. Regarding the experimental campaign, four different types of GFRP bars were tested, provided by different manufacturers, therefore featuring different constituent materials (types and proportions/fractions of reinforcement/polymer matrix), thermophysical and mechanical properties.

The first part of the chapter (Section 3.3) comprises material and thermophysical characterization tests of the GFRP materials, namely dynamic mechanical analysis (DMA), differential scanning calorimetry analyses (DSC) and thermogravimetric analysis (TGA), which allowed to determine the T_g and T_d of the

bars. In the second part of the study (Section 3.4), the bars were subjected to tensile tests at different elevated temperatures, under steady-state conditions, from 20 ºC up to 715 ºC. This temperature range covered the entire glass transition and decomposition processes of the polymeric resin and is representative of the temperatures to which the bars may be exposed during fire prior to failure. The main goal of the experiments was to determine the tensile response at elevated temperature of the bars, namely to assess the effects of elevated temperature on tensile strength, tensile modulus and failure modes. In the last part of the study, analytical formulae are proposed for the reduction of the tensile strength and modulus with temperature, based on the results obtained herein and in other studies from the literature. It is worth mentioning that the DMA and tensile tests on the sand coated (SC) bars were carried out within the framework of the *FireComposite* project, part of which in collaboration with a Master student [26].

3.2. Description of the GFRP bars

Four different types of GFRP bars, illustrated in Figure 3.1, were used in the experimental campaign, which included sand coated (SC) and ribbed (RB and RBP) bars; their main geometrical, thermophysical and mechanical properties are summarized in Table 3.1. SC bars, illustrated in Figure 3.1a, were supplied by *Owens Corning* (model *Aslan 100* [183]) and were produced by pultrusion using E-CR glass fibres impregnated with a vinylester resin. The bars presented a slight surface undulation created by external helical wound fibres (*i.e.*, wrapping the bars' core); both the sand particles and the helical fibres were applied after pultrusion, but prior to the full curing of the polymeric resin. The bars had a nominal (core) diameter of 10 mm; the average effective diameter of the bars (*i.e.*, including the core and surface coating) was approximately 11 mm.

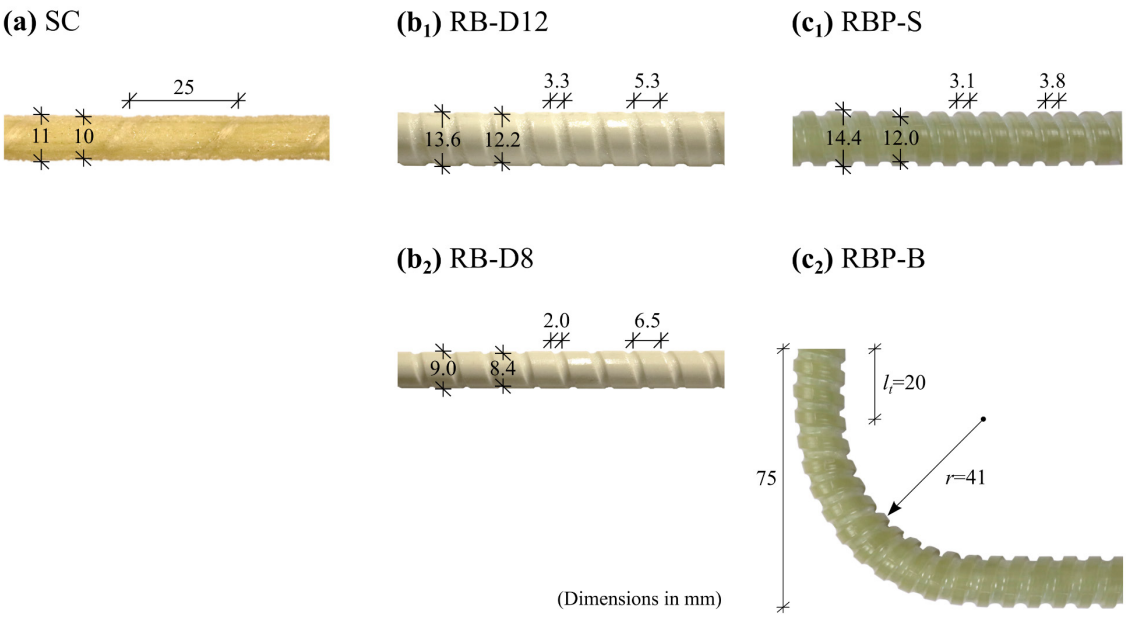

Figure 3.1. GFRP reinforcing bars tested (dimensions in mm).

Table 3.1. Properties of the straight GFRP bars.

Bar label	SC	RB-D12	RB-D8	RBP
Surface finish	Fibre-wrapped sand coated	Ribbed	Ribbed	Ribbed
Space between ribs: width × depth [mm×mm]	-	3.3 × 0.7	2.0 × 0.3	3.8 × 1.2
Nominal diameter [mm]	10	12	8	12
Diameter including coating/ribs [mm]	11.0	13.6	9.0	14.4
Equivalent diameter, D (1) [mm]	-	13.1	8.9	13.3
Cross-sectional area (2) [mm^2]	71.0	113.0	50.3	106.0
Tensile strength (3) [MPa]	1045	1380	1482	1184 (6)
Tensile modulus (3) [GPa]	48	60	58	60
Mass fibre content (3)	75%	87%	88%	72%
Resin	Vinylester	Vinylester	Vinylester	Vinylester-epoxy
Glass transition temperature, T_g (4) [ºC]	98	157	157	104
Decomposition temperature, T_d (5) [ºC]	374	400	400	400
Thermal expansion coefficient (axial direction) (1) [×10^{-5}/ºC]	-	0.6	0.6	0.6
Thermal expansion coefficient (transverse direction) (1) [×10^{-5}/ºC]	-	2.2	2.2	2.2

(1) Data provided in the manufacturers' catalogues [49,183].
(2) Equivalent diameter considering the ribs (considered to compute the area embedded in concrete).
(3) Properties experimental determined by the authors.
(4) T_g obtained based on the onset of the storage modulus curve obtained by DMA.
(5) T_d obtained based on the middle temperature of the sigmoidal mass change obtained by DSC (air atmosphere).
(6) Tensile strength in straight section (700 MPa in bent section [49]).

The ribbed RB and RBP bars were supplied by *Schöck* (model *ComBAR* [49]). RB bars had core diameters of 12 mm (RB-D12, shown in Figure 3.1b$_1$) and 8 mm (RB-D8, depicted in Figure 3.1b$_2$). In turn, RBP bars had a core diameter of 12 mm and were supplied as straight (RBP-S, Figure 3.1c) and 90º bent bars (RBP-B, Figure 3.1d). The bars were manufactured using E-CR glass fibres impregnated with a vinylester resin, in the case of RB bars, and a vinylester-epoxy resin, in the case of RBP bars.

The manufacturing process, including the procedure to shape the grooves/ribs was different in the two bars. In the case of bar RB, the helical grooves were mechanically ground into the pultruded (hardened) bars. As for RBP bars, to produce a ribbed surface and 90º bent extremities, the bars were moulded and cured inside a polypropylene pipe (removed before testing), inside which the fibre rovings were aligned and embedded in resin. The pipe had a deformed surface which shaped the outer surface of the bars before they were thermally cured. Due to this process, unlike the RB bars, the ribs of the RBP bars were composed solely of resin. As shown in Figure 3.1 (also *cf.* Table 3.1), the spacing between ribs and their profile were more pronounced (width and depth wise) in RBP bars than in RB bars.

The bent extremities of RBP-B bars (cut to obtain straight RBP bars) were moulded at a 90º angle with an inner bend radius (r) of 41 mm, corresponding to 3.1 times the equivalent bar diameter (or 3.4 times the nominal bar diameter, d, fulfilling the recommendations of ACI 440.1R [6], which, for design purposes, defines a minimum r/d ratio of 3). The tensile properties at ambient temperature conditions of the straight portion of the RBP bars are listed in Table 3.1 (as determined in the tensile tests presented ahead); the guaranteed (as reported by the manufacturer) tensile strength in the bent section is 700 MPa.

3.3. Thermophysical properties and inorganic content

Dynamic mechanical analyses (DMA) were performed according to the ASTM E1640 standard [184] in order to determine the T_g of the bars. The coupons, extracted from the core of the bars, were tested in a *Q800* dynamic mechanical analyser from *TA Instruments* using a three-point bending configuration and an oscillatory frequency of 1 Hz. The tests were conducted from 30 ºC up to 250 ºC in air atmosphere at a heating rate of 1 ºC/min. The curves of the storage modulus (*E'*), loss modulus (*E"*) and tangent delta (tan δ) as a function of temperature are plotted in Figure 3.2. The glass transition temperatures obtained from each of the curves are listed in Table 3.2. To provide a lower (conservative) bound to the beginning of the glass transition process, the T_g of the bars was set based on the onset of the storage modulus curve decay (plotted using a linear scale) resulting in the following values: 98 ºC for SC bars, 157 ºC for RB bars and 104 ºC for RBP bars.

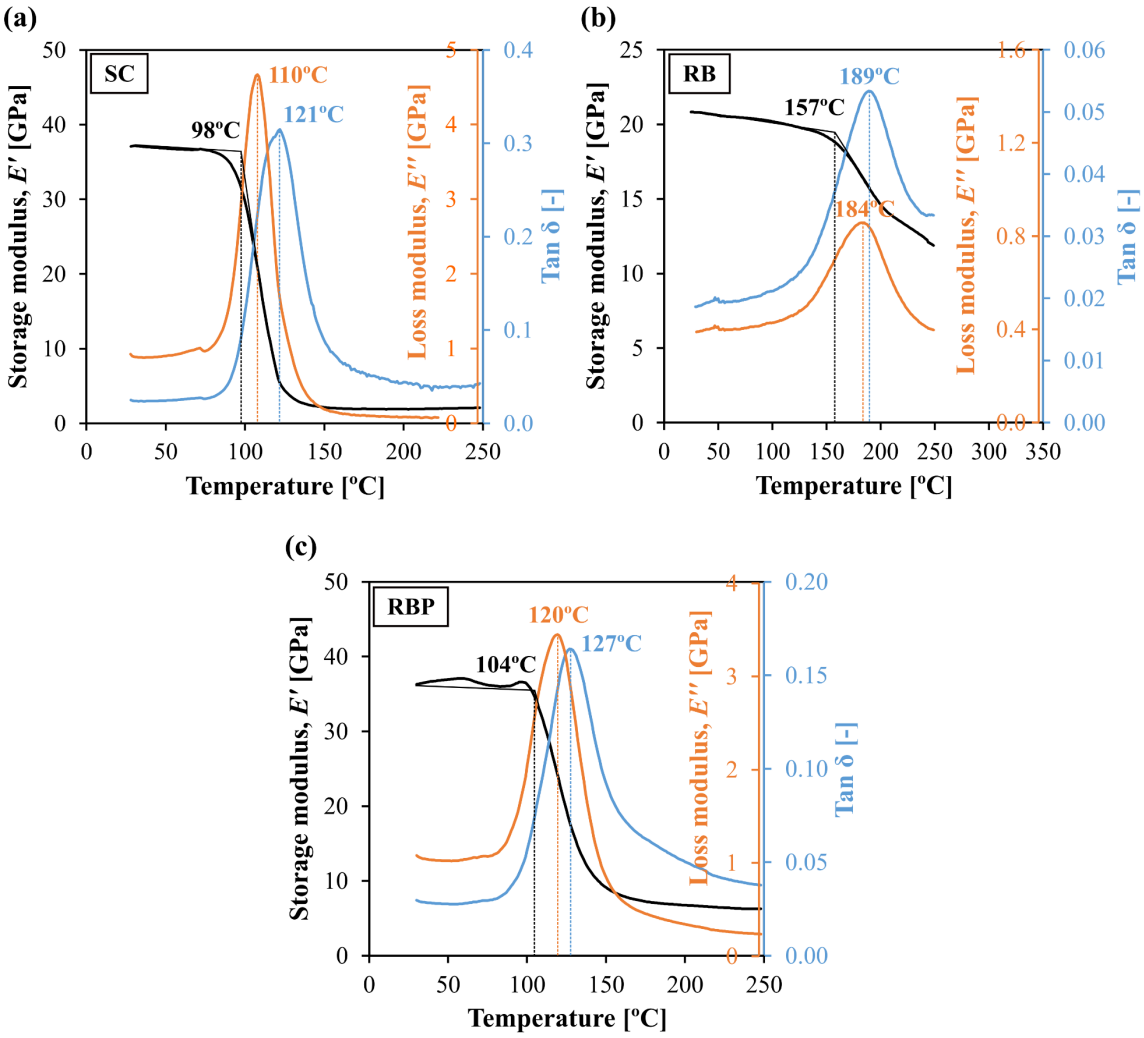

Figure 3.2. DMA curves of bars (a) SC, (b) RB and (c) RBP: storage modulus, loss modulus and tangent delta as a function of temperature.

Table 3.2. Results from DMA tests.

Bar	SC	RB	RBP
T_g, ***E'*** **[ºC]**	98	157	104
T_g, ***E"*** **[ºC]**	110	184	120
T_g, **tan δ [ºC]**	121	189	127

T_g values determined based on the onset of the storage modulus (*E'*) curve decay, and on the peak of the loss modulus (*E"*) and tangent delta (tan δ) curves.

Differential scanning calorimetry (DSC) and thermogravimetric analyses (TGA) were performed to the GFRP bars to determine the mass and energy variations of the materials as a function of temperature and, in particular, their decomposition temperature (T_d). The experiments were conducted according to the ISO 11357 standard [185] on a *Perkin Elmer STA6000* combined analyser, in an oxidative (air) atmosphere, from 30 ºC up to 850 ºC, and in an inert (nitrogen) atmosphere, from 30 ºC up to 700 ºC, in both cases at a heating rate of 10 ºC/min. These tests provided the remaining mass (Figure 3.3a) and heat flow *vs.* mass ratio (Figure 3.3b) as a function of temperature. The T_d of the bars was defined based on the middle temperature of the sigmoidal mass change, resulting in the values listed in Table 3.3. It can be seen that the values of T_d obtained in air atmosphere are only slightly lower than those obtained in nitrogen atmosphere. According to [57], the thermal decomposition of polymers in air atmosphere occurs over a lower temperature range due to the presence of oxygen, which accelerates the decomposition reaction. However, the oxidation process is mostly relevant at the surface layer of the bar, while the interior layers decompose mainly by the action of heat (similar to what occurs in a nitrogen atmosphere). In this respect, it is also worth referring that inside concrete, under normal circumstances, the reinforcement is exposed to an inert atmosphere. However, if wide (and deep) cracks develop, then locally the environment will be oxidative.

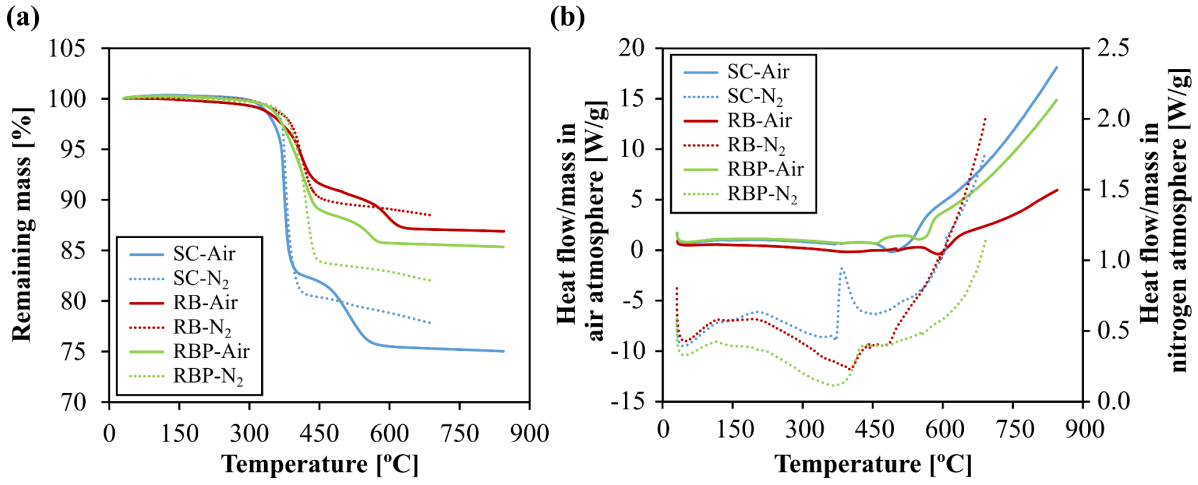

Figure 3.3. Remaining mass (a) and heat flow/mass ratio (b) as a function of temperature obtained from TGA/DSC tests in air and nitrogen (N_2) atmospheres.

Calcination (or burn-off) tests were carried out in a muffle, up to 800 ºC, according to the ISO 1172 standard. These tests provided the inorganic (*i.e.*, fibre) mass content of each bar (including the ribs in the case of ribbed bars): 75% in SC bars, 87% in RB-D12 bars, 88% in RB-D8 bars and 72% in RBP bars (*cf.* Table 3.3).

Table 3.3. Results from TGA, DSC and calcination tests.

Bar	SC	RB-D12	RB-D8	RBP
T_d**, air [ºC]**	374	400	400	400
T_d**, nitrogen [ºC]**	380	407	407	415
Mass fibre content	75%	87%	88%	72%

(1) T_g values determined based on the onset of the storage modulus (*E'*) curve decay, and on the peak of the loss modulus (*E''*) and tangent delta (tan δ) curves.

3.4. Mechanical properties of GFRP bars at elevated temperatures

3.4.1. Test programme

The effects of elevated temperatures on the tensile properties of the GFRP bars were determined on bar samples (straight geometry) subjected to temperatures varying between 20 ºC (ambient temperature) and 715 ºC (for which the strength of bar RB-D12 was almost null[2]). Table 3.4 lists the four series of tests performed, one for each bar, under steady-state conditions; all the bars were tested from 20 ºC up to 300 ºC (*i.e.*, temperatures below the T_d), while RB-D12 bars were also tested at 450 ºC, 575 ºC and 715 ºC, *i.e.* beyond the resin decomposition process. As described next, different test setups and instrumentation were used in the tests up to 300 ºC (*cf.* Section 3.4.2.1) and above 300 ºC (*cf.* Section 3.4.2.2). For each temperature and bar, at least three test repetitions were carried out (a total of 117 bars were tested).

Table 3.4. Tensile tests series.

Bar	**Temperatures [ºC]**
SC	20, 50, 100, 150, 200, 250, 300
RB-D12	20, 150, 200, 300, 450, 575, 715
RB-D8	20, 50, 100, 150, 200, 250, 300
RBP-S	20, 100, 150, 200, 300

[2] In the fire resistance tests performed in GFRP-RC slabs (Chapter 6), the temperature of the GFRP bars at the time of failure was 713 ºC.

It is worth noting that, compared to steady-state tests (as carried out in this study), transient tests provide a more realistic simulation of the thermomechanical conditions to which rebars used in structural members are exposed to during a fire (the bars are subjected to a sustained load while temperature is increased). Yet, as shown in Section 2.2.1, some studies (*e.g.* [19,107]) have reported that steady-state tests may provide slightly more conservative results regarding the reduction of the tensile properties of the bars with temperature and therefore can be used for design purposes.

3.4.2. Test setup, instrumentation and procedure

3.4.2.1. Tensile tests up to 300 ºC

The GFRP bar specimens tested at temperatures up to 300 ºC were cut to a length of 1000 mm and tested in tension according to the ISO 10406-1 standard [186], using the setup depicted in Figure 3.4, which comprised an *Instron* universal testing machine (250 kN load capacity) and a *Tinius Olsen* electrical thermal chamber (maximum operating temperature of 300 ºC). The inner dimensions of the chamber are 250 mm (width), 330 mm (depth) and 605 mm (height, corresponding to the heated length of the specimens).

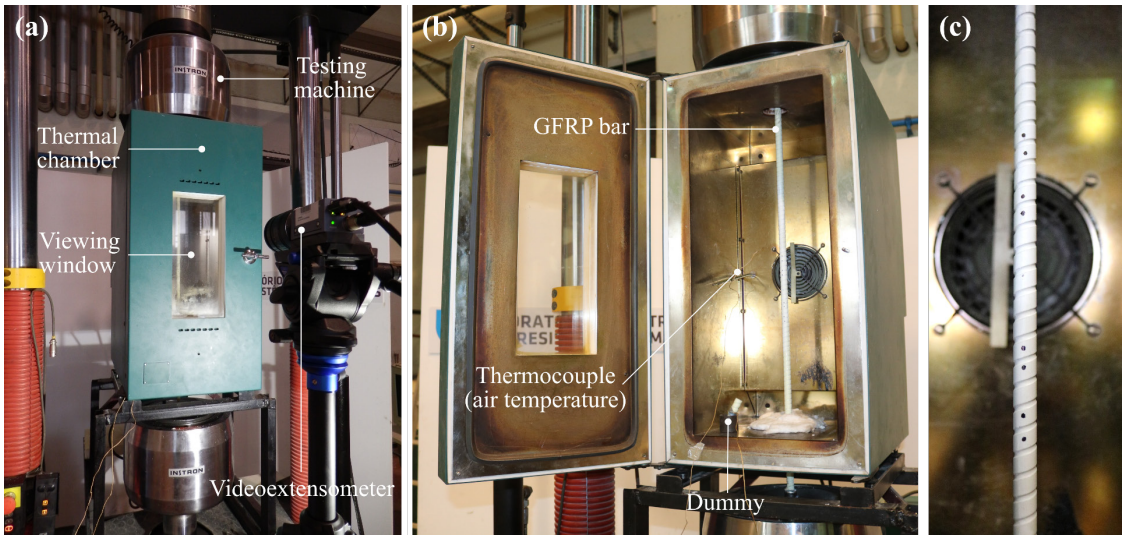

Figure 3.4. Setup of tensile tests performed at temperatures up to 300 ºC: (a) general view and equipment; (b) view of the thermal chamber; (c) target dots marked on the surface of the bar.

Given the low transverse strength of GFRP bars, and in order to prevent premature failure mechanisms due to their crushing in the grips of the test machine, both extremities of the samples were protected using stainless steel tubes filled with a bi-component epoxy resin (*Sikadur-330,* from *Sika*); in the case of RB-D12 bars tested at 20 ºC, instead of the filling resin, a grout (*SikaGrout-213*, also from *Sika*) was used to prevent bond failure in the grips. The characteristics of the steel anchors are specified in Table

3.5 in terms of tube length, external diameter, tube thickness and filling material – designed according to the recommendations of [187]. Note that longer and thicker tubes were required to anchor the bars that were tested at lower temperatures, due to the higher tensile loads applied. It should also be pointed out that the steel anchors were kept outside the thermal chamber during the tests (*i.e.*, at ambient temperature) to ensure cold anchorages and therefore avoid premature bond failures in the grips.

Table 3.5. Anchor specifications for tensile tests.

Bar	Temperatures	Anchor dimensions[1] [mm]	Filling material
SC	20 ºC	L=250, Φ=20, e=1.25	Bi-component resin
	50 ºC	L=100, Φ=20, e=1.25	
	100 ºC – 300 ºC	L=70, Φ=20, e=0.50	
RB-D12	20 ºC	L=200, Φ=45, e=2.00	Grout
	100 ºC – 300 ºC	L=100, Φ=22, e=1.25	Bi-component resin
	450 ºC – 715 ºC	L=200, Φ=45, e=2.00	Grout
RB-D8	20 ºC – 100 ºC	L=200, Φ=20, e=1.50	Bi-component resin
	150 ºC – 300 ºC	L=100, Φ=18, e=0.70	
RBP-S	20 ºC	L=200, Φ=22, e=1.50	Bi-component resin
	100 ºC – 300 ºC	L=100, Φ=22, e=1.25	

[1] Anchor length (L), external diameter (Φ), tube thickness (e).

In order to not compromise the integrity of the (loaded) test specimens, the temperature of the GFRP material was measured in a dummy specimen (replaced after each test) placed next to it (*cf.* Figure 3.4b). Type K thermocouples (0.25 mm of conductor diameter) were installed at mid-depth of the dummy specimen in 2.5 mm diameter holes and fixed with an epoxy adhesive; a thermocouple was also used to monitor the temperature of the air inside the chamber. The experimental procedure comprised a first stage during which the bars were heated at an average (initial) rate of 11 ºC/min (temperature of dummy specimen). To minimize the heating time, the temperature of the chamber was initially programmed 10 ºC above the dummy's target temperature, T_{target}, and then reduced to T_{target}. To ensure a uniform temperature distribution in the bars' cross-section, after attaining T_{target}, a (short) soaking time of 5–10 min was set. During the heating stage, the lower grip of the test machine was kept open to avoid any axial restriction due to the thermal expansion of the GFRP bars. Figure 3.5 shows examples of

temperature *vs.* time curves for the GFRP bars and for the air inside the thermal chamber, for tests performed at 300 ºC; the average heating times are listed in Table 3.6 for each target temperature.

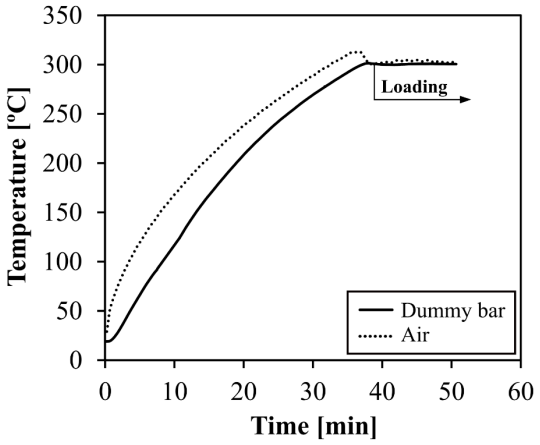

Figure 3.5. Example of temperature *vs.* time curves of the dummy RBP bar and of the air inside the thermal chamber for a target temperature of 300 ºC.

Table 3.6. Average heating times of the GFRP material (measured in dummy bar).

Target temperature, T_{target} [ºC]	**Average heating time of bars [min]**
150	26
200	29
300	49
450	117
575	70
715	60

In a second stage, after the stabilization of the temperature in the dummy specimen (at T_{target}), the bars were monotonically loaded until failure, under displacement control, at an average speed of 6 mm/min, set in order to reach failure within the first 5 minutes of loading, according to [186]. During the loading stage, the axial deformation of the bars was measured through video extensometry, thus allowing to determine the corresponding tensile modulus of the material. The data acquisition equipment consisted of a high-resolution *Sony* video camera (model *XCG 5005E*, with *Fujinon* lens, model *Fujifilm HF50SA-1*) placed on a tripod, as shown in Figure 3.4a. This system allowed to measure the relative displacement (*i.e.*, the axial strain) between target dots market on the surface of the GFRP bar as shown in Figure 3.4c – a minimum gauge length (*i.e.*, distance between dots) of 50 mm was adopted.

3.4.2.2. Tensile tests above 300 ºC

The setup used to perform tensile tests on the RB-D12 bars at 450 ºC, 575 ºC and 715 ºC is depicted in Figure 3.6 and Figure 3.7. The specimens were heated using a cylindrical split furnace from *Thermolab* (height of 450 mm and inner diameter of 150 mm, Figure 3.6a), which comprises a set of six electrical resistances spaced of 60 mm. The setpoint temperature of the furnace (maximum operating temperature of 1200 ºC) was defined by a *Shimaden* temperature controller, model *FP21*. The top and bottom openings of the furnace were covered using circular boards of calcium silicate and the remaining gaps were insulated using ceramic wool. The furnace was fixed to a steel reaction frame as depicted in Figure 3.7a.

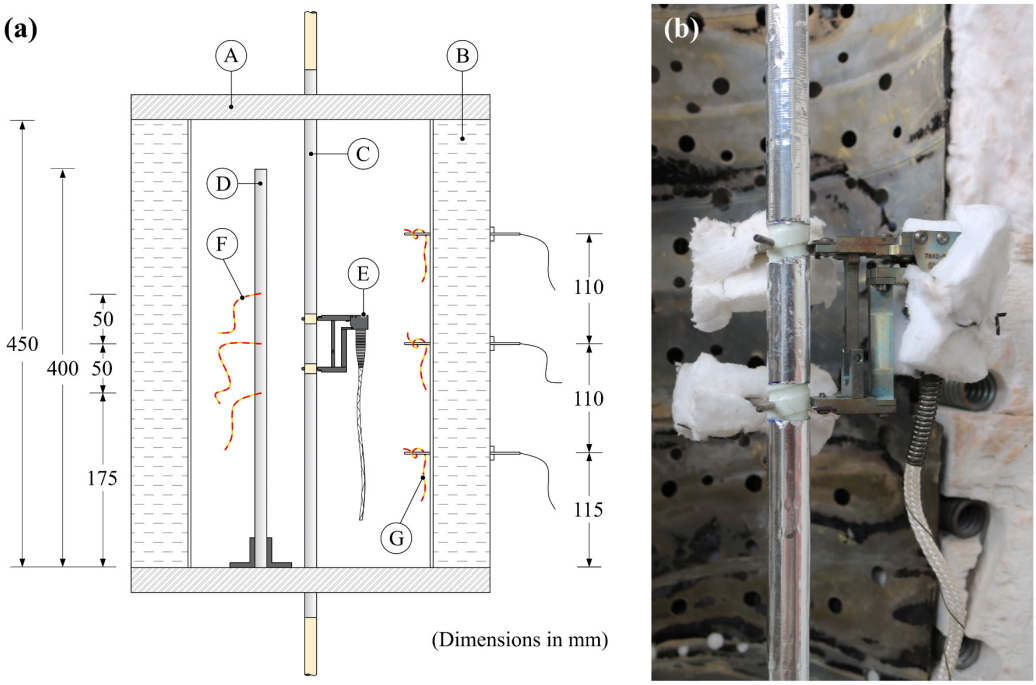

Figure 3.6. (a) Scheme of the split furnace used in tensile tests performed above 300ºC (detail of dummy bar, extensometer and thermocouples' placement); (b) high temperature extensometer installed in loaded bar.

The load was applied through a hydraulic jack (*Enerpac*, load capacity of 20 ton), positioned below the reaction frame, as illustrated in Figure 3.7, and controlled with a *Walter + Bai* pressure unit. The applied load was measured with a load cell from *Novatech* (load capacity of 100 kN) positioned below the jack. The anchorages of the bars consisted of 200 mm long stainless-steel tubes filled with grout (*SikaGrout-213* from *Sika*, *cf.* Table 3.5). Because the extremities of the bars could not be mechanically griped, the length of the tubes and filling material were selected so that the frictional forces between the

bar and the grout were enough to prevent bond failures, thus guaranteeing the occurrence of tensile failure of the bars. The upper anchorage reacted against a steel reaction triangle fixed to the frame's column (*cf.* Figure 3.7c) and the lower anchorage was pulled resorting to a small steel reaction frame, which was connected to the jack using a *dywidag* bar (*cf.* Figure 3.7d). The axial strains in the centre of the heated length of the GFRP bars were measured using a high temperature extensometer from *Epsilon* (model 7642, gauge length of 50 mm), shown in Figure 3.6 (the remaining bar length was covered with aluminium foil as described ahead).

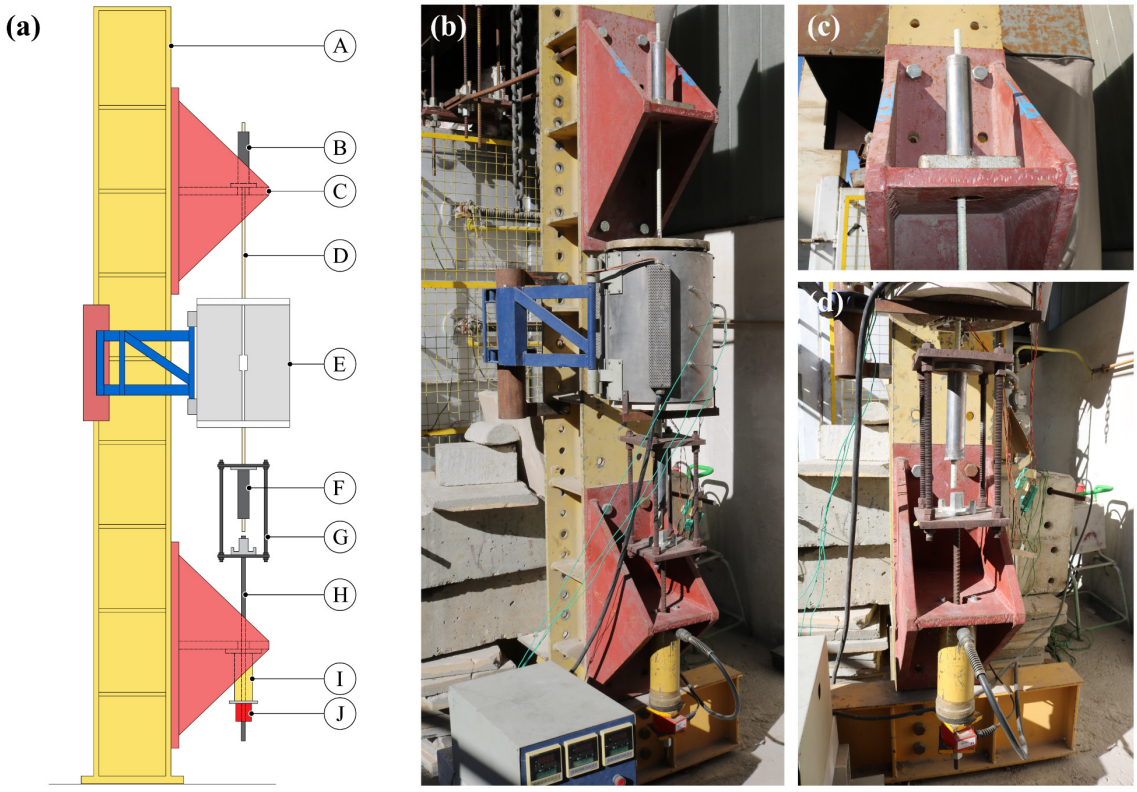

Figure 3.7. Setup of tensile tests performed above 300ºC: (a, b) general view and equipment; (c) top anchorage; (d) bottom anchorage, steel reaction frame, hydraulic jack and load cell.

The loaded specimen was 1600 mm long and it was exposed to heat inside the furnace over a length of 450 mm. Type K thermocouples (0.51 mm of conductor diameter) were used to measure the temperature of the GFRP material and of the air inside the furnace – as depicted in Figure 3.6a, the temperature of the GFRP material was monitored in a dummy bar (400 mm in length) placed alongside the loaded bar (replaced after each test). Temperatures were measured at three different heights, corresponding to the centre of the loaded specimen and also 50 mm above and below this position. The thermocouples were installed at half thickness of the dummy bar inside 2.5 mm diameter holes and fixed with an epoxy

adhesive. The temperature of the air inside the thermal chamber was also monitored at different heights of the furnace, as shown in Figure 3.6a, each one corresponding to the location of the inbuilt furnace thermocouples. To ensure a less oxidative decomposition environment, thereby decreasing the magnitude of the exothermic peak during the ignition and flaming combustion of the polymeric matrix (*cf.* Figure 3.8), both the dummy specimen and the length of the loaded bar exposed to heat were wrapped with two layers of aluminium foil, as illustrated in Figure 3.6b.

The bar specimens were first heated at an average (initial) rate of 27 ºC/min (temperature of dummy specimen). The temperature of the furnace was initially set several degrees below T_{target} and then once the temperatures in the dummy specimen stabilized (after the exothermic peak), the setpoint temperature of the furnace was increased in small increments, until reaching T_{target} in the GFRP. After that the bars were maintained at T_{target} during 3-5 min; this procedure is illustrated in Figure 3.8. The average heating times, listed in Table 3.6, were higher than those registered in the tests performed up to 300 ºC and this is due to the different settings of the furnace/thermal chamber used and the heating procedure adopted; it should be pointed out that the effect of the exposure duration to elevated temperature on the tensile properties of the bars[3] was beyond the scope of this study. The loading stage began after the temperatures of the dummy specimen stabilized at the target temperature. To avoid damaging the extensometer at the time of failure, the strength and modulus of the bars were determined in separate bars. To assess the tensile strength of the bars, the load was monotonically applied up to failure (under load control and at an approximate rate of 0.3 kN/s). In the tests carried out to determine the tensile modulus of the bars, the high temperature extensometer was gripped to the loaded specimen from the beginning of the heating stage and the tests were interrupted prior to failure to prevent damaging this equipment.

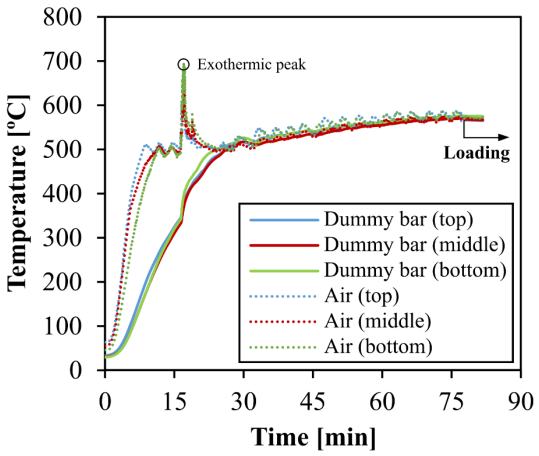

Figure 3.8. Example of temperature *vs.* time curves of the dummy bar and of the air inside the furnace for a target temperature of 575 ºC.

[3] According to [108], the degradation of the tensile properties of the bars increases with the exposure time at a constant temperature level.

3.4.3. Results and discussion

3.4.3.1. Load *vs.* displacement curves

Figure 3.9 presents the load *vs.* (cross-head) displacement curves of one representative specimen for each temperature, corresponding to an intermediate curve obtained within each temperature series. The curves are only shown up to 300 ºC, since in the tests performed at higher temperatures the displacements were not measured (only strains) and the setup was different.

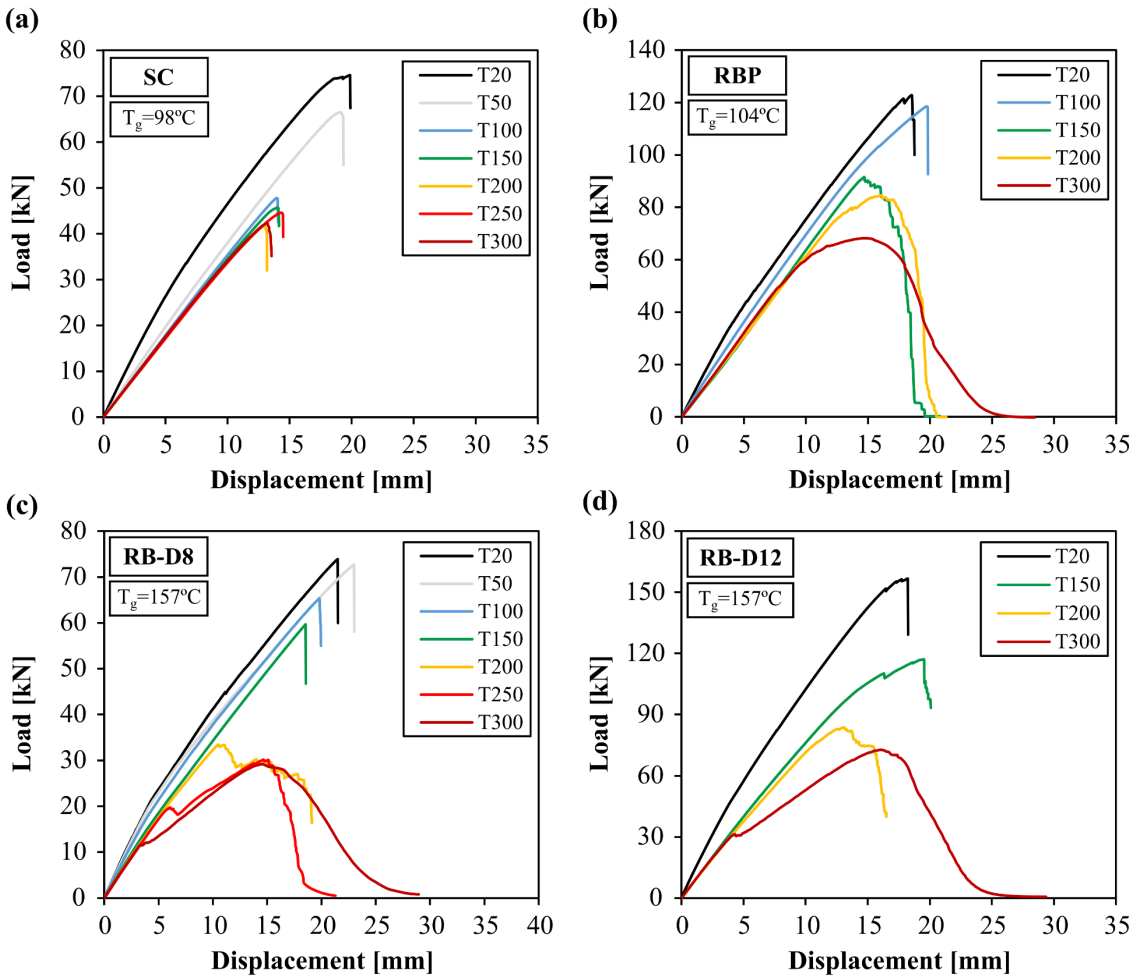

Figure 3.9. Representative load *vs.* (cross-head) displacement curves on tensile tests up to 300 ºC for bars: (a) SC, (b) RBP, (c) RB-D8 and (d) RB-D12.

In all the bars, after an initial non-linear region (due to adjustments in the setup), the curves presented an approximately linear behaviour during the first stage of loading. Regarding RB and RBP bars (Figure 3.9b to Figure 3.9d), this initial linear behaviour was followed by a non-linear response, characterized by a gradual decrease in (global) stiffness when approaching the peak load. This behaviour became more marked with increasing temperatures, especially for temperatures above the bars' T_g (for example, in the

curves of RBP bars – T_g of 157 ºC – obtained at 200 ºC and 300 ºC (*cf.* Figure 3.9b)). It can also be seen that the behaviour of the curves in the post-peak stage was also markedly different at temperatures below and above the T_g of the corresponding bars. For test temperatures below T_g, the load decreased abruptly after reaching the peak load. However, for higher temperatures, the load reduction was smooth, which was attributed to the softening of the matrix during the glass transition process, causing an increase in material viscosity and deformation capacity. The changes in the load-displacement behaviour before and after the glass transition also match the changes in the failure modes, described in detail in Section 3.4.3.4. Note that in the case of SC bars (Figure 3.9a, the only one with sand coating finish), the shape of the post-peak curve did not change with temperature: for all tested temperatures, load increased linearly and then dropped steeply after attaining the peak load; the reason for this behaviour, which was also reflected in the failure modes (*cf.* Section 3.4.3.4), is not fully clear.

Figure 3.9 shows that the maximum load and overall stiffness (during the initial linear stage) of all bars were gradually reduced with temperature due to the matrix softening. Also note that in RB-D12 bars tested at 300 ºC (Figure 3.9d), and also in RB-D8 bars tested at 250 ºC and 300 ºC (Figure 3.9c), a significant decrease in global stiffness, which was preceded by a small load drop, occurred well before the maximum load was attained. As illustrated ahead in Section 3.4.3.4 (*cf.* Figure 3.18) this change in the development of the curves at the highest temperatures matches the appearance of the first cracks at the surface of the bars. In bars tested at higher temperatures these cracks occurred sooner (*i.e.*, at lower loads) than in bars tested at lower temperatures, as the result of the more advanced softening state of the matrix in the former bars.

3.4.3.2. Stress *vs.* strain curves

Figure 3.10 presents the stress *vs.* strain curves of one representative specimen for each target temperature (intermediate curve obtained within each series). Note that while the curves of SC bars (Figure 3.10a) are shown until failure, those of RBP bars (Figure 3.10b) and RB bars (Figure 3.10c and d) are not plotted up to the ultimate load – instead, the results are generally shown up to 50% of the tensile strength (for RB-D12 bars tested above 300 ºC, results are shown up to 25% of the tensile strength). As explained in Section 3.4.3.4, in these bars, the sequential rupture of core fibres caused radial expansion of the specimens, which damaged their surface coating (including the ribs) where the target dots used for the video extensometry were marked. Consequently, any measurements obtained beyond this point would lack physical significance. In the case of bars tested at 450 ºC and above (Figure 3.10d), the material response is plotted up to a common load, corresponding to 25% of the bars' ultimate strength, as the tests were interrupted prior to failure. The figures show that for the different temperatures tested, the mechanical response in tension was typically linear elastic. As further detailed in Section 3.4.3.3, the tensile strength and modulus were gradually reduced with increasing temperatures, due to the degradation of the mechanical properties

of the constituent materials and of the corresponding interaction, especially across the glass transition and resin decomposition.

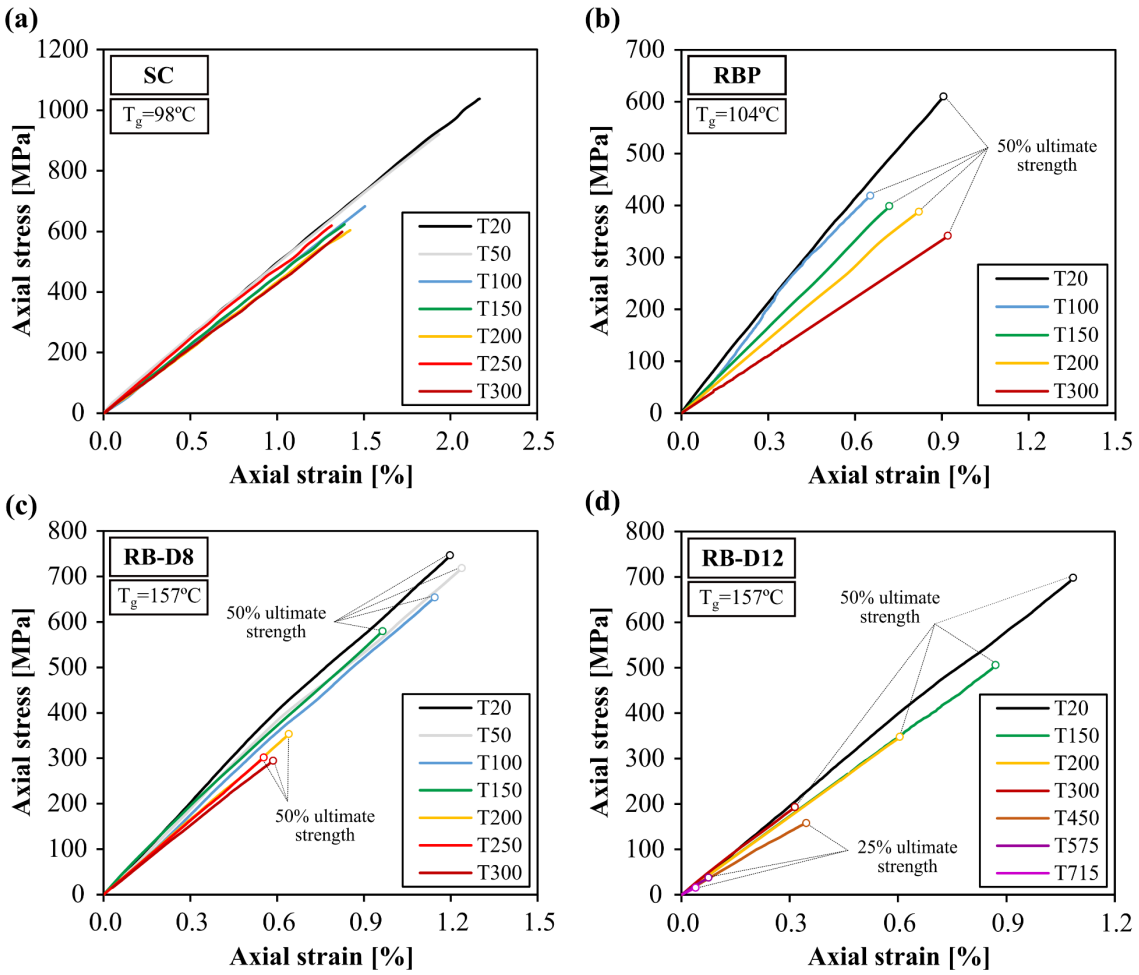

Figure 3.10. Representative axial stress *vs.* strain curves obtained for bars: (a) SC (curves plotted up to failure); (b) RBP, (c) RB-D8 and (d) RB-D12 (curves plotted up to 25% or 50% of the ultimate stress).

3.4.3.3. Tensile strength and modulus

Table 3.7 summarizes the tensile strength and modulus of the different bars (slope of the stress *vs.* strain curves presented in Figure 3.10), both in absolute and normalized values with regard to ambient temperature. The results of each individual specimen can be consulted in Appendix A (Table A.1 to Table A.5). Figure 3.11 plots the normalized values of the average tensile strength and modulus as a function of temperature, where the error bars correspond to the respective standard deviation.

It can be seen that a significant decay in the tensile strength occurs for temperatures close to the T_g (varying between 98 ºC and 157 ºC). As mentioned, when the polymer matrix changes from a vitreous to a softened state, it is no longer able to effectively/uniformly transfer stresses among adjacent fibres.

The results obtained show that for temperatures near the T_g (100 ºC in SC and RBP bars, 150 ºC in RB bars), the tensile strength reduction varied between 6% (in RBP bars) and 35% (in SC bars). While in SC bars the tensile strength presented a steep reduction up to the T_g (~100 ºC), in the other bars such reduction developed for ~50 ºC beyond the T_g (*i.e.*, up to 150 ºC in RBP bars or 200 ºC in RB bars). From those temperatures onwards, the degradation trend of the tensile strength of bars SC and RB reached a relatively stable plateau that extended until (at least) 300 ºC (450 ºC in the case of RB-D12 bars). At 300 ºC the tensile strength reduction varied between 43% and 61% (in SC and RB-D8 bars, respectively). The tensile strength of the RB-D12 bars (Figure 3.11d) (the only ones tested beyond 300 ºC) did not show significant reductions from 200 ºC up to 450 ºC; however, from 450 ºC to 715 ºC, a severe decay occurred due to the thermal decomposition and combustion of the polymeric matrix: the tensile strength reduced to 10% at 575 ºC and 4% at 715 ºC compared to ambient temperature.

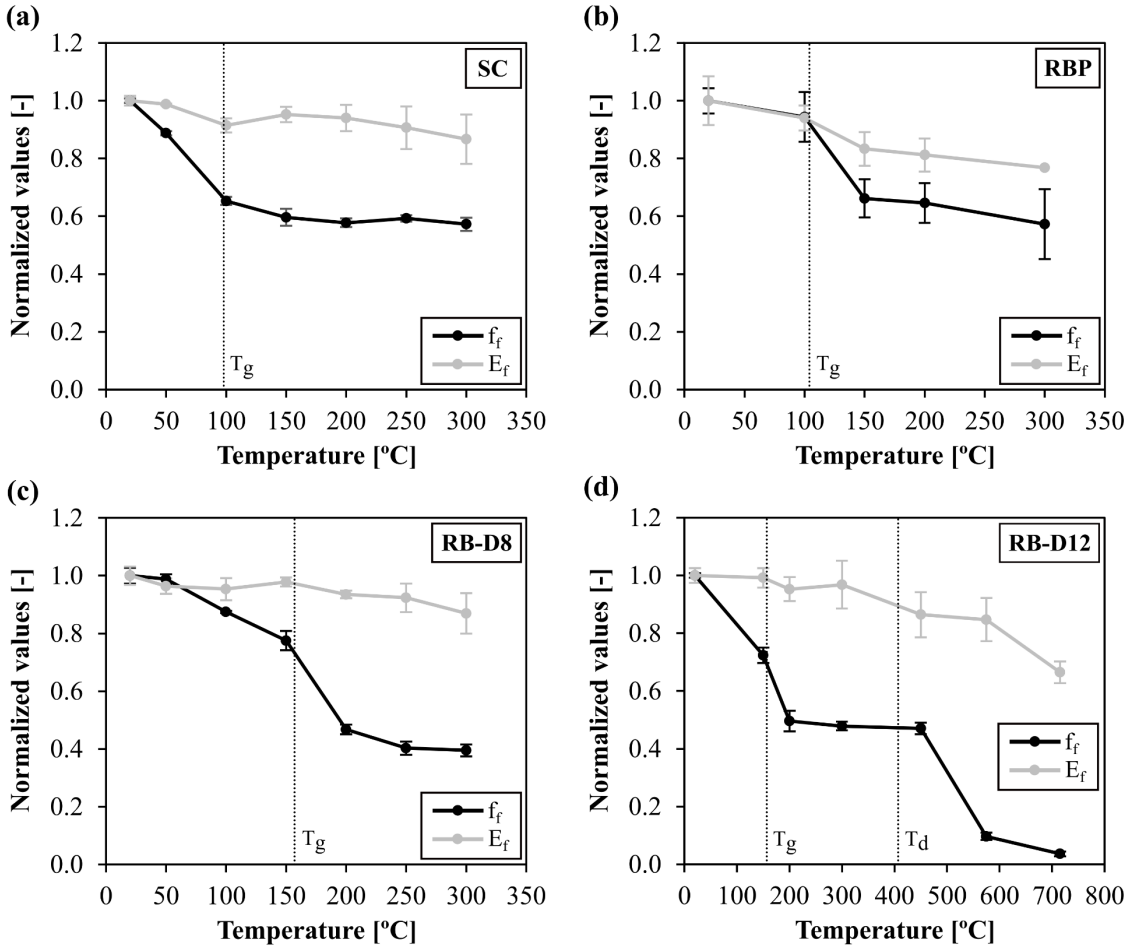

Figure 3.11. Normalized average tensile strength (f_f) and modulus (E_f) as a function of temperature obtained for bars SC (a), RBP (b), RB-D8 (c) and RB-D12 (d) (dotted lines identify the T_g and T_d of the bars).

Table 3.7. Tensile test results (average, standard deviation and coefficient of variation).

Bar	Temperature [ºC]	Tensile strength [MPa]	Normalized tensile strength reduction [-]	Tensile modulus [GPa]	Normalized tensile modulus reduction [-]
SC	20 ± 2	1045.1 ± 8.4 (0.8%)	-	48.2 ± 0.8 (1.7%)	-
	50 ± 2	927.5 ± 8.0 (0.9%)	11%	47.6 ± 0.1 (0.2%)	1%
	100 ± 2	682.4 ± 14.6 (2.1%)	35%	44.1 ± 1.2 (2.7%)	9%
	150 ± 2	623.2 ± 30.6 (4.9%)	40%	45.9 ± 1.3 (2.8%)	5%
	200 ± 2	603.7 ± 15.1 (2.5%)	42%	45.3 ± 2.2 (4.9%)	6%
	250 ± 2	619.3 ± 11.2 (1.8%)	41%	43.7 ± 3.6 (8.2%)	9%
	300 ± 2	598.2 ± 23.5 (3.9%)	43%	41.8 ± 4.1 (9.8%)	13%
RB-D8	20 ± 2	1481.7 ± 39.8 (2.7%)	-	57.6 ± 1.1 (2.0%)	-
	50 ± 2	1463.9 ± 25.2 (1.7%)	1%	55.5 ± 1.5 (2.7%)	4%
	100 ± 2	1295.8 ± 5.1 (0.4%)	13%	54.9 ± 2.2 (4.0%)	5%
	150 ± 2	1148.3 ± 48.8 (4.2%)	22%	56.4 ± 0.9 (1.6%)	2%
	200 ± 2	692.7 ± 24.7 (3.6%)	53%	53.9 ± 0.8 (1.4%)	6%
	250 ± 2	597.1 ± 33.8 (5.7%)	60%	53.2 ± 2.9 (5.4%)	8%
	300 ± 2	585.2 ± 30.9 (5.3%)	61%	50.1 ± 4.0 (8.0%)	13%
RB-D12	20 ± 2	1380.3 ± 10.3 (0.7%)	-	60.0 ± 1.5 (2.5%)	-
	150 ± 2	998.5 ± 36.4 (3.6%)	28%	59.5 ± 2.0 (3.4%)	1%
	200 ± 2	684.7 ± 48.8 (7.1%)	50%	57.2 ± 2.5 (4.3%)	5%
	300 ± 2	660.9 ± 20.7 (3.1%)	52%	58.1 ± 5.0 (8.5%)	3%
	450 ± 5	649.4 ± 27.1 (4.2%)	53%	51.9 ± 4.7 (9.1%)	14%
	575 ± 5	133.6 ± 17.2 (12.9%)	90%	50.9 ± 4.5 (8.9%)	15%
	715 ± 5	49.6 ± 11.7 (23.6%)	96%	39.9 ± 2.3 (5.7%)	34%
RBP-S	20 ± 2	1184.4 ± 52.1 (4.4%)	-	60.1 ± 5.1 (8.5%)	-
	100 ± 2	1117.9 ± 101.9 (9.1%)	6%	56.5 ± 2.6 (4.6%)	6%
	150 ± 2	783.9 ± 78.1 (10.0%)	34%	50.1 ± 3.5 (7.1%)	17%
	200 ± 2	765.6 ± 81.7 (10.7%)	35%	48.8 ± 3.4 (7.0%)	19%
	300 ± 2	678.3 ± 142.8 (21.1%)	43%	46.2 (1)	23%

(1) Value obtained from one single specimen

Regarding the effects of elevated temperatures on the tensile modulus, the results obtained confirmed that this property is much less affected by increasing temperature than the tensile strength up to 300 ºC, providing also new data and insights for temperatures above decomposition. Although both properties are fibre-dominated, the tensile modulus depends essentially on the (glass) fibres, which offer much higher thermal stability than the polymeric matrix; on the other hand, tensile strength also depends on the fibre-matrix interface, which is jeopardized by elevated temperature. Minor reductions of tensile modulus occurred up 300 ºC – at that temperature, the decrease in modulus was only 3% in RB-D12 bars, 13% in SC and RB-D8 bars, and 23% in RBP bars. This means that with exception of RBP bars, the tensile modulus was only slightly affected by the glass transition process. On the other hand, the results obtained for RB-D12 bars at temperatures above 300 ºC (Figure 3.11d) show that the tensile modulus is mainly affected by the softening of the glass fibres: at 450 ºC and 575 ºC the reduction was 14-15% and at 715 ºC a further reduction to 34% occurred. The tensile modulus is likely negligible after the softening of the fibres; in the study of Dimitrienko [98], cited by Bisby [115], glass fibres presented strength and stiffness reductions of 20% at 600 ºC and 70% at 800 ºC, and at 1200 ºC only minor strength and stiffness were obtained.

As expected, the variation of the tensile properties with temperature presented very similar trends for bars with similar constitution, but different diameters (*cf.* Figure 3.12); yet, strength and modulus reductions for temperatures above 200 ºC were slightly higher in bars with smaller diameter. Moreover, the tensile strength of bars with similar T_gs (bars SC and RBP) presented different magnitudes when approaching that temperature: the tensile strength reduction of SC bars occurred for lower temperatures and was steeper than in RBP bars. Conversely, after the T_g, the tensile modulus of SC bars was less affected with increasing temperatures than that of RBP bars. In spite of these differences (which should be due to differences in constituent materials and manufacturing processes), the overall results obtained for the different bars present a relatively narrow variation range, as observed in Figure 3.12.

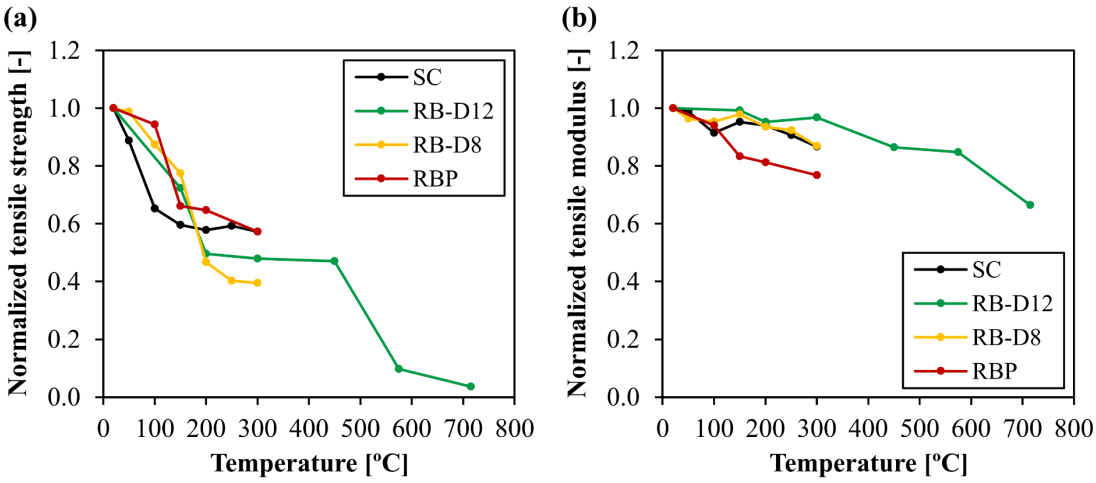

Figure 3.12. Comparison of the normalized average tensile strength (a) and modulus (b) as a function of temperature obtained for bars SC, RB-D8, RB-D12 and RBP.

3.4.3.4. Failure and post-failure assessment

Visual observations of the bars after the tests are presented from Figure 3.13 to Figure 3.16. As shown, the heat exposure caused significant changes in the colour of the bars surface and glass fibres. For temperatures up to 150 ºC (in RB and RBP bars) and 200 ºC (in SC bars), specimens did not show signs of discoloration. However, for higher temperatures they presented yellowing and eventually became charred at around 300 ºC, for which the fibres appeared to be almost depleted of resin. As depicted in Figure 3.14, when exposed to 450 ºC and 575 ºC the surface of the rovings became grey, and at 715 ºC they turned completely white as the result of the complete decomposition of the resin.

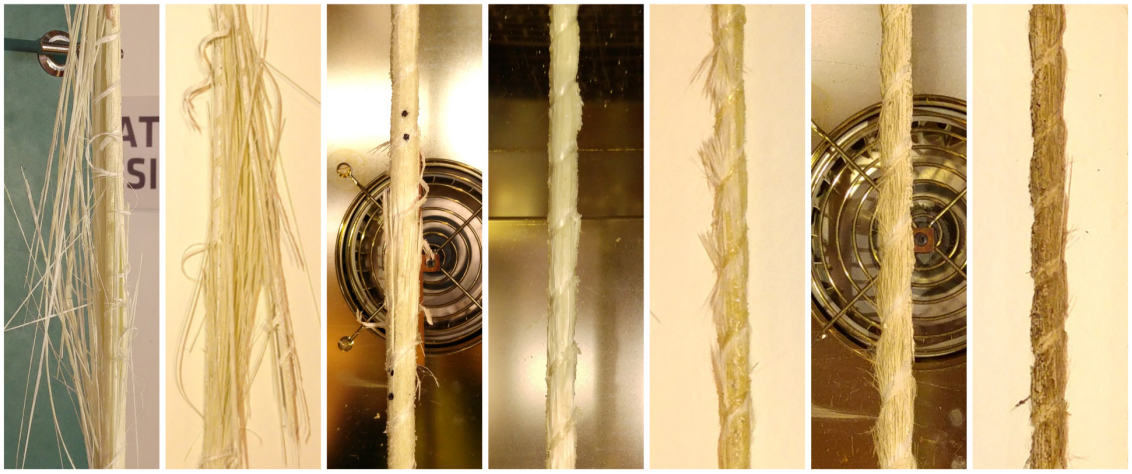

Figure 3.13. SC bars after failure.

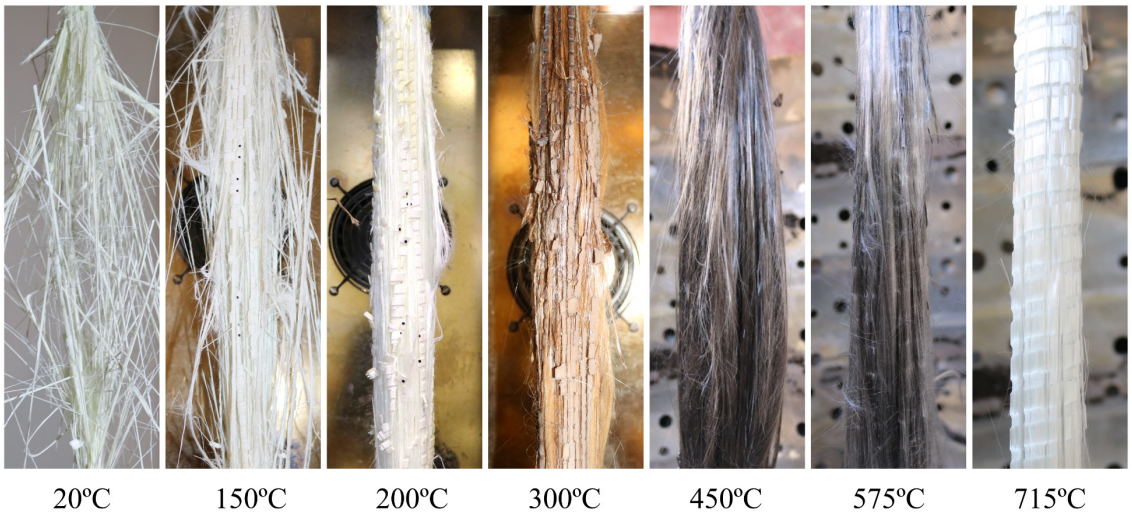

Figure 3.14. RB-D12 bars after failure.

Figure 3.15. RB-D8 bars after failure.

Figure 3.16. RBP bars after failure.

Also noteworthy are the changes observed in the failure modes as the test temperature increased. Next, when justified, the failure processes of the bars are described separately for "unwrapped" ribbed (RB and RBP bars) and wrapped bars (SC bars). In tests performed at ambient temperature and up to 50 ºC (in SC bars), 100 ºC (in RBP bars) or 150 ºC (in RB bars), the bars presented the same type of failure mode: rupture occurred in an explosive way, sectioning the bars in two parts (note that in the case of RB and RBP bars, those temperatures of 100 ºC and 150 ºC respectively, virtually match the bars' T_g). Figure 3.17 illustrates the damage progression observed for this type of failure, in this case for an RB-D8 bar tested at 100 ºC. Figure 3.17b shows that the bar remained intact up to a load level (42 kN) close to the ultimate tensile capacity (43 kN). Then, suddenly, cracks started to develop lengthwise, being well visible at the surface of the bar, causing delamination between the fibre rovings (Figure 3.17c). Rapidly those cracks became wider and propagated longitudinally along the bar, involving further delamination and, in the case

of SC bars, also causing the breakage of the wrapped fibres; shortly after cracking initiated, the loose individual fibres ruptured, which corresponded to the peak load. Subsequently, as described in Section 3.4.3.1, the load decreased abruptly while the remaining fibres continued to break (Figure 3.17d), eventually leading to the rupture of the bar (Figure 3.17e).

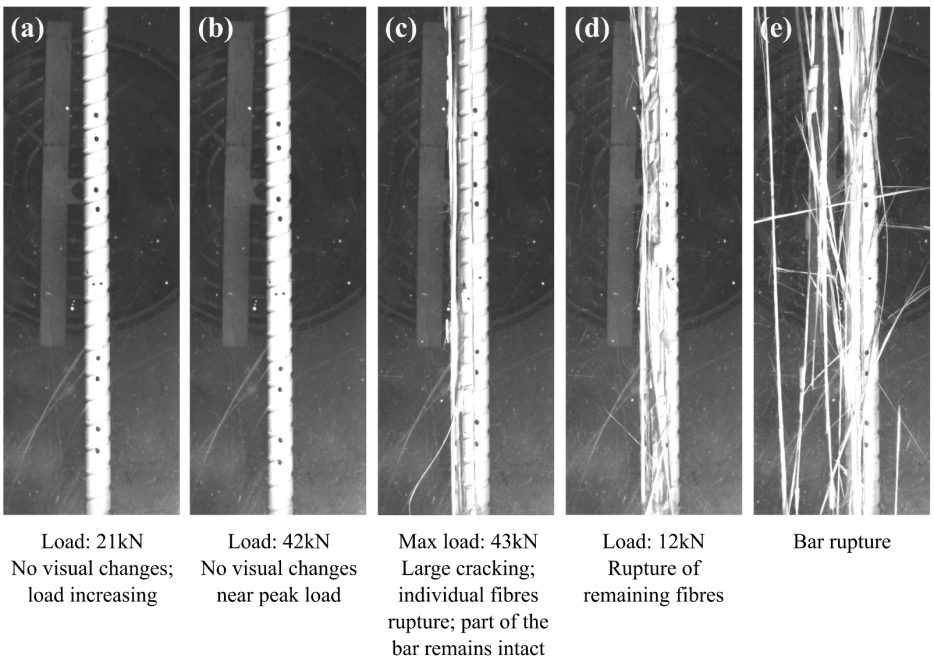

Figure 3.17. Damage progression of RB-D8 bar tested at 100 ºC.

Regarding RB and RBP bars, a change in the failure mode was observed between 150 ºC and 200 ºC (in RB bars) and between 100 ºC and 150 ºC (in RBP bars), *i.e.*, when the test temperature increased above the T_g, as illustrated in Figure 3.18 (ahead) for RB-D8 bars tested at 200 ºC and 250 ºC. Above T_g, the failure process prior to the peak load was similar to that previously described for lower temperatures, however, the rupture of the individual fibres was more gradual and less brittle. This is attributed to the softening of the resin with increasing temperatures, which also explains the smoother post-peak response reflected in the load-displacement curves (*cf.* Figure 3.9). In RB-D8 bars tested at 200 ºC the occurrence of the first cracks immediately preceded the attainment of the peak load (Figure 3.18b), whereas in bars tested at 250 ºC the cracks appeared much sooner and well below the peak load (Figure 3.18g), due to the more advanced softening state of the resin; as explained in Section 3.4.3.1, this damage observed at 250 ºC matches the early decrease in stiffness visible in the load-displacement curves of RB bars (Figure 3.9c and Figure 3.9d). In tests performed at temperatures above the T_g, once the maximum load was attained, the bars began to radially expand due to the progressive rupture of the core fibres (Figure 3.18d), an effect that continued until the moment of failure (Figure 3.18e). The main differences in failure modes observed in the wrapped SC bars at 100 ºC and above should be related to the presence of the helically wound fibres, which held the core fibres in place (cf. Figure 3.13), and the fact that the

rupture of the fibres at elevated temperatures was much less gradual than in the unwrapped bars – as shown in Figure 3.9a, the post-peak stage of the load-displacement curves of SC bars comprised a sharp decrease in load regardless of the exposure temperature.

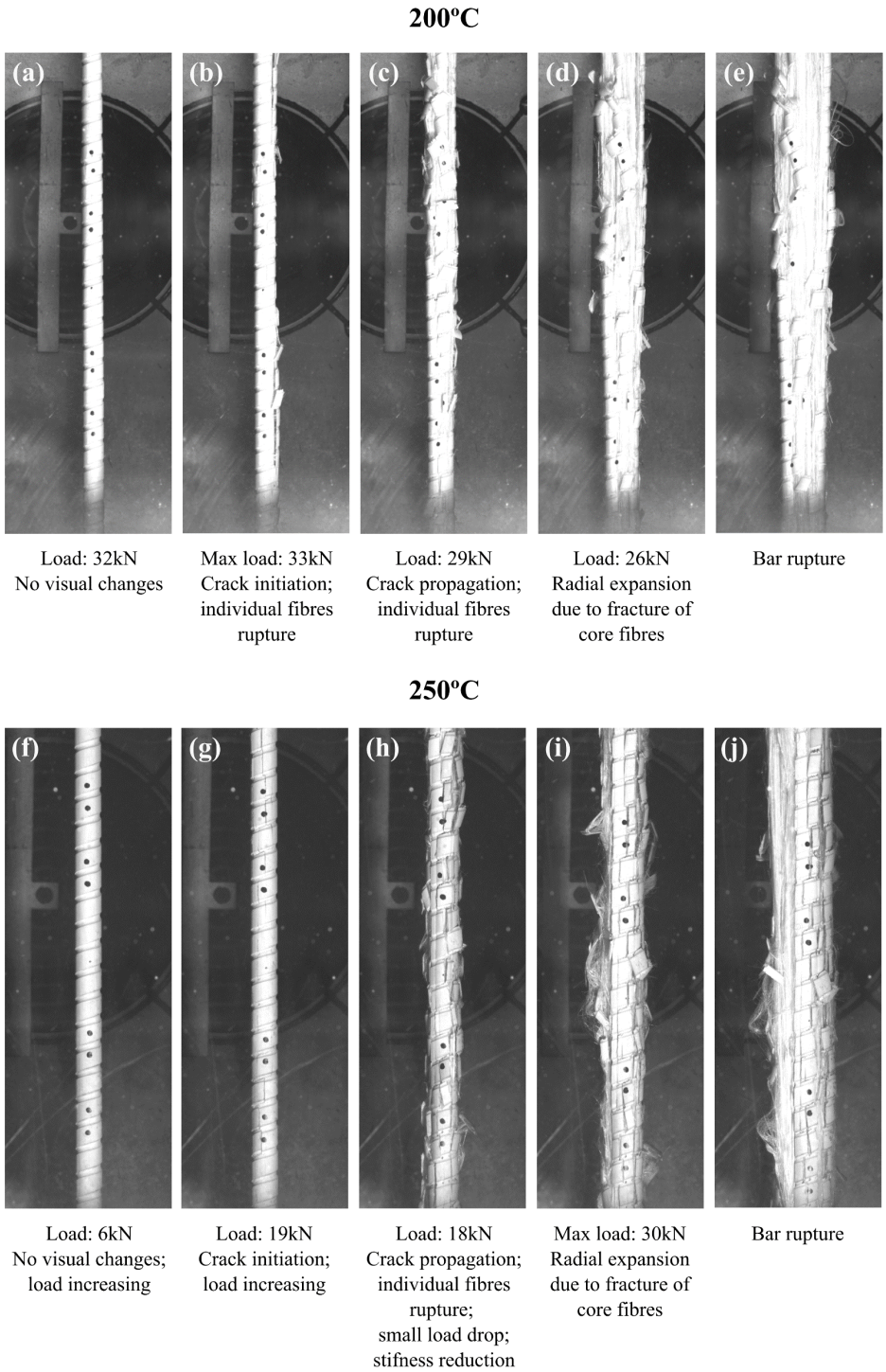

Figure 3.18. Damage progression of RB-D8 bar tested at 200 ºC (a, b, c, d, e) and 250 ºC (f, g, h, i, j).

A distinct feature of the failure modes of all bars for temperatures above the T_g and up to 450 ºC is that they were not fully sectioned after failure (yet there was no load transfer between them either). This was not verified in tests performed at 575 ºC and 715 ºC. Even though it was not possible to monitor the damage progression at those temperatures (the furnace used in these tests has no viewing window), visual observations of the bars after failure (*cf.* Figure 3.14) indicated that the resin had completely burned off, no lateral expansion seemed to have occurred during loading and the glass rovings also broke in a less explosive manner compared to tests below the T_g.

3.4.3.5. Comparison with results from the literature

In this section, the variation of the tensile properties of the GFRP bars with temperature obtained in the present study is benchmarked with results available in the literature referring to tensile tests performed under steady-state temperature conditions on GFRP bars from different manufacturers. Figure 3.19 shows the comparison between the normalized tensile strength obtained here and in [15,19,63,69,77,93,95–102,104–107], while Figure 3.20 compares the normalized tensile modulus obtained here with results reported in [94–97,99,101,102,107] – in both figures, the values of T_g and T_d

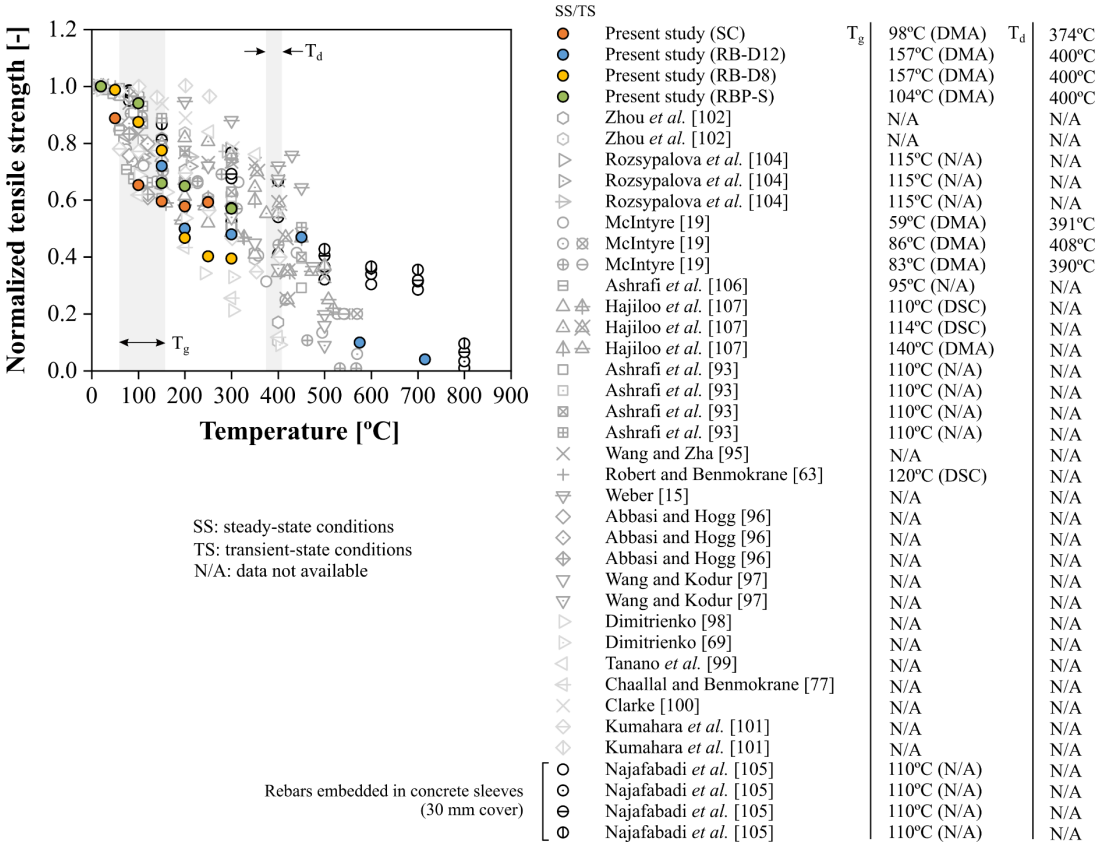

Figure 3.19. Comparison of normalized tensile strength of GFRP bars as a function of temperature: results obtained in the present study and those from [15,19,63,69,77,93,95–102,104–107].

are reported, as well as the test methods (when available). With the exception of the results of Najafabadi *et al.* [105], which refer to concrete covered bars, the remaining data considered were obtained from tests conducted in bare bars, both under short-term exposure to elevated temperatures (soaking times of 15 to 60 min and total heating durations of 30 to 174 min). The results shown in Figure 3.19 and Figure 3.20 present a considerable scatter over a large range of temperatures, particularly between T_g and T_d, indicating that the effects of elevated temperatures in the mechanical properties of the bars differ greatly amongst manufacturers. Nevertheless, it can be seen that the results obtained in this thesis lie within the scatter band of available data and, more importantly, provide relevant results for temperatures above T_d – in fact, almost no data was available in the literature for temperatures above 500 ºC.

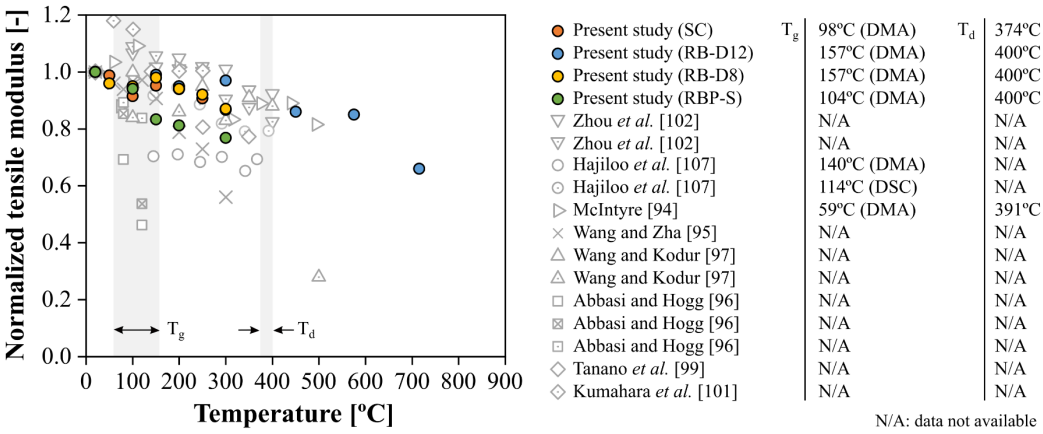

Figure 3.20. Comparison of normalized tensile modulus of GFRP bars as a function of temperature: results obtained in the present study and those from [94–97,99,101,102,107].

The results depicted in Figure 3.19 confirm that the tensile strength exhibits significant degradation in the T_g range (which, for this set of data, varies between 59 ºC and 157 ºC). For temperatures close to the T_g, in the most severe cases the decrease of tensile strength was 43% while other bars were much less affected presenting strength reductions of only 6%. For temperatures above T_g, the tensile strength of the bars gradually degraded with increasing temperatures, also undergoing a severe reduction near the T_d (which, for this set of data, varied between 374 ºC and 400 ºC, being reported only for a few number of studies). At 400 ºC, the reduction of tensile strength can be reduced as much as 91%, being 28% in the least severe case; above 500 ºC, the bars retain less than 10% of their tensile capacity at ambient temperature.

As reference, the strength degradation with temperature of the (bare) bars tested in the present study was compared to that obtained in Najafabadi *et al.* [105] for bars embedded in concrete (30 mm cover), marked in black in Figure 3.19. It is observed that the overall reduction with temperature of the tensile strength of the bare bars was higher than that of the covered bars, particularly at temperatures above 300 ºC and after the resins started to decompose (the bars' T_d was not reported in [105]); in fact, the tensile capacity of bare bars was almost entirely reduced at 715 ºC, while in covered bars such reduction occurred only near 800 ºC with significant and much higher strength retention from 400 ºC to 700 ºC.

The inferior performance of bare bars at elevated temperatures, also verified in [105], results from the faster decomposition rate of polymeric resins in media with high oxygen levels. However, this behaviour is not representative of a typical exposure environment of embedded reinforcement; in any case, it may resemble the exposure conditions observed in widely cracked sections of GFRP-RC flexural members (as reported in the fire resistance testes conducted in Chapter 6). Therefore, at this stage, it is conservative to consider the variation with temperature of the tensile properties of unprotected FRP bars for the purpose of designing FRP-RC structures subjected to fire.

As shown in Figure 3.20, less data is available regarding the effects of elevated temperatures on the tensile modulus of GFRP bars, particularly for temperatures above 400 ºC. Nevertheless, the results depicted in Figure 3.20 confirm that this property is much less affected by elevated temperature than the tensile strength, either by the glass transition process (near the T_g) or by the thermal decomposition process (above T_d). Most studies show that, with respect to the value at ambient temperature, the decay of the tensile modulus near the T_g is typically below 20%. However, two studies ([96,107]) report considerably higher reductions in this temperature range, of about 30% [107] and 54% [96], thought the latter does not report the T_g of the bars. The tensile modulus is further reduced up to the T_d, yet at a (much) slower rate than the tensile strength. The results obtained here are consistent with those reported in [94], both studies reporting reductions in the tensile modulus of less than 20% up to 500 ºC; in the present study, this reduction is 34% at 715 ºC, reflecting the significant stiffness retention of GFRP bars after the full decomposition of the polymeric matrix and prior to the softening of the glass fibres.

3.4.3.6. Degradation models

In this subsection, analytical models are presented to describe the average variation of the tensile strength and modulus of GFRP bars with temperature, encompassing a wide range of temperatures, from ambient temperature (20 ºC, taken as reference) up to 715 ºC. The models proposed here were obtained by fitting the experimental data, considered as the results of individual specimens whenever available, using a standard procedure that minimized the mean square errors between test data and predictions. The database comprised the properties of bare GFRP bars under short-term exposure to elevated temperatures obtained through steady-state tensile tests; the results obtained in the present study and those reported in the literature regarding the tensile strength ([15,19,63,69,77,93,95–102,104,106,107]) and tensile modulus of GFRP bars ([94–97,99,101,102,107]) were considered (*cf.* Section 3.4.3.5). It should be pointed out that the models proposed herein depend solely on the exposure temperature, although the degradation of the bars' mechanical properties with temperature is also influenced by their T_g and T_d and, as discussed in Section 2.2.3.2, the heat exposure conditions (duration and medium). Ideally, these parameters should be considered in analytical models used for fire-design purposes. However, it was not possible to attain such goal in the present study, because only a few of the

above-mentioned studies provide the information mentioned, namely about the thermophysical properties of the bars (thereby considerably narrowing the sample data).

The model describing the variation of the tensile strength with temperature is plotted in Figure 3.21 and was obtained through a second order polynomial fit, resulting in Equation (3.1),

$$f(T) = 6.40 \times 10^{-7} \cdot T^2 - 1.84 \times 10^{-3} \cdot T + 1.04 \quad (3.1)$$

where *f(T)* is the normalized tensile strength of the bars with reference to ambient temperature and *T* is the absolute temperature in ºC.

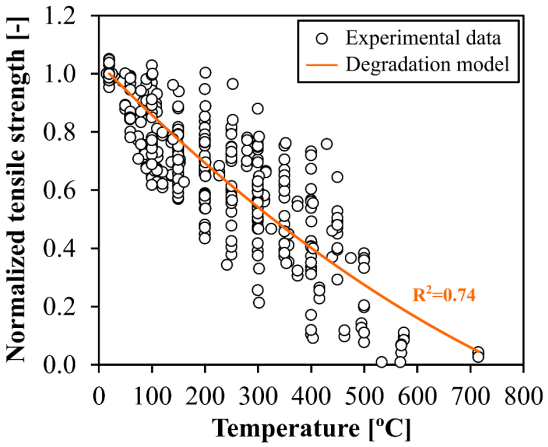

Figure 3.21. Normalized tensile strength (compared to ambient temperature) *vs.* temperature: experimental results and modelling curve (Equation (3.1)).

With respect to the reduction of the tensile modulus with temperature, the model was proposed based on the linear regression of the experimental data, resulting in Equation (3.2),

$$E(T) = 1.01 - 5.18 \times 10^{-4} \cdot T \quad (3.2)$$

where *E(T)* is the normalized tensile modulus of the bars with reference to ambient temperature and *T* the absolute temperature in ºC; the fitting curve and experimental data are plotted together in Figure 3.22. Figure 3.21 and Figure 3.22 show that both proposed models provide reasonably accurate estimates of the average reduction of the tensile strength and modulus with temperature; this is attested by the values of the mean absolute percentage error (MAPE) obtained, respectively 10% and 23%.

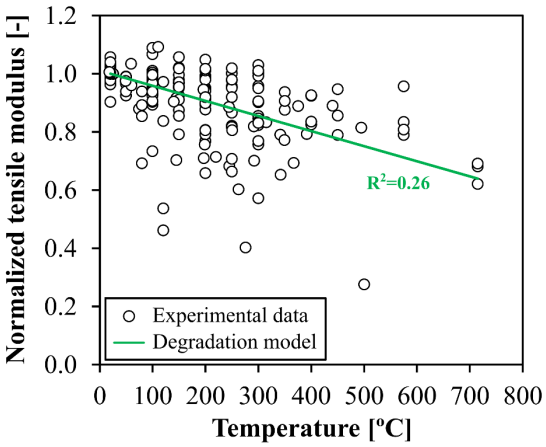

Figure 3.22. Normalized tensile modulus (compared to ambient temperature) *vs.* temperature: experimental results and fitting curve (Equation (3.2)).

3.5. Concluding remarks

This chapter presented an experimental study with the aim of characterizing the mechanical properties of four different types of GFRP bars through steady-state tensile tests from ambient temperature up to 715 ºC. Analytical models were also proposed to simulate the degradation of the tensile strength and modulus of GFRP bars with temperature; to that end, results from the present study and the literature were considered. The study provided a wealth of test data and improved the understanding of the effects of elevated temperatures on the tensile strength and modulus of GFRP bars, particularly for temperatures above the decomposition of the resin, for which very few data was available in the literature.

The results obtained confirmed that the tensile strength is significantly more affected by elevated temperature than the tensile modulus. Severe reductions in tensile strength (w.r.t. ambient temperature) occur near the glass transition temperature of the bars, between 6% and 35% at 100 ºC in SC and RBP bars (T_g = 104 ºC), and between 22% and 28% at 150 ºC in RB bars (T_g = 157 ºC). These reductions proceed above the decomposition temperature, from 50% at 300 ºC (on average) up to 96% at 715 ºC. The tensile modulus, on the other hand, experiences much lower reductions up to 300 ºC, between 3% and 23%. The highest reduction in tensile modulus occurs after the resin is fully decomposed; yet, at 715 ºC the bars are still able to retain 66% of the tensile modulus at ambient temperature.

The results obtained in this study are within the high scatter of experimental data available; the high magnitude of this scatter, due to differences in GFRP bars (constituent materials and manufacturing processes) highlight the importance of experimentally characterizing the mechanical behaviour of different types of FRP bars at elevated temperatures in the context of fire design. This information, together with the GFRP-concrete bond at elevated temperature (*cf.* Chapter 4) is useful and necessary to accurately predict the thermomechanical behaviour and fire resistance of RC structural members comprising FRP reinforcement.

Part III

Bond behaviour of GFRP bars in concrete at elevated temperature

Chapter 4

Pull-out tests on GFRP bars embedded in concrete at elevated temperature

4.1. Introduction and objectives

Elevated temperatures are responsible for significant deteriorations of the bond capacity of GFRP reinforcement in concrete and that this can potentially affect the structural safety of load bearing members exposed to fire. Indeed, even moderately elevated temperatures have been reported to cause premature loss of bond in tension lap-splices and thereby lead to significant reductions in the fire resistance of structural members, as demonstrated for example in [13,15]. Similar premature collapses were observed in the fire resistance tests carried out within the present investigation in GFRP-RC slabs strips (*cf.* Chapter 6).

Despite the relevance of the topic, the number of existing studies about the reduction with temperature of the bond properties of GFRP bars to concrete is still very limited, especially given the wide variety of commercially available bars. Additional experimental studies are needed to further evaluate the temperature dependence of several geometrical and material characteristics of the bars, expected to affect their bond properties at elevated temperature. It is worth noting that although significant data is available regarding the bond behaviour of straight FRP bars to concrete (*e.g.* [58,124,126,128,129,136]), far less research has been conducted regarding the bond properties of bent FRP reinforcement at elevated temperatures; in this respect, the only study reported in the literature is that of Kiari *et al.* [137] and it focused on CFRP bars (therefore with limited representativeness of the FRP bars more often used in real applications, *i.e.*, GFRP bars).

The study presented in this chapter includes additional and more comprehensive investigations on the complex GFRP-concrete interaction at moderately elevated temperatures. In the first part of the study, an extensive experimental campaign (described in Section 4.2 and Section 4.3) comprising steady-state pull-out tests on different types of GFRP bars, embedded in concrete cylinders, was performed from ambient temperature at temperatures up to 300 ºC. These tests allowed to evaluate the influence of several parameters on the bars' bond properties to concrete, namely their bonded length to concrete, surface finish, diameter and geometry. The first part of the study is presented in three sections: (i) firstly, Section 4.4 presents a study on fibre-wrapped sand coated bars (SC) with two different embedment

lengths in concrete; (ii) next, Section 4.5 shows a comparison between the bond behaviour of two types of ribbed bars (RB and RBP) with that of the sand coated bars, also presenting tests in ribbed bars (RB) with two different core diameters; (iii) lastly, Section 4.6 reports an investigation of the effects of temperature on the bond performance of bars with straight and 90º bent anchoring geometries. In the second part of study, the degradation of the bond strength of the GFRP bars with temperature obtained in the experiments is benchmarked against the results available in the literature (Section 4.7) and the accuracy of two empirical models, described in the literature, for modelling the effect of temperature on the bond strength is assessed (Section 4.8).

The data obtained in the experiments served as the basis of the numerical studies developed in Chapter 5. Part of the experiments presented in this section were developed in collaboration with Master students, namely the pull-out tests performed in SC bars [27] and in RBP bars with straight [28] and bent geometries [29].

4.2. Test programme

The experimental campaign presented herein comprised pull-out tests of different types of GFRP bars embedded in concrete cylinders, performed under steady-state conditions from ambient temperature (20 ºC) up to 300 ºC. This range included temperatures above the glass transition temperature but below the decomposition temperature of the bars' resin (the bars' T_d is between 374 and 400 ºC, *cf.* Table 3.1). The six series of pull-out tests carried out in this study are summarized in Table 4.1 and described below. The test series were labelled according to the type of bar used: (i) SC, RB or RBP, according to the type of surface finish; (ii) D8 or D12, according to the bar diameter (8 or 12 mm respectively), and (iii) S or B, according to the bar geometry (straight or 90º bent, respectively). The bars used in the study were previously shown in Figure 3.1 and their features were described in detail in Section 3.2.

Two series of tests were carried out in sand-coated SC bars (Figure 3.1a), each corresponding to two different embedment lengths (L_b) of the bars in the concrete: 5 and 9 times the nominal diameter (D=10 mm) of the bars – 50 mm and 90 mm, respectively (5D and 9D series). The embedment length adopted in the 5D series (also adopted in the RB and RBP-S series) corresponds to that recommended in most test standards (*e.g.* ASTM D7913 [188] and ACI 440.3R-12 [189]), whereas specimens from 9D series were produced to evaluate the influence of adopting a longer embedment length on the GFRP-concrete bond at elevated temperature. All specimens with SC bars (T_g=98 ºC) were tested at (constant) temperatures ranging from 20 ºC up to 140 ºC (200 ºC in the case of the 5D series).

Table 4.1. Pull-out tests series.

Bar geometry	Bar/ test series	Bar embedment length in concrete	Temperatures [ºC]
Straight	SC	5D = 50 mm	20, 40, 60, 80, 100, 140, 200
		9D = 90 mm	20, 40, 60, 80, 100, 140
	RB-D12	5D = 65.5 mm	20, 60, 100, 140, 170, 200, 250
	RB-D8	5D = 44.5 mm	20, 60, 100, 140, 200, 250, 300
	RBP-S	5D = 66.5 mm	20, 60, 100, 120, 140, 220, 300
90º bent	RBP-B	~12D = 161.3 mm (1)	20, 60, 100, 120, 140, 220, 300

(1) Total embedment length of bent bar corresponds to the straight embedment length (L_b) of 5D (66.5 mm), a 90º bend and a tail length of 20 mm.

Next, three series of tests were carried out in ribbed bars with the aim of evaluating the influence of the surface finish and the T_g of ribbed bars (with different rib profiles) on their bond behaviour to concrete at elevated temperature. The influence of the geometry of the ribs on the bond to concrete was assessed by comparing two ribbed bars – RB-D12 (Figure 3.1b$_1$) and RBP-S (Figure 3.1c$_1$). The bars had the same nominal core diameter (12 mm) and similar tensile modulus at ambient temperature, but different surface geometries, tensile strengths and thermophysical properties (namely, different T_g). Tests were also conducted in RB bars with two diameters (12 mm and 8 mm, Figure 3.1b$_1$ and Figure 3.1b$_2$, respectively) – it is noteworthy that the profile of their ribs is different (as expected, this also had significant influence on their bond behaviour). The tests on RB (T_g=157 ºC) and RBP bars (T_g=104 ºC) were performed under steady-state conditions from 20 ºC up to 300 °C (250 ºC in the case of the RB-D8 series).

The last series of tests assessed the influence of the anchorage geometry on the bond behaviour. To that end, pull-out tests were performed on 90º bent bars (RBP-B, Figure 3.1c$_2$) and the results were compared to those obtained on the previous series in straight bars with the same surface finish and T_g (RBP-S, Figure 3.1c$_1$). The specimens with straight and bent bars were casted from the same concrete batch and the pull-out tests were performed maintaining the same test setup and procedure, with slight adaptations (described in the next section). The tests performed in bent bars were also carried out from 20 ºC up to 300 ºC.

4.3. Pull-out specimen description, instrumentation and test procedure

The concrete cylinders were produced using concrete class C25/30 with cement type CEM II/A-L 42.5R and limestone aggregates with maximum size of 22 mm. The specimens with sand coated bars and ribbed bars were casted separately, thereby resulting in concrete mixes with different mechanical

properties. Table 4.2 presents the compressive and splitting tensile strengths of both concrete batches, determined at the age of the pull-out tests according to standard procedures ([190] and [191], respectively); the modulus of elasticity of concrete, estimated according to [192], is also shown. Prior to the tests, the pull-out specimens, as well as the cylinders and cubes used to characterize the concrete's properties, were cured in the laboratory facilities at ambient temperature and relative humidity (indoor, but not controlled).

Table 4.2. Properties of concrete used in pull-out specimens (average strength and coefficient of variation, in brackets).

Test series	Age [days]	Average cube compressive strength, $f_{cm,cube}$ [MPa]	Average splitting tensile strength, f_{ctm} [MPa]	Modulus of elasticity [GPa]
SC	111	43.3 (2.0%)	3.1 (21.2%)	28.7
RB, RBP	272	31.7 (3.6%)	1.7 (9.4%)	26.2

The geometry of the pull-out specimens is illustrated Figure 4.1. The specimens comprising straight bars, depicted in Figure 4.1a, consisted of concrete cylinders (height and diameter of 150 mm) with a single GFRP bar (total length of 745 mm) embedded vertically along the cylinders' revolution axis. In the majority of specimens (except series SC-9*D*), an embedment length to concrete of 5 times the equivalent diameter (*D*) of the bars[4] (*cf.* Table 3.1) was adopted, as recommended in most test guidelines (*e.g.* ASTM D7913 [188] and ACI 440.3R-12 [189]). In the case of series SC-9*D*, the embedment length to concrete was higher and equal to 9*D*. The bonded length considered in each test series is shown in Table 4.1. The unbonded length of the bar, positioned at the bottom of the cylinder, was set using a bond breaker made of a PVC tube (1.3 mm thick, outer diameter of 16 mm or 12 mm when used in GFRP bars with respectively 12 mm or 8 mm in diameter). At the free (*i.e.*, upper) end, the bars were slightly protruded from the concrete cylinder, thus allowing to read the slip between that end of the bars and the top surface of the concrete (using a video extensometer, as explained ahead).

The specimens comprising bent RBP bars are illustrated in Figure 4.1b. The concrete cylinders had the same cross-section as those used for straight bars (150 mm in diameter), but had a (larger) height of 230 mm. The embedment length comprised a straight length (L_b) corresponding to 5D (66.5 mm, the same as in the straight RBP bars) and a 90º bend followed by a tail length (l_t) of 20 mm; the total embedment length of the bent bar was 161.3 mm, corresponding to approximately 12*D*. The low concrete thickness adopted above and at the end of the tail length aimed at replicating the cover provided

[4] In the case of ribbed bars, the actual depth and width of the ribs were considered in order to calculate the contacting area along the embedded length of the bars.

in (thin) GFRP-RC slab strips tested and presented in Chapter 6. The unbonded length of the bar was also assured using a PVC tube bond breaker.

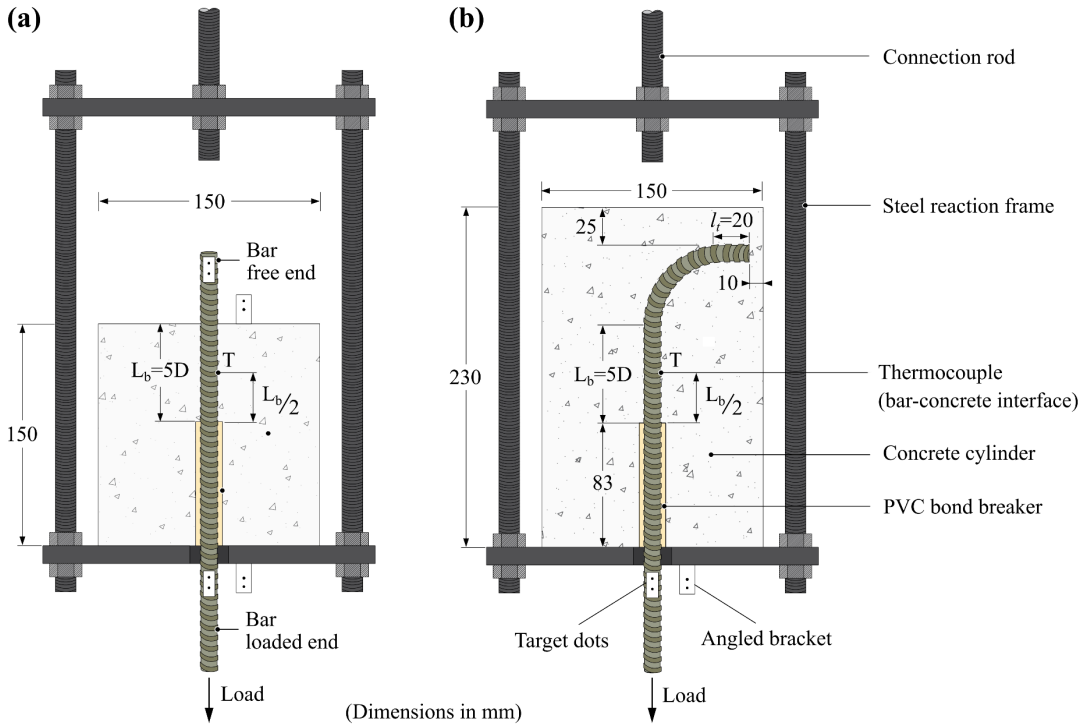

Figure 4.1. Specimen geometry of pull-out specimens with (a) straight and (b) bent bars.

As in the tensile tests, the loaded end of the all bars was protected with 100 mm long stainless-steel tubes filled with a bi-component epoxy resin (*Sikadur-330* from *Sika*) to avoid premature failure modes due to crushing of the bars in the grips of the universal test machine. The tubes used in specimens with RB-D8 bars had an outer diameter of 18 mm (22 mm in the remaining bars) and a thickness of 0.7 mm (1.25 mm in the remaining bars).

Preliminary pull-out tests performed in RBP-S specimens up to 140 °C presented (undesirable) splitting failure modes. For this reason, in order to properly evaluate the bond capacity of those bars, all specimens with RBP-S bars were confined using four stainless steel clamps (28 mm wide, 1.5 mm thick) distributed evenly along the height of the cylinder and tightened with a torque of 15 N.m. To validate the comparison between specimens with different bars (specimens using SC[5] and RB bars did not require any type of extra confinement in order to obtain pull-out failures), additional pull-out tests were carried out in specimens with RB bars at ambient temperature and 200 ºC to confirm the influence of the same level of confinement on the bond stress *vs.* slip response. The results showed that the bond stress *vs.* slip response was not significantly affected by this additional confinement; the maximum value of the

[5] As mentioned in Section 4.4.2, one specimen from SC-9D series failed by concrete splitting at ambient temperature and therefore additional tests were performed at that temperature in confined specimens.

average bond stress obtained at 20 ºC in the confined and unconfined specimens was 12.3 MPa and 11.5 MPa, respectively, while at 200 ºC it was 3.4 MPa for both types of specimens. To assure a confinement level similar to the specimens with straight bars, additional radial confinement was also provided to the specimens with bent bars, in this case by means of six (identical) stainless steel clamps distributed evenly along the cylinders' height (see Figure 4.2c) and also tightened with a torque of 15 N.m. In some of specimens the clamps were instrumented with electrical strain gauges to measure the variation of axial strain during the application of the torque; these measurements allowed to estimate the initial level of confinement of concrete at ambient temperature, which was then reproduced in the numerical models developed in Section 5.3 .

The pull-out tests were carried out according to the test setup depicted in Figure 4.2 (and also in Figure 4.1). The specimens were positioned in a frame composed by two metal plates, connected with steel rods, which acted as a reaction device. The frame, in turn, was installed inside a *Tinius Olsen* thermal chamber and was coupled to an *Instron* universal testing machine with load capacity of 250 kN, as shown in Figure 4.2a. The temperature of the specimens was controlled by a type K thermocouple (0.25 mm of conductor diameter) adhesively bonded to the surface of the bar and positioned at mid-height of the straight embedment length before the concrete casting (*cf.* Figure 4.1). An additional thermocouple was used to monitor the temperature of the air inside the thermal chamber.

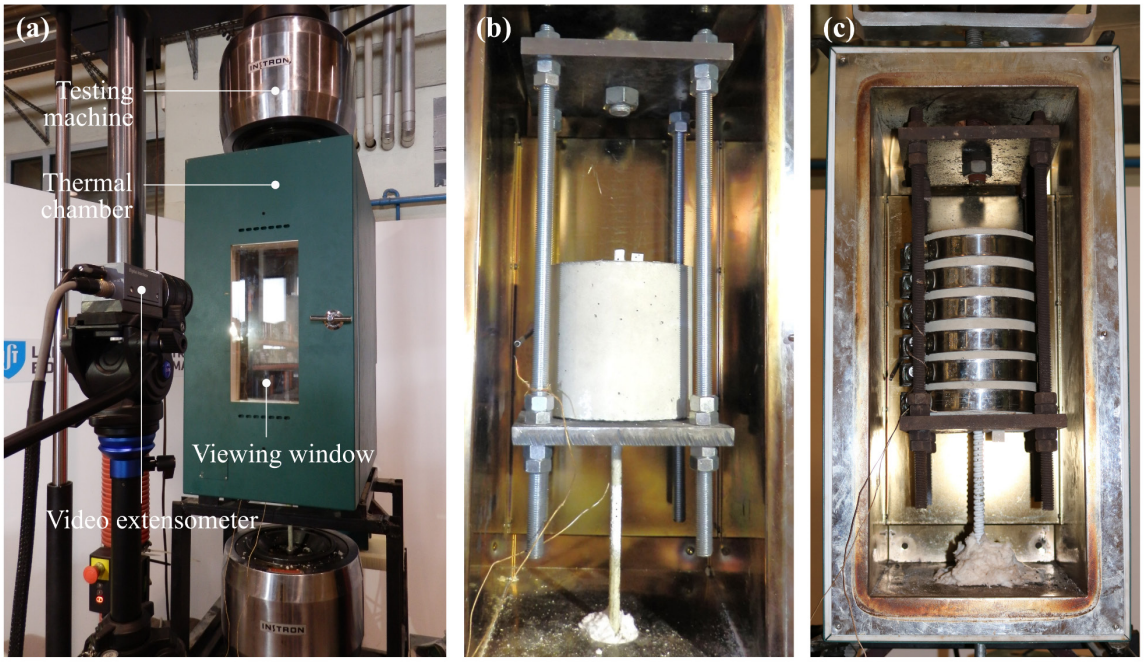

Figure 4.2. Test setup of pull-out tests: (a) external view of the thermal chamber and video extensometer; inside view of the specimens with (b) straight and (c) bent bars inside the thermal chamber.

The slip of the bars was measured at both free (upper) and loaded (lower) ends using a video extensometer. This equipment consisted of a high-resolution *Sony* video camera (model *XCG 5005E*, with *Fujinon* lens, model *Fujifilm HF50SA-1*) placed on a tripod, as shown in Figure 4.2a. This technique allowed measuring the relative displacement of the bar (*i.e.*, the slip) over time using as reference target dots marked on the GFRP bar (on both free and loaded ends) and on steel angles (bolted to the concrete cylinders' top surface and bottom plate of the reaction frame, respectively), illustrated in Figure 4.1. It is worth referring that the portion of slip corresponding to the elongation of the bars (considered from the beginning of the embedment length to the target dots) was subtracted from the slip measurements, considering the reduction with temperature of the tensile modulus of the bars determined from tensile tests (*cf.* Figure 3.11 in Section 3.4).

The experimental procedure comprised two stages. In the first stage, the specimens were heated up to the predefined (target) temperature at the average heating rate indicated in Table 4.3. In order to minimize the specimen's heating time, the predefined temperature of the thermal chamber was set 10 ºC above the specimen's target temperature. Once the temperature at the GFRP-concrete interface (from now on referred to as "specimen temperature") approached the T_{target} (*i.e.*, 2 ºC lower), the temperature of the thermal chamber was reduced (to the target value), guaranteeing a constant temperature in the specimen during the second stage of the tests (*i.e.*, the loading stage, as described below). This procedure is exemplified in Figure 4.3, which shows for two different target temperatures (100 ºC and 200 ºC) the temperature-time curves of air inside the thermal chamber (continuous line) and of the GFRP-concrete interface (dashed line), in this case for two RB-D12 specimens. It is worth mentioning that during the first stage of the test procedure, the lower grip of the testing machine was kept open, thus avoiding any axial restriction due to thermal expansion of the specimens and text fixture.

Table 4.3. Average heating rates of the air inside the thermal chamber and of the GFRP-concrete interface obtained in pull-out tests.

Specimen	**Average heating rate [ºC/min]**	
	Air inside the thermal chamber	**GFRP-concrete interface**
SC	0.9	10.2
RB-D8	1.7	7.1
RB-D12	1.5	6.3
RBP-S	1.3	9.8
RBP-B	1.1	7.3

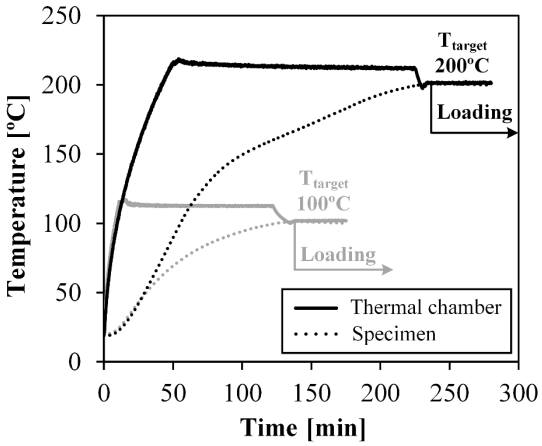

Figure 4.3. Example of temperature-time curves of the specimens (RB-D12; measured at the bar-concrete interface) and of the air inside the thermal chamber, for target temperatures of 100 ºC and 200 ºC.

In the second stage of the test, after assuring a constant temperature at the GFRP-concrete interface, the lower end of the bars was loaded under displacement control at an approximate speed of 1 mm/min; the test speed was defined to meet the requirements set in ASTM D7913 [188]. During this stage, the applied load, the cross-head displacement of the test machine and the position of the target dots (used for the video extensometer measurements) were monitored. Due to the limited height of the thermal chamber viewing window, the tests were performed until the target dots were no longer traceable by the video extensometer (*i.e.*, before the complete pull-out of the bar from the concrete cylinder, though for slip values significantly higher than those expected in actual structural members). For each temperature and each test series, at least three replicate specimens were tested, resulting in a total of 121 tests.

4.4. Results and discussion of pull-out tests on sand coated bars

4.4.1. Average bond stress *vs.* slip curves

The following subsections present the results obtained in the pull-out tests performed in sand coated bars (SC series). Figure 4.4 presents for each target temperature and embedment length (5*D* and 9*D* series) the average bond stress *vs.* slip curves, with the slip measured at the free and loaded ends of the bars, respectively. To simplify the analysis described in the present section and for better visualization of the pre- and post-peak responses, the curves are only plotted up to slips of 15 mm – moreover, higher slip values are not expected to be attained in actual structures (note that the bond strength obtained from direct pull-out tests is normally higher than that attained in beam tests, the latter being more realistic in simulating the confinement and loading conditions of an RC member in flexure [193]). It is worth

reminding that at the loaded end, the portion of slip corresponding to the elongation of the bar (considered from the beginning of the embedment length to the target dots) was subtracted from the slip measurements. In these calculations and for each of the temperatures tested, the degradation of the tensile modulus of the GFRP bar with temperature was based on the results obtained in the tensile tests described in Section 3.4.

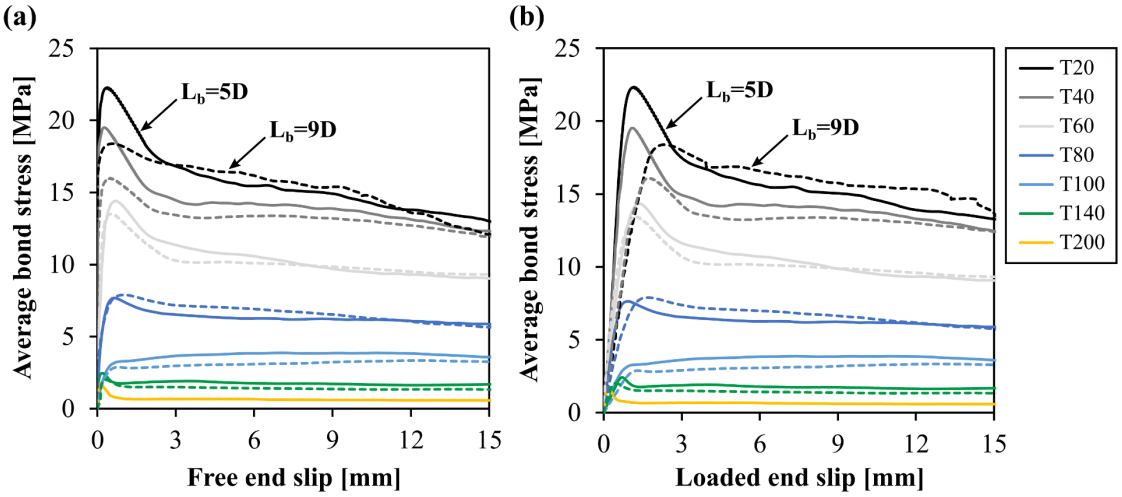

Figure 4.4. Average bond stress *vs.* slip curves obtained at the (a) free and (b) loaded ends of SC bars (embedment length of 5*D* – continuous line; embedment length of 9*D* – dashed line).

Regardless of the embedment length, the curves presented an approximately linear behaviour until the maximum stress was attained and the slope of these ascending branches (*i.e.*, the bond stiffness) was progressively reduced as the test temperature increased – this stiffness reduction is clearly noticed in Figure 4.4b. After the maximum average bond strength was attained, a stress drop occurred (with exception of the specimens tested at 100 ºC, where a stress peak did not occur and consequently no such drop exists); this drop was then followed by a progressive stress reduction, with the curves exhibiting almost a plateau for higher slips. This final stage of the curves extended up to the end of the tests, which were interrupted before the complete pull-out of the bars (due to the loss of the target dots, as mentioned in Section 4.3). The specimens tested at 100 ºC presented a different post-peak behaviour compared to the remaining ones: after the average bond strength was attained (which occurred for considerably higher slip values), the stress values presented a progressive reduction – this behaviour may be related to the fact that this temperature virtually matches the T_g of the bars (98 ºC), for which the viscoelasticity of the material is known to be maximum.

As shown in Figure 4.4, the curves obtained at the free and loaded ends of the specimens presented a similar overall behaviour. However, the following differences should be noted: while the slip at the loaded end of the bars increased from the beginning of the loading stage (Figure 4.4b), the same did not occur at the free end (Figure 4.4a) – for specimens tested at 20 ºC and 40 ºC, as expected, the initial

branch of the curves is approximately vertical (*i.e.*, the slip at the free end is negligible). These results indicate that the bond length was only partially mobilized for relatively high stress values, *i.e.*, up to approximately the average bond strength (*cf.* Figure 4.4a); the moment when the free end slip presents a significant increase should be related to the loss of adhesion between the sand coating and the core of the bar (further discussion is provided in Section 4.4.2). However, for specimens tested at temperatures above 40 ºC, the slip at the free end starts as soon as loading begins, which indicates that even relatively low temperatures (including below the bar's T_g) have a non-negligible effect on the degradation of the bar-concrete bond, particularly on the sand coating-bar's core interface.

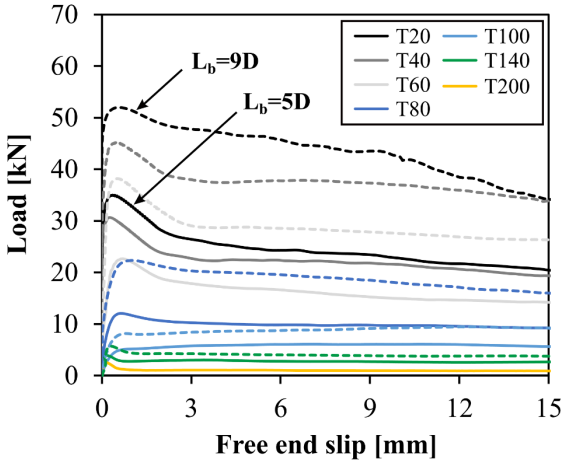

Figure 4.5. Load *vs.* slip curves (slip measured at the free end) obtained in SC bars (embedment length of 5*D* – continuous line; embedment length of 9*D* – dashed line).

The plateau of the curves after the stress peak should have been caused by the progressive penetration of the free end length of the bars into the concrete cylinder (note that this stems from the standard test setup adopted). When in contact with the concrete's surface, this undamaged (mechanically) portion of the bars may have provided an increase in the GFRP-concrete friction, compared to the one afforded by the damaged (and initially embedded) length of the bars, thus providing an additional contribution to the overall resistance against slip.

Figure 4.4 also shows that: (i) for a certain temperature, as expected, the specimens with longer embedment length (9*D* series) presented lower average bond stresses; and (ii) the bond strength was progressively reduced with temperature (*cf.* Table 4.4 and Table 4.5 in Section 4.4.3). The effect of elevated temperature was also noticeable in the bond stiffness reduction (corresponding to the slope of the initial linear branch); this result was also expected, since for elevated temperatures the stiffness and strength of the constituent materials and especially of the GFRP-concrete interface are reduced. Figure 4.5 presents for each target temperature and embedment length the load *vs.* free end slip curves; this figure allows confirming that specimens with longer embedment length (9*D* series) attained higher loads and, for those specimens, slip starts to increase for higher load values comparing to the 5*D* series.

4.4.2. Failure modes and post pull-out observations

For all test temperatures, failure of specimens from 5*D* series occurred due to pull-out of the GFRP bars, *i.e.* slippage of the bars along the embedment length in the concrete cylinder. The experimental results (described in the previous section) and the visual observations of the specimens throughout the tests (*e.g.*, Figure 4.6) confirmed the occurrence of this expected failure mode. Regarding the specimens from 9*D* series, in general pull-out of the bars also occurred, with the exception of some specimens tested at ambient temperature, which presented splitting of the concrete[6]. In order to avoid this type of failure (and to obtain the desired pull-out failure), additional specimens were confined using four stainless steel clamps evenly distributed along the height of the cylinder. The tests on these specimens (carried out at ambient temperature) showed that despite the confinement provided to the concrete (which successfully avoided splitting failures), the bond stress *vs.* slip response was not affected, presenting a similar behaviour (*i.e.*, identical stiffness of the ascending branch and maximum average bond stress) to that obtained in unconfined specimens (cf. Section 4.4.1). Indeed, the maximum value of the average bond stress obtained in the confined and unconfined specimens was very similar: 19.4 and 19.2 MPa, respectively (*cf.* Table B.2 in Appendix B).

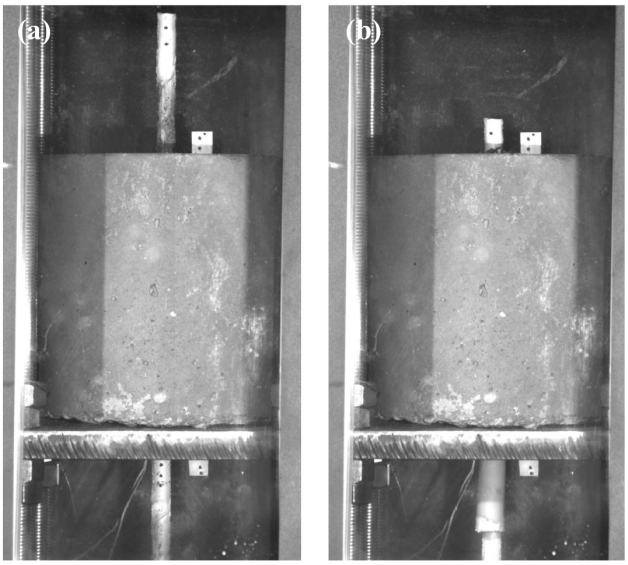

Figure 4.6. Pull-out of SC bars from the concrete cylinders: representative specimen at (a) the beginning and (b) end of the tests.

After the tests, all concrete cylinders were sawn cut into two pieces to assess the failure modes and evaluate the damage underwent by the materials and at the bars-concrete interface. As shown in Figure 4.7a, in specimens tested at elevated temperatures the external layer of the GFRP bars was significantly abraded, with exposure of the longitudinal and wound fibres; in particular, the wound fibres were ripped

[6] The specimens that failed due to splitting were not considered for the calculation of the average bond strength.

and the superficial sand-coated layer was peeled. Residues of crushed resin, some broken wound fibres and most of the sand particles were attached to the concrete (along the embedment length of the bar); no damage on the core of the bars was observed. In the specimens tested at ambient temperature (Figure 4.7b), the abrasion introduced to the bar was more severe: the superficial sand-coated layer and the wound fibres were completely removed, the core of the bar was exposed and some longitudinal fibres were broken and stripped from the core. The visual inspections of the pull-out specimens after the tests demonstrated that the bond behaviour of the sand-coated GFRP bars to concrete, at both ambient and elevated temperatures, was influenced by the adhesion (and friction) between the surface finish (sand coating and wound fibres) and the bar's core.

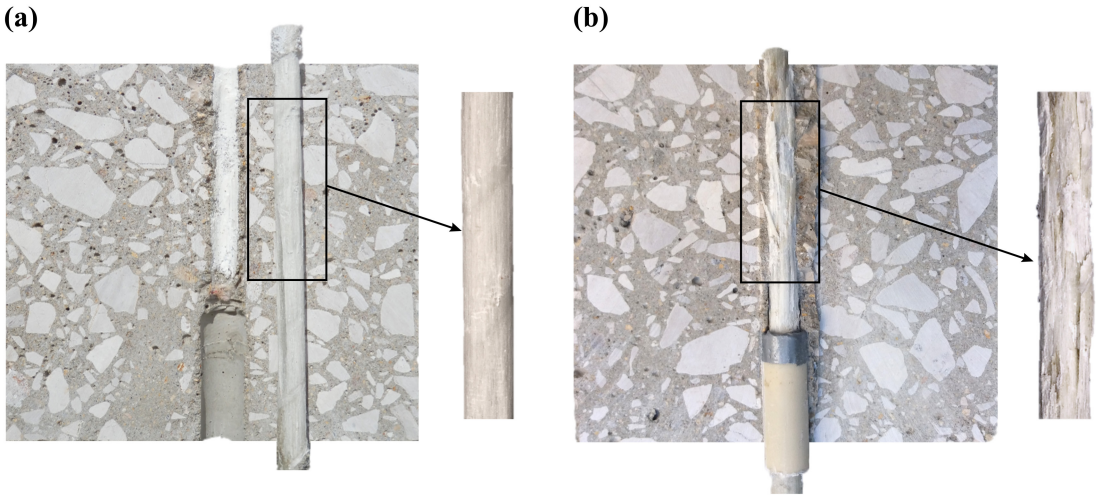

Figure 4.7. Surface of SC bars after pull-out test at (a) elevated and (b) ambient temperature.

4.4.3. Bond strength and stiffness

Figure 4.8 presents the variation with temperature of the following parameters (normalized average values w.r.t. the ambient temperature ones): (i) the average bond strength; (ii) the bond stiffness (corresponding to the slope between 25% and 50% of the maximum value of the average bond stress *vs.* loaded end slip curves); (iii) the tensile strength, (iv) the tensile modulus, and (v) the storage modulus curve (obtained from DMA) of the bars. Table 4.4 and Table 4.5 (presented ahead) summarize the results obtained in series 5*D* and 9*D*, respectively; the results of each specimen are available in Table B.1 and Table B.2 from Appendix B.

The results depicted in Figure 4.8 show that the bond strength was significantly reduced with temperature, even for values well below the T_g of the GFRP bars. For temperatures as low as 60 ºC, bond strength reductions were at least 29%, while for 100 ºC and 140 ºC, the reductions were around 80% and 90%, respectively. Between 140 ºC and 200 ºC, the decrease in bond strength was marginal. Moreover, the results depicted in Figure 4.8 highlight that: (i) the bond strength exhibited a similar

reduction with temperature for the two test series (*i.e.*, for the two different embedment lengths); (ii) the reduction of the GFRP-concrete bond strength (and stiffness) – governed by the softening of the binding resin of the sand coating (applied after pultrusion) – occurred for lower temperatures than the mechanical degradation at the material level (as measured in the tensile tests and in the DMA tests) – in this case, the degradation is controlled by the softening of the core's resin, which was cured in a different manner when compared to that of the binding resin of the sand coating.

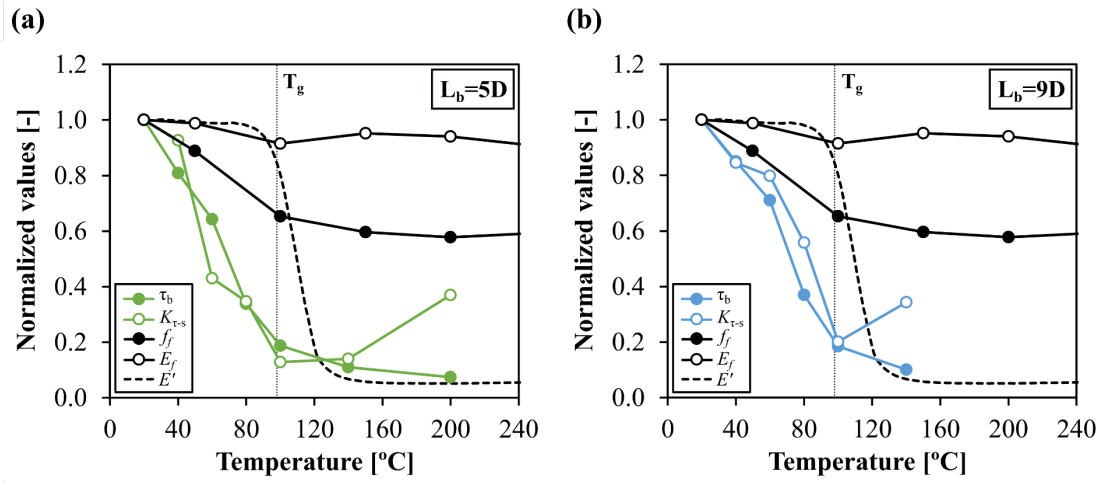

Figure 4.8. Normalized values of bond strength (τ_b) and stiffness ($K_{\tau\text{-}s}$), tensile strength (f_f), tensile modulus (E_f) and storage modulus (E'') of SC bars as a function of temperature.

Table 4.4 and Table 4.5 show that for temperatures up to 60 ºC for 5*D* series and 80 ºC for 9*D* series, the ratio between the maximum tensile stress developed in the GFRP bars during the pull-out tests and the tensile strength of the bars at ambient temperature is higher than 25%; in most design guidelines, this value is defined as the maximum stress level that can be developed in the GFRP reinforcing bars for serviceability limit states. Regarding the stiffness of the GFRP-concrete interface, the results obtained also show that it was significantly affected by temperature: (i) at 60 ºC, the bond stiffness reduction was at least 44%, progressing to 80% at 100 ºC; and (ii) the steepest reduction occurred (below the T_g) in specimens with a shorter embedment length. It is still worth noting that in both series the bond stiffness presented an increase when the tested temperature raised from 100 ºC to 140 ºC, especially for 9*D* series – this result (unexpected *a priori*) may be partially explained by the fact that for such temperature variation the radial expansion of the bar was possibly more significant than the thermal degradation of the materials; therefore, it may have increased the normal stresses between the bar's core and the superficial surface finish and, consequently, the bond stiffness. Additional investigations are needed to confirm this phenomenon.

Table 4.1: Pull-out test results obtained in SC bars with embedment length of 5*D* (average ± standard deviation).

T [°C]	Maximum pull-out load [kN]	Average bond strength [MPa]	Normalized bond strength reduction [-]	Ratio maximum axial stress/ tensile strength at elevated temperature	Ratio maximum axial stress/tensile strength at ambient temperature	Bond stiffness (loaded end) ($K_{\tau\text{-}s}$) [MPa/mm]	Normalized bond stiffness reduction [-]	Failure mode [(1)]
20 ± 2	36.3 ± 3.2	23.1 ± 2.0	-	49%	49%	34.9 ± 3.3	-	PO
40 ± 2	29.4 ± 2.0	18.7 ± 1.3	19%	43%	39%	32.4 ± 10.6	7%	PO
60 ± 2	23.3 ± 1.3	14.8 ± 0.8	36%	37%	31%	15.0 ± 5.7	57%	PO
80 ± 2	13.8 ± 3.1	8.8 ± 2.0	66%	25%	18%	12.1 ± 4.7	65%	PO
100 ± 2	6.8 ± 1.3	4.3 ± 0.8	81%	14%	9%	4.5 ± 1.3	87%	PO
140 ± 2	4.0 ± 0.3	2.5 ± 0.2	89%	9%	5%	4.9 ± 1.2	86%	PO
200 ± 2	2.7 [(2)]	1.7	93%	6%	4%	12.9 [(2)]	63%	PO

[(1)] PO: pull-out

[(2)] One single specimen was tested.

Table 4.2. Pull-out test results obtained in SC bars with embedment length of 9*D* (average ± standard deviation).

T [ºC]	Maximum pull-out load [kN]	Average bond strength [MPa]	Normalized bond strength reduction [-]	Ratio maximum axial stress/ tensile strength at elevated temperature	Ratio maximum axial stress/tensile strength at ambient temperature	Bond stiffness ($K_{\tau\text{-}s}$) (loaded end) [MPa/mm]	Normalized bond stiffness reduction [-]	Failure mode [(1)]
20 ± 2	54.6 ± 3.1	19.3 ± 1.1	-	73%	73%	14.7 ± 1.8	-	PO/SPT
40 ± 2	46.5 ± 2.0	16.4 ± 0.7	15%	67%	62%	12.5 ± 1.0	15%	PO
60 ± 2	38.8 ± 5.5	13.7 ± 2.0	29%	62%	52%	11.8 ± 1.2	20%	PO
80 ± 2	20.1 ± 3.2	7.1 ± 1.1	63%	36%	27%	8.2 ± 0.1	44%	PO
100 ± 2	10.1 ± 2.7	3.6 ± 1.0	82%	21%	14%	3.0 ± 0.9	80%	PO
140 ± 2	5.5 ± 0.4	1.9 ± 0.2	90%	12%	7%	5.1 ± 1.8	66%	PO

[(1)] PO: pull-out; SPT: splitting of concrete.

4.5. Results and discussion of pull-out tests on straight bars with ribbed surface finish

4.5.1. Average bond stress *vs.* slip curves

The results obtained in the pull-out tests performed in straight ribbed bars (series RB-D12, RB-D8 and RBP-S) are discussed in the following subsections. Figure 4.9 presents, for each target temperature and bar, the average bond stress *vs.* slip curves obtained from slip measurements taken at the free (dashed line) and loaded (continuous line) ends of the bars (in the latter, the slip was subtracted from the corresponding elastic deformation of the bars). For some temperatures, the bond stress *vs.* slip response measured at both ends of the bars appears to be coincident, which is a result of the scale of slips plotted. Overall, the bond stress *vs.* slip response was similar in all types of ribbed bars: it comprised (i) a pre-peak stage, in which bond stress increases rapidly with low slip values, and (ii) a post-peak stage in which stress reduces gradually after reaching the peak and then stabilizes, maintaining a residual bond stress for high values of slip.

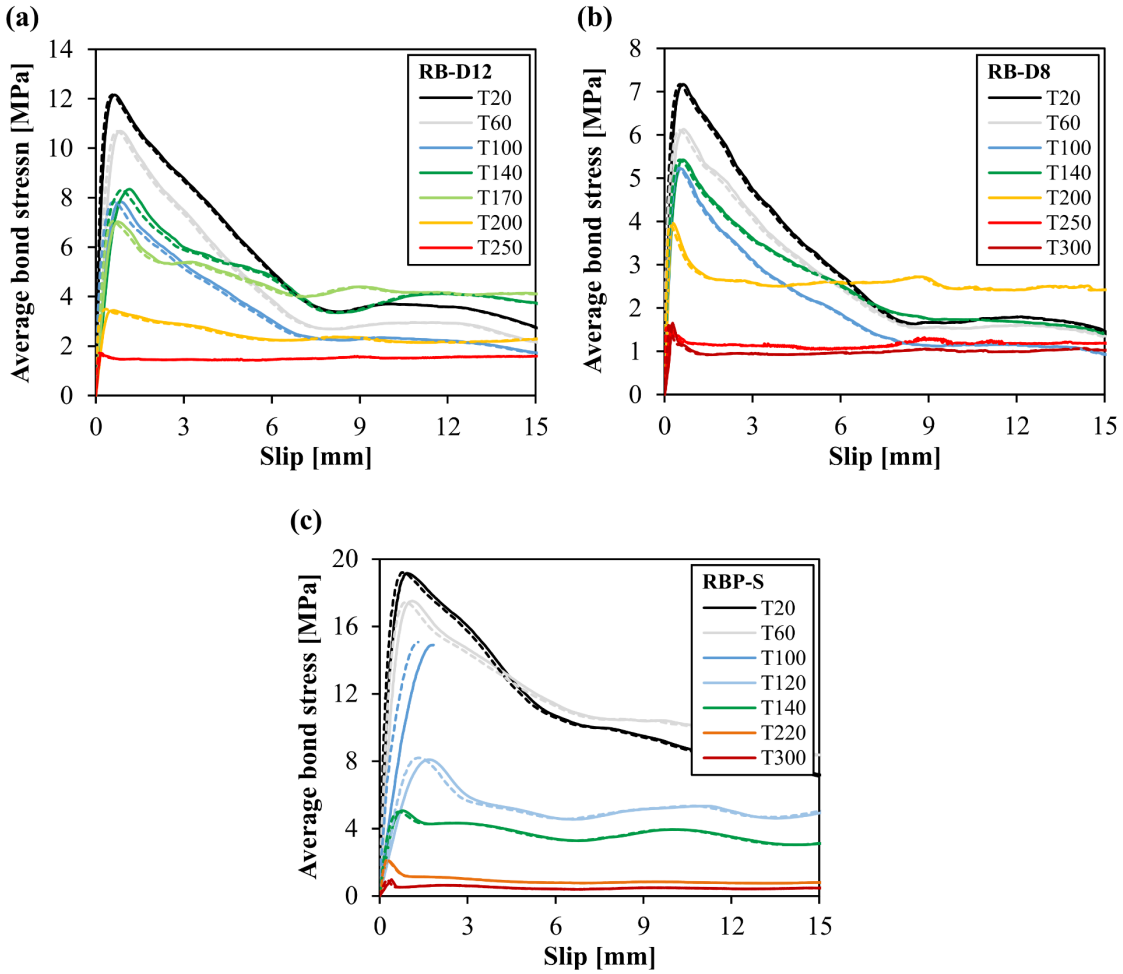

Figure 4.9. Average bond stress *vs.* slip curves for specimens with bars (a) RB-D12, (b) RB-D8 and (c) RBP-S (loaded end – continuous line; free end – dashed line).

As depicted in Figure 4.9, the initial pre-peak behaviour was approximately linear until the maximum stress was attained; in this stage, bond was mainly governed by chemical adhesion and the mechanical interlock of the ribs in the surrounding concrete. When the maximum stress was reached, and for temperatures up to the corresponding T_gs, the concrete corbels between the bar's ribs fractured and the bond stress at the GFRP-concrete interface started to gradually decrease with increasing slip, while the concrete corbels were probably sheared off; therefore, for temperatures up to T_g, the post-peak behaviour of the bond stress *vs.* slip curves was governed mainly by the friction between the surrounding concrete and the sheared off concrete corbels.

For temperatures higher than the T_g, the post-peak behaviour was governed by the shearing off of the bar's ribs themselves, as further analysed in Section 4.5.2; this, however, did not seem to change the overall bond stress *vs.* slip response. For these temperatures (*i.e.,* higher than the T_g), the post-peak response was governed by (i) the friction between the sheared off ribs and the bar's core, and (ii) the wedging effect provided by the mechanically undamaged length of the bar (corresponding to the initial free end length) as it slipped into the embedded length in the concrete cylinder. For high slip values, the bond interface retained some level of resistance against slip – this bond stress plateau is mostly a consequence of the friction and wedging effects mentioned above. It is worth reminding that the presence of the free end length of the bar is a feature of most standard test methods (*e.g.* [188,189]), although it may not be fully representative of the bond behaviour of a bar inside a concrete member.

For all test series, the curves show that for temperatures below their T_g, the bars retained a relatively low value of bond stress after the peak stress was attained (resulting in a more marked peak) comparing to the stress plateau obtained for temperatures above the T_g (in which the reduction in bond stress after the peak stress was significantly less pronounced). The differences in the bond stress *vs.* slip response after peak stress are consistent with the changes in the failure modes (at the bond interface) when temperature increased above the T_g. As the resin softens, the superficial layer of the bar becomes more viscous and the (resin rich) ribs become more susceptible to the damage caused by the concrete-rib friction, being more likely to be detached/sheared off from the bar's core (as exemplified in Figure 4.10b). Under these circumstances, the effectiveness of the mechanical interlock between the ribs and the concrete (the main load bearing mechanism in ribbed bars) is compromised and therefore a steeper reduction in the post-peak bond stress would be expected. However, the thermal expansion of the bar may have outweighed this effect, by improving the bond stresses in the normal direction at the GFRP-concrete interface, and therefore allowing the bar to retain a significantly high bond capacity for high slip values; this was also observed in SC bars, as referred in Section 4.4.3.

As expected, the bond properties of the bars were severely affected by temperature, as proven by the gradual reduction in the maximum values of the average bond stress (*i.e.* the bond strength) with increasing temperatures. The bond stiffness, corresponding to the slope of the ascending branch of the bond stress *vs.* slip curves, was also affected due to the degradation of the mechanical properties of the

constituent materials and consequently of the GFRP-concrete interface. This behaviour was observed in all specimens, although the bond properties obtained for the RB bars remained fairly unaffected between 100 ºC and 140 ºC. Further results and discussion are provided in Section 4.5.3.

4.5.2. Failure modes and post-pull out observations

For the tests conducted at temperatures up to the bars' T_g, failure occurred in the GFRP-concrete interface by pull-out of the bar from the concrete cylinder, showing that even for the specimens that were not mechanically confined using steel clamps, the concrete cylinders provided adequate confinement to the bars and allowed to determine their maximum bond stress (no signs of splitting cracks were detected in any of the specimens tested). This failure mode was however not observed in specimens with RBP bars tested at 100 ºC; for this temperature (which matches the ribbed bars' T_g) the specimens presented splitting failure despite being confined with steel clamps. A possible explanation for this unexpected result may be related to the fact that at this temperature, the radial expansion of the bars was possibly more significant than the thermal degradation of the GFRP-concrete interface (as shown ahead in Figure 4.14, most of the bond strength reduction of RBP bars occurred for temperatures above 100 ºC). This may have resulted in a significant increase of radial stresses in the (confined) concrete and increase in the normal stresses between the bar and the concrete. Moreover, these results show that, only for this particular case, the confinement applied using steel clamps was not sufficient to avoid this undesired failure mode.

As previously mentioned, the failure modes observed at the GFRP-concrete interface changed when the temperature increased above the bars' T_g. This had repercussions on the bond strength (discussed in Section 4.5.3) and in the level of residual bond stress observed for high values of slip (already addressed in Section 4.5.1). As the test temperature increased, the bars suffered from yellowing, eventually becoming completely charred when tested at 300 ºC. Figure 4.10 and Figure 4.11 illustrate the damage at the failure interface of RB (in both diameters tested) and RBP-S specimens, respectively, after being sawn cut in half. From ambient temperature up to a temperature close to T_g (140 ºC in RB specimens and 100 ºC in RBP-S specimens), failure occurred between the surface of the bar and the surrounding concrete, *i.e.* involving the shearing off of the concrete corbels, while the surface of the bar remained practically undamaged (the top surface of the bar ribs was only slightly abraded, as shown in Figure 4.10a and Figure 4.11a), and no signs of resin or glass fibre residue were found in the concrete.

Figure 4.10. Specimens RB-D12 and RB-D8 representative of pull-out tests at: (a) 20 °C-140 °C, (b) 170 ºC-250 °C; (c) 300 °C.

Figure 4.11. Specimens RBP-S representative of pull-out tests at: (a) 20 °C, (b) 100 °C-220 °C; (c) 300 °C.

Above T_g, for temperatures between 170 ºC and 250 ºC in RB specimens (Figure 4.10b) and between 100 ºC and 220 ºC in RBP-S specimens (Figure 4.11b), the damage seemed to have been mostly concentrated at the interface between the ribs and the core of the bars – the core of the bar slipped while the ribs remained attached to the concrete along the embedded length. The softening of the resin weakened the adhesion of the ribs to the core, easing them from being progressively sheared off and detached from the core during the pull out of the bar. Residues of broken ribs coming from the free end length of the bar were found at the top surface of the concrete cylinder, resulting from the wedging effect between the ribs and the concrete as the bar slipped into the concrete. The damage observed at the failure interface was even more severe at 300 ºC (Figure 4.10c and Figure 4.11c), as almost all the (charred) ribs were detached from the bar's core and a significant amount of longitudinal fibres located at the surface of the bar were broken and depleted of resin. In RBP-S specimens tested at 60 °C, mixed failure modes were observed, characterized by damage in both concrete-bar and core-ribs interfaces.

4.5.3. Bond strength and stiffness

4.5.3.1. Bond strength

In this subsection, the results obtained in ribbed bars are compared to those obtained in Section 4.4 regarding sand coated (SC) bars. A thorough comparison of the results obtained in these test series cannot, however, neglect the relevant differences found regarding the failure modes of the concrete-bar interface, and how they were affected by the concrete's strength. In the tests performed in SC bars, it

was concluded that the damage was mostly limited to the bar's surface (with the abrasion of the sand coating and ripping of the wound fibres) (*cf.* Section 4.4.2). In the ribbed bars, however, and for temperatures below the T_g, failure occurred with shearing off of the concrete corbels between ribs, indicating that the GFRP-concrete bond mechanisms were more dependent on the concrete's strength. This aspect becomes particularly relevant in this analysis due to the fact that the properties of the concrete used in specimens with ribbed bars were lower comparing to those of the concrete used in specimens with sand coated bars: the cube's compressive strength ($f_{cm,cube}$) was 31.7 MPa (*vs.* 43.3 MPa) and the splitting tensile strength (f_{ctm}) was 1.7 MPa (*vs.* 3.1 MPa), respectively (*cf.* Table 4.2 in Section 4.3). A more accurate and valid comparison between the bond behaviour of ribbed and sand coated bars (namely regarding their bond strength) would therefore require similar concrete mixtures (*i.e.* properties). However, given the failure mode of pull-out specimens with SC bars (much less dependent on the concrete's properties), the significant differences observed regarding the influence of elevated temperatures on the bond strength of specimens with SC bars and of specimens with ribbed bars (described below) were not determined by the differences in concrete strength. Nevertheless, for the conditions of this study and for the embedment lengths corresponding to 5 times the bars' diameter, the ribbed bars presented lower average values of bond strength at ambient temperature (between 7 MPa and 19 MPa, depending on the type of ribbed bar) compared to those of SC bars (average of 23 MPa).

As reference, a set of pull-out tests was also performed (only at ambient temperature) in steel bars (A500 NR SD, nominal diameter of 12 mm) in identical conditions to ones described in the present study. The embedment length in concrete was 5D and the properties of concrete at 28 days of age were the following: $f_{cm,cube}$ = 31.1 MPa and f_{ctm} = 2.5 MPa. The specimens failed by pull-out due to the shearing off of the concrete corbels between the bars' surface indentations (similar to what was observed in ribbed GFRP bars). The average bond strength obtained in the steel specimens (average of three tests) was 19.5 ± 0.6 MPa. In comparison, the average bond strengths obtained at 20 ºC in GFRP bars with the similar diameter were the following: 12.1 MPa in RB-D12 bars, 19.0 MPa in RBP bars and 23.1 MPa in SC bars. These results show that sand coated bars and ribbed bars with deeper grooves (RBP bars) present comparable (and even slightly higher) bond strength than that of the conventional (deformed) steel bars. This conclusion is consistent with that obtained for example in Katz *et al.* [128], where the authors verified that GFRP bars with large surface deformations (*i.e.*, moulded indentations resembling steel surface deformations) and bars with wrapped fibres combined with fine sand particles presented superior bond performance at ambient temperature comparing to traditional steel bars.

Figure 4.12a presents the average bond strength (in absolute value) as a function of temperature obtained in the three types of specimens with ribbed bars. The results are plotted together with those obtained in SC bars. The main results obtained in the tests of ribbed bars are summarized at the end of the present subsection, in Table 4.6 to Table 4.8. The individual results of each series can be found in Appendix B with respect to specimens RB-D8 (Table B.3), RB-D12 (Table B.4) and RBP-S (Table B.5).

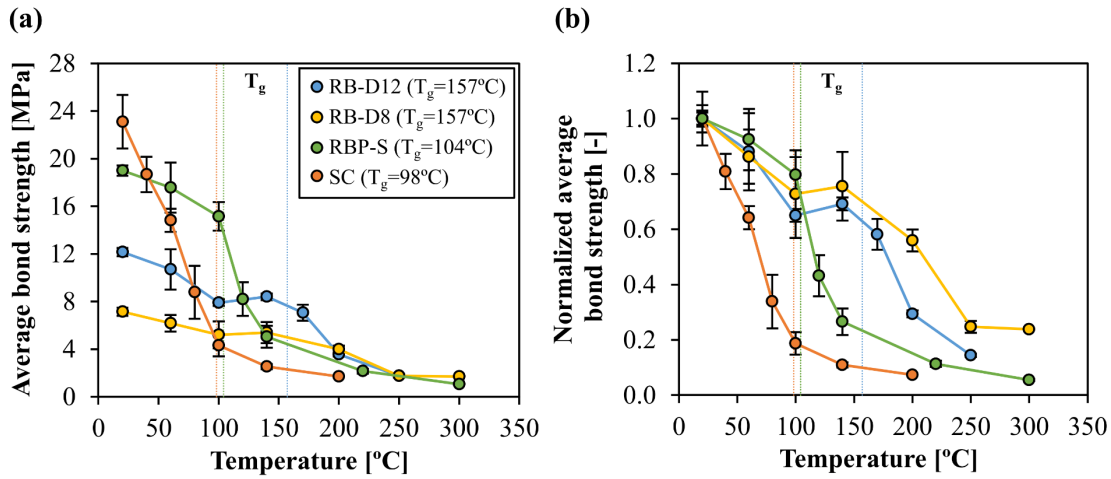

Figure 4.12. Average bond strength (and corresponding standard deviation bars) as a function of temperature in (a) absolute values and (b) normalized values (T_g of the bars marked as vertical lines).

At ambient temperature, the bars with wider and deeper grooves (RBP) presented significantly higher average bond strength (57% higher) compared to bars RB with the same core diameter, due to the development of higher stresses at the bond interface (necessary to mobilize the bigger concrete corbels between ribs), *i.e.*, providing a higher mechanical interlock. The bond strength was consistently higher in bars RBP up their T_g. Above the corresponding T_gs, the bond strength of both bars tended to level out, which is explained by similar failure modes occurring at the interface between the ribs and core of the bars (*cf.* Section 4.5.2). This result indicates that the bond strength was not governed by the geometry of the grooves; in fact, such behaviour seems to have been predominantly controlled by the T_g of the resin – bars RBP, despite having deeper grooves, have a T_g that is 53 ºC lower than that of bars RB, thus experiencing the effects of the thermal degradation at the GFRP-concrete interface level for much lower temperatures (*cf.* Figure 4.12b). As shown in Figure 4.12a, despite the differences in materials, diameters, ribs' geometry and T_g*s* of the three types of bars tested, the bond strengths obtained above 200 ºC (*i.e.* well above the corresponding T_gs) were similar (and marginal).

Regarding the influence of the bars' diameter, as shown in Figure 4.12a, the average bond strength up to the bar's T_g (157 ºC) obtained for specimens with 12 mm diameter bars (RB-D12 series) was higher compared to that of specimens with 8 mm bars (RB-D8 series). To some point, this result was unexpected, since it is known from the literature that bars with larger diameter are prone to develop lower bond strengths. However, while some authors have found an almost linear relation between the decrease in bond strength with the increase in the bar diameter (*e.g.* [194,195]), others (*e.g.* [196,197]) have shown that such linearity is not always verified, especially when comparing a very narrow range of bar sizes. Figure 4.12b shows that although a bar with a smaller diameter leads to a slightly less pronounced bond strength reduction with temperature, the overall bond strength reduction with temperature of RB series was fairly similar for the two diameters tested. Other authors (*e.g.* [58,136])

also did not find a clear relation between the reduction in bond strength with temperature and the diameter of the bars. More importantly, and in light of the results obtained in the present study, and for the type of bars tested, the influence of the diameter could not be precisely quantified, as the profile of the ribs was not fully comparable – as depicted in Figure 3.1, the ribs of the 8 mm diameter bars (Figure 3.1b) are shallower and their spacing is higher when compared to that of the 12 mm diameter bars (Figure 3.1a).

Figure 4.12b presents the normalized bond strength values (compared to those presented at ambient temperature) as a function of temperature. As expected, with the temperature increase, a continuous bond strength reduction occurs for all types of bars. As mentioned in Section 4.5.1, the bond strength of bars RB (for both diameters) was however not affected between 100 ºC and 140 ºC. This may have been related to the effect of the thermal expansion of the bars, whose beneficial effect (*i.e.,* an increase in the normal stress between the sheared ribs and the bars' core – *cf.* Section 4.5.2) at those temperatures may have overcome the overall degradation at the GFRP-concrete interaction.

Unlike what was found in the SC bars, in which most of the bond strength was lost at temperatures below the T_g, in the ribbed bars the bond strength reduction was more severe for temperatures above their T_g*s*; a similar trend was observed regarding the tensile strength, as described in Section 3.4.3.3. Comparing the results obtained in the SC bars (T_g of 98 ºC) to those of the ribbed bar with a similar glass transition temperature (RBP bar, T_g of 104 °C), most of the bond strength reduction of the latter occurred for much higher temperatures – at 100 °C, the reduction in the RBP bar was only 20% compared to the bond strength obtained at ambient temperature, whereas in SC bars it was approximately 80%. The explanation for this result seems to be related to the different surface finish of each bar, as well as to the different mechanical properties of the constituent materials; by involving different load bearing mechanisms, the failure modes occurring at the GFRP-concrete interface of each bar will be expectably different, hence influencing their bond behaviour. In the case of the SC bars, for all elevated temperatures (*i.e.* higher than 20 °C) failure occurred with abrasion of the superficial sand coating and ripping of the helicoidally wrapped fibres, smoothing completely the bar's surface (a completely different failure mode to those described in Section 4.5.2 for the ribbed bars). It is worth noting that the superficial layer of these bars is made of a polymeric material that bonds the sand particles to the bar's core; this failure mode indicated that this material seems to be more susceptible to elevated temperatures than the bulk resin of the ribbed bars (as mentioned in Section 4.5.2, bond failure at elevated temperatures on the ribbed bars involved shearing off of the resin rich ribs).

Table 4.3: Pull-out test results obtained in RB-D8 bars (average ± standard deviation).

T [ºC]	Maximum pull-out load [kN]	Average bond strength [MPa]	Normalized bond strength reduction [-]	Ratio maximum axial stress/ tensile strength at elevated temperature	Ratio maximum axial stress/tensile strength at ambient temperature	Bond stiffness ($K_{\tau-s}$) (loaded end) [MPa/mm]	Normalized bond stiffness reduction [-]	Failure mode [(1)]
20 ± 2	8.9 ± 0.4	7.2 ± 0.4	-	12%	12%	23.5 ± 3.7	-	PO
60 ± 2	7.6 ± 0.9	6.2 ± 0.7	14%	11%	10%	22.6 ± 4.7	4%	PO
100 ± 2	6.5 ± 1.4	5.2 ± 1.1	27%	10%	9%	17.0 ± 5.0	28%	PO
140 ± 2	6.7 ± 1.1	5.4 ± 0.9	24%	11%	9%	17.9 ± 3.8	24%	PO
200 ± 2	5.0 ± 0.4	4.0 ± 0.3	44%	14%	7%	17.6 ± 1.1	25%	PO
250 ± 2	2.2 ± 0.2	1.8 ± 0.2	75%	7%	3%	10.1 ± 0.5	57%	PO
300 ± 2	2.1 ± 0.0	1.7 ± 0.0	76%	7%	3%	5.3 ± 0.1	78%	PO

[(1)] PO: pull-out.

Table 4.4: Pull-out test results obtained in RB-D12 bars (average ± standard deviation).

T [°C]	Maximum pull-out load [kN]	Average bond strength [MPa]	Normalized bond strength reduction [-]	Ratio maximum axial stress/ tensile strength at elevated temperature	Ratio maximum axial stress/tensile strength at ambient temperature	Bond stiffness ($K_{\tau-s}$) (loaded end) [MPa/mm]	Normalized bond stiffness reduction [-]	Failure mode [1]
20 ± 2	32.8 ± 1.0	12.2 ± 0.4	-	22%	22%	48.2 ± 7.3	-	PO
60 ± 2	28.9 ± 4.6	10.7 ± 1.7	12%	22%	20%	24.9 ± 5.6	48%	PO
100 ± 2	21.4 ± 0.8	7.9 ± 0.3	35%	18%	15%	15.8 ± 1.8	67%	PO
140 ± 2	22.6 ± 0.8	8.4 ± 0.3	31%	21%	15%	12.8 ± 2.0	74%	PO
170 ± 2	19.1 ± 1.7	7.1 ± 0.7	42%	21%	13%	14.0 ± 2.9	71%	PO
200 ± 2	9.6 ± 0.4	3.6 ± 0.2	71%	13%	7%	10.4 ± 2.9	78%	PO
250 ± 2	4.8 ± 0.1	1.8 ± 0.1	86%	7%	3%	13.3 ± 2.9	72%	PO

[1] PO: pull-out.

Table 4.5: Pull-out test results obtained in RBP-S bars (average ± standard deviation).

T [ºC]	Maximum pull-out load [kN]	Average bond strength [MPa]	Normalized bond strength reduction [-]	Ratio maximum axial stress/ tensile strength at elevated temperature	Ratio maximum axial stress/tensile strength at ambient temperature	Bond stiffness ($K_{\tau-s}$) (loaded end) [MPa/mm]	Normalized bond stiffness reduction [-]	Failure mode [(1)]
20 ± 2	52.9 ± 1.3	19.0 ± 0.4	-	42%	42%	48.2 ± 26.9	-	PO
60 ± 2	48.8 ± 5.9	17.6 ± 2.1	8%	40%	39%	33.6 ± 8.5	30%	PO
100 ± 2	42.1 ± 3.4	15.2 ± 1.2	20%	36%	34%	12.3 ± 1.1	74%	SPT
120 ± 2	22.8 ± 4.1	8.2 ± 1.4	57%	22%	18%	7.1 ± 0.7	85%	PO
140 ± 2	14.1 ± 1.8	5.1 ± 0.9	72%	16%	11%	8.5 ± 0.7	82%	PO
220 ± 2	6.0 ± 0.6	2.2 ± 0.2	89%	8%	5%	14.2 ± 2.5	70%	PO
300 ± 2	3.0 ± 0.4	1.1 ± 0.1	94%	4%	2%	5.0 ± 3.5	90%	PO

[(1)] PO: pull-out; SPT: splitting of concrete.

4.5.3.2. Bond stiffness

The variation of bond stiffness with increasing temperatures is shown in Figure 4.13. Despite the significant scatter of the results (also *cf.* Table 4.6 to Table 4.8), the stiffness measured in specimens with 12 mm (RB and RBP) and 10 mm (SC) diameter bars was rapidly degraded below their T_g. At 100 ºC, the reduction in stiffness was almost 80% (compared to that estimated at ambient temperature), although in the case of the ribbed bars, above 100 ºC, the stiffness decay with temperature progressed at a slower rate. It should be noted that the stiffness measured in RB-D12 specimens was greatly reduced below its T_g, contrarily to what had been observed regarding bond strength (*cf.* Figure 4.12b). It can also be seen that the bond stiffness decay was markedly less steep in specimens with a smaller diameter bar (RB-D8): the large extent of the decay occurred between 200 ºC and 300 ºC, *i.e.* well above the T_g. The reason for these differences was not clearly identified, namely between RB-D8 and RB-D12 bars – it is likely that they result from the different profile of their ribs – as shown in Figure 3.1, the ribs of bar RB-D8 are considerably wider compared to those of bar RB-D12.

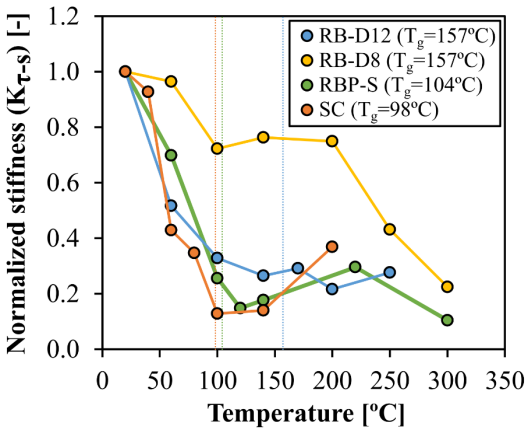

Figure 4.13. Normalized bond stiffness of ribbed and sand coated bars as a function of temperature (T_g of the bars marked as vertical lines).

Figure 4.14 compares the variation with temperature of (i) the normalized bond strength and stiffness obtained in the pull-out tests with (ii) the tensile properties (strength and modulus) and (iii) storage modulus (from DMA) of the corresponding ribbed bars. As expected, the results show that the bond properties (both stiffness and strength) are more affected by elevated temperatures than the tensile properties. Overall, the degradation of the bond strength with temperature followed a similar trend to that of the storage modulus, though in the former property such degradation occurred for lower temperatures and in a steeper way.

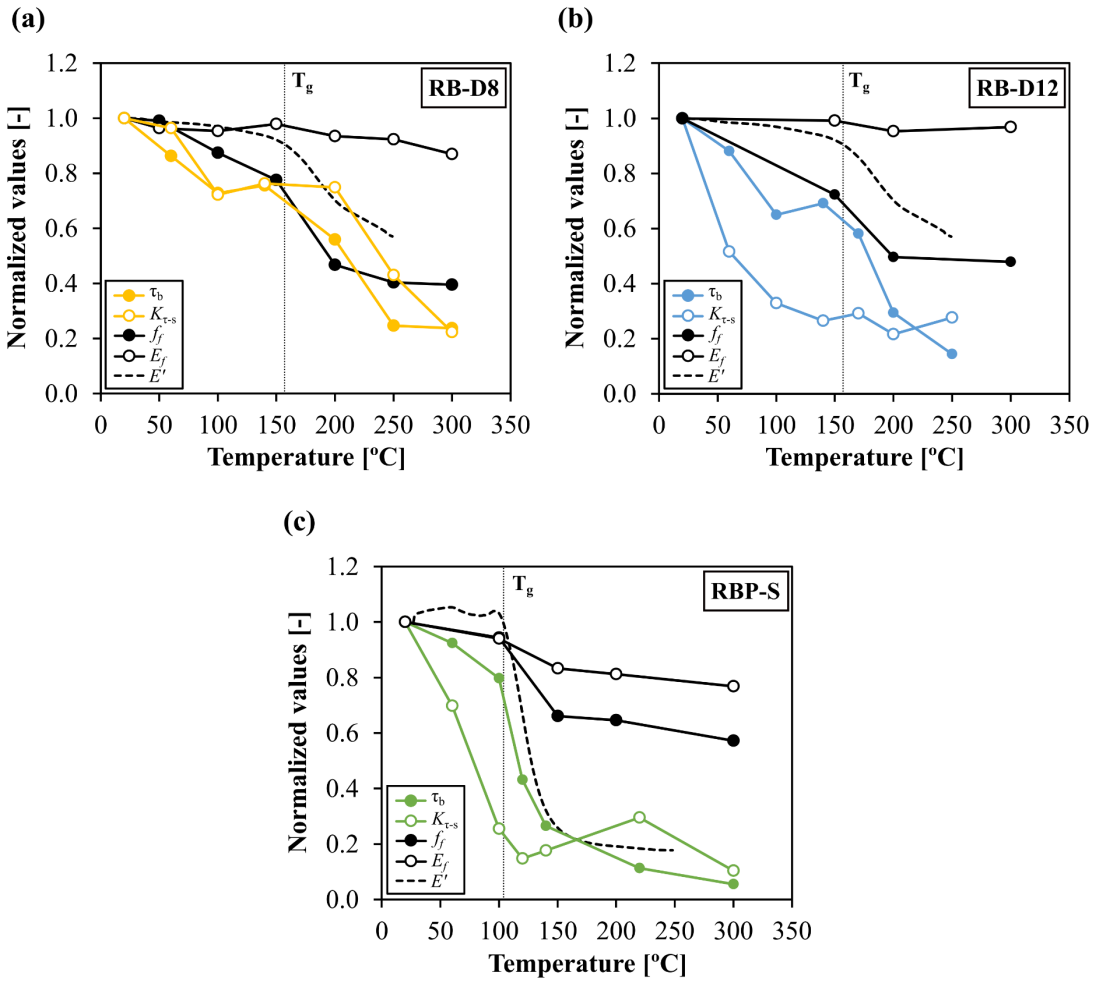

Figure 4.14. Normalized values of the average bond strength (τ_b), bond stiffness ($K_{\tau\text{-}s}$), tensile strength (f_f), tensile modulus (E_f) and storage modulus (E') of the GFRP bars as a function of temperature – results from specimens with bars (a) RB-D8, (b) RB-D12 and (c) RBP-S.

4.6. Results and discussion of pull-out tests on 90º bent bars

4.6.1. Load *vs.* slip curves

Figure 4.15a plots representative load *vs.* slip curves obtained for each target temperature, in which the slip corresponds to the relative displacement between the loaded end of the bar and concrete, after subtracting the corresponding elastic deformation of the bars. More than one curve is presented at 60 ºC due to the relatively high scatter of initial stiffness obtained at that temperature.

For relatively low slip values (*i.e.*, in the ascending branch), the curves exhibit an approximately linear behaviour, governed by the chemical bond and mechanical interlock of the ribs in the surrounding concrete. For temperatures up to T_g, the attainment of the maximum load was marked by the fracture of the concrete corbels between the bars' ribs, after which the bond stress began to decrease with increasing

slip while the corbels were sheared off. The post-peak stage was in this case governed by the friction between the bar (*i.e.*, the ribs and the crushed concrete between the ribs) and the surrounding concrete. For temperatures equal to or above T_g, the post-peak stage was governed by the friction between the core of the bar and the surrounding concrete and sheared ribs. Regardless of the temperature, a residual bond stress was attained for high values of slip, deriving from the residual friction between the materials described above. It should be pointed out that in the particular case of specimens tested at 220 ºC and 300 ºC, plotted in detail in Figure 4.15b, the maximum load was not attained following the initial linear stage (first peak) but rather in a second peak, after a small reduction in load and stiffness. This behaviour, observed in all specimens tested at these temperatures, may be related to the local failure (fracture and shearing off) of the ribs taking place consecutively in opposite sides of the bar in the bent zone. Further insights about this hypothesis are provided in Section 5.3, based on the numerical simulations of the tests.

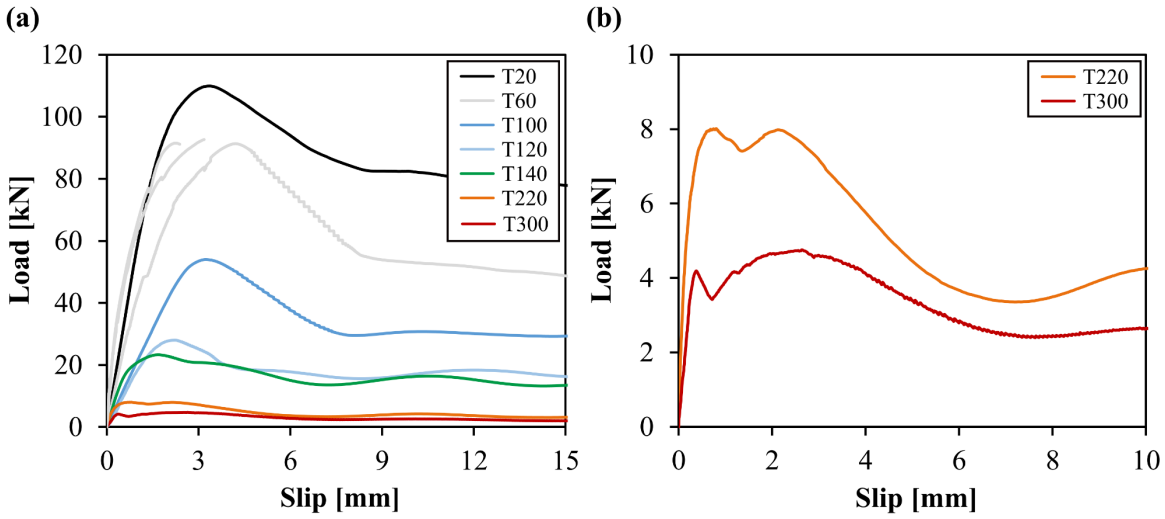

Figure 4.15. Representative load *vs*. slip (at the loaded end) curves obtained in pull-out tests of 90º bent (RBP-B) bars: (a) all tested temperatures; (b) 220 ºC and 300 ºC.

4.6.2. Failure modes and post-pull-out observations

The following subsections present and discuss the results of pull-out tests performed in 90º bent bars (RBP-B series). The failure modes obtained at each temperature are listed at the end of the subsection in Table 4.9.

At 20 ºC, different failure modes were obtained, each corresponding to a different type of damage at the GFRP-concrete interface (Table B.6 from Appendix B). Two of the specimens failed due to tensile rupture of the fibre rovings, therefore no damage at the surface of the bars was observed. In two other specimens, failed occurred due to splitting or spalling of concrete above the bend, although the concrete cylinders were confined with steel clamps; in these cases, as explained below, significant damage was

observed at the GFRP-concrete interface. Note that the load *vs.* slip curve presented in Figure 4.15a for 20 ºC refers to a specimen that failed by concrete spalling above the bend. It is worth referring that the maximum loads obtained in the above-mentioned specimens were fairly similar regardless of the failure mode, which means that the load capacity corresponding to those failure modes should be similar.

At elevated temperatures, apart from one specimen tested at 60 ºC (which also failed due to concrete spalling above the bend), pull-out failure occurred, as intended. It should also be referred that after the tests most of the cylinders presented superficial cracks (mild in specimens tested at elevated temperatures) that propagated from the extremity of the tail length, likely due to the lower cover provided in that zone.

After each test, the cylinders were saw cut above the bend and then sectioned in half along their revolution axis, as depicted in Figure 4.16. Similarly to specimens with straight bars (RBP-S series, *cf.* Section 4.5.2), the failure interface changed when the test temperature increased above the T_g. As shown in Figure 4.16a, in specimens tested at 20 ºC (with failure due to splitting or spalling of concrete above the bend) the bars slipped along the rib-concrete interface: the concrete corbels between the ribs were fractured and sheared off from the surrounding concrete, while the top surface of the ribs was only slightly abraded. A different behaviour was observed above the T_g since, due to the softening of the resin, the ribs lost their adhesion to the core of the bar and, consequently, the core slipped while the ribs remained adherent to the concrete in most of the embedment length (Figure 4.16b). At 220 ºC and 300 ºC the damage was even more severe: a significant amount of ribs were broken and sheared from the bar, and in the case of bars tested at 300 ºC (Figure 4.16c) some of the fibres located at the surface of the core were also broken and without any residue of resin due to its thermal decomposition.

Figure 4.16. Surface of RBP-B bars after being tested at: (a) 20 ºC, (b) 100 ºC-220 ºC; (c) 300 ºC.

Table 4.6. Pull-out test results obtained in bent (RBP-B) bars (average ± standard deviation).

T [ºC]	Maximum pull-out load [kN]	Normalized maximum pull-out load reduction [-]	Ratio maximum axial stress/ tensile strength at elevated temperature (1)	Bond stiffness ($K_{F\text{-}s}$) [kN/mm]	Normalized bond stiffness reduction [-]	Failure mode (2)	Ratio maximum pull-out load of bent/straight bars
20 ± 2	99.8 ± 7.2	-	79%	57.3 ± 2.1	-	T/T/SPL/SPT	1.89
60 ± 2	91.9 ± 0.7	8%	75%	55.0 ± 15.9	4%	PO/PO/SPL	1.88
100 ± 2	54.2 ± 8.0	46%	46%	20.5 ± 4.3	64%	PO	1.29
120 ± 2	29.9 ± 1.6	70%	29%	21.8 ± 7.2	62%	PO	1.31
140 ± 2	24.7 ± 0.6	75%	27%	33.0 ± 14.7	42%	PO	1.76
220 ± 2	9.1 ± 0.6	91%	12%	34.9 ± 19.0	39%	PO	1.52
300 ± 2	4.9 ± 0.4	95%	7%	13.7 ± 1.9	76%	PO	1.66

(1) Reference to the tensile strength in the straight zone of the bar.

(2) T: tensile rupture of the bar; SPL: spalling of the concrete cover above the bend; SPT: splitting of concrete; PO: pull-out.

4.6.3. Maximum pull-out load and stiffness

Figure 4.17 plots the maximum pull-out load obtained in the 90º bent RBP bars ($L_b \approx 12D$) as a function of temperature, in absolute (Figure 4.17a) and normalized values (Figure 4.17b), the latter with reference to the values obtained at 20 ºC; data obtained in Section 4.5 for straight RBP bars ($L_b = 5D$) are also plotted as reference (note that the total embedment lengths of bent and straight bars are different). The main results obtained in these experiments are summarized in Table 4.9 and those of individual specimens are listed in Table B.6 from Appendix B.

The results show that the hook effect provided in the bend and tail sections of the bars provided a considerable improvement of the bond strength compared to straight bars in the entire range of temperatures tested – adding a bend after the straight embedment length resulted in an increase in the maximum pull-out load between ~30% (at 100-120 ºC) and ~90% (at 20-60 ºC). As depicted in Figure 4.17b, overall the normalized decrease in bond strength was similar in both types of bars, especially in the vicinity of the T_g where it was particularly severe, being also in line with the reduction of storage modulus obtained from DMA. In relation to the results obtained at 20 ºC, the maximum load of the bent bars was reduced by 75% at 140 ºC (73% in straight bars) and by 95% at 300 ºC (94% in straight bars). Yet, close to the T_g (100 ºC and 120 ºC) the bond strength of the bent bars was more significantly reduced than that of straight bars. This suggests that in the early stages of the glass transition process, the effects of resin softening in bond degradation are more severe in bent bars than in straight bars, likely due to the local weakness of the ribs in the curved section and local stress peaks developing in that region; further insights on this matter are provided in Section 5.3.

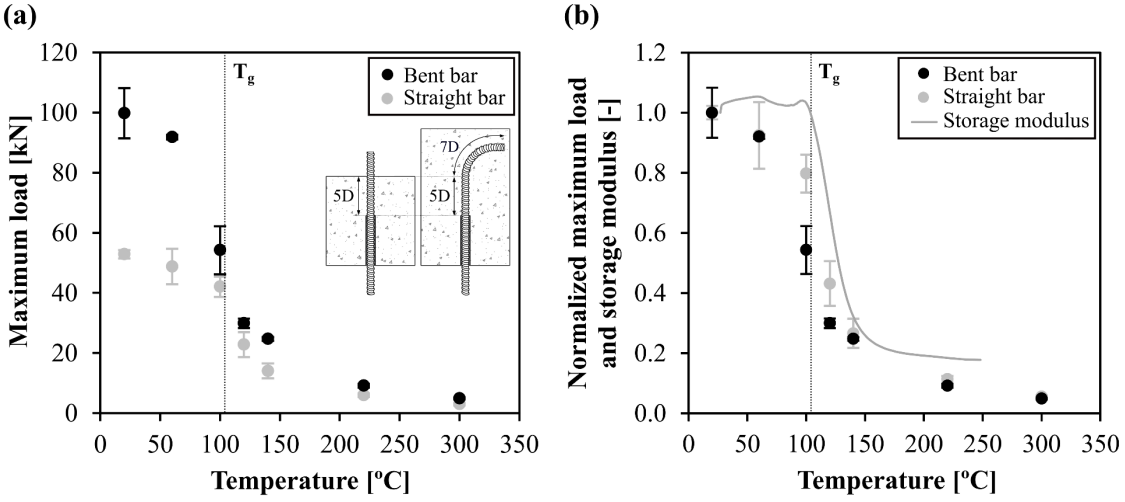

Figure 4.17. Maximum pull-out load of straight (RBP-S) bars ($L_b = 5D$) and 90º bent (RBP-B) bars ($L_b \approx 12D$) as a function of temperature in: (a) absolute and (b) normalized values (including storage modulus obtained from DMA).

As previously shown in Figure 4.15, the initial bond stiffness (*i.e.* the slope of the ascending branch of the load *vs*. slip curves) was also gradually reduced with increasing temperatures. The results summarized in Table 4.9 indicate that the degradation of stiffness was steeper when approaching the T_g, reducing by 64% at 100 ºC in bent bars (74% in the straight bars). However, unlike the maximum load, the decay in stiffness was not steady up to 300 ºC, slightly increasing between 100 ºC and 220 ºC, and decreasing again thereafter. This non-monotonic variation with temperature may be partially explained by a relevant increase in normal stresses between the core of the bars and the surrounding materials (concrete and sheared ribs), as a consequence of the transverse expansion of the bars, which, in turn, outweighed the thermal degradation of the materials for such temperature range. The high scatter of data concerning the bond stiffness may be due to the intrinsic variability of the complex phenomena governing the bond behaviour of bent bars described above, especially the non-uniform damage at the bar-concrete interface (and at the ribs-core interface) along the bent length. Further discussion about this phenomenon is also presented in Section 5.3.

4.7. Comparison with bond test results from the literature

Figure 4.18 presents a comparison of the normalized bond strength obtained in the present study with the test data reported in previous studies from the literature ([15,19,122,124,126,128]), reviewed in Chapter 2. In this comparative analysis, only GFRP bars were considered; data available on BFRP bars [129] and CFRP bars [19,136,137] were not included. The studies considered in the figure comprised pull-out tests in GFRP bars from different manufacturers, thereby with different geometries (*i.e.*, diameters), surface finishes (including sand coated, ribbed and rough surfaces) and thermophysical properties. The T_g of the bars varied between 60 ºC and 164 ºC, though obtained through different test methods (DMA or DSC) (*cf.* Figure 4.18). The majority of the results were obtained from pull-out tests with similar test procedures to that adopted in the present study: the loading stage took place while the specimens were at a constant (elevated) target temperature, which was maintained during a short period of time. The studies of Mousavi *et al.* [122] and Hajiloo and Green [126] provide results from tests carried out in transient state conditions, which were also included in these analyses (similar reduction of bond strength with temperature were obtained in these studies in the tests performed in steady state and transient state regimes). The embedment lengths of the bars in the concrete specimens were 4*D* in [19,107], 5*D* in [15,124,128] and 22*D* in [122]. It is worth noting that in the following studies ([124,126,128]) pull-out failure modes occurred at all tested temperatures. Conversely, the remaining studies ([15,19,122]) report failures modes by both pull-out of the bars and splitting of the concrete; therefore, these data (identified with different bullets in Figure 4.18) represent a lower bound of the actual bond strength of the bars.

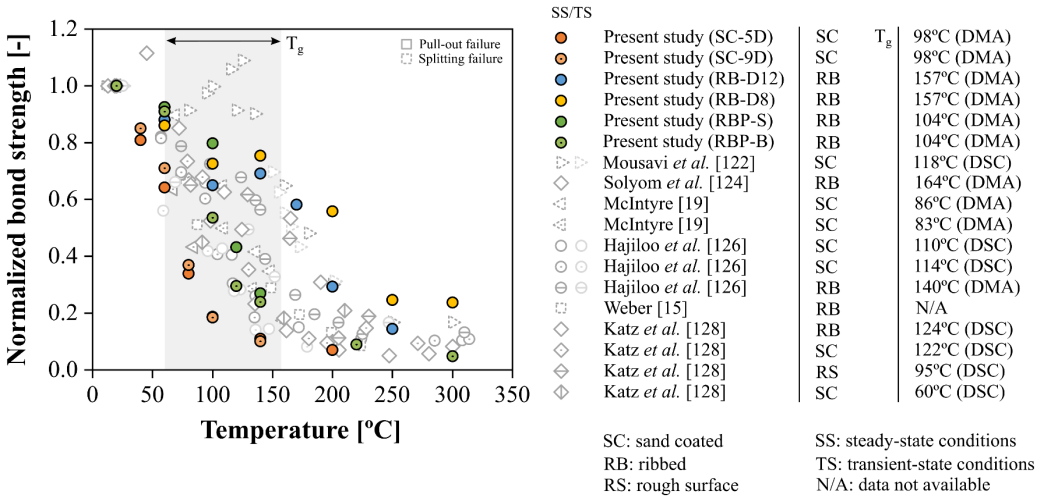

Figure 4.18. Comparison of normalized bond strength as a function of temperature: results obtained in the present study and those from [15,19,122,124,126,128].

Figure 4.18 shows that the effects of elevated temperatures in the bond strength can differ greatly from manufacturer to manufacturer, especially in the temperature range from 60 ºC to 200 ºC. For temperatures above 200 ºC (well above T_g), minor additional bond strength reductions take place; for those temperatures, the bars are able to retain a small level of bond capacity (overall, below 20% of that at ambient temperature). Despite the significant differences in the bond behaviour of FRP bars found within each manufacturer (*e.g.* different bond strengths and failure modes), the results confirm that the bond properties of bars exposed to elevated temperatures are highly influenced by the type of surface finish, as well as their T_g. Overall, the test data show that the bond to concrete of GFRP bars with sand coating is usually more susceptible to the effects of elevated temperatures – in fact, most of the bond strength is lost below the T_g – while in ribbed bars the bond strength degradation is more severe after the beginning of the glass transition process; these conclusions are consistent with those obtained in the present study. It should also be mentioned that the bars tested in Solyom *et al.* [124] (Φ8 mm) and one of the bars tested by Hajiloo and Green [126] (Φ16 mm) were provided by the same manufacturer as the ribbed RB bars tested in Section 4.5; accordingly, similar reductions of bond strength with temperature were observed in these studies.

4.8. Bond strength degradation models

In this subsection, the ability of the empirical models proposed by Gibson *et al.* [22] and Correia *et al.* [23] to simulate the variation of the average bond strength of GFRP bars with temperature was assessed. These relaxation models involve curve fitting procedures to the experimental data (here considered as the results of the individual bar specimens obtained in this study) and have been successfully used to simulate the mechanical properties of FRP materials at elevated temperatures [23]. The analytical study

was conducted separately in bars with sand coating (SC) and ribs (RB-D12, RB-D8 and RBP-S), as it was demonstrated in previous sections that the degradation of bond strength with temperature of the former bars is more severe (especially near the T_g) than that of the latter.

According to Gibson *et al.* [22], the variation of a generic mechanical property (P) with temperature (T) can be defined by the following equation,

$$P(T) = P_u - \frac{P_u - P_r}{2} \times (1 + \tanh[k'(T - T_{g,mech})]) \tag{4.1}$$

where P_u is the value of the property at ambient temperature and P_r is the value of the property after the glass transition (but before decomposition). The parameters k' and $T_{g,mech}$ are obtained by fitting the theoretical curve to the experimental data.

Correia *et al.* [23] proposed the following model, which is based on the Gompertz statistical distribution, where the parameters B and C are fitted to the experimental data,

$$P(T) = P_r + (P_u - P_r) \times (1 - e^{Be^{C \times T}}) \tag{4.2}$$

In both models, the theoretical curves (*i.e.* the defining parameters) were obtained using a standard procedure that minimizes the mean square error to the experimental results.

Figure 4.19 plots the fitting curves for both models, together with the normalized experimental values of (normalized) average bond strength. Figure 4.19a refers to the analytical study conducted on the sand coated bars (including the two embedment lengths tested) and Figure 4.19b refers to the study performed on straight ribbed bars tested in this study.

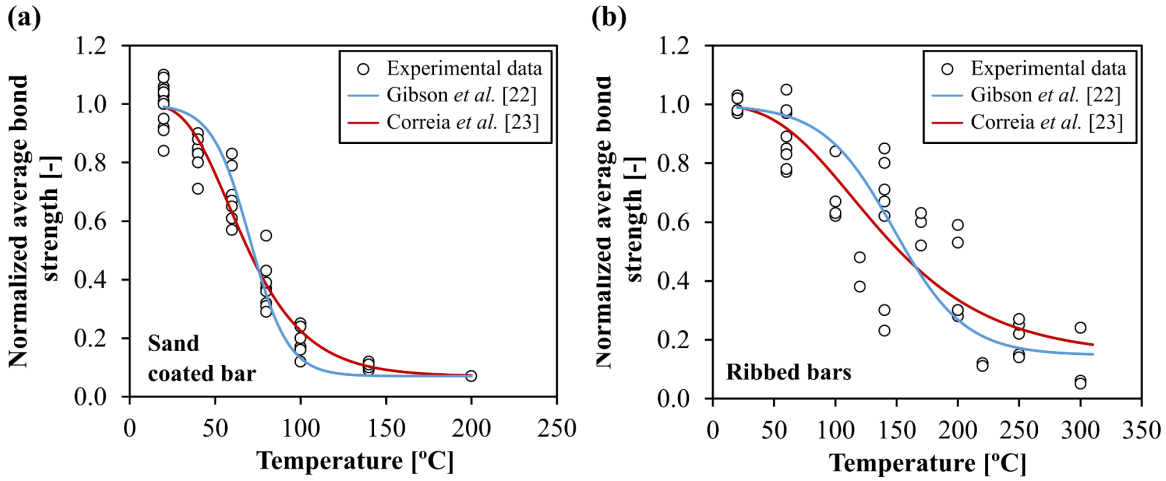

Figure 4.19. Normalized average bond strength (compared to ambient temperature) *vs.* temperature: experimental results and modelling curves of (a) sand coated and (b) ribbed GFRP bars.

Table 4.10 lists the values of the parameters obtained for the two models assessed and the two types of bar surface finishes, as well as the respective mean absolute percentage error (MAPE). It can be seen that both models present a very good agreement with the experimental results, as they are able to provide accurate estimates of the average GFRP-concrete bond strength reduction with temperature. In the case of the sand coated bars (Figure 4.19), the model of Correia *et al.* [23] provides slightly more accurate predictions of the average reduction of bond strength with temperature, as attested by the lower value of MAPE. Regarding the ribbed bars (Figure 4.19), although the model of Correia *et al.* [23] presents slightly higher MAPE than that of Gibson *et al*. [22], the former is able to capture more accurately the average reduction of bond strength between 60 ºC and 200 ºC.

Table 4.10. Simulation of the bond strength degradation of sand coated and ribbed bars with temperature – defining parameters and absolute mean percentage error (MAPE).

Model	Parameter	Sand coated bar	Ribbed bars
Gibson *et al*. [22]	k' [-]	0.045	0.017
	$T_{g,mech}$ [ºC]	70.46	147.84
	MAPE [%]	16.0	36.3
Correia *et al.* [23]	B [-]	-10.10	-6.12
	C [-]	-0.0401	-0.0160
	MAPE (%)	12.2	39.2
P_u		1.00	1.00
P_r		0.07	0.15

4.9. Concluding remarks

This chapter presented experimental and analytical studies on the bond behaviour between GFRP bars and concrete from ambient temperature up to 300 ºC, aiming to investigate the influence of several parameters on the degradation of the bond strength and stiffness under moderately elevated temperatures. The experimental campaign comprised pull-out tests performed under steady-state conditions on different types of bars embedded in concrete cylinders.

The first part of the study (Section 4.4) examined the bond of fibre-wrapped sand coated bars with two different embedment lengths in concrete. As expected, the strength and stiffness of the GFRP-concrete interface were significantly affected with increasing temperatures. The average bond strength was severely reduced for temperatures well below the T_g of the bars (98 ºC), presenting reductions of 29% and 89% at respectively 60 ºC and 140 ºC, compared to the average bond strength at ambient

temperature. The bond stiffness (measured at the loaded end) experienced reductions of 44% and 80% at 60 ºC and 100 ºC, respectively, comparing to the stiffness at ambient temperature. For the materials, test setup and procedure, and range of temperatures tested herein, similar bond strength reductions with temperature were obtained for embedment lengths of 5 and 9 times the diameter of the bars. Visual observations of the specimens after the tests showed that the bond behaviour of this type of bars, at both ambient and elevated temperatures, is mainly influenced by the adhesion (and friction) between the superficial finish and the bars' core.

The second part of the study (Section 4.5) aimed at assessing the effects of elevated temperatures on the bond between concrete and different types of ribbed GFRP bars comprising different diameters and rib geometries; the results were then compared to those formerly obtained in sand coated bars in specimens with the same embedment length in concrete (5*D*). The study demonstrated that the T_g and the type of surface finish are the dominant characteristics governing the bond behaviour of GFRP bars in concrete at elevated temperatures. Most of the bond strength of the ribbed bars was degraded above the bars' T_g, whereas in fibre wrapped-sand coated bars the bond was almost entirely lost below T_g. These results stem from differences in the bar surfaces and, consequently, from differences in the failure mechanisms occurring at the GFRP-concrete interface. The maximum bond strength reduction obtained in the ribbed bars at 100 °C (T_g of 104 ºC and 157 ºC) was 34% compared to the strength presented at ambient temperature, while for sand coated bars (T_g of 98 ºC) such reduction was considerably higher, around 80%. Nevertheless, the average bond strength reduction at temperatures above 250 ºC was similar in all bars (around 80% and 90%).

The influence of the bar diameter could not be precisely evaluated in these experiments because the geometry of the rib profiles of the GFRP bars was not comparable; the results obtained showed that the overall bond strength reduction with temperature was reasonably similar for ribbed bars with 8 and 12 mm in diameter (slightly more pronounced in the bars with larger diameter).

The last part of the experimental study (Section 4.6) aimed at comparing the bond behaviour of straight and 90º bent GFRP bars at elevated temperature. The main goal was to assess the increase in anchorage strength with the adoption of a hook after the straight zone of the bar. To that end, both types of specimens comprised the same straight embedment length (5*D*), yet in the case of bent bars, the 90º bend and the tail also contributed to the resistance against slip (totalling an embedded length of approximately 12*D*). Although the bond strength of straight and bent bars was found to be severely reduced for temperatures close to the T_g in a similar manner (at 140 ºC, bond strength reductions of around 73%-75% were obtained), the adoption of bent extremities allowed to significantly improve the anchorage strength (between 30% and 90%) with respect to straight bars, at both ambient and elevated temperatures. Accordingly, as shown in Chapter 6, the potential of using bent reinforcement to improve the anchoring conditions in concrete was demonstrated at a larger scale in the fire resistance tests carried out in RC slab strips with bent-end tension lap splices exposed to heat.

The final part of the chapter presented analytical investigations, which involved the assessment of empirical models, namely those proposed by Gibson *et al*. [22] and Correia *et al*. [23] to describe the GFRP-concrete average bond strength reduction with temperature of sand coated and ribbed bars. Both models were quite successful, with the model of Correia *et al*. [23] providing slightly more accurate predictions of the overall degradation of bond strength with the temperature increase.

Chapter 5

Numerical modelling of the bond behaviour of GFRP bars in concrete at elevated temperature

5.1. Introduction and objectives

The limited knowledge about the effects of elevated temperatures on the bond behaviour of FRP bars in concrete is currently reflected on the limited test data available but also on the lack of comprehensive numerical studies. Accordingly, standardized temperature-dependent bond stress *vs.* slip laws are not yet available for FRP reinforcement, despite being needed to accurately simulate the behaviour of FRP-RC members at elevated temperature and under fire exposure. Consequently, very few numerical studies ([30,142,143,168]) have explicitly modelled the bond interaction between straight FRP bars and concrete as a function of temperature and, in the case of bent FRP reinforcement, no numerical investigations have yet been carried out.

Until recently, the only temperature-dependent laws for straight FRP bars found in the literature were proposed in [120,124,127,130,132,135]. However, the majority of them only described the pre-peak bond stress *vs.* slip response [124,127,130,132], some were obtained based on the residual behaviour of the FRP-concrete specimens after exposure to moderately elevated temperatures (and subsequent cooling to ambient temperature) [130,132] and in [135] they refer to the long-term exposure to elevated temperatures. Furthermore, these laws were obtained based on curve fitting procedures to the experimentally obtained average bond stress *vs.* slip curves, thus assuming a uniform stress distribution along the embedment length of the bars. This however is not an accurate assumption, as the shear stresses along the bar-concrete interface decrease from the loaded end towards the free end of the bar.

The studies presented in this chapter aim to fulfil the aforementioned gaps in knowledge by numerically investigating the bond behaviour at elevated temperature of straight and 90º bent GFRP bars. In the first part of the chapter (Section 5.2), temperature-dependent local bond stress *vs.* slip relationships were numerically calibrated for each of the straight bars tested in this thesis, including the sand coated bar and the three types of ribbed bars with different rib geometries and core diameters. In the following section (Section 5.3), 3D solid FE models were developed using the commercial package *ABAQUS Standard* [198] to simulate the pull-out tests carried out on the straight and 90º bent bars, previously described in Chapter 4. The bond laws calibrated for straight bars were implemented in the 3D FE

models to describe the GFRP-concrete bond interaction along the straight development of the bars, while in the bent development local bond laws were separately calibrated based on an inverse analysis. In the last part of the study, described in Section 5.4, the validated models were used to conduct design-oriented parametric studies to assess the influence of elevated temperatures on the anchorage strength of straight bars with different surface finishes and of 90º bent bars with varying tail and development lengths. From the parametric analysis carried out, optimal anchorage lengths were proposed as a function of temperature for beam and slab applications.

5.2. Numerical calibration of temperature-dependent bond laws

5.2.1. Methodology

A numerical methodology originally developed by Sena-Cruz and Barros [199] and later upgraded by Azevedo *et al.* [200] was used in this thesis to model the complete behaviour (*i.e.* the pre- and post-peak bond stress *vs.* slip response) of the fibre-wrapped sand coated bars up to 200 ºC, as well as of the ribbed bars up to 300 ºC, considering a reference embedment length in concrete of 5*D*. In this numerical approach, the experimental results (*i.e.*, the load *vs.* slip results obtained from pull-out tests) are used to calibrate a set of parameters defining the analytical local bond stress *vs.* slip law for each temperature. In addition to the geometrical features of the bars (cross section and bonded length to concrete), the results obtained in terms of tensile modulus as a function of temperature (described in Section 3.4) are also used as input data to calibrate the analytical laws.

The computational code developed in [199,200] was used to solve the differential Equation (5.1) that governs the slip of the bar along the embedment length to the concrete,

$$\frac{d^2 s}{dx^2} = \frac{4}{d_b E_f}\tau(s) \tag{5.1}$$

where s is the slip, x is the position along the embedment length, $\tau(s)$ is the bond stress for a given slip value, d_b is the diameter and E_f is the tensile modulus of the bar. The analytical expression considered for the local bond law was proposed by Sena-Cruz [144] and is defined by the following equations,

$$\tau(s) = \begin{cases} \tau_m \left(\frac{s}{s_m}\right)^{\alpha} & if\ s \le s_m \quad (5.2a) \\ \tau_m \frac{1}{1 + \left(\frac{s - s_m}{s_1}\right)^{\alpha'}} & if\ s > s_m \quad (5.3b) \end{cases}$$

where τ_m and s_m are the bond strength and the corresponding slip, and α, α' and s_1 are the parameters defining the shape of the bond stress *vs.* slip curves. Equation (5.2a) defines the bond strength for the

pre-peak phase, following the model proposed by Eligehausen *et al.* [201], while Equation (5.3b) simulates the post-peak phase (slip softening stage), following the approach of Stang and Aarre [145]. This numerical method thus allowed considering a non-uniform distribution of the bond stress along the embedment length of the bars, which is a more accurate and realist approach compared to that considered in curve fitting procedures (which assume a uniform stress distribution). For each temperature and type of bar, the above-mentioned five parameters were calibrated following a numerical procedure that simultaneously minimized the relative differences (area) underneath the experimental and analytical load *vs.* slip curves (obtained for both the free and loaded ends of the bars), while also minimizing the differences between the experimental and analytical maximum load and corresponding slip, and (initial) bond stiffness.

The numerical methodology adopted herein was successfully used earlier to model the bond behaviour of near-surface mounted (NSM) CFRP strips and concrete [199]. However, in the present study and with respect to the sand coated bars, when using the tensile modulus of the bars obtained from the tensile tests, the resulting analytical load *vs.* slip curve (obtained for the slip at the loaded end) presented significantly higher stiffness (as defined by the slope of the initial linear branch) than that measured in the experiments. This deviation, exemplified in Figure 5.1a for a temperature of 20 ºC, was consistent for all test temperatures. However, in ribbed bars these relative differences were not observed: as shown ahead in Figure 5.4, the analytical load *vs.* slip curves reproduced quite accurately the experimental data at 20 ºC.

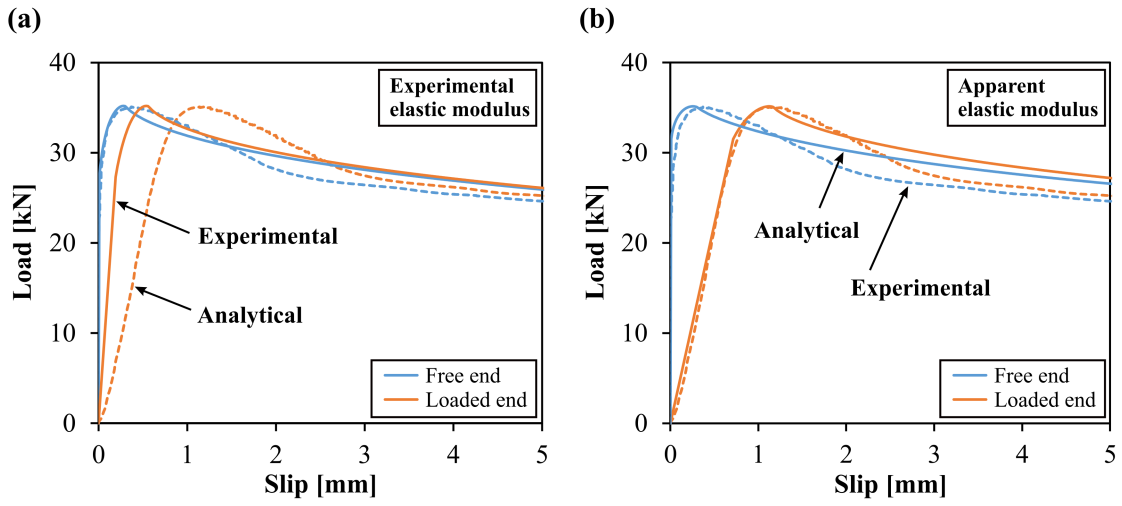

Figure 5.1. Comparison between experimental and analytical load *vs.* slip curves of SC bars at 20 ºC: modelling using (a) elastic modulus obtained from tensile tests and (b) apparent (calibrated) tensile modulus.

The author believes that these relative differences obtained for the sand coated bars (which did not occur for the ribbed bars) are related to the deformability of its constituent materials/layers; in fact, as shown in Section 4.4.2, in a few pull-out specimens it was quite clear that slippage occurred mainly between the core of the bars and its superficial sand coating. Therefore, this evidence suggested that the bars could be seen as a composite reinforcement, in which the deformability of the core and that of the superficial layer of sand and resin are different. The heterogeneity of the bars throughout its thickness was addressed (numerically) by calibrating, for each temperature, an apparent tensile modulus (as a percentage of the modulus experimentally obtained from tensile tests). This approach allowed for a significant accuracy increase regarding the stiffness of the analytical load *vs.* slip curves (slip measured at the loaded end), as exemplified in Figure 5.1b, also for a temperature of 20 ºC. The temperature-dependent calibrated values (used to obtain the analytical local bond stress *vs.* slip laws) of the apparent tensile modulus of the SC bars are listed in Table 5.1 (*cf.* next section).

Regarding the ribbed bars, as described in Section 4.5.2, once the T_g was reached, the softening of the resin caused the failure modes at the GFRP-concrete bond interface to change: below T_g failure occurred with shearing off of the concrete corbels, while above T_g failure occurred at the rib-core interface. In order to consider the increase in deformability of the surface of the ribbed bars during and after glass transition, a reduction factor was also applied to the tensile modulus values obtained from tensile tests at temperatures above T_g. The tensile modulus values of the ribbed bars used in the calibration of the corresponding bond stress *vs.* slip laws for each temperature tested are listed in Section 5.2.2.2, from Table 5.2 to Table 5.4. As shown in these tables, the relative difference between this calibrated tensile modulus to that experimentally obtained from tensile tests increase with temperature, simulating the progressively higher deterioration of the materials at the failure interface. As in the sand coated bars, this procedure also provided an improvement in the fit between the experimental and analytical load *vs*. slip curves of the ribbed bars, in particular regarding the bond stiffness.

5.2.2. Local bond stress *vs.* slip relationships

5.2.2.1. Bond stress *vs.* slip laws for sand coated bars

The parameters defining the calibrated local bond laws of SC bars, plotted in Figure 5.3, are listed in Table 5.1. The comparison between the experimental and analytical curves is shown in Figure 5.2a (for the slip at the free end) and in Figure 5.2b (for the slip at the loaded end), demonstrating the overall good performance of the numerical strategy adopted for deriving the bond stress *vs.* slip relationship in the context of modelling the GFRP-concrete interface. This is also attested by the low values of relative difference obtained (below 7%), indicating a very good fit of the analytical curves to the experimental data. As previously mentioned in Section 4.4.1, the behaviour of the specimens tested at 100 ºC was somehow different from the specimens tested at the other temperatures. For this reason, a better fit of

the experimental data could have been obtained by using a different analytical expression for the local bond law than the one chosen in this study (Equation (5.3b)); nevertheless, the results obtained herein were considered quite satisfactory.

Table 5.1. Parameters defining the calibrated local bond stress *vs.* slip relationship of SC bars (including tensile modulus of the bars considered in the modelling).

T [ºC]	Calibrated tensile modulus [GPa]	s_m [mm]	τ_m [MPa]	α [-]	α' [-]	s_1 [-]
20	14.5 (30%E_{exp})	0.32	23.70	0.15	0.59	20
40	12.0 (25%E_{exp})	0.35	21.80	0.25	0.44	20
60	11.7 (25%E_{exp})	0.61	15.00	0.50	0.59	24
80	11.0 (24%E_{exp})	0.69	7.90	0.45	0.45	120
100	4.4 (10%E_{exp})	0.75	3.90	0.50	2.00	70
140	2.2 (5%E_{exp})	0.40	2.91	0.50	0.20	110
200	9.1 (20%E_{exp})	0.09	1.90	0.45	0.50	2

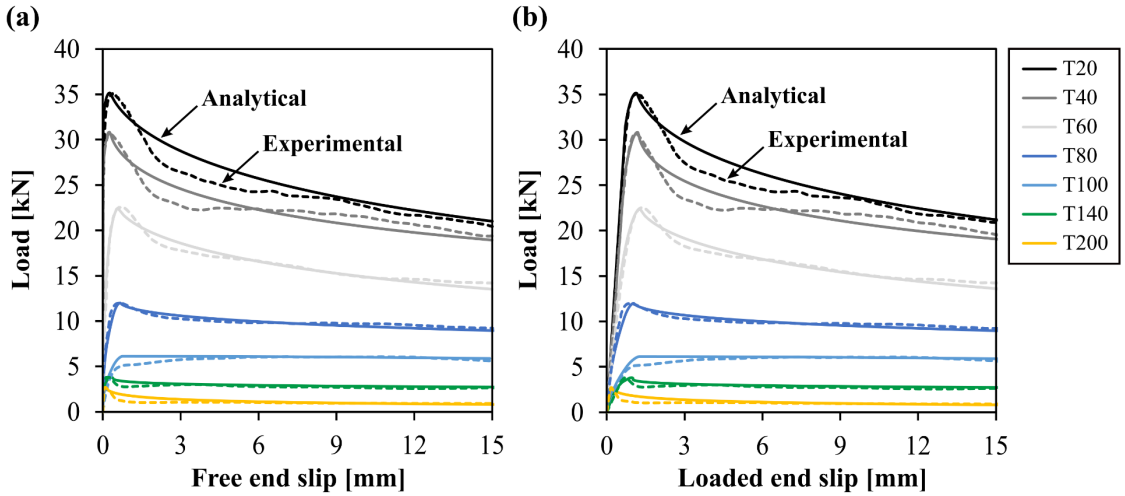

Figure 5.2. Comparison between analytical (continuous) and experimental (dashed) load *vs.* slip curves obtained at the (a) free and (b) loaded ends of SC bars.

The calibrated GFRP-concrete bond constitutive laws obtained for each of the tested temperatures are plotted in Figure 5.3. These curves prompt the following main remarks: (i) the maximum bond stress and stiffness are progressively reduced as temperature increases; (ii) for all temperatures, at relatively high slip values a significant bond stress is retained; (iii) up to 100 ºC, the slip corresponding to the bond strength (s_m) increases with temperature, while from 100 ºC to 200 ºC, such slip is significantly reduced (*cf.* Table 5.1). This non-monotonic variation of the slip corresponding to the maximum bond stress should be related to the thermo-physical changes undergone by the polymer during the glass transition process, whose viscosity presents a maximum during glass transition (note that the peak of the loss modulus curve occurs at 110 ºC, *cf.* Figure 3.2a – page 71), decreasing for lower and higher temperatures.

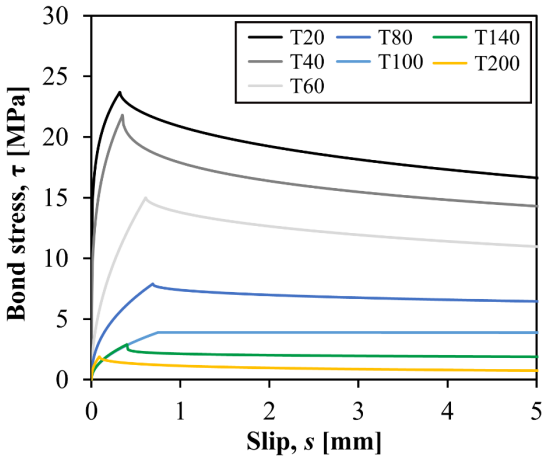

Figure 5.3. Local bond stress *vs.* slip laws calibrated for SC bars at different temperatures.

5.2.2.2. Bond stress *vs.* slip laws for ribbed bars

Figure 5.4 shows that the analytical load *vs.* slip curves for specimens RB-D8 followed closely the experimental responses measured at both free and loaded ends at all tested temperatures. Though the comparison is only presented (as an example) for the referred specimens, it is intended to illustrate the good adjustment of the analytical curves to the experimental data obtained in the three types of specimens with ribbed bars (RB-D8, RB-D12 and RBP-S) and for all temperatures. The numerical procedure adopted led to differences between experimental and analytical maximum loads (in average) below 1%, while the differences related to the slip at peak load were in average around 5%.

The local bond stress *vs.* slip laws calibrated for each of the tested temperatures are plotted in Figure 5.5 and the defining parameters are presented from Table 5.2 to Table 5.4. Figure 5.5a and Figure 5.5b compare the effects on the local bond response of respectively the surface finish and the diameter of the bars. The laws reflect the progressive reduction in the maximum bond stress and stiffness with temperature increase, as well as the considerable level of bond stress retention for high slip values. As

expected, the variation in parameter τ_m follows closely the decay of the bond strength with temperature presented in Figure 4.12b. The corresponding slip (parameter s_m) increased with temperature up to the bars' T_g, decreasing significantly above that temperature; in the case of specimens RB-D8, this parameter does not vary significantly up to T_g. Overall, parameter α increases with temperature, although not linearly. Regarding the post-peak response, parameter α' gradually reduces with temperature, while parameter s_1 presents an overall increasing trend with temperature (in the case of specimens with RBP bars, this parameter increased up to T_g, but decreased thereafter).

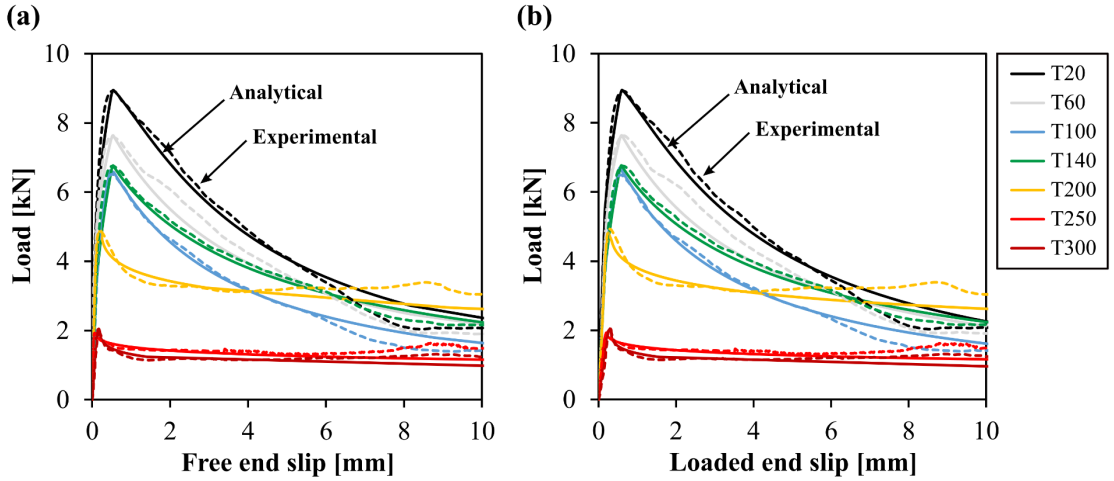

Figure 5.4. Comparison between analytical (continuous) and experimental (dashed) load *vs.* slip curves obtained for specimens with RB-D8 bars and reporting to the (a) free and (b) loaded end slip.

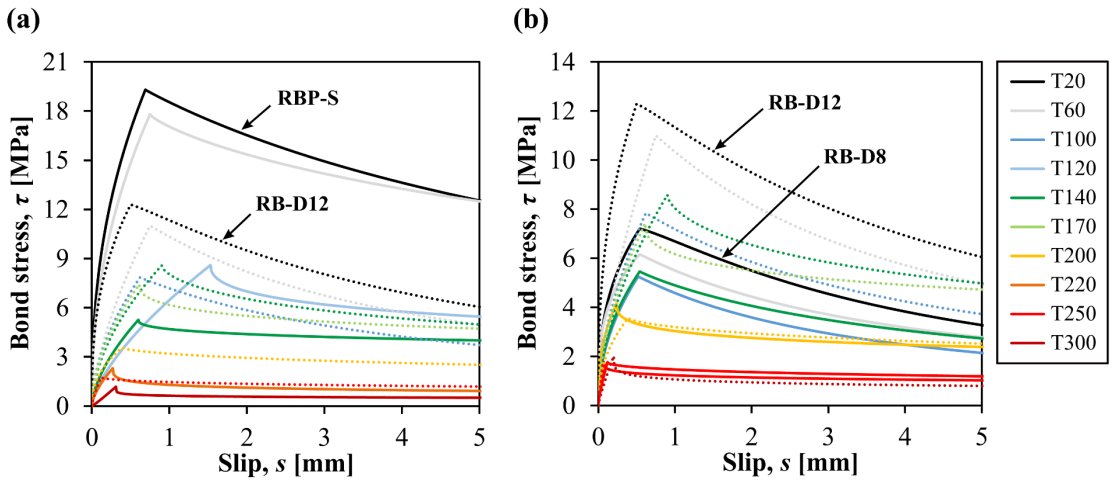

Figure 5.5. Local bond stress *vs.* slip laws of ribbed bars calibrated for different temperatures – comparison of the effect of bar: (a) surface finish (bars RB-D12 and RBP-S) and (b) diameter (bars RB-D12 and RB-D8).

Table 5.2. Parameters defining the calibrated local bond stress *vs.* slip laws of RB-D8 bars (including the tensile modulus of the bars considered in the modelling).

T [ºC]	Calibrated tensile modulus [GPa]	s_m [mm]	τ_m [MPa]	α [-]	α' [-]	s_1 [-]
20	57.6 (100% E_{exp})	0.54	7.20	0.36	1.21	3.8
60	55.3 (100% E_{exp})	0.54	6.16	0.30	1.02	3.7
100	54.9 (100% E_{exp})	0.52	5.25	0.48	1.03	3.1
140	56.1 (100% E_{exp})	0.54	5.46	0.46	0.95	4.5
200	27.0 (50% E_{exp})	0.24	4.15	0.37	0.38	10.5
250	6.4 (12% E_{exp})	0.07	1.77	0.90	0.30	14.1
300	6.8 (15% E_{exp})	0.20	2.00	0.85	0.30	1.2

Table 5.3. Parameters defining the calibrated local bond stress *vs.* slip laws of RB-D12 bars (including the tensile modulus of the bars considered in the modelling).

T [ºC]	Calibrated tensile modulus [GPa]	s_m [mm]	τ_m [MPa]	α [-]	α' [-]	s_1 [-]
20	60.0 (100% E_{exp})	0.50	12.29	0.38	1.14	4.4
60	59.9 (100% E_{exp})	0.75	11.00	0.64	1.04	3.5
100	59.7 (100% E_{exp})	0.62	7.84	0.55	1.02	4.0
140	59.6 (100% E_{exp})	0.90	8.58	0.55	0.64	6.8
170	34.8 (60% E_{exp})	0.61	7.41	0.55	0.43	16.3
200	19.8 (35% E_{exp})	0.39	3.57	0.44	0.63	18.5
250	18.6 (35% E_{exp})	0.12	1.76	0.76	0.51	20.5

Table 5.4. Parameters defining the calibrated local bond stress *vs.* slip laws of RBP-S bars (including the tensile modulus of the bars considered in the modelling).

T [ºC]	Calibrated tensile modulus [GPa]	s_m [mm]	τ_m [MPa]	α [-]	α' [-]	s_1 [-]
20	60.1 (100% E_{exp})	0.69	19.30	0.42	0.98	8.1
60	58.3 (100% E_{exp})	0.75	17.80	0.45	0.80	12.4
120	43.1 (80% E_{exp})	1.53	8.60	0.67	0.46	11.5
140	25.7 (50% E_{exp})	0.60	5.26	0.61	0.40	80.0
220	24.2 (50% E_{exp})	0.27	2.30	0.63	0.35	1.5
300	6.9 (15% E_{exp})	0.31	1.18	1.10	0.22	1.3

5.3. Numerical simulation of the pull-out tests at elevated temperature

5.3.1. Objectives

The numerical simulations presented in this section aimed to validate the implementation in FE models of the proposed local bond stress *vs.* slip laws (calibrated for straight bars) to describe the complex interaction between GFRP reinforcement and concrete at elevated temperature. To that end, 3D solid FE models were developed using *ABAQUS Standard* [198] to simulate the steady-state pull-out tests carried out in 90º bent bars (bars RBP-B) and in three straight bars with distinctive surface finishes (bars SC, RB-D12 and RBP-S), formerly presented in Chapter 4. The following subsections present a detailed description of the numerical models, including the rationale behind the calibration of bond stress *vs.* slip laws for the bent length of RBP-B bars based on an inverse analysis; finally, in Section 5.3.3, the numerical and experimental load *vs.* slip responses are compared and the main differences in the bond behaviour of straight and bent bars in concrete at elevated temperature are discussed.

5.3.2. Description of the numerical models

5.3.2.1. Geometry, type of elements and mesh

The geometry and mesh of the FE models comprising straight and bent bars are shown in Figure 5.6a and Figure 5.6b, respectively; the dimensions of the parts (concrete and GFRP bar) were defined according to the dimensions of the tested pull-out specimens specified in Figure 4.1 – page 101. To reduce computational costs, due to symmetry conditions, only one quarter and one half of the specimens

with straight and bent bars was modelled, respectively; to that end, appropriate boundary conditions were defined as described in Section 5.3.2.4.

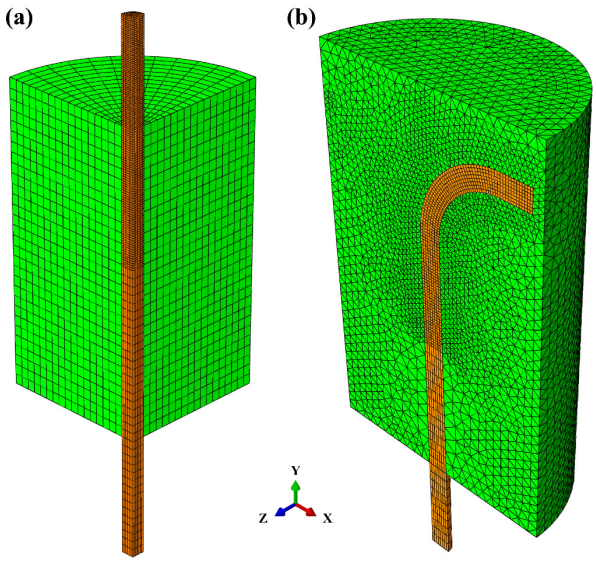

Figure 5.6. Geometry and mesh of 3D FE models with: (a) straight and (b) bent bars.

The GFRP bars were modelled using 8-node linear brick elements with reduced integration and hourglass control (type C3D8R), while the concrete cylinders were modelled using C3D8R elements in the model with straight bars and 4-node linear tetrahedron elements (type C3D4) in the model with bent bars; the latter type of elements was preferred to brick elements as they are less sensitive to distortion and therefore better suited to model the curve-shaped groove in the cylinder. Mesh sensitivity analyses were performed, allowing to define the following maximum dimensions for the FE elements: (i) in the models with straight bars, 4 mm in the concrete and 4 mm in the bars (0.8 mm in the embedded zone); and (ii) in the models with bent bars, 6 mm in the concrete and 7 mm in the bars (1.7 mm in the embedded zone). The models with straight and bent bars comprised a total of 24,168 FEs and 145,642 FEs, respectively. A more refined mesh for the concrete near the bent portion of the bar was adopted (length of 3 mm) to correctly capture the local stress variations that occur in that region.

5.3.2.2. Material properties

In the models with straight bars, namely bars SC, RB-D12 and RBP-S, both concrete and bars were modelled as isotropic linear elastic materials, as the non-linear response of the pull-out specimens was mainly due to the non-linearity of the GFRP-concrete bond. The modulus of elasticity of concrete was defined as 26.2 GPa in the models with RB and RBP bars, and 28.7 MPa in the model with SC bars (*cf.* Table 4.2); its variation with temperature was defined according to the Eurocode 2 (EC2) – Part 1-2 [79]. The GFRP bars were modelled considering the elastic moduli obtained from tensile tests (*cf.* Table

3.7 and Figure 5.7) and the following Poisson's ratios (υ): $\upsilon_{SC\ bar}$ = 0.26, $\upsilon_{RB\ bar}$ = 0.24 and $\upsilon_{RBP\ bar}$ = 0.39, computed using the rule of mixtures and assumed constant with temperature.

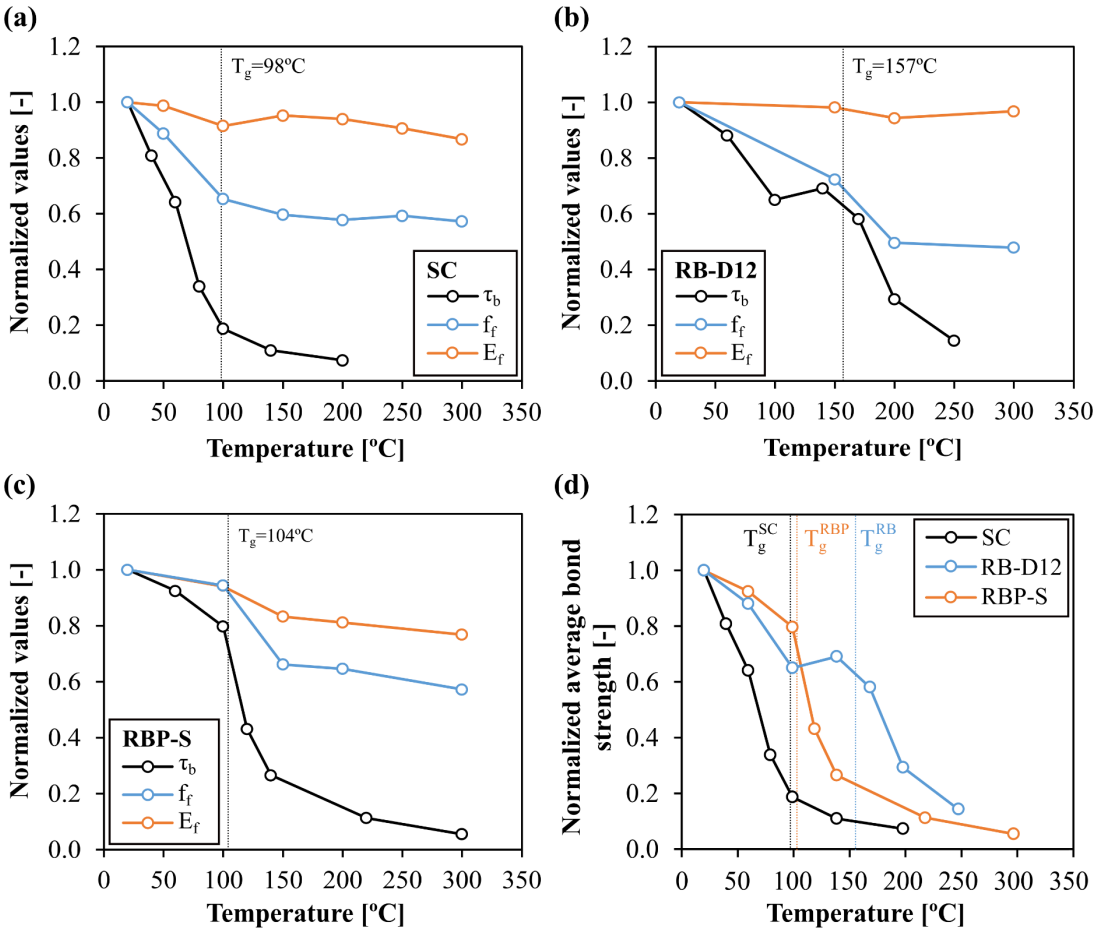

Figure 5.7. Normalized average values of bond strength (τ_b), tensile strength (f_f) and tensile modulus (E_f) as a function of temperature of bars (a) SC, (b) RB-D12 and (c) RBP-S; (d) bond strength degradation with temperature obtained for the three bars.

In the model with bent RBP bars, the isotropic inelastic behaviour of concrete was simulated using the Concrete Damaged Plasticity (CDP) material model, considering an elastic-plastic stress-strain relationship. The option for this material model was justified by the aforementioned local stress variations that occur in the bent portion of the bars, which locally exceed the elastic properties (not the case in the model with straight bars). The following parameters were defined: dilation angle, ψ = 20º, defined according to [202]; flow potential eccentricity, e = 0.1; ratio of initial equibiaxial compressive yield stress to initial uniaxial compressive yield stress, f_{b0}/f_{c0}, was decreased from the default value of 1.16 to 1.001, a mathematical artifice to prevent (unrealistic) confining effects triggered by the symmetry boundary conditions used; ratio of the second stress invariant on the tensile meridian to that on the compressive meridian, K_c = 2/3, and viscosity $\mu = 1\times10^{-5}$ [203]. The constitutive relationship of concrete at ambient temperature was defined according to EC2 – Part 1-1 [192], considering the following mechanical properties (obtained from tests, also *cf.* Table 4.2): equivalent cylinder

compressive strength f_{cm} = 25.3 MPa, modulus of elasticity E = 26.2 GPa, tensile strength f_{ctm}= 1.7 MPa and Poisson's ratio υ = 0.2. For the tensile behaviour, a classical bilinear model was used ([204]) due to its simplicity and well-established values for ambient temperature. The variation of the mechanical properties of concrete with temperature was defined according to EC2 – Part 1-2 [79], with the exception of the Poisson's ratio and fracture energy (G_f = 0.06 N/mm estimated according to [205]) that were assumed constant with temperature.

Bent bars were modelled as a linear elastic orthotropic (transversely isotropic) material; for that purpose, the bent section was divided in 10º segments, in which local axes were assigned so as to correctly define the corresponding properties in the longitudinal and transverse directions. The mechanical properties of the bent bars were implemented as engineering constants (*cf.* Table 5.5), namely the elastic moduli (E), Poisson's ratios (υ) and shear moduli (G) in the longitudinal (L) and transverse (T) directions. With the exception of E_L (assumed equal to the modulus in the straight zone), the elastic constants of the bent bars at ambient temperature were predicted using the rule of mixtures and the elastic properties of the constituent materials, namely the matrix (m) and the fibres (f), defined according to the manufacturer's technical sheet [49] and the recommendations of the Fib Bulletin 40 [10]: E_m = 5.0 GPa, E_f = 80.5 GPa, υ_m = 0.39 and υ_f = 0.22. The tensile strength of the bars in the straight section and its variation with temperature were defined according to the tensile tests conducted in Section 3.4 (*cf.* Table 3.7 and Figure 5.7c). Due to the lack of experimental data, the strength of the bar in the bent zone at 20 ºC was considered as indicated by the manufacturer (700 MPa) and its variation with temperature was assumed to be the same as that obtained in the straight zone. This assumption should be assessed/confirmed in the future by means of specific mechanical characterization tests performed on bent bars at elevated temperatures. The variation with temperature of the transverse tensile modulus and shear modulus (matrix-dominated properties) was considered to be similar to that reported by Rosa *et al.* [206] for the shear modulus of pultruded GFRP laminates (the degradation model based on the Gompertz statistical distribution was considered to extrapolate data above 180 ºC [206]). The Poisson's ratios were assumed constant with temperature.

Table 5.5. Elastic constants considered for the bent bars as a function of temperature.

Temperature [ºC]	**E_L [GPa]**	**E_T [GPa]**	**υ_{LT}**	**υ_{TT}**	**G_{LT} [GPa]**	**G_{TT} [GPa]**
20	60.1	15.4	0.27	0.39	5.6	5.5
60	58.3	10.6			3.9	3.8
100	56.5	5.7			2.1	2.1
120	53.9	4.8			1.8	1.7
140	51.4	3.5			1.3	1.2
220	48.3	1.8			0.7	0.7
300	46.2	1.7			0.6	0.6

5.3.2.3. GFRP-concrete interaction

The bond interaction between the bars and the concrete was modelled with cohesive interface surfaces, using the *surface-to-surface contact* interaction in *ABAQUS* and adopting a *small sliding* contact formulation. Although the *finite sliding* contact formulation of *ABAQUS* is acknowledged as the most accurate to simulate contact interaction problems involving curved surfaces (as it considers the deformed shape of the model), its use led to a substantial increase in computational effort and serious convergence difficulties. The results obtained using the *finite sliding* formulation were compared with those provided by the *small sliding* formulation (*i.e.*, considering the undeformed shape of the model) and it was concluded that the latter retrieved very similar results when performing geometrically non-linear analyses.

The parameters that define the cohesive behaviour and the bond damage initiation and evolution of the straight bars (and straight zones of the bent bars) were implemented in the models according to the temperature-dependent local bond stress *vs.* slip laws presented in Section 5.2 (plotted in Figure 5.3 and Figure 5.5). For the bent section of the bar, local bond laws were calibrated specifically (and separately), as described ahead. Table 5.1 to Table 5.4 (*cf.* Section 5.2.2.1 and Section 5.2.2.2) list the parameters defining the bond interaction in the tangential direction, given by Equation (5.2), as a function of temperature. Due to the non-linearity of the bond stress *vs.* slip laws near the maximum bond stress, the stiffness and maximum nominal stress components implemented in the models were defined considering a peak stress at 90% of the calibrated bond strength, τ_m. The effects of temperature in the bond damage in the normal direction were not addressed in this study even though they were found to affect the predictions of the pull-out loads of bent bars; however, because no data was available to accurately quantify this parameter and its variation with temperature, contact pressure stiffness (10 000 MPa/mm, equivalent to rigid) and maximum normal (bond) stress (33 MPa) in the normal direction were defined (high enough to not affect the global response). In the models with straight bars, the interaction between the free end of the bars and the concrete was simulated considering a friction coefficient of 0.5 (average value found in the literature, *e.g.* [207]) and a contact pressure stiffness of 1000 MPa/mm, both constant with temperature.

It is worth mentioning that, as an initial approach, the bond interaction in the bent portion of the bar was modelled with the bond laws calibrated for straight bars. As shown in Figure 5.8, although a good agreement was obtained for test results at 20 ºC, this approach led to significant overestimations of the maximum pull-out loads obtained in tests at elevated temperatures (exemplified in that figure for 60 ºC and 120 ºC). These preliminary results indicated that at elevated temperatures such model was unable to capture the localized damage that seems to occur in the ribs of the bend portion of the bars, a zone with higher stress variations under pull-out loads (*cf.* Figure 5.11, Section 5.3.3). This localized damage seems to be the result of (i) the three-dimensional stress state in the ribs and (ii) the severe reduction of the

ribs' shear strength due to the softening of the resin (the sole component of the ribs). This result also indicated that at elevated temperatures the bond strength in the bent zone should be lower than that considered in straight zones of the bar, which *a priori* is counter intuitive.

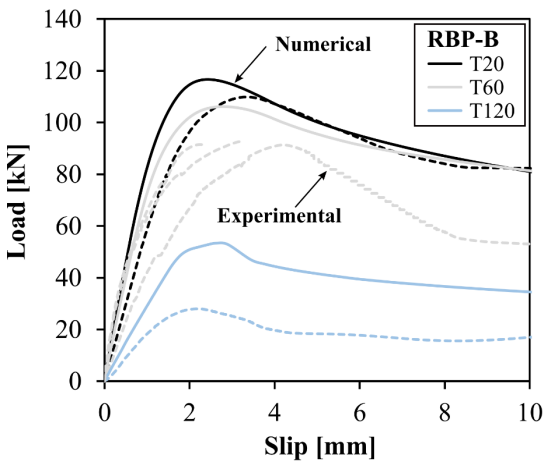

Figure 5.8. Example of numerical (continuous) and experimental (dashed) load *vs.* slip curves of bent RBP bars obtained considering the bond laws calibrated for straight bars (preliminary results).

Simulating this complex behaviour at the material level would require explicitly modelling the actual geometry and material of the ribs or, alternatively, to model the material damage in the ribs by considering the evolution of shear damage in the bar; however, the *ABAQUS* material library does not provide shear damage models for orthotropic materials, nor the required input data would be available. The study of this localized phenomenon in the numerical models was beyond the scope of this work. Additionally, in order to accurately reproduce the behaviour of the bars, their mechanical properties in the transverse direction and the GFRP-concrete bond interaction in the normal direction also had to be known as a function of temperature, which was not the case.

In light of these limitations, local bond laws were calibrated specifically for the bent zone of the bar based on an inverse analysis and only for temperatures above 20 ºC. With this approach, the localized damage in the ribs was implicitly considered in the interaction law, while the GFRP-concrete bond along the tail and straight embedment lengths was described using the local bond laws calibrated (earlier) for straight bars. The local bond strength in the bend (τ_m') was defined by decreasing the bond strength established in the bond law of straight bars (τ_m) through a reduction factor, indicated between brackets in Table 5.6. The calibration of the reduction factors was performed through an inverse analysis, aiming at minimizing the differences between the experimental and numerical maximum pull-out loads at each temperature. The remaining parameters defining the bond stress *vs.* slip laws (s_m, α, α' and s_1, Equation (5.2)) were not changed, with respect to those defined in the bond laws of straight bars. The non-monotonic variation of the local bond strength in the bent portion of the bar (unexpected *a priori*) is justified by the fact that it implicitly includes several (and complex) temperature-dependent phenomena

responsible for the localized damage of the ribs in the bent zone (including the materials' degradation and the bond interaction in the bend), as well as the influence of the thermal deformation in friction.

Table 5.6. Parameters defining the local bond stress *vs.* slip laws (Equation (5.3)) of straight and bent RBP bars.

Temperature [ºC]	s_m [mm]	Straight section	Bent section	α [-]	α' [-]	s_1 [-]
		τ_m [MPa]	τ_m' [MPa]			
20	0.69	19.30	19.30	0.42	0.98	8.1
60	0.75	17.80	9.79 (0.55 τ_m)	0.45	0.80	12.4
120	1.53	8.60	0.43 (0.05 τ_m)	0.67	0.46	11.5
140	0.60	5.26	1.58 (0.30 τ_m)	0.61	0.40	80.0
220	0.27	2.30	0.23 (0.10 τ_m)	0.63	0.35	1.5
300	0.31	1.18	0.41 (0.35 τ_m)	1.10	0.22	1.3

5.3.2.4. Loading, boundary conditions and type of analyses

As mentioned, only one quarter of the specimens with straight bars and one half of the specimens with bent bars was modelled (*cf.* Figure 5.6). For this purpose, the nodes located in the *xy* symmetry plane, and in the case of the model with straight bars also the nodes located in the *yz* plane, were restrained from displacing along the *z*- and *x*-axis, respectively. The reaction provided by the steel frame was set restraining the displacements in the bottom face of the cylinder in the *y* direction. In order to simulate the confinement provided by the steel clamps (used in the experiments to prevent splitting failures), a uniform pressure load was applied to the cylinders' surface in strips matching the position of the clamps. The confining pressure at ambient temperature was estimated based on the strains measured in the clamps during the application of the torque; for higher temperatures, the thermal expansion of the clamps was deducted from the strain measured at 20 ºC.

Two types of static analyses were carried out (both implicit iterative incremental): geometrically linear analyses in specimens with straight bars and geometrically nonlinear analyses in specimens with bent bars. The pull-out load was applied to the lower extremity of the bars in small increments along the *y*-axis.

5.3.2.5. Summary of modelling assumptions

In summary, the following main assumptions and simplifying hypotheses were considered in the numerical simulations of the pull-out tests, as well as in the parametric studies (described ahead in Section 5.4):

(i) The straight bars were modelled as isotropic materials.

(ii) The fracture energy of concrete and the Poisson's ratios of bars and concrete were assumed constant with temperature.

(iii) The shear and transverse elastic moduli of bars were estimated according to the rule of mixtures and their variation with temperature was considered equal to that of the shear modulus of pultruded GFRP laminates.

(iv) The tensile modulus at ambient temperature and the variation with temperature of the tensile modulus and strength of the bent zone of the bars was assumed equal to that of straight bars.

(v) The bond interaction was modelled using the *small sliding* contact formulation in *ABAQUS.*

(vi) The bond of the straight zone of bent bars was modelled according to bond laws obtained for straight bars; the calibration of bond laws for the bent zone was made through inverse analysis.

(vii) The effect of temperature on the bond degradation on the normal direction (*i.e.* perpendicular to the axial direction of the bars) was not considered.

5.3.3. Comparison between experimental and numerical responses

Experimental and numerical load *vs.* slip curves are compared in Figure 5.9 for the straight bars and in Figure 5.10 for the 90º bent bars. A very good agreement was obtained between experimental and numerical bond responses and failure modes (due to pull-out, as depicted in Figure 5.11), demonstrating that the bond laws implemented as a function of temperature allowed to reproduce the degradation of the bond strength and initial stiffness with increasing temperatures. The maximum pull-out loads were predicted with a mean absolute error (considering all temperatures) of 4% in straight bars and 5% in bent bars. With respect to straight bars, a very good fit was obtained for the three types of surface finishes at both the loaded end (Figure 5.9a, Figure 5.9c and Figure 5.9d) and the free end of the bars (exemplified in Figure 5.9b for the RBP-S bar).

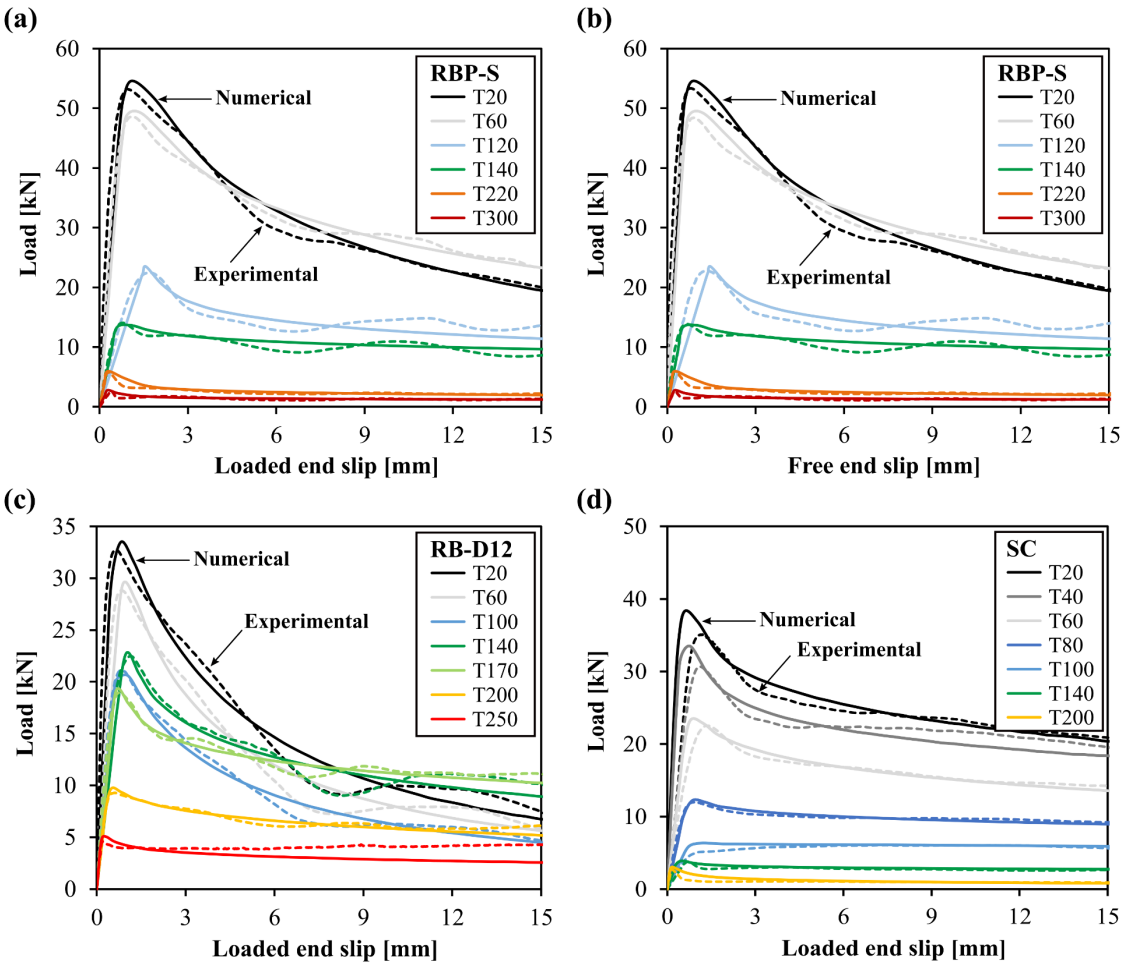

Figure 5.9. Numerical (continuous) and experimental (dashed) load *vs.* slip curves obtained in RBP bars at the (a) loaded and (b) free end; curves obtained in bars RB (c) and SC (d) at the loaded end.

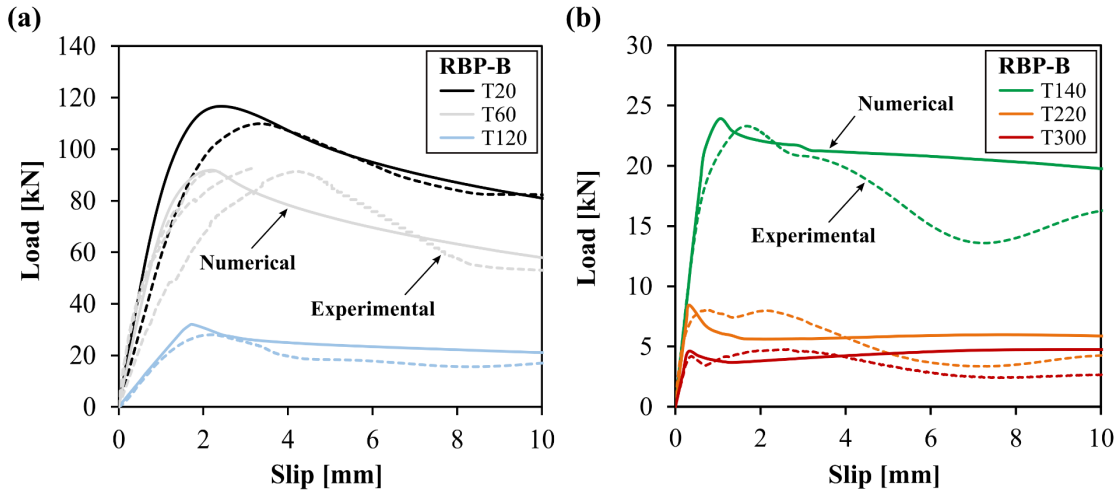

Figure 5.10. Numerical (continuous) and experimental (dashed) load *vs.* slip curves obtained in bent bars at: (a) 20 ºC, 60 ºC and 120 ºC; (b) 140 ºC, 220 ºC and 300 ºC.

Regarding the results obtained for bent bars at 60 ºC (Figure 5.10a), the numerical curve presented a good fit to two of the three curves obtained in the experiments (note there was a high scatter in the initial bond stiffness). However, as depicted in Figure 5.10b, the models were less accurate in simulating the bond response of the bent bars tested at 220 ºC and 300 ºC for high values of slip, including the prediction of the two peak loads obtained in the experiments. This is explained by the fact that, given the simplifications adopted in this study, it was not possible to explicitly simulate the complex failure mode that occurs at those higher temperatures, namely the advanced softening state of the resin and consequent shearing off of the ribs. As previously described in Section 4.6.1, these phenomena were responsible for the local failure of the ribs, which may have occurred successively in opposite sides of the bars in the bent zone, therefore explaining the two peak loads obtained in the tests – *i.e.* each peak matched the formation of a shearing surface, the first occurring in the inner side of the bend (where higher stresses develop, *cf.* Figure 5.11b) and the second in the outer side of the bend. Note that this double peak behaviour was not observed in the load-slip curves obtained in straight bars (*cf.* Figure 4.9c), since in that case the distribution of stress is uniform within the bars' cross-section, as shown in Figure 5.11a.

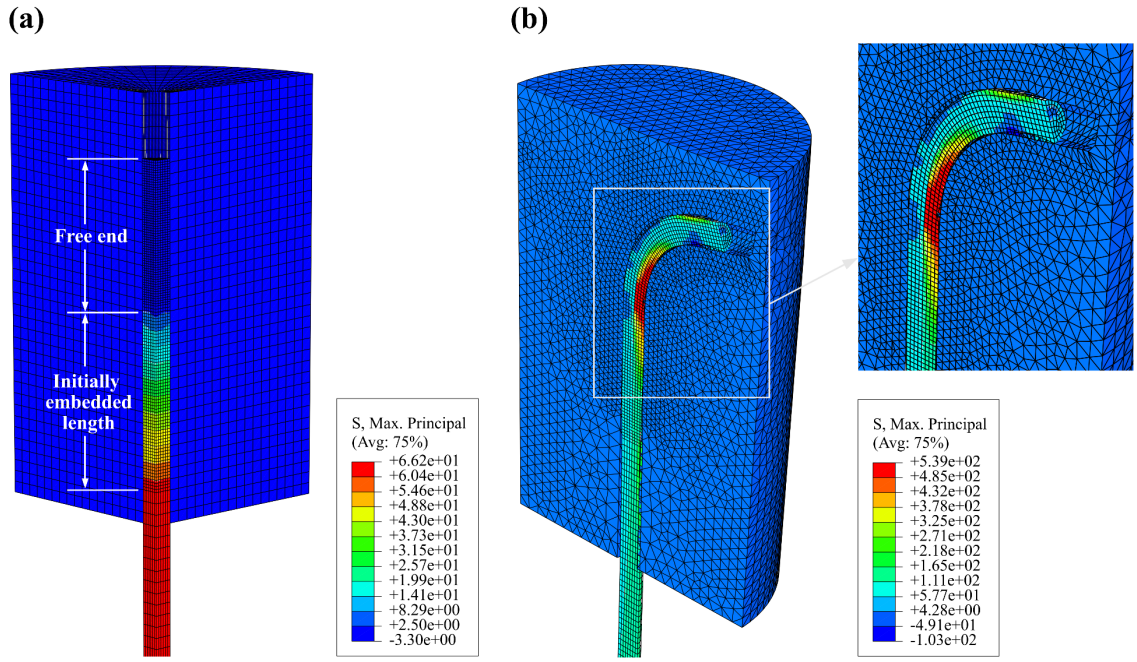

Figure 5.11. Distribution of maximum principal stresses (in MPa) along the embedment length of: (a) straight and (b) bent RBP bars (example of simulation performed at 140 ºC; stress state corresponding to an imposed displacement of 25 mm).

The curves plotted in Figure 5.10a show that the bond interaction between bent GFRP bars and concrete at ambient temperature can be modelled in the entire embedded length considering the bond laws calibrated for straight bars – this is a relevant result. This is due to the fact that, for the materials used in the present study, the bond strength at 20 ºC for both straight and bent bars was governed by the strength of the concrete between ribs and not by the ribs' shear strength, as discussed in Sections 4.5.2 and 4.6.2.

At elevated temperature, the accurate predictions of the maximum pull-out loads of bent bars relied on considering the reduction of the local bond strength in the bend with respect to that considered in the straight zone. The results obtained seem to confirm that, on the one hand, the bond strength at high temperatures of this type of bar (and surface finish) depends on the loss of adhesion between the ribs and the bars' core, a degradation mechanism accounted for in the bond laws calibrated for straight bars. On the other hand, the bond strength also relies on the strength of the ribs at elevated temperatures, especially considering the localized damage that seems to develop in the bent portion of the bars. This localized damage should be the result of: (i) the combination of forces in the longitudinal and transverse directions of the bend, making this zone prone to higher stress concentrations, as depicted in Figure 5.11b, and (ii) the (steep) decrease of the ribs' shear strength due to the softening of its resin during glass transition. Moreover, Figure 5.11b shows that the distribution of stresses in the bent zone is not uniform within the bars' cross section, comprising compressive stresses in the outer bend and bottom face of the tail length, and tensile stresses of higher magnitude in the inner bend. This stress state differs greatly from that developed in straight bars (Figure 5.11a), where the stress distribution is uniform within the bars' cross-section and principal stresses are marginal comparing to the tangential stresses that develop along the failure interface (*i.e.*, the ribs are mainly subjected to shear).

Figure 5.12 shows the maximum pull-out loads obtained in the tests in the straight (A) and bent (B) bars; these are also compared with those numerically predicted for a straight bar with the same total embedment length as the bent bar (C). The conclusions are consistent for all temperatures and show that adding a hook after a straight zone allows to significantly improve the anchorage strength obtained with a straight bar (A *vs.* B). Yet, the anchorage capacity of the bent bar is affected by the local weakness of the ribs in the curved section, which explains why it presents a lower bond strength than a straight bar with the same embedment length (B *vs.* C). It should be stated that this analysis features a scenario in which the temperature distribution is uniform along the bar, hence the loss of bond progresses at the same rate in all sections of the FRP reinforcement. Yet, in a real fire scenario the bent portion of the FRP bar is not subjected to a constant temperature along its length, as the extremity of the tail length can be anchored in a cooler zone of the structural member, where bond is (much) less degraded. In other words, in a real fire scenario, the actual bond strength of the bent bar will be higher than that depicted here and thus the adoption of a hook will expectedly contribute to the considerable improvement of the anchorage strength, as it was verified in the fire resistance tests described in Chapter 6.

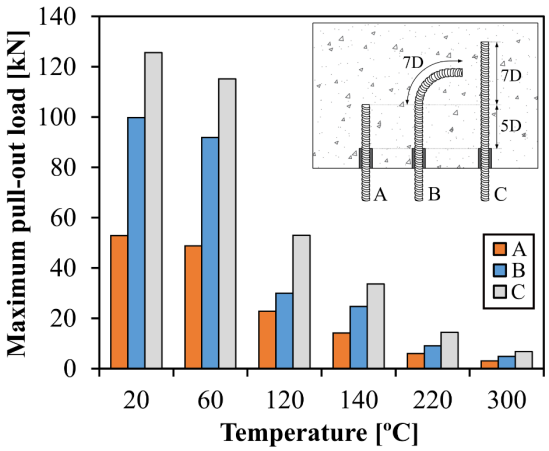

Figure 5.12. Comparison of the maximum pull-out load of straight and bent bars at different temperatures.

5.4. Parametric studies

5.4.1. Methodology and objectives

Following the validation of the numerical models, described in the previous section, parametric investigations were carried out to investigate the influence of the bars' geometry and surface finish on their bond behaviour at ambient and elevated temperatures. The main objectives were to perform design-oriented parametric studies, aiming at assessing: (i) the anchorage strength of straight and 90º bent bars at different temperatures as a function of the anchorage length, and (ii) the optimal bar configuration (development and tail lengths required to explore the bars' tensile strength) as a function of temperature for beam and slab applications. It is worth highlighting that although the tensile stresses in GFRP bars for service conditions are relatively low, during fire exposure both the bond stresses and tensile stresses may present significant increases (as shown in Hajiloo *et al.* [11] and also in the present study, *cf.* Section 7.4) – this justifies the (conservative) procedure adopted to determine the development length in fire conditions.

The development length of bent bars was considered as in the ACI 318-11 standard [208], corresponding to the distance measured from the critical section to the outer face of the hook, as depicted schematically in Figure 5.13. In order to attain the abovementioned objectives, the embedment length of the straight bars, and the tail and straight embedment lengths of the bent bars were varied as multiples of the bar diameter (D), while the bent radius was kept constant (equal to that adopted in the experimental study, *cf.* Section 4.3). The optimal anchorage length was defined as the length beyond which the increase in the embedded area does not provide a relevant increase in load capacity.

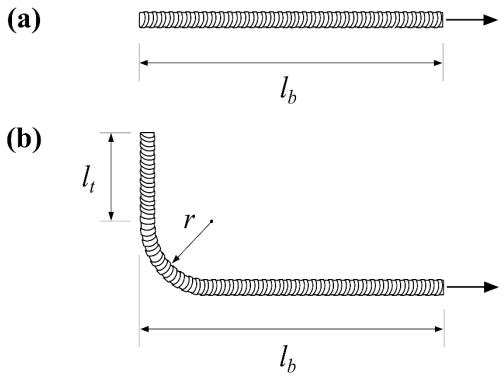

Figure 5.13. Development length (l_b) of (a) straight and (b) bent bars (tail length (l_t) and bend radius (r)).

The parameters, bars and temperatures that were analysed in this study are summarized in Table 5.7. The parametric analyses did not comprise temperatures above 140 ºC (200 ºC in the case of bar RB) since the optimal anchorage lengths for such temperature range (for which the bond strength retention is very low) resulted in too lengthy and hence impractical/unrealistic designs.

Table 5.7. Summary of parameters analysed in the numerical studies.

Anchorage geometry	**Surface finish**	**Parameters**	**Variation range**	**Temperatures [ºC]**
Straight	Sand coated (SC)	Anchorage length (l_b)	[5D; 90D]	20, 60, 100, 140
	Ribbed (RB)			20, 60, 140, 170, 200
	Ribbed (RBP)			20, 60, 120, 140
90º bend (3.1D radius)	Ribbed (RBP)	Tail length (l_t)	[1.5D; 24D]	20, 60, 120, 140
		Straight anchorage length (l_b)	[5D; 35D]	

With respect to the studies performed in straight bars, three types of surface finishes (one sand coated and two ribbed) were analysed. In the case of bent bars, the parametric study was divided in two stages: first, maintaining a straight anchorage length of 5D (as in the models validated with the experimental results), the optimal tail length was determined for each temperature; then, considering the optimal tail length previously obtained, the optimal straight anchorage length was assessed. The studies were carried out envisaging the use of FRP reinforcement in concrete beams and slabs; therefore, in order to consider the typical ranges of thickness of GFRP-RC slabs, the maximum tail length admissible for slab applications was set at 10D (corresponding to a total bar height of 187 mm in the bent zone). As an example, GFRP reinforcement was used before in parking garage slabs with thicknesses of 150 mm [50] and 260 mm [51]. Note that in beams the maximum tail length requirement was not set (because the beam bars can

be anchored in the columns). To accommodate longer bars, the dimensions of the concrete cylinders considered in the FE models described in Section 5.3.2.1 were increased: cylinders with diameter of 800 mm were considered, while their height was set at 1400 mm and 700 mm in the models comprising straight and bent bars, respectively.

5.4.2. Results and discussion

5.4.2.1. Development length of straight bars

The variation of the pull-out load of the straight RBP, RB and SC bars as a function of the anchorage length is presented from Figure 5.14a to Figure 5.14c, while the variation of the development length of all bars as a function of temperature is depicted in Figure 5.14d. The results show that: (i) as expected, the anchorage strength increases with the increase in the embedded length up to a certain limit; and (ii) at elevated temperatures, longer development lengths are required to mobilize the bars' tensile strength compared to ambient temperature, particularly for temperatures above the T_g.

As depicted in Figure 5.14d, the development length generally increases with the increase of temperature; however, in the case of RB bars, it can be seen that the development length does not vary for temperatures up to 170 ºC, because, as shown in Figure 5.7b, the degradation of the bond and tensile strengths for this temperature range is fairly similar. Regarding the SC and RBP bars, despite having similar T_gs, longer development lengths are needed to anchor SC bars because, in comparison to RBP bars, their bond strength is lost at considerably lower temperatures (*cf.* Figure 5.7d), owing to the higher susceptibility of the sand coating to elevated temperatures; moreover, note that bars RB and RBP, both ribbed, also require markedly different development lengths at a given temperature, especially for higher temperatures.

These results highlight that the design of GFRP anchorages should not be based on a single parameter (such as the T_g or the geometry/roughness of the bars' surface), because the mechanical and bond performance of the bars at elevated temperatures can vary significantly depending on the bars' T_g, the susceptibility of constituent materials (matrix and fibres) to elevated temperatures and, in the case of bond, also the surface finish. Knowing the variation of the bond and tensile properties of the bars with temperature is therefore a crucial aspect to consider in the fire design of GFRP anchorages. In this way, for a given fire resistance rating, the temperature of the reinforcement at a certain critical section can be determined (through numerical thermal analyses or standard temperature profiles) and the data provided in Figure 5.14 can be used to estimate the development length required to anchor GFRP bars with comparable bond and mechanical characteristics to those considered in this study.

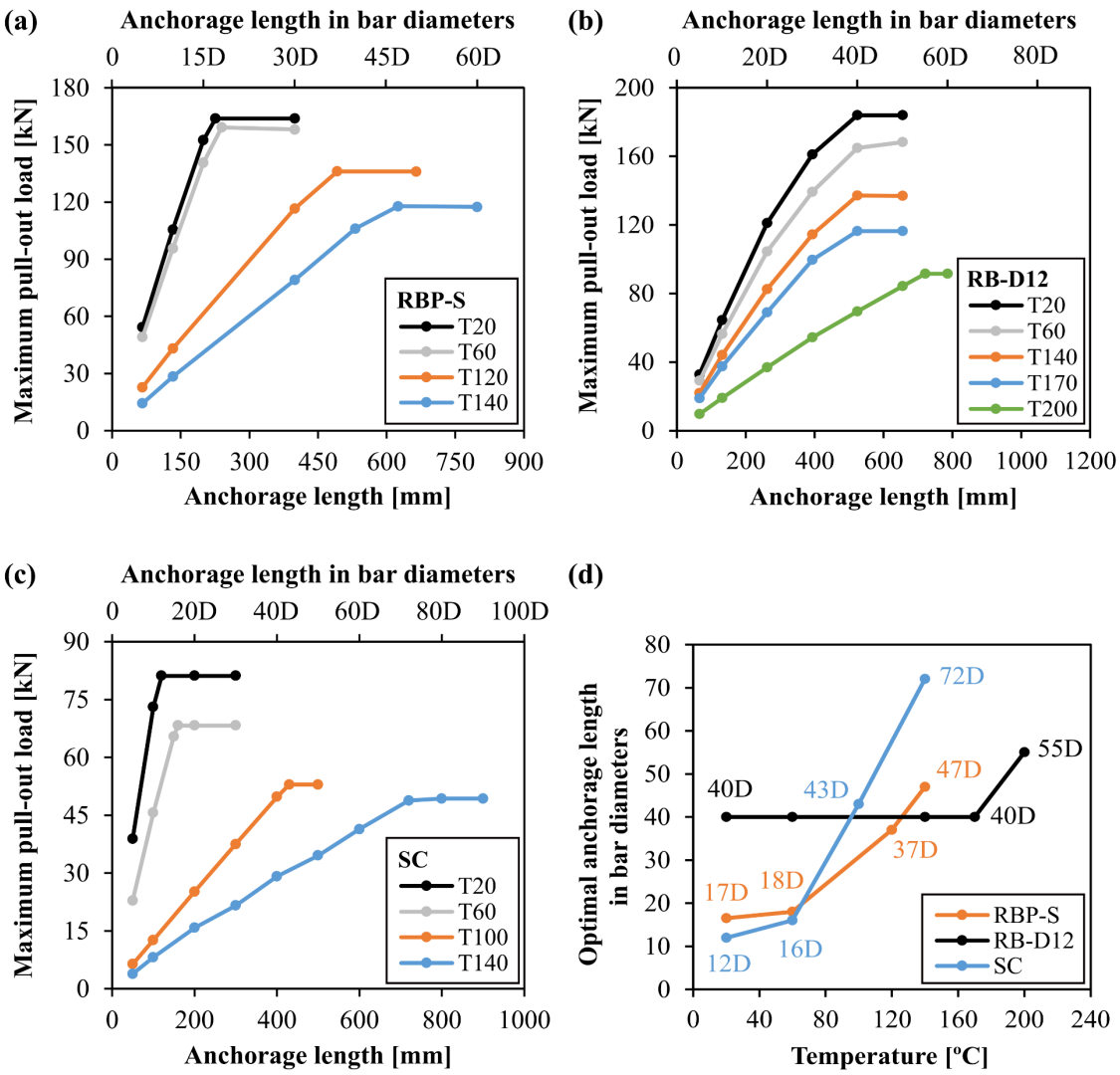

Figure 5.14. Results of parametric studies performed in straight bars: maximum pull-out load as a function of anchorage length of bars (a) RBP, (b) RB and (c) SC; (d) optimal anchorage length of all bars as a function of temperature.

5.4.2.2. Development length of bent bars

As previously mentioned, the parametric studies performed in 90º bent bars were carried out in two stages. Figure 5.15 presents the results obtained in the first stage of the study, in which the influence of the tail length (for a straight length of 5*D* and r = 3.1*D*) in the anchorage strength at elevated temperatures was assessed. The results demonstrated that increasing the tail length improved the anchorage strength for all temperatures (Figure 5.15a) and that the optimal tail length increased with the increase in temperature (Figure 5.15b). However, as shown in Figure 5.16, increasing the tail length above the optimal value (depicted in Figure 5.15b) while adopting a relatively short straight anchorage length (in this case 5*D*) did not allow attaining the ultimate strength of the bar – this is because the stress concentration that develops in the bend causes the bars to fail in that section at a lower stress than the

tensile strength of the GFRP bars in the straight section. These results highlight the importance of adopting the recommended development lengths at each temperature (shown ahead in Figure 5.17b and Table 5.8) to avoid localized failures in the bend and thus explore the full anchorage strength.

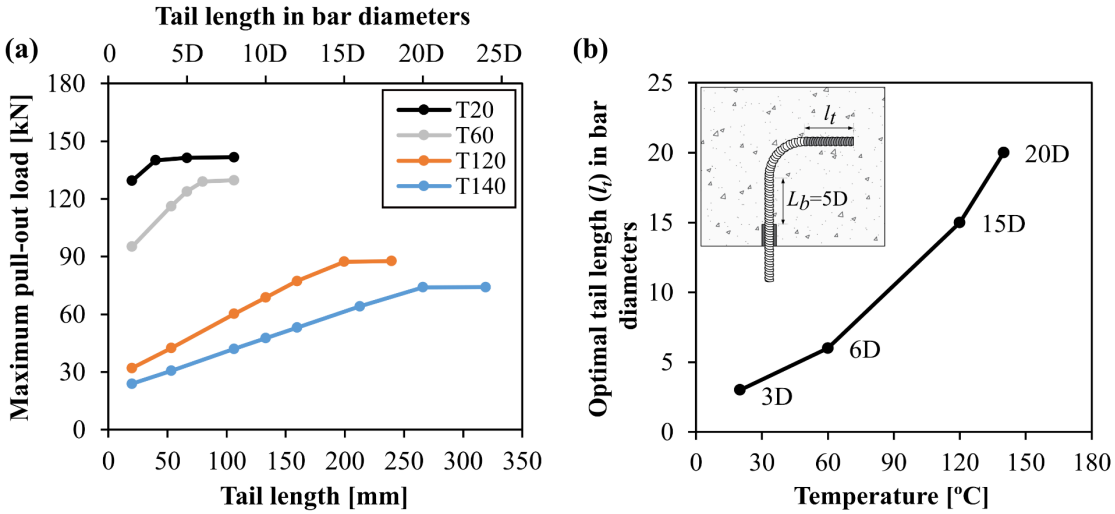

Figure 5.15. Results of parametric studies performed in bent bars – stage 1 (assessment of the optimal tail length (l_t) considering a straight anchorage length (L_b) of 5D): (a) maximum pull-out load as a function of l_t; (b) optimal l_t as a function of temperature (for r = 3.1D).

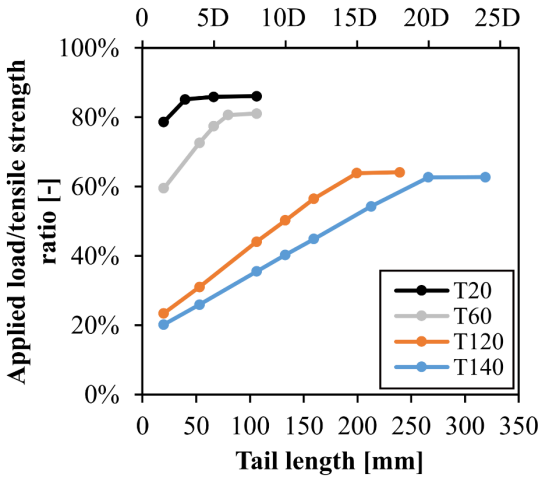

Figure 5.16. Ratio between applied load and tensile strength (of straight section) as a function of the tail length (bent geometry with fixed straight anchorage length of 5D and r = 3.1D).

The results obtained in the second stage of the study are presented in Figure 5.17, regarding the influence in the anchorage strength of the straight anchorage length (when adopting the optimal tail length, for r = 3.1D). As depicted in Figure 5.17a, adopting the optimal tail length for each temperature and increasing the straight anchorage length allows improving the anchorage strength and making a better use of the higher tensile strength of the bars in the straight section (*cf.* Figure 5.18).

The optimal straight anchorage lengths obtained are plotted in Figure 5.17b as a function of temperature, showing that, as expected, the length required to attain the ultimate strength of the bars increased with temperature. It can be seen in Figure 5.15b that the optimal tail lengths obtained at 120 ºC and 140 ºC (15*D* and 20*D*, respectively) exceed the maximum length possible for slab applications (assumed as 10*D*). Therefore, as shown in Figure 5.17b, longer development lengths are required to anchor the bars in slabs than in beams at the referred temperatures; for example, at 140 ºC a straight anchorage length of 23*D* is sufficient to attain the bar's tensile strength in a beam application, while in a slab the required straight length is 34*D*.

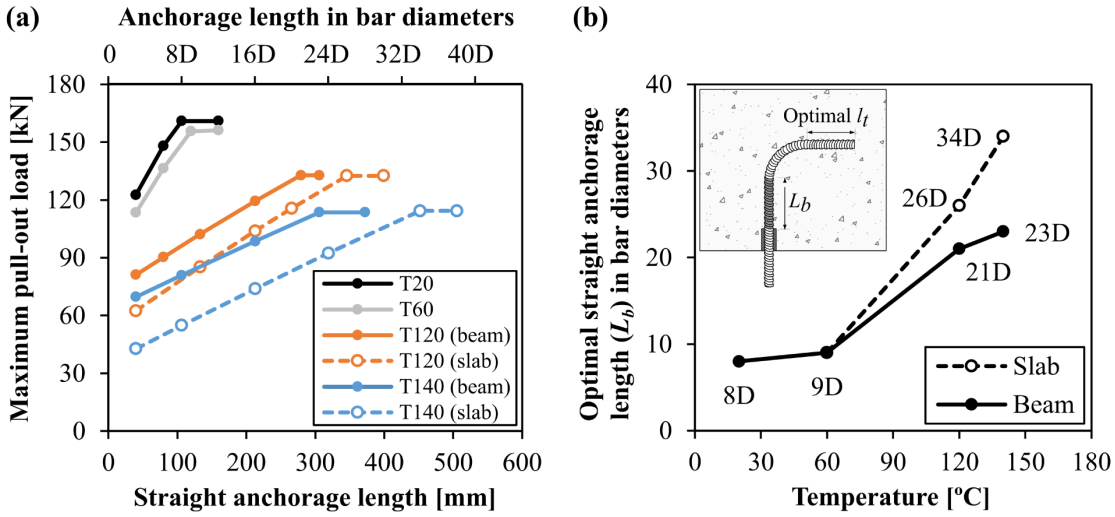

Figure 5.17. Results of parametric studies performed in bent bars - stage 2 (assessment of the optimal straight anchorage length (L_b) considering the optimal tail length determined from the first stage): (a) maximum pull-out load as a function of the L_b; (b) optimal L_b as a function of temperature (in slabs, the maximum tail length of 10*D* was set due to slab thickness constraints).

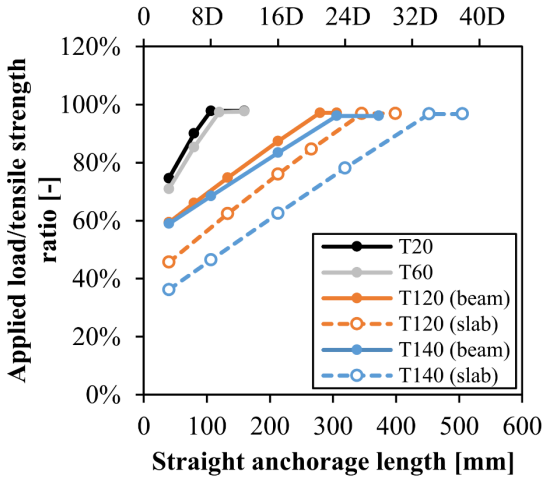

Figure 5.18. Ratio between applied load and tensile strength (of the straight section) as a function of the straight embedment length (bent geometry with fixed optimal tail length obtained for each temperature).

Table 5.8 compares the recommended development lengths obtained for straight and 90º bent bars with the same surface finish. Note that in realistic circumstances in which the anchorage length is under a temperature gradient (because the bars are embedded in beams and columns), the temperature of the bars in the warmer zone should be (conservatively) considered. It can be seen that shorter development lengths are required to mobilize the bars' strength if bent extremities are used and the recommended tail length is adopted. Considering the example of GFRP-RC beams, the development length required for a temperature of 140 ºC is reduced from 47*D* if straight bars are used to 27*D* if bent bars with a tail length of 20*D* are adopted.

Table 5.8. Development lengths recommended for straight and bent bars given as function of the bar diameter (for $r = 3.1D$).

Structural member	T [ºC]	Straight bars	90º bent bars		
		Development length of straight bar (l_b)	Development length of bent bar (l_b) [(1)]	Optimal tail length (l_t)	Total anchorage length of bent bar [(2)]
Slabs and beams	20	17*D*	12*D*	3*D*	17*D*
	60	18*D*	13*D*	6*D*	21*D*
Beams	120	37*D*	25*D*	15*D*	42*D*
	140	47*D*	27*D*	20*D*	49*D*
Slabs	120	37*D*	30*D*	10*D* [(3)]	42*D*
	140	47*D*	38*D*	10*D* [(3)]	50*D*

[(1)] Development length of bent bar corresponding to the sum of the straight anchorage length, inner bend radius (3.1*D*) and bar diameter.
[(2)] Total anchorage length corresponding to the sum of the tail, bent and straight anchorage lengths.
[(3)] Maximum tail length of 10*D* set due to slab thickness constraints.

As reference and with respect to the design at ambient temperature, the American ACI 440.1R guide [6] recommends that the development and tail lengths of 90º bent FRP bars should not be less than 12*D*. In light of the results obtained in this study, it can be concluded that those recommendations are insufficient to adequately anchor FRP bars in a fire scenario. The recommendations proposed in Table 5.8 are however limited to the type of bars considered in this study and generalizations of the results cannot be made given the wide variety of bars available. Moreover, in light of the assumptions made in the models (*cf.* Section 5.3.2.5) and the aspects not considered in the parametric study (namely the effect of cracking on the confinement conditions) these recommendations should be confirmed through tests designed specifically for that purpose, namely in structural members/assemblies exposed to fire. The tests should allow to confirm if the recommendations proposed are adequate and conservative. Further studies are necessary to assess the influence of different types of surface finishes and other geometrical features, such as the bend radius and the angle of the bend, on the bond behaviour of bent FRP reinforcement at

elevated and ambient temperatures. The methodology adopted in the present study, combining experiments and numerical simulations, can be used in this respect to propose recommendations for the development length of GFRP rebars at elevated temperature.

5.5. Concluding remarks

The investigations presented in this chapter aimed to address the absence of comprehensive numerical studies on the bond behaviour of straight and 90º bent GFRP bars in concrete at elevated temperatures. One of the main contributions of this research was the proposal of temperature-dependent local bond stress *vs.* slip laws, here numerically calibrated herein to describe the GFRP-concrete bond interaction up to 300 ºC of bars with different surface finishes (sand coated and ribbed) and core diameters. This output addresses the lack of bond stress *vs.* slip laws specifically calibrated for FRP reinforcement at different elevated temperatures, which are needed in order to improve the accuracy of numerical models in simulating the thermo-mechanical response of concrete members reinforced with GFRP bars exposed to elevated temperature or fire (especially when failure can be triggered by the loss of bond in the splices or in the anchorage zones of the reinforcement).

The bond stress *vs.* slip implemented in 3D solid FE models, calibrated for straight GFRP bars, allowed to accurately predict the load *vs*. slip behaviour of straight bars at ambient and elevated temperatures, as well as of 90º bent ribbed bars at ambient temperature. However, in order to simulate the higher localized damage that occurs in the bend at elevated temperatures, local bond stress *vs.* slip laws had to be calibrated to implicitly consider both the localized damage in the ribs and the different bond behaviour of the bars along the bend (compared to that along the straight development).

Based on the results of parametric numerical studies, development lengths were proposed as a function of temperature for straight bars with different surface finishes (sand coated and ribbed), as well as development and tail lengths for 90º bent bars – this output constitutes a very relevant contribution to the state-of-the-art since it has a practical application in the design of GFRP anchorages in RC beams and slabs likely to be subjected to fire. The results obtained showed that the development lengths designed for ambient temperature are insufficient to mobilize the bars' tensile strength at elevated temperatures and that the design of GFRP anchorages must consider the type of surface finish of the bar, the bars' constituent materials (matrix and fibres) and their T_g, as these parameters affect the bars' tensile and bond properties at elevated temperatures Furthermore, it was shown that the development length required to anchor a straight bar can be reduced by adopting a bent extremity and an adequate tail length beyond the bend. Further studies are needed to assess the influence of other parameters, such as the surface finish, the bend radius and the angle of the bend on the bond behaviour of GFRP bars at elevated temperatures.

Part IV

Fire behaviour of GFRP-reinforced concrete slab strips

Chapter 6

Fire resistance tests of GFRP-reinforced concrete slab strips

6.1. Introduction and objectives

As shown in previous chapters, the susceptibility of FRP reinforcement to elevated temperatures justifies the concerns about the fire performance of FRP-RC members. However, despite its relevance, and as shown in Section 2.4.1, this topic has not yet been fully addressed in the literature. Particularly, there is a lack of comprehensive studies regarding the effects of the GFRP-concrete bond degradation with temperature in the behaviour of lap splices of FRP reinforcement in RC members exposed to fire, despite their remarkable impact in the members' fire resistance (*e.g.* [11,19,148]). Also in this regard, there is a gap in the literature with respect to studies comprising the use of bent reinforcement as a means to improve the splices' anchoring conditions at elevated temperatures; it is worth reminding that promising results were obtained with the use of bent rebars in beams' lap splices [16–18] and in the "cold" end anchors of beams [18] and slabs [14].

Previous studies also have not accurately related the evolution of temperature in FRP-RC beams and slabs during a fire event with the degradation of the tensile modulus and tensile strength of the FRP rebars at very high temperatures, because, until recently ([19]), such data was only available for temperatures up to 500 ºC, while many studies reported tensile failure of FRP reinforcement for temperatures exceeding that threshold (*e.g.* [19,148]). Moreover, additional studies are needed to further assess the feasibility of adopting thinner concrete cover thicknesses than those currently proposed in the design guidelines (*e.g.* [8]), as suggested in [11,12].

This chapter presents an experimental study whose main objective was to provide a better understanding of the fire behaviour of RC slabs with GFRP reinforcement, namely regarding the effects of (i) the presence of cold anchorages, (ii) the presence of straight or 90º bent tension lap splices with different overlap lengths directly exposed to fire, (iii) the type of rebar surface finish (sand coated or ribbed), (iv) the rebar diameter, (v) the concrete cover thickness, and (vi) the concrete strength. For this purpose, fire resistance tests were carried out in concrete slab strips, subjected to a sustained fire load and the ISO 834 standard fire [24]. The evolution of temperature was extensively monitored throughout the tests along the entire exposed span and cold anchorage zones, thus allowing to correlate the thermomechanical behaviour of the slabs with the progressive degradation of the rebars' tensile and bond properties with increasing temperature. The results obtained are discussed separately for slabs with sand coated rebars in

Section 6.4 and for ribbed rebars in Section 6.5; in both sections the results of reference steel-RC slabs are also presented for comparison. The fire resistance tests presented in Section 6.3 that were performed in GFRP-RC slabs with concrete type I were developed in collaboration with Santos [26], in the scope of his Master dissertation.

6.2. Experimental programme

6.2.1. Test programme

Fire resistance tests were conducted in 19 GFRP-RC slabs strips and 2 reference steel-RC slab strips to assess their fire performance when exposed to the ISO 834 standard fire [24]. Additionally, flexural tests were also performed in identical slab strips to characterize their mechanical response up to failure at ambient temperature conditions.

The test series are summarized in Table 6.1. The one-way slab strips, hereafter simply referred as slabs, differed on the following parameters: (i) type of reinforcement (GFRP or steel); (ii) type of surface finish of the GFRP bars; (iii) presence of lap splices with different overlapping lengths *vs.* continuous reinforcement; (iv) bar geometry in the ends of lap splices and (v) concrete cover; (vii) bar diameter, and (viii) concrete strength. The slabs were labelled as follows:

- The first label indicates the type of reinforcement (SR for steel bars; SC, RB and RBP for GFRP bars).
- The second label refers to the bar continuity (*C* for continuous or *LS* for spliced reinforcement). For continuous bars the letter "*C*" is followed by the (clear) concrete cover in centimetres (2.5 or 3.5 cm). For spliced bars, the letters "*LS*" are followed by the straight overlap length in centimetres (32.5, 65 or 84.5 cm) and the lap splice-end geometry in parentheses ("*S*" for straight, "*B*" for bent"); in this case, the clear concrete cover (always 2.5 cm) is omitted from the notation.
- The third label refers to the diameter (*D*, in mm) of the bottom reinforcement (8, 10 or 12 mm).
- A fourth label is used in the series of slabs with steel (SR) and SC bars to distinguish the concrete type (I, II or III).

As an example, RBP-LS84.5(B)-D12 refers to a slab with RBP rebars (12 mm in diameter) and bent-end tension lap splices with straight overlapping length of 84.5 cm. It should be noted that two identical RBP-C2.5-D12 slabs were tested (*cf.* Table 6.1); the number of the test specimen was identified by "1" or "2" in the end of the label.

Table 6.1. Nomenclature and reinforcement configurations of the slab strips.

Slab strip	Concrete type	Cover [cm]	Bar	Anchorage geometry	Bar continuity	Splice end geometry	Splice length (1) [cm]	Fig.
SR-C2.5-D10	II, III	2.5	Steel	90º bent	Continuous	-	-	6.1
SC-C2.5-D10	I, II	2.5	SC	Straight	Continuous	-	-	6.2
SC-C3.5-D10	I, II	3.5	SC	Straight	Continuous	-	-	6.2
SC-LS30(S)-D10	I	2.5	SC	Straight	Spliced	Straight	30	6.2
SC-LS60(S)-D10	I	2.5	SC	Straight	Spliced	Straight	60	6.2
SC-LS65(S)-D10	II	2.5	SC	Straight	Spliced	Straight	65	6.2
RB-C2.5-D12	II	2.5	RB-D12	Straight	Continuous	-	-	6.3
RB-C3.5-D12	II	3.5	RB-D12	Straight	Continuous	-	-	6.3
RB-LS32.5(S)-D12	II	2.5	RB-D12	Straight	Spliced	Straight	32.5	6.3
RB-LS65(S)-D12	II	2.5	RB-D12	Straight	Spliced	Straight	65	6.3
RB-C2.5-D8	II	2.5	RB-D8	Straight	Continuous	-	-	6.4
RBP-C2.5-D12-1	II	2.5	RBP	Straight	Continuous	-	-	6.3
RBP-C2.5-D12-2								
RBP-LS32.5(S)-D12	II	2.5	RBP	Straight	Spliced	Straight	32.5	6.3
RBP-LS32.5(B)-D12	II	2.5	RBP	90º bent	Spliced	90º bent	32.5	6.5
RBP-LS65(S)-D12	II	2.5	RBP	Straight	Spliced	Straight	65	6.3
RBP-LS84.5(S)-D12	III	2.5	RBP	Straight	Spliced	Straight	84.5	6.6
RBP-LS84.5(B)-D12	III	2.5	RBP	Straight	Spliced	90º bent	84.5	6.6

(1) Splice length corresponding to the straight overlap length.

6.2.2. Materials

The GFRP rebars used as internal (main) reinforcement in the GFRP-RC slabs were those illustrated in Figure 3.1 – page 68 (properties summarized in Table 3.1 from Section 3.2 – page 69), specifically: (i) SC bars (sand coated) with core diameter of 10 mm; (ii) straight RB bars (ribbed) with two core diameters of 8 and 12 mm (bars RB-S-D8 and RB-S-D12, respectively); and (iii) RBP bars (core diameter of 12 mm) with straight and 90º bent ends (bars RBP-S-D12 and RBP-B-D12, respectively). The geometry of the 90º bent bars was identical to that adopted in the pull-out tests presented in Chapter 4: the height of the bend was 75 mm, including a tail length of 20 mm, as shown in Figure 3.1c$_2$ (*cf.*

Section 3.2 – page 68). In the reference steel-RC slab, A500 NR SD steel bars with 10 mm of core diameter were used as main reinforcement with the following average properties: yielding tensile strength of 551 MPa and ultimate strength of 676 MPa (data provided by the manufacturer).

The slabs were produced using a ready-mixed concrete with Portland cement type CEM II/A-L 42.5 R and limestone aggregates with maximum size of 22 mm. As shown in Table 6.2 (also *cf.* Table 6.1), three different concrete types were used. Series SC were casted with two different concrete mixes with a higher (type I) and a lower (II) strength; the majority of the slabs from series RB and RBP were casted with concrete type II, while the slabs from series RBP-LS84.5 were casted with concrete type III. The steel-RC slabs were casted with concrete types II and III. The average compressive and splitting tensile strengths of the concrete mixes at the age of the fire tests were obtained according to standards procedures [190,191] and are summarized in Table 6.2. The slabs, as well as the cubes and cylinders used to test the concrete's mechanical properties were cured indoors in the laboratory facilities. In order to attain a stable and low moisture content, and thereby reduce the possible occurrence of concrete spalling due to the pore pressure increase during water evaporation, the fire resistance tests were performed at least one year after casting.

Table 6.2. Properties of concrete used in RC slabs (average strength and coefficient of variation, in brackets).

Concrete type	**Type of test**	**Age [days]**	$f_{cm,cube}$ **[MPa]**	f_{ctm} **[MPa]**
I	Flexural tests at ambient temperature and fire resistance tests	135	53.3 (4.0%)	2.8 (8.1%)
II	Flexural tests at ambient temperature	337	31.3 (7.4%)	2.3 (3.1%)
	Fire resistance tests	643	35.1 (6.5%)	2.0 (6.6%)
III	Fire resistance tests	457	27.9 (7.5%)	2.1 (9.4%)

6.2.3. Geometry of the slab strips

The geometry and detailing characteristics of the slabs is summarized in Table 6.1 and illustrated from Figure 6.1 to Figure 6.6. The GFRP-RC slabs were designed according to CNR-DT 203/2006 [7] (similar design philosophy to Eurocode 2) as over-reinforced members so that failure at ambient temperature would occur by concrete crushing. The steel-RC slab was designed according to Eurocode 2 [192]. All slabs, designed without shear reinforcement, were 1500 mm long (clear span between supports of 1400 mm) and had cross-section of 250 × 110 mm (width and height). The internal reinforcement of slabs with RB and RBP bars (except slab RB-C2.5-D8) consisted of 3 longitudinal bars

with diameters of 12 mm and 8 mm respectively for the bottom and top layers (10 mm and 6 mm, respectively, in the case of slabs with SC and steel slabs). The reinforcement ratio of the GFRP-RC slabs ranged between 1.1% and 2% (the minimum ratio required in [7] is 1%). Slabs RB-C2.5-D12 and RB-C2.5-D8, which differed on the diameter of the main reinforcement, were designed to have the same flexural resistance at ambient temperature; to that end, 3 RB-S-D12 ($\rho = 1.5\%$, Figure 6.3) and 6 RB-S-D8 rebars ($\rho = 1.7\%$, Figure 6.4) were adopted, respectively. Top and bottom transverse reinforcement was applied in all slabs (to control crack development): 8 mm diameter RB bars were used in slabs from RB and RBP series (spaced at 170 mm) and 6 mm diameter bars were used in slabs with SC and steel bars (spaced at 160 mm). The reference (clear) concrete cover thickness adopted in all slabs was 2.5 cm, except in slabs SC-C3.5-D10 and RB-C3.5-S-D10, where a cover of 3.5 cm was adopted (the concrete cover to bar diameter ratio, *c/d*, ranged between 2.1 and 3.5).

As mentioned above, the study included slabs with continuous or spliced reinforcement, and rebars with straight or 90º bent extremities, either in the anchorage zones or in the splices. The tension lap splices were designed based on the recommendations of ACI 440.1R [6] for ambient temperature conditions (as this is not covered by CNR-DT 203/2006 [7]), resulting in a splice length (l_{splice}) of 64 cm. Based on this reference value, the following development lengths were tested: (i) 30 or 32.5 cm (~0.5 l_{splice}); (ii) 60 or 65 cm (~l_{splice}), and (iii) 84.5 cm (~1.3 l_{splice}). In the slabs with bent-end splices, development lengths of 32.5 cm and 84.5 cm were used (in RBP-LS32.5(B)-D12 and RBP-LS84.5(B)-D12, respectively), corresponding to the straight overlapping length excluding the bend (*cf.* Figure 6.5 and Figure 6.6). Unlike common practice, the splices were intentionally positioned at the centre of the span and directly exposed to fire to trigger the local failure of the overlapping rebars (note that in buildings, splicing should be performed in less loaded zones).

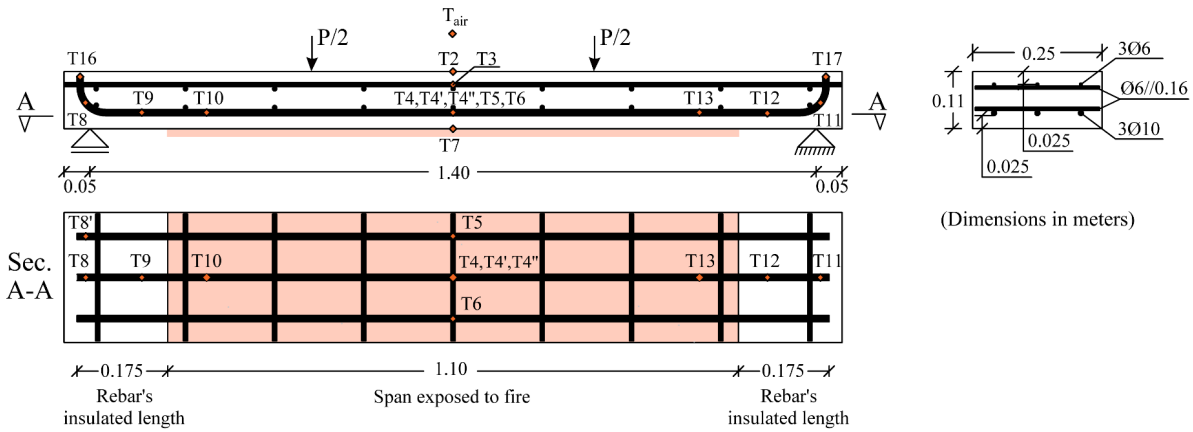

Figure 6.1. Reinforcement distribution and position of thermocouples of slabs with continuous reinforcement and bent anchorages: slabs SR-C2.5-D10 and RBP-C2.5-D12.

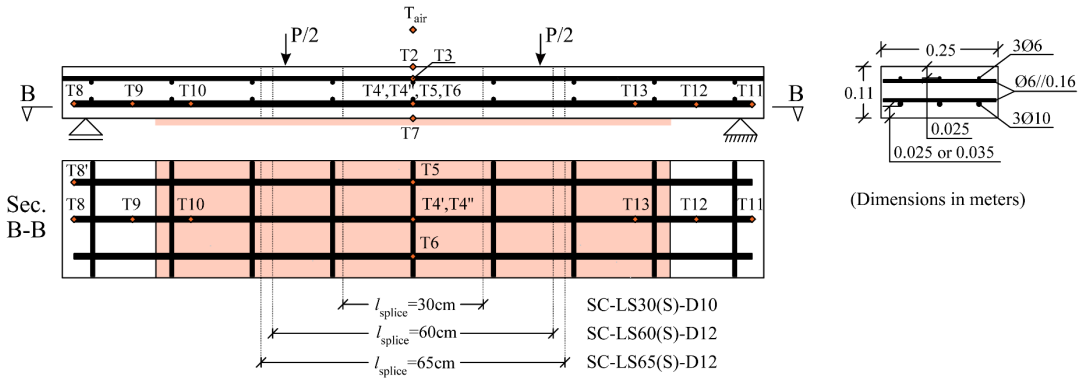

Figure 6.2. Reinforcement distribution and position of thermocouples of slabs from SC series: slabs SC-C2.5-D10, SC-C3.5-D10, SC-LS32.5(S)-D10, SC-LS60(S)-D10 and SC-LS65(S)-D10.

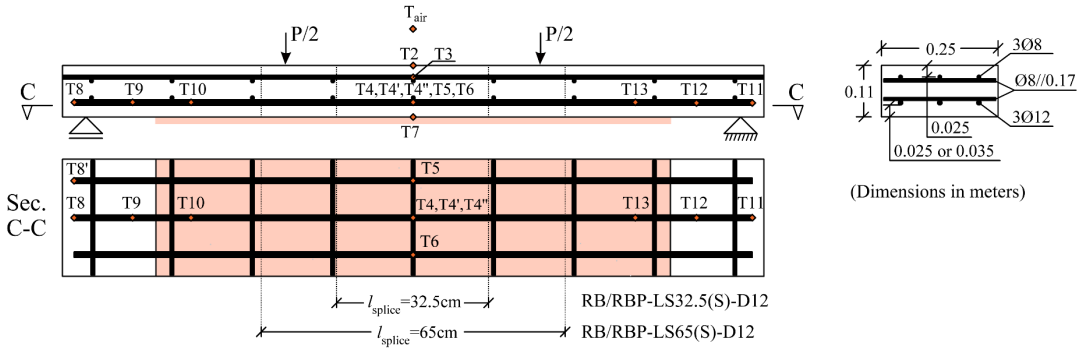

Figure 6.3. Reinforcement distribution and position of thermocouples of slabs with continuous and spliced reinforcement (12 mm diameter) with straight ends: slabs RB/RBP-C2.5-D12, RB-C3.5-D12, RB/RBP-LS32.5(S)-D12 and RB/RBP-LS65(S)-D12.

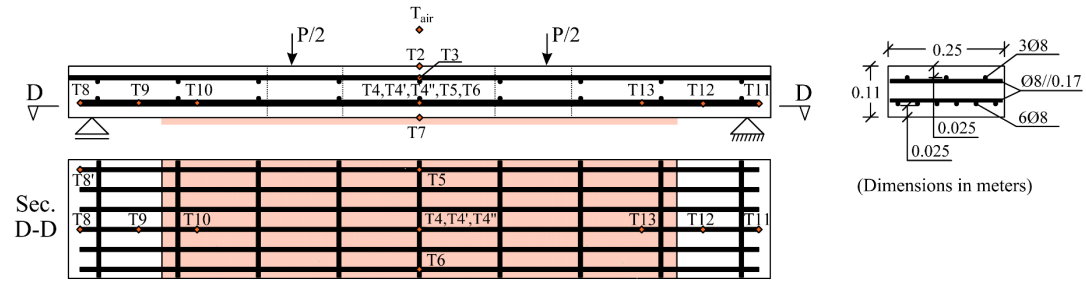

Figure 6.4. Reinforcement distribution and position of thermocouples of slab RB-C2.5-D8 (bars with 8 mm diameter).

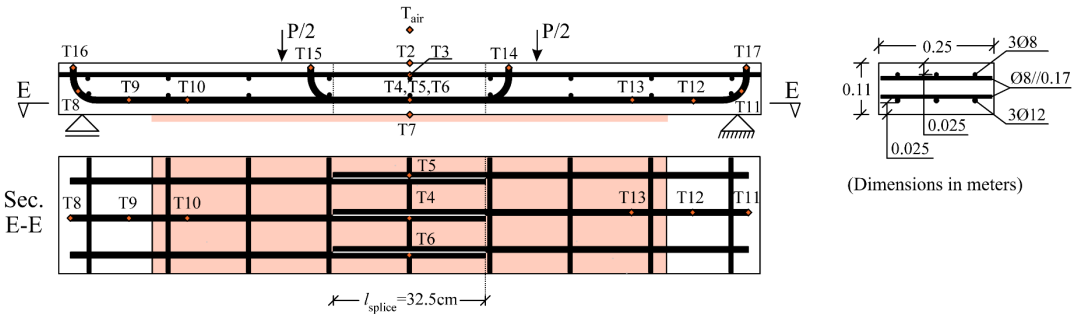

Figure 6.5. Reinforcement distribution and position of thermocouples of slab RBP-LS32.5(B)-D12 (similar to slab RBP-LS32.5(S)-D12 excluding the bent ends).

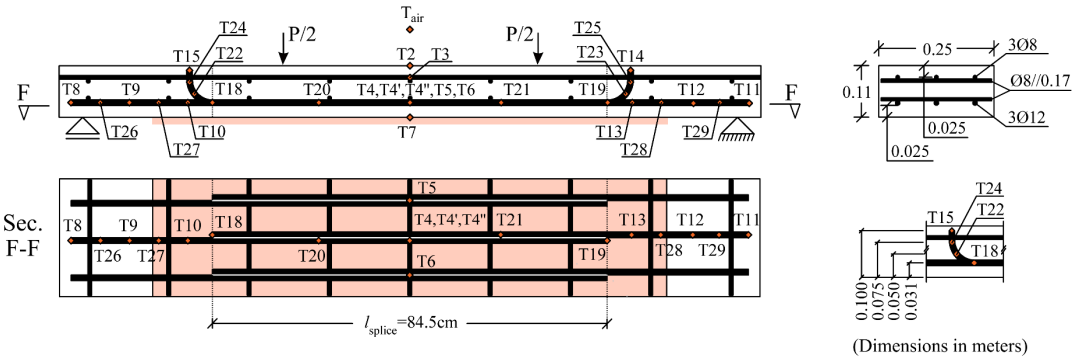

Figure 6.6. Reinforcement distribution and position of thermocouples of slab RBP-LS84.5(B)-D12 (similar to slab RBP-LS84.5(S)-D12 excluding the bent ends).

6.2.4. Flexural tests at ambient temperature

Flexural tests at ambient temperature were performed to characterize the mechanical response of the slab strips at ambient temperature and the corresponding failure modes. The tests were carried out in a four-point bending simply supported configuration with two concentrated loads applied at thirds of the 1.40 m span, as illustrated ahead in Figure 6.7; a similar configuration was used in the fire resistance tests (*cf.* Section 6.2.5). The midspan displacement of the slabs was measured with an electric displacement transducer from *TML* (model *CDP-100* and a stroke of 100 mm) and the applied load was measured with a *Novatech* load cell (load capacity of 200 kN). Crack widths were measured at predefined load values (the cracking load and 25%, 50%, 60%, 70% and 80% of the design load) using a *DinoCapture* digital microscope. Additionally, strain gauges were installed in the longitudinal reinforcement in the midspan section. Table 6.3 summarizes the results obtained in terms of maximum load, strains measured in the bottom reinforcement at maximum load and failure modes. It should be noted that the slabs with concrete type III (SR-C2.5-D10 and RBP-LS84.5(S)/(B)-D12) were not tested at ambient temperature, only in fire.

Table 6.3. Results of flexural tests at ambient temperature.

Slab strip	Concrete type	Bar continuity	Maximum load [kN]	Strain in rebars at maximum load [%]	Failure mode
SR-C2.5-D10	II	Continuous	45.7	1.23	Shear failure
SC-C2.5-D10	I	Continuous	29.2	1.36	Shear failure
SC-C2.5-D10	II	Continuous	30.8	1.07	Shear failure
SC-C3.5-D10	I	Continuous	23.2	1.36	Shear failure
SC-C3.5-D10	II	Continuous	19.9	1.05	Shear failure
SC-LS30(S) -D10	I	Spliced	31.5	0.69	Slippage in splices
SC-LS60(S)-D10	I	Spliced	34.8	0.71	Shear failure
SC-LS65(S)-D10	II	Spliced	31.8	0.60	Shear failure
RB-C2.5-D12	II	Continuous	42.4	0.74	Shear failure
RB-C3.5-D12	II	Continuous	27.2	0.65	Shear failure
RB-LS32.5(S)-D12	II	Spliced	37.8	0.37	Slippage in splices
RB-LS65(S) -D12	II	Spliced	43.6	0.43	Shear failure
RB-C2.5-D8	II	Continuous	39.5	0.82	Shear failure
RBP-C2.5-D12-1	II	Continuous	38.1	0.87	Shear failure
RBP-C2.5-D12-2	II	Continuous	40.1	0.76	Shear failure
RBP-LS32.5(S)-D12	II	Spliced	38.5	0.40	Shear failure
RBP-LS32.5(B)-D12	II	Spliced	36.9	0.41	Shear failure
RBP-LS65(S)-D12	II	Spliced	42.5	0.53	Shear failure

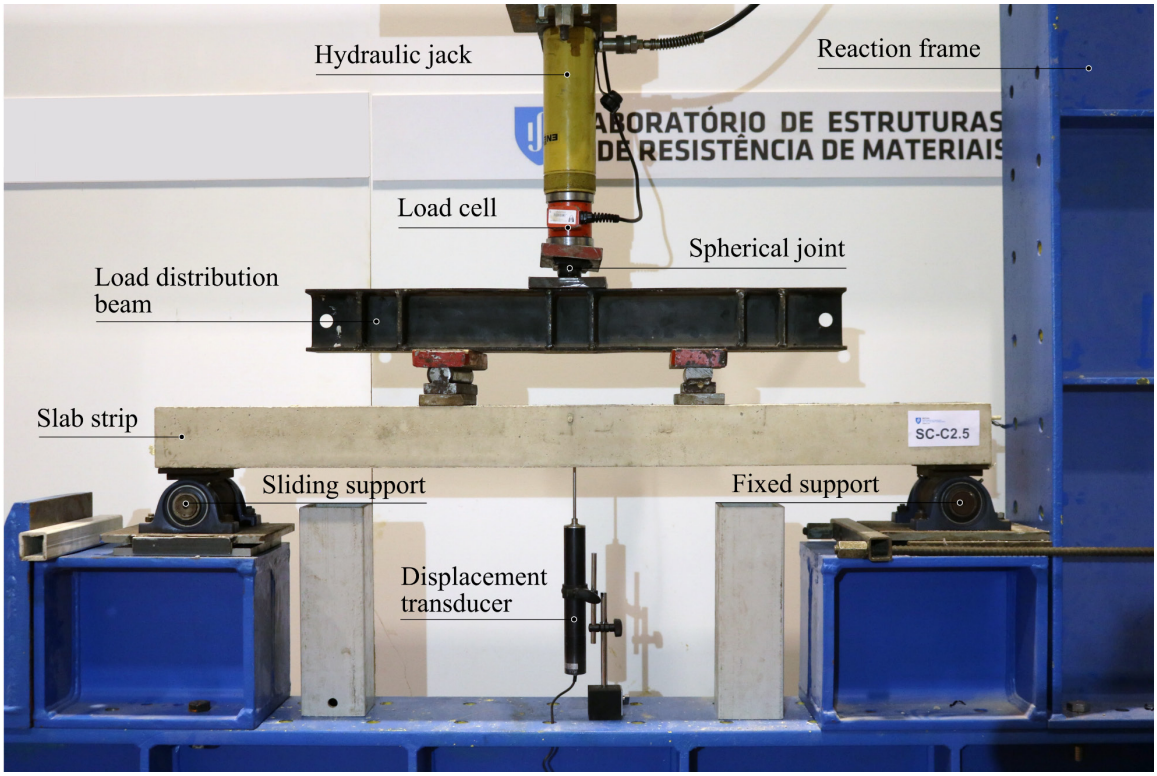

Figure 6.7. Setup of flexural tests at ambient temperature.

The load *vs.* midspan displacement responses obtained are shown in Figure 6.8a for slabs with SC bars, in Figure 6.8b for slabs with RB bars and in Figure 6.8c for slabs with RBP bars. As expected, all slabs presented similar stiffness up a certain load level (approximately 8 kN), corresponding to the elastic uncracked branch of the response. For higher loads, their stiffness was considerably reduced due to cracking; in this phase, the behaviour was markedly different in the steel-RC and GFRP-RC slabs, as shown in Figure 6.8a, with the former being much stiffer due to the higher tensile modulus of steel compared to GFRP. In the steel-RC slab, stiffness was approximately constant up to 35-40 kN and then the response became again non-linear with stiffness reduction. Failure occurred due to shear (because the actual concrete properties were lower than those considered in design – a concrete class C25/30 had been assumed) and this also explains the relatively low ductility and deformations reflected in the load-displacement curve.

Regarding the behaviour of the GFRP-RC slabs after cracking, all presented approximately constant stiffness up to the maximum load and similar displacements at failure (even if for different loads); both strength and (cracked) stiffness were significantly lower compared to the steel-RC slab. A stiffening effect was observed in slabs with spliced reinforcement (LS series) comparing to slabs with continuous bars – this is attributed to the presence of overlapped bars in the midspan sections, which locally increases (doubles) the reinforcement ratio. It is worth noting the small load reductions observed in

Figure 6.8 for slabs with FRP reinforcement, which are likely due to momentary slip between the reinforcement and concrete during the development of a new crack.

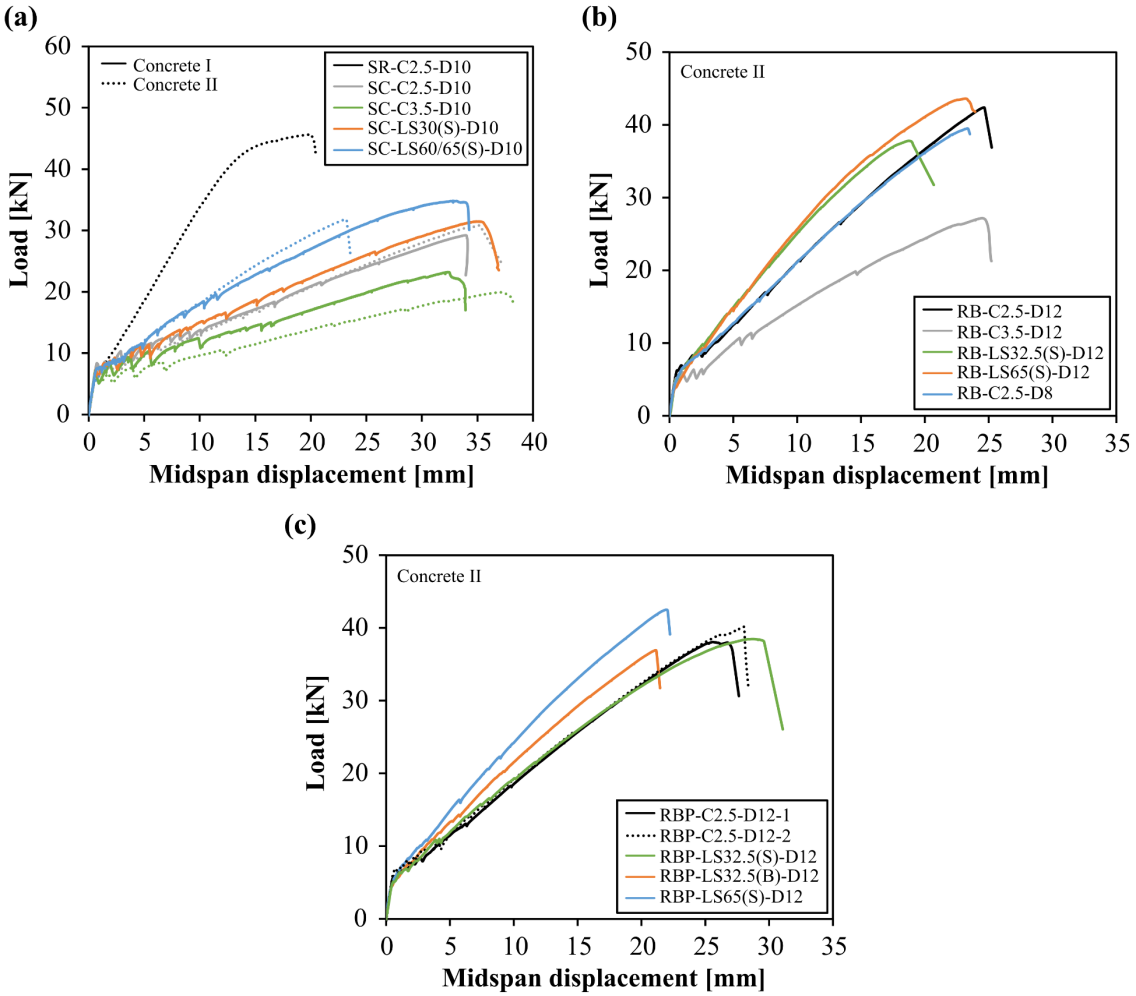

Figure 6.8. Load *vs.* midspan displacement curves from flexural tests at ambient temperature of slabs from series (a) SR and SC, (b) RB and (c) RBP.

Unlike what the author expected, almost all slabs (except slabs SC-LS30 and RB-LS32.5-S, *cf.* Table 6.3) failed prematurely by shear (as illustrated in Figure 6.9a), instead of concrete crushing. Two main reasons explain this premature failure: (i) the lower properties of concrete compared to what was considered at design; (ii) and the possible overestimation, by the CNR-DT 203/2006 [7] standard, of the contribution of the FRP reinforcement to the shear capacity of the slabs through dowel effect[7]. In case of slabs SC-LS30(S)-D10 and RB-LS32.5(S)-D12, failure occurred due to pull-out of the rebars along

[7] Considering the actual concrete properties and disregarding the dowel effect, the predicted failure mode matches that observed in the tests and fairly good predictions of the load capacity are obtained. Although the dowel strength of the GFRP rebars was not determined, in some slabs it was possible to observe that the rebars were broken in the transverse direction, aligned with the main shear crack, as shown in Figure 6.9d. This suggests that the contribution of the rebars to the dowel effect may be lower than that assumed in [7] (even if the shear strength of the rebars is not explicitly considered) and therefore the design shear strength of the slabs is overestimated.

the lap-splices (Figure 6.9b and Figure 6.9c), with extensive cracking and local spalling of part of the concrete cover. This was one of the expected failure modes since the development length of 30/32.5 cm is about half of the minimum recommended development length for FRP reinforcement (at ambient temperature).

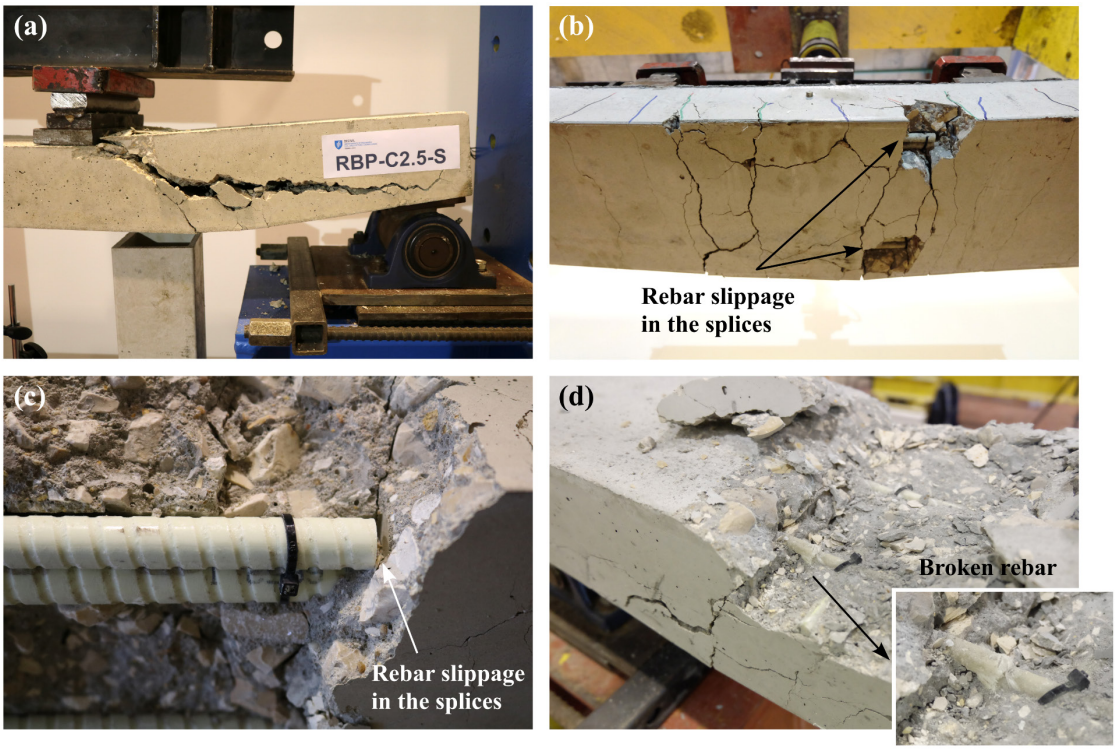

Figure 6.9. Typical failure modes observed in flexural tests performed in GFRP-RC slab strips at ambient temperature: (a) shear failure; (b,c) rebar slippage and local concrete spalling; d) section of GFRP rebar fractured in transverse direction, aligned with shear crack.

As shown in Figure 6.10, the behaviour of slabs with steel and GFRP reinforcement also presented some differences in terms of crack opening. For the same load level and concrete cover, GFRP-RC slabs presented wider cracks comparing to the steel-RC slab, owing to the lower tensile modulus of the GFRP rebars. As expected, wider cracks were also observed in slabs where rebars had higher concrete cover (*i.e.* concrete type II, *cf.* Figure 6.10a); nevertheless, all GFRP-RC slabs fulfilled the admissible crack width requirements for serviceability limit states defined in ACI 440.1R-15 [6]. The influence of concrete strength on the load-deflection response of the slabs was well reflected in the maximum loads of slabs from series SC-C3.5-D10 and SC-LS60/65(S)-D10 (Figure 6.9a): as expected, in those slabs slightly higher loads were attained with higher concrete strength. For slabs SC-C2.5-D10 such effect was not clear in the tests, possibly due to the higher scatter associated to the shear failure mode. In the case of series SC-C3.5-D10, the slab with lower strength concrete presented lower stiffness and significantly wider cracks than those measured in the corresponding slab with higher strength concrete. In fact, as expected, wider cracks were consistently observed in slab strips with lower strength concrete.

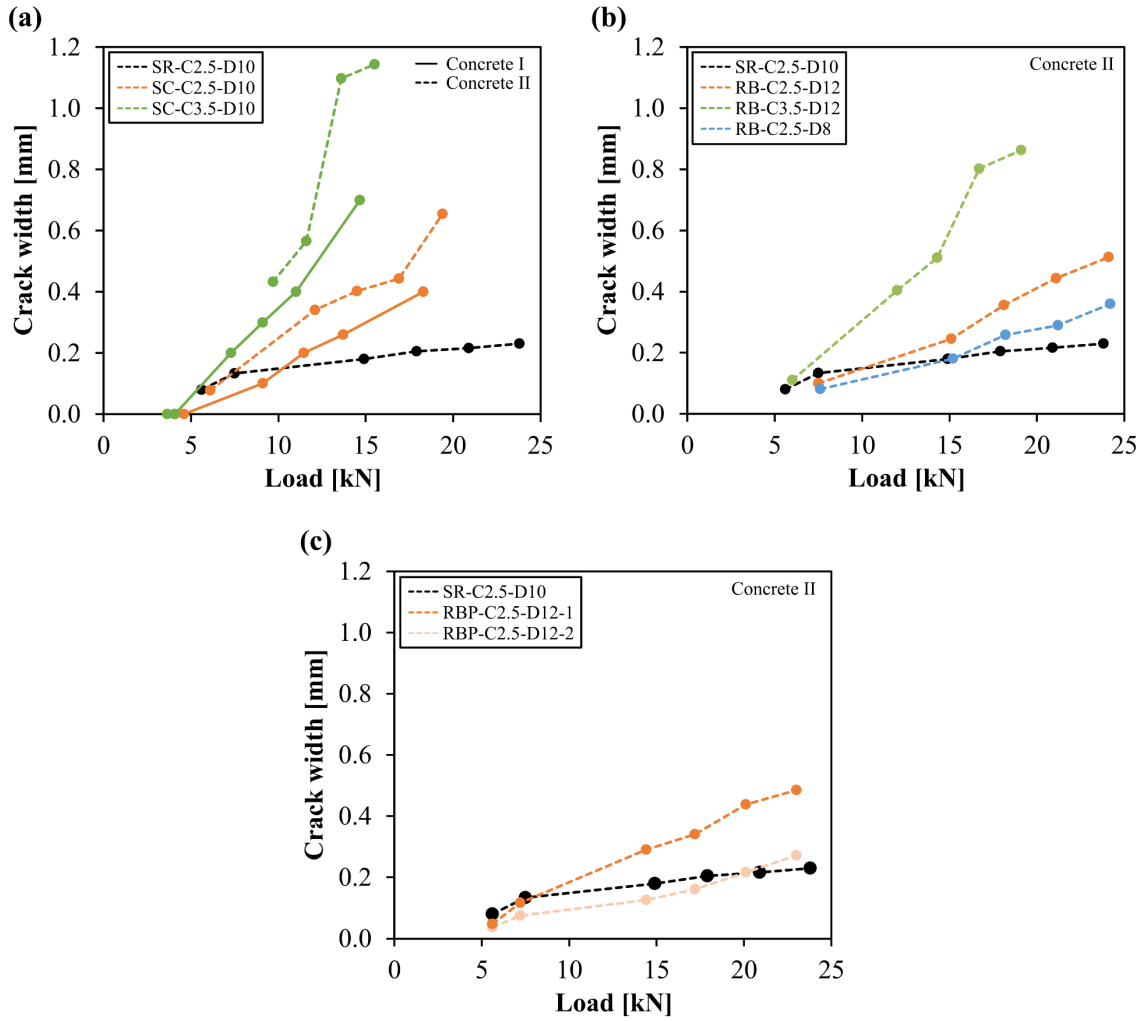

Figure 6.10. Crack width as a function of applied load, measured in flexural tests carried out at ambient temperature – slab SR-C2.5-D10-II and slabs from (a) SC series, (b) RB series and (c) RBP series.

6.2.5. Fire resistance tests setup, instrumentation and procedure

In the present section, the test setup, instrumentation and procedure adopted in the fire resistance tests is described. The test setup is presented in Figure 6.11 and Figure 6.12. The tests were performed in an intermediate scale furnace (exterior dimensions of 2.10 m (height) × 1.35 m (width) × 1.20 m (depth)) that heated the bottom surface of the slabs according to the ISO 834 standard fire curve [24]. The slabs (0.25 m wide) were positioned over the furnace top opening (area of 1.10 m × 0.80 m) and the remaining area was insulated with a set of metallic modules filled with ceramic wool (Figure 6.11a). Strips of ceramic wool were also placed near the supports (Figure 6.11b), as well as along the lateral sides of the slabs, protruding from their bottom surface (Figure 6.12c), to ensure proper lateral insulation. As illustrated in Figure 6.11b, the slabs were directly exposed to fire over a length of 1.10 m and the anchorage zones of the reinforcement were insulated over a length of 175 mm in each extremity (the

total slab length protected from direct fire exposure was 200 mm in each end). As showed in Figure 6.12d, a non-flammable fabric was used to cover the space between the exhaustion system of the furnace and the slab's top edges to minimize air convection during the tests.

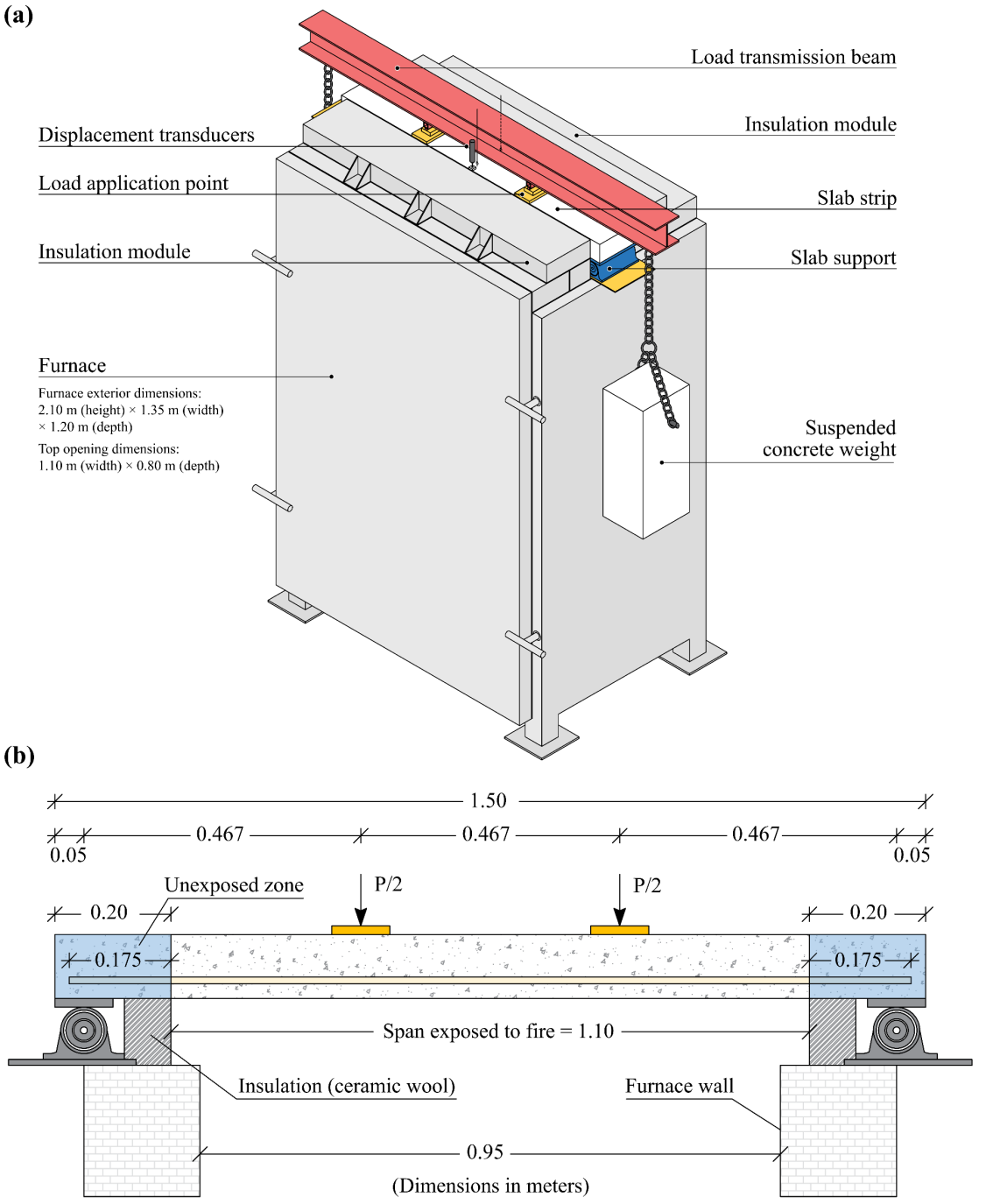

Figure 6.11. Fire resistance tests setup: (a) general view; (b) longitudinal scheme.

Figure 6.12. Fire resistance tests setup: (a) general view during loading stage; (b) displacement transducers installed at midspan; (c) bottom view of the slab; (d) general view during the tests.

As shown in Figure 6.11, the slabs were placed at the top of the furnace over one fixed support and one sliding support (same configuration used in the flexural tests at ambient temperature described in Section 6.2.4, *cf.* Figure 6.7), which were connected to a steel reaction frame by means of steel rods (*cf.* Figure 6.12a). Concrete weights were suspended at both extremities of a load transmission beam, as shown in (Figure 6.11a and Figure 6.12a), applying two concentrated loads in the slabs at thirds of their span. A combined system of pulleys, chains and hydraulic jacks were used to lift and then slowly lower the weights into position; this system minimized the dynamic effects derived the load application and avoided the transmission beam to move laterally during the loading process.

The sustained fire load applied to the slabs, listed in Table 6.4, were calculated according to the recommendations of Eurocode 2 [79] – corresponding to 70% of the design load capacity[8] at ambient temperature. The strains and estimated stresses in the main reinforcement at the midspan section of each slab at the beginning of the fire tests are also presented in Table 6.4, calculated based on the strain measurements obtained in the flexural tests performed at ambient temperature. The fire loads corresponded to a fraction of the slabs' failure load at ambient temperature, ranging from 47% and 68%.

[8] All fire loads were calculated assuming the design values of a concrete class C25/30 (according to [192]).

Table 6.4. Mechanical loading applied in the fire tests and corresponding tensile stresses and strains in bottom reinforcing bars.

Slab strip	Concrete type	Bar continuity	Fire load [1] [kN]	Fire load as a percentage of failure load at ambient temperature	Initial (t=0 min) tensile stress [2] [MPa]	Initial (t=0 min) tensile strain [2] [%]
SR-C2.5-D10	II	Continuous	20.9	46%	370	0.18
SR-C2.5-D10 [3]	III	Continuous	20.9	-	-	-
SC-C2.5-D10	I	Continuous	16.9	58%	351	0.73
SC-C2.5-D10	II	Continuous	16.9	55%	241	0.50
SC-C3.5-D10	I	Continuous	13.6	59%	301	0.62
SC-C3.5-D10	II	Continuous	13.6	68%	314	0.65
SC-LS30(S)-D10	I	Spliced (S)	16.9	54%	124	0.26
SC-LS60(S)-D10	I	Spliced (S)	16.9	49%	152	0.32
SC-LS65(S)-D10	II	Spliced (S)	16.9	53%	136	0.28
RB-C2.5-D12	II	Continuous	21.1	50%	215	0.36
RB-C3.5-D12	II	Continuous	16.7	62%	232	0.39
RB-LS32.5(S)-D12	II	Spliced (S)	21.1	56%	107	0.18
RB-LS65(S)-D12	II	Spliced (S)	21.1	48%	129	0.21
RB-C2.5-D8	II	Continuous	21.2	54%	239	0.41
RBP-C2.5-D12-1	II	Continuous	20.1	53%	240	0.40
RBP-C2.5-D12-2	II	Continuous	20.1	50%	209	0.35
RBP-LS32.5(S)-D12	II	Spliced (S)	20.1	52%	112	0.19
RBP-LS32.5(B)-D12	II	Spliced (B)	20.1	54%	132	0.22
RBP-LS65(S)-D12	II	Spliced (S)	20.1	47%	147	0.24
RBP-LS84.5(S)-D12 [3]	III	Spliced (S)	20.1	-	-	-
RBP-LS84.5(B)-D12 [3]	III	Spliced (B)	20.1	-	-	-

[1] Total fire load (*i.e.*, sum of the two point loads).
[2] Tensile stresses and strains at the level of the bottom reinforcement in the midspan section.
[3] Slab not tested at ambient temperature.

Regarding the instrumentation, two electrical wire-displacement transducers from *TML* (model *CDP-500* with a stroke of 500 mm) and an electric displacement transducer also from *TML* (model *CDP-100* with a stroke of 100 mm) were used to measure the midspan displacement at the top (cold) surface of the slabs, placed at different alignments of the slabs' width, as shown in Figure 6.12b. The vertical displacement in the supports was also measured with additional electrical displacement transducers.

The slabs were instrumented with thermocouples (type K, conductor diameter of 0.25 mm), placed in both the reinforcement and the concrete according to the distributions illustrated in Figure 6.1 to Figure 6.6. The instrumentation was designed in order to monitor the temperature evolution in locations where failure was likely to occur and with the purpose of measuring the thermal gradients along the height and length of the slab strips; this way, the midspan section, the fire exposed span and the insulated anchorage zones of the reinforcement were thoroughly instrumented in several alignments, allowing to comprehensively assess these zones. Table 6.5 shows the location of each thermocouple. In slabs from RBP-LS84.5 series (Figure 6.6), temperatures were measured along the entire overlapping length and bent ends of the splices. The distribution of temperatures along the transverse direction of the slabs was assessed by placing thermocouples in the same longitudinal alignment but in different rebars, namely at midspan (T4, T5 and T6) and in one of the extremities of the slabs (T8 and T8'). Temperature was also measured at midspan in the following locations: (i) in the concrete, at the top (T2) and bottom (T7) surfaces of the slabs; (ii) in the upper longitudinal reinforcement, 2.5 cm below the slabs' top surface (T3), and (iii) in the air above the slab (T_{air}). The thermocouples were fixed at the surface of the rebars, at their mid-height; in some slabs, the central bottom rebar (at midspan) was also instrumented in the bottom (T4') and top (T4'') sides with the purpose of measuring the thermal gradient through the rebars' diameter.

The tests were conducted according to the test recommendations provided in [24]. First, the sustained structural loading was applied (slowly) on the slabs through the load transmission beam. Then, after a period for stabilization of the slabs' deflection, the ISO 834 standard fire curve [24] was initiated and maintained until collapse. During the entire duration of the tests, the midspan deflection, the temperature within the slabs and of the air above the slabs were monitored; the furnace temperature was also measured with thermocouples located close to the lateral walls of the furnace.

Table 6.5. Location of thermocouples in the slab strips.

Thermocouple	Location	Distance to centre of slab [cm]	Distance to bottom face of slab [cm]
T_{air}	Air above slab (midspan)	0	-
T2	Top slab surface (midspan)	0	11
T3	Top reinforcement layer (midspan)	0	10
T4, T5,T6	Bottom reinforcement layer (midspan)	0	3.1 / 4.1 (3)
T4' (1)	Bottom reinforcement layer (midspan)	0	2.5 / 3.5
T4'' (2)	Bottom reinforcement layer (midspan)	0	3.7 / 4.7
T7	Bottom slab surface (midspan)	0	0
T8, T8', T11	Anchorage extremity (straight bar)	70.9	3.1 / 4.1 (3)
T9, T12	Insulated length	60.0	3.1 / 4.1 (3)
T10, T13	Span exposed to fire	47.5	3.1 / 4.1 (3)
T14, T15	Splice (bent bar extremity)	21.2 / 47.2 (4)	10
T16, T17	Anchorage extremity (bent bar)	71.9	10
T18, T19	Splice (bent development)	46.1	5
T20, T21	Splice (straight development)	21.1	3.1
T22, T23	Splice (end of straight development)	42.3	3.1
T24, T25	Splice (bent development)	47.1	7.5
T26, T29	Insulated length	66.3	3.1
T27, T28	Span exposed to fire	53.8	3.1

(1) Thermocouple placed on the top side of the rebar.
(2) Thermocouple placed on the bottom side of the rebar.
(3) Concrete cover + half (nominal) bar diameter: 3.1 cm in slabs with 2.5 cm cover; 4.1 cm in slabs with 3.5 cm cover.
(4) 21.2 cm in slab RBP-LS32.5-B, 47.2 cm in slab RBP-LS84.5-B.

6.3. Fire performance criteria

According to EC2 – Part 1-2 [79], concrete members with load bearing and separating functions exposed to standard fire exposure should comply with three performance requirements, defined in EN 1363-1 [209], concerned with load bearing capacity, thermal insulation and integrity. The load bearing capacity criterion for flexurally loaded members is defined by a deflection limit (D) and a deflection rate limit given by Equation (6.1) and Equation (6.2), respectively,

$$D = \frac{L^2}{400d}\,[\text{mm}] \tag{6.1}$$

$$\frac{dD}{dt} = \frac{L^2}{9000d}\,[\text{mm/min}] \tag{6.2}$$

where L is the clear span of the structural member and d is the distance from the extreme fibre of the cold design compression zone to the extreme fibre of the cold design tension zone of the members' cross-section. For the slabs tested in this study, the deflection limit was 44.5 mm and the rate of deflection limit was 2 mm/min. The insulation criterion is satisfied while: (i) the average temperature at the unexposed surface of the member does not increase more than 140 ºC w.r.t. the initial average temperature, and (ii) the temperature at the unexposed surface, at any location, does not increase more than 180 ºC w.r.t. the initial average temperature. The integrity criterion was not able to be assessed in the experiments (yet, no passage of flames through the slabs occurred).

6.4. Fire resistance tests of slabs with sand coated rebars – results and discussion

6.4.1. Thermal behaviour

The following subsections present the results obtained in the fire resistance tests performed in slabs with sand coated bars (series SC, concrete types I and II) and in one reference steel-RC slab (concrete type II). Representative temperature profiles obtained during the tests are presented in Figure 6.13a for slab SR-2.5-D10, Figure 6.13a b for slabs SC-C2.5-D10 and Figure 6.13a c for slabs SC-C3.5-D10. The temperatures measured (at midspan) in slabs with lap spliced reinforcement were slightly higher (maximum differences of 30 ºC) than those registered in slab SC-C2.5-D10 (with continuous rebars), most likely due to more extensive cracking in the former. It should be noted that the analysis presented herein is valid for both types of concrete tested, since no relevant differences were found regarding the temperature profiles obtained for the two types of concrete; for that reason, and as an example, temperature profiles refer to slabs made with concrete type II. Moreover, due to a problem related with the setup (*cf.* Section 6.4.2), the test of slab SR-C2.5-D10-II had to be interrupted before failure; consequently, in this case the temperature profiles are only plotted up to that moment (100 min).

The temperature measured by the thermocouple located next to the slabs' bottom surface (T7) followed closely the ISO 834 standard fire curve. Temperatures progressively increased with time in all thermocouples, even if at different rates. As expected, temperatures decreased from the bottom to the top section of the slabs; for the same time (83 min) the temperature difference between the bottom (T7) and top (T2) surfaces of the strips was 678 ºC in slabs with 2.5 cm of cover and 549 ºC in slabs with 3.5 cm of cover. In all slabs, when the concrete temperature approached 100 ºC, the heating rates decreased

considerably (increasing again a few minutes later) due to the moisture evaporation. It is worth mentioning that no spalling was detected at the end of the tests, except for slab SC-LS30(S)-D10, in which local spalling occurred, but due to the splices and not to the water steam pressure.

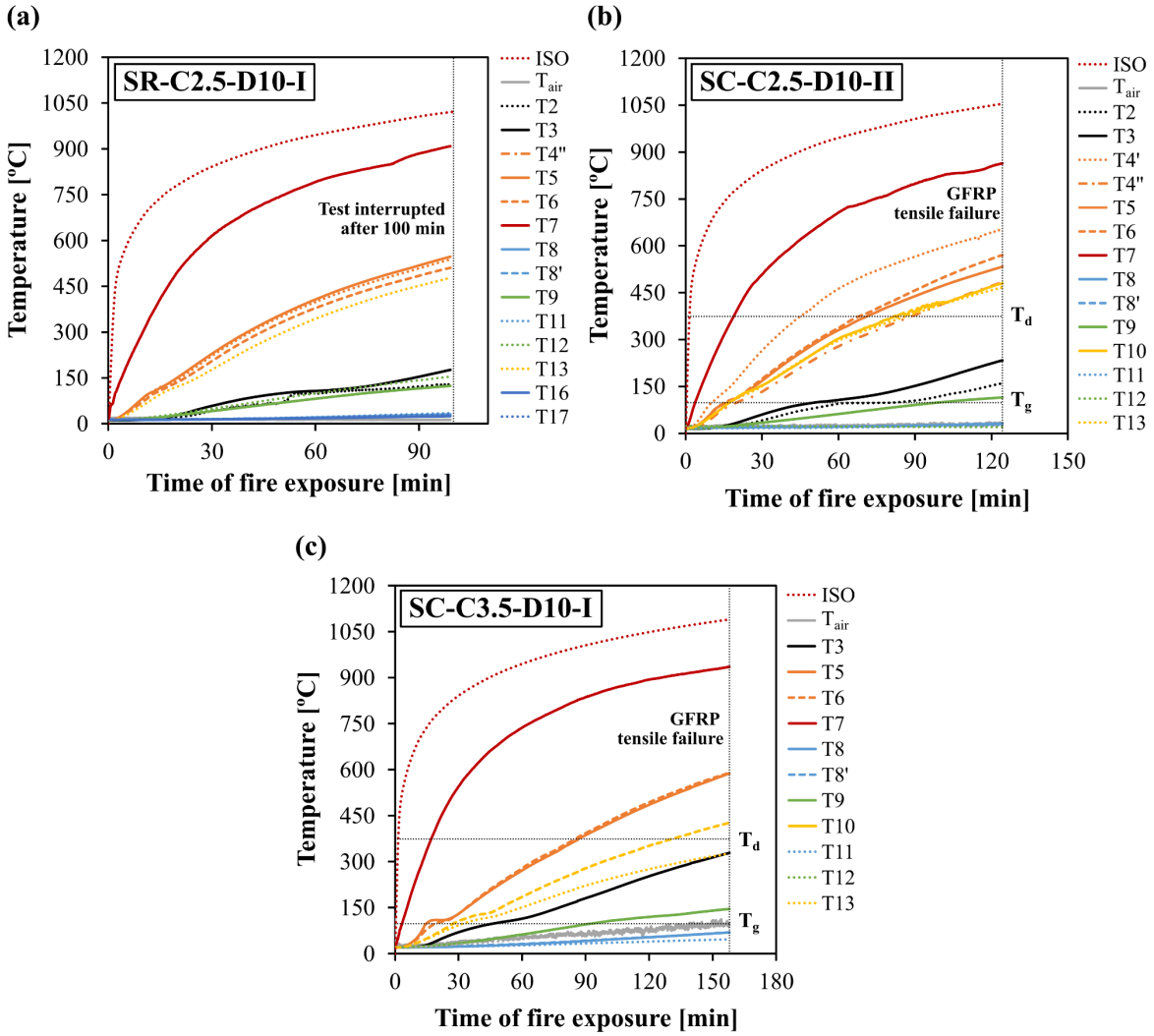

Figure 6.13. Representative temperature profiles obtained during fire resistance tests: a) slab SR-C2.5-D10-I; b) slab SC-C2.5-D10-II; c) slab SC-C3.5-D10-I.

As mentioned, in slabs with GFRP reinforcement the measurements of thermocouples T4' and T4'' allowed to evaluate the thermal gradient through the thickness of the rebars located at midspan. Since FRP rebars have low thermal conductivity, temperature at the top of the rebars was significantly lower than in the bottom. In the longest test (SC-C2.5-D10-I, Figure 6.13b) temperatures in the bottom and top parts of the rebars differed 189 ºC after 124 min of exposure to fire. Measurements on thermocouples T4, T5 and T6 (at midspan) and T8 and T8' (at the anchorage extremity) confirmed that the distribution of temperatures in the transverse direction of the slabs was relatively uniform. Additionally, the measurements of thermocouples located symmetrically along the longitudinal direction (*e.g.* T10 and

T13) also showed similar readings. The minor differences observed, especially noticeable in the midspan section, are justified by the heterogeneity of concrete, small differences in the position of the temperature sensors or due to cracks opened/developed during the tests.

6.4.1.1. Effect of type of reinforcement (steel *vs.* sand coated GFRP)

Comparing slabs SR-C2.5-D10 (Figure 6.13a) and SC-C2.5-D10 (Figure 6.13b), both with the same concrete cover (2.5 cm) but with steel and GFRP rebars, respectively, no significant differences were found regarding the temperatures measured in the end anchorages (T8 and T11) and in the top layer of reinforcement at midspan (T3). However, in the remaining thermocouples, temperatures measured in the steel rebars were slightly higher than those obtained in the GFRP rebars, especially for the thermocouples located in the bottom reinforcement at midspan (*cf.* Figure 6.14a ahead). As an example, for 100 min of fire exposure, the temperature at thermocouples T5 (midspan) was 541 ºC in slab SR-C2.5-D10 and 470 ºC in slab SC-C2.5; at a distance of 15 cm from the end of the slab, thermocouples T9 measured 125 ºC in slab RC-C2.5-D10 and 99 ºC in slab SC-C2.5-D10. These results derive mostly from the higher thermal conductivity of steel comparing to GFRP, but also from the heterogeneity of concrete, the different cracking behaviour or possible (small) differences in the position of the rebars and the thermocouples.

6.4.1.2. Effect of concrete cover thickness

The effect of the concrete cover thickness on the thermal response of the GFRP-RC slabs can be assessed by comparing Figure 6.13b for slab SC-C2.5-D10 (2.5 cm cover) with Figure 6.13c for slab SC-C3.5-D10 (3.5 cm cover). As expected, slab SC-C3.5 presented lower temperatures in the reinforcement due to the increased thermal protection afforded by a thicker layer of concrete cover. The benefit of the increase in cover was not relevant in the anchorage zones since proper insulation of that region was intentionally provided by the test setup adopted (*cf.* Figure 6.11b); however, significant differences were obtained in thermocouples located in the span exposed to fire. After 83 min of fire exposure, the relative difference between the temperatures measured in slabs SC-C2.5-D10 and SC-C3.5-D10 was around 57 ºC in thermocouple T5 (midspan) and 78 ºC in thermocouple T10 (27.5 cm from the end of the slab), with higher temperature being registered, as expected, in the slabs with thinner concrete cover.

6.4.1.3. Unexposed anchorage zones

The temperature progression of some thermocouples located in relevant sections of the bottom reinforcement are plotted in Figure 6.14, depicting the non-linear distribution of temperatures along the slab's length. Temperatures in the bottom reinforcement varied significantly from the directly exposed zones (centre) to the unexposed (anchorage) ones (Figure 6.13 and Figure 6.14).

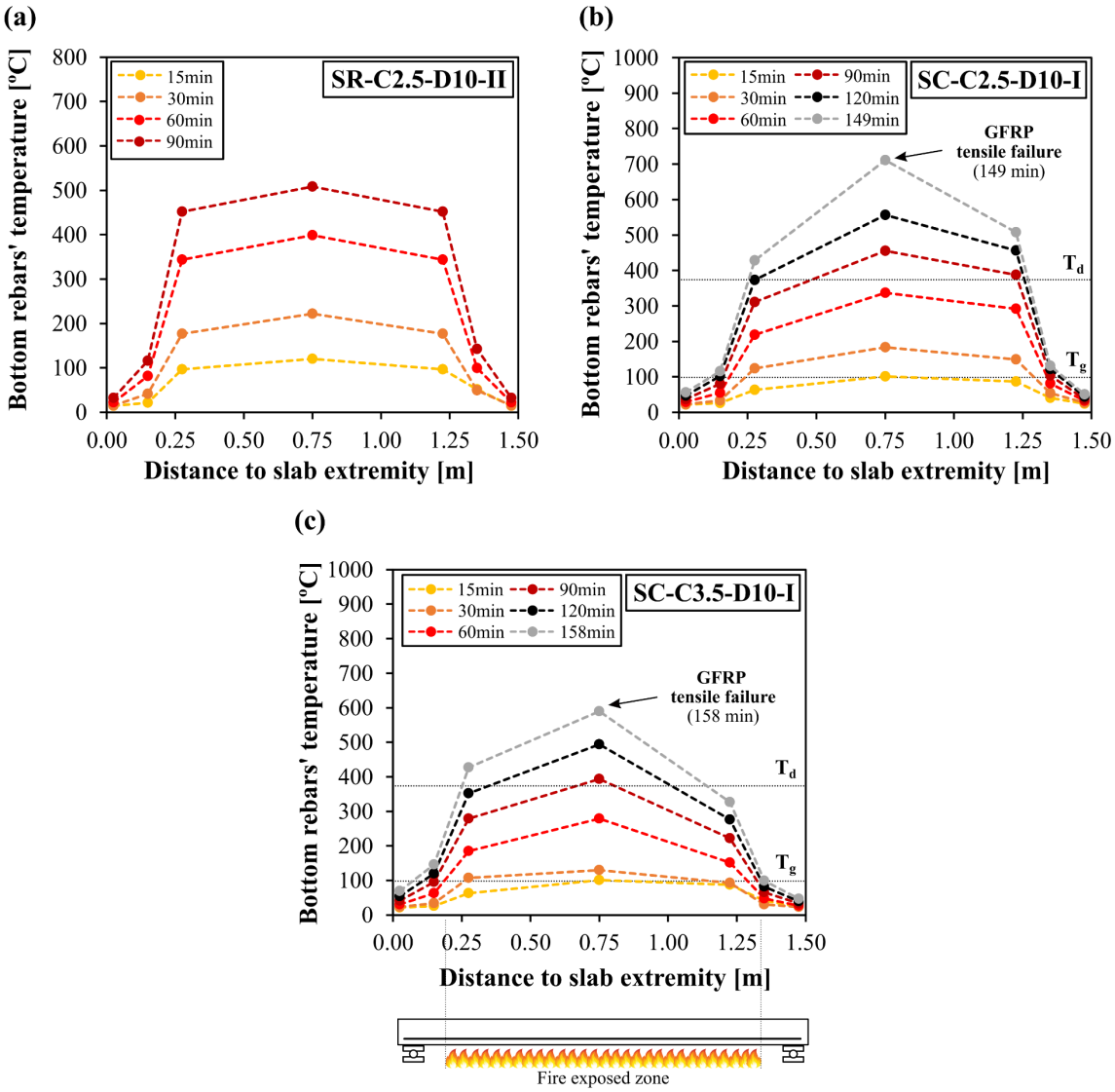

Figure 6.14. Temperature evolution in the lower reinforcement along the length of slabs (a) SR-C2.5-S10-II, (b) SC-C2.5-D10-I and (c) SC-C3.5-D10-I.

Taking the example of the slab with the highest fire endurance (slab SC-C3.5-D10 with concrete type I), the temperature of the bottom bars in the midspan section (T5 and T6) was, at the time of failure (158 min), around 427 ºC, while at the extremities (T8, T8' and T11) it was around 69 ºC, *i.e.* still below the T_g (~98 ºC). However, in thermocouples positioned 12.5 cm away from T8 (T9 and T12, still located in the unexposed zone) temperature was significantly higher (146 ºC) and already above the T_g. This means that even though the unexposed length of reinforcement was 17.5 cm long (on each side), a significant portion of the bars was already undergoing the process of glass transition and, therefore, along that length, the bond was already severely degraded. However, as discussed in the following section, the anchoring length kept below the glass transition temperature was sufficient to avoid slippage of the rebars at both ends, allowing to extend the fire resistance of the slabs and to explore the remaining tensile capacity of the rebars for temperatures considerably above the T_g.

6.4.2. Deflection behaviour

Figure 6.15a presents the variation of the midspan deflection as a function of the time of fire exposure (time zero refers to the onset of the heating stage). The limiting deflection criterion defined in EN 1363-1 [30] described in Section 6.3 is also plotted with a horizontal dashed line. Two aspects should be pointed out beforehand: (i) the displacement measurements show some noise (particularly visible at the end of the tests) due to the relatively low sensitivity of the (high range) wire-displacement transducers; (ii) as mentioned, after 100 min of fire exposure, the fire test of slab SR-C2.5-D10 had to be interrupted due to loss of effectiveness of the thermal insulation system in one of the lateral sides of the slab.

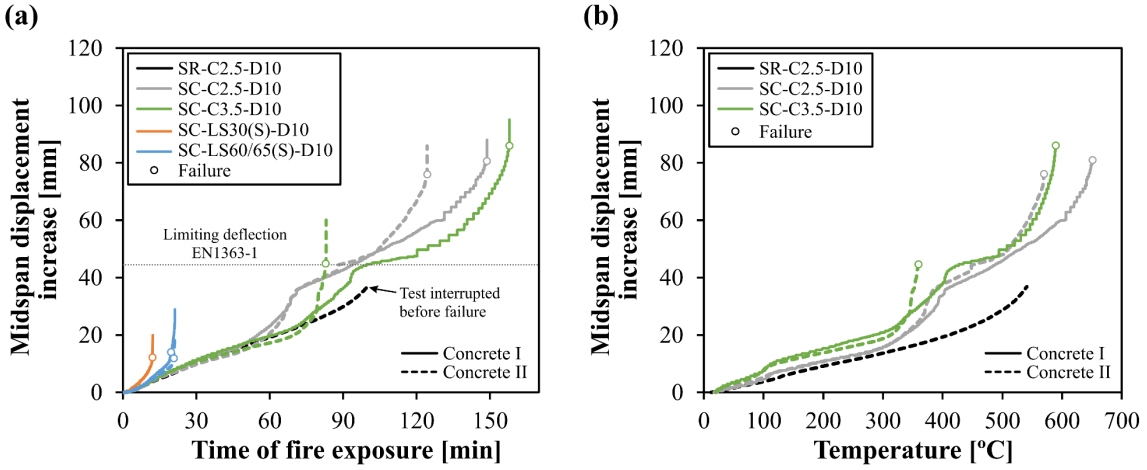

Figure 6.15. Midspan displacement increase with (a) time of fire exposure and (b) temperature of rebars at midspan of slab SR-C2.5-D10 (concrete type II) and slabs from SC series.

The midspan displacements in slabs SR-C2.5-D10 and SC-C2.5-D10 (same concrete cover but different type of reinforcement) presented a similar variation in the first 50 min of fire exposure. Then, the displacements in slab SC-C2.5-D10 increased more rapidly than in slab SR-2.5-D10, most likely due to the higher susceptibility of GFRP rebars to high temperatures: as previously stated, comparing to steel reinforcement, GFRP rebars present a steeper degradation of their mechanical and bond properties as temperature increases. After 100 min of fire exposure, the midspan displacements in those slabs had increased 37 mm and 47 mm, respectively.

From a qualitative point of view, the midspan displacement *vs.* time curves of slabs SC-C2.5-D10 and SC-C3.5-D10 presented the same five stages. As further discussed below, the beginning of each stage was triggered at similar temperatures (*cf.* Figure 6.15b), though occurring at different time intervals (*cf.* Figure 6.15a). Each stage is characterized by different rates of displacement increase explained by: (i) the varying thermal gradients throughout the slabs' thickness, and (ii) the (non-linear) variation with temperature of the mechanical properties of the materials and of the concrete-rebar bond properties. Next, a brief description of the midspan displacement *vs.* time of the referred curves is given.

During the first 5 min, no significant displacement increase was observed, since the rebar's temperature was low (below 30 ºC), as well as the thermal gradient in the midspan section. In the second stage, which took place between 5 and 52 min of fire exposure (67 min in the case of slab SC-C3.5), the displacement presented a moderate increase at an approximately constant rate, similar to that observed in the slab SR-C2.5-D10. As shown in Figure 6.15b, the displacement increased (even if momentarily) for temperatures slightly above the glass transition temperature (~98ºC); this increase, only noticeable in slabs with GFRP reinforcement, may have been related with the loss of bond in the midspan section probably leading to the development of extensive cracking.

In the third stage, after 52 min and 67 min of fire exposure the displacement rates increased significantly in slabs SC-C2.5-D10 and SC-C3.5-D10, respectively. In those instants, the temperatures in the bottom reinforcement at midspan were very similar, 305 ºC and 310 ºC, respectively; since most of the bond strength (and stiffness) of these rebars is lost up to the beginning of glass transition (*cf.* Figure 4.8 in Section 4.4.3 – page 109), for those temperatures (well above the T_g) the effectiveness of the load transferring mechanisms between the concrete and the GFRP rebars was already severely affected, leading to the development of wider cracks. For this reason, this increase on the displacement rates may be related to the loss of bond, which started from the heated span of the slabs and developed progressively towards the insulated extremities. For the instants referred above, the temperature of the thermocouples distanced 27.5 cm from the end of the slabs (*e.g.* T10, located in the span exposed to fire) was around 257 ºC in slab SC-C2.5-D10 and 210 ºC in slab SC-C3.5-D10, while all thermocouples in the unexposed zones registered temperatures below T_g.

After 72 min and 94 min of fire exposure, respectively in slabs SC-C2.5-D10 and SC-C3.5-D10, the rates of displacement increase reduced considerably, maintaining an approximately constant rate (similar to what was observed in the second stage) up to around 130 min and 114 min of exposure, respectively. The temperatures of the GFRP rebars in the region directly exposed to fire were close to the T_d (>380 ºC): approximately 378 ºC in slab SC-C2.5-D10 and 407 ºC in slab SC-C3.5-D10. At those temperatures, the GFRP-concrete bond is expected to be completely deteriorated along the exposed span of the slabs – from this moment, the behaviour of the GFRP rebars can be compared to that of a "cable", anchored in the cooler extremities of the slabs, which if kept below T_g, provide adequate anchorage for the rebars – a similar mechanism was previously reported by Firmo *et al*. [210,211] for FRP-strengthened beams. The reduction in the displacement rate is partially explained by the degradation with temperature of the tensile modulus of the rebars, which is significantly less pronounced than the degradation of the GFRP-concrete bond (*cf.* Section 3.4.3.3). Further studies are however needed in order to confirm this mechanism. The final stage extended until failure of the slabs, which occurred due to tensile rupture of the rebars at midspan (more details are provided in Section 6.4.3), through a continuous increase in the displacement increase rate.

6.4.3. Fire resistance

Table 6.6 summarizes the results of the fire resistance tests regarding the deflection response of the slabs, specifically (i) the maximum deflection increase and deflection rate, both measured at the midspan section, (ii) the time until failure, (iii) the failure mode, and (iv) the time during which the load bearing criteria defined in EN 1363-1 [209] (specified in Section 6.3) were fulfilled.

Table 6.6. Summary of results obtained in fire resistance tests performed in slab SR-C2.5-D10-II and slabs from SC series – results in terms of the failure mode, maximum deflection increase (D_{max}) and deflection rate ($(dD/dt)_{max}$), time until failure ($t_{failure}$) and time during which the load bearing criteria of EN 1363-1 [209] are met (limiting deflection (D = 44.5 mm) and limiting deflection rate (dD/dt = 2 mm/min)).

Slab strip	**D_{max} [mm]**	**$\left(\frac{dD}{dt}\right)_{max}$ [mm/min]**	**$t_{failure}$ [min]**	**Time during which the load bearing criteria of EN 1363-1 are satisfied [min]**		**Failure mode (1)**
				Deflection (D)	**Deflection rate $\left(\frac{dD}{dt}\right)$**	
SR-C2.5-D10-II	-	-	-	-	-	I
SC-C2.5-D10-I	78	1.4	149	94	149	TR
SC-C2.5-D10-II	81	2.2	124	88	66	TR
SC-C3.5-D10-I	88	1.2	158	100	158	TR
SC-C3.5-D10-II	50	1.0	83	83	83	TR
SC-LS30(S)-D10-I	12	1.8	12	12	12	SS/SP
SC-LS60(S)-D10-I	11	1.2	19	19	19	SS
SC-LS65(S)-D10-II	10	0.6	20	20	20	SS

(1) CC: concrete crushing; SP: local spalling of concrete cover of the spliced rebars; SS: slippage in the splices; TR: tensile rupture of reinforcement; I: interrupted before failure.

Table 6.7 presents the results obtained in terms of the thermal response of the slabs, regarding the maximum temperatures measured in relevant locations of the bottom rebars and the time of fire exposure during which the insulation criteria of EN 1363-1 [209] were met. According to Table 6.6, the slabs with GFRP continuous reinforcement satisfied the load bearing criteria during at least 83 min (slab SC-C2.5-D10-II) and 100 min (slab SC-C3.5-D10-I) of fire exposure. It was not possible to evaluate the compliance of the insulation criteria given that the slabs were only instrumented with one thermocouple (T2) at their unexposed surface. Regardless, as shown in Table 6.7, it was verified that overall the

temperature increase limit of 180 ºC was satisfied until the slabs' failure (or until the deflection criterion was no longer verified, as in the case of the slabs from series SC-C2.5.

Table 6.7. Summary of results obtained in fire resistance tests performed in slab SR-C2.5-D10-II and slabs from SC series – results in terms of the time until failure ($t_{failure}$), maximum temperatures measured in the bottom reinforcement, maximum temperature increase in the unexposed surface of the slab and time during which the insulation criterion of EN 1363-1 [209] is satisfied.

Slab strip	$t_{failure}$ **[min]**	**Maximum (average) temperature in the bottom reinforcement [ºC]**				**Maximum temperature increase in unexposed surface [ºC]**	**Time during which the insulation criterion of EN 1363-1 is satisfied (ΔT ≤ 180ºC) [min]**
		Midspan section	**T10/ T13**	**T9/ T12**	**Anchorage end (T8, 11)**		
SR-C2.5-D10-II	-	541[(1)]	480[(1)]	155[(1)]	35[(1)]	-	-
SC-C2.5-D10-I	149	651	506	131	56	233	118
SC-C2.5-D10-II	124	570	480	115	31	144	124
SC-C3.5-D10-I	158	589	427	146	69	-	-
SC-C3.5-D10-II	83	359	294	71	28	108	83
SC-LS30(S)-D10-I	12	105	89	36	29	3	12
SC-LS60(S)-D10-I	19	146	122	45	40	9	19
SC-LS65(S)-D10-II	20	176	124	24	21	7	20

[(1)] Temperature measured in thermocouple T18/T19 in straight-end splices and in thermocouples T14/T15 in bent-end splices.
[(2)] Values of temperature measured after 100 min of fire exposure.

Slabs SC-C2.5-D10 and SC-C3.5-D10 using concrete I failed above 120 min (149 min and 158 min, respectively), with maximum displacement increases (at failure) of 78 mm and 88 mm (L/18 and L/16, respectively, L being the span). As previously shown in Figure 6.15, both the referred slabs fulfilled the deflection fire resistance requirement defined EN 1363-1 [30] during a similar time of fire exposure (94-100 min). When failure occurred, the temperatures of the reinforcement were slightly lower in the slabs with higher concrete cover: 651 ºC and 589 ºC in the slabs with covers of respectively 2.5 cm and 3.5 cm. In other words, for the range of geometries tested, and the boundary conditions used, the increase in concrete cover (from 2.5 cm to 3.5 cm) seems to have had little influence (only 9 min) on the fire resistance of the slab strips.

Overall, the slabs with higher grade concrete (type I) endured longer time of fire exposure than those with lower grade concrete (type II). Comparing slabs from series SC-C2.5-D10, the time to failure of the slabs with concrete types I and II were respectively 149 min and 124 min – yet note that according to the

European fire performance criteria [209], both slabs present similar fire resistance (94-100 min). At the time of failure, temperature in the rebars at midspan was 651 ºC and 570 ºC, respectively, with similar displacements at failure. As shown in Figure 6.15, both slabs presented a qualitatively similar mechanical response with the temperature increase (though with a time-lag), as well as similar temperature profiles up to 70 min. Thereafter, owing to the lower mechanical properties of concrete type II and, consequently, the higher/faster propensity for more extensive cracking (*cf.* Figure 6.10), temperature in that slab increased more rapidly in the final stages of the test, triggering failure to occur sooner. This seems to explain the premature failure of slab SC-C3.5-D10 with concrete type II, which occurred after only 83 min of fire exposure, for a relatively low deflection (50 mm) and for temperatures in the rebars (in the instrumented section) considerably lower than those in the remaining slabs. Such premature failure may be explained by (i) the higher tensile stresses installed in the bottom reinforcement (at midspan section) at the beginning of the fire test (comparing to slab SC-C2.5-D10 using the same concrete), and (ii) the probable occurrence of significantly wider cracks, leading to higher temperatures in the reinforcement in those cracked sections. These temperatures were possibly much higher than those measured in the instrumented section, since as shown ahead in Figure 6.16c and Figure 6.16d, the critical crack occurred in a section near (but not coincident) with the instrumented section (midspan).

As shown in Figure 6.15a, all slabs with lap-spliced reinforcement presented a continuous deflection increase up to failure, which occurred due to loss of bond in the splices. For the two slabs with longer overlap length (SC-LS60(S)-D10 and SC-LS65(S)-D10), the deflection-time response during the first 10 min was similar to that of slabs with continuous reinforcement; however, failure occurred after only 19/20 min of fire exposure with maximum displacement increases (at failure) of approximately 11 mm. Reducing the overlap length from 60 cm (recommended for design at ambient temperature) to 30 cm decreased the fire endurance to 12 min (with similar increase in midspan displacement as the remaining lap-spliced slabs). The maximum temperature attained by the main reinforcement of slab SC-LS30(S)-D10 in the exposed area was 105 ºC (beginning of glass transition), while in the case of the slabs with longer splice lengths, slippage occurred for temperatures above the T_g, but well below the T_d (146 ºC and 176 ºC in slabs with concrete I and II, respectively). These results confirmed the significant influence of lap splices in the fire resistance of GFRP-reinforced concrete slabs, especially if located in spans directly exposed to heat. This constructive detail remarkably reduced the fire endurance of the slabs (to less than 30 min), comparing to the slabs with continuous reinforcement (fire endurances above 120 min). Special detailing considerations must therefore be considered when designing lap-spliced GFRP-RC elements, namely avoiding splicing along spans susceptible to fire (preferably locating the splices over the supports) or, if not possible, implementing fire protection systems in critical locations (*e.g.* through the application of insulation materials).

6.4.4. Failure modes and post-fire assessment

The heat-exposed surface of the slabs with continuous reinforcement (SR-C2.5-D10, SC-C2.5-D10 and SC-C3.5-D10), whose exposure to fire was longer, exhibited considerable disaggregation of the superficial cement paste (Figure 6.16b and Figure 6.16d). This is typical of concrete exposed to very high temperatures and then cooled down. Spalling of the concrete cover was not observed in the tests, with the exception of slab SC-LS30(S)-D10, where local spalling occurred in the splice zones (detailed ahead).

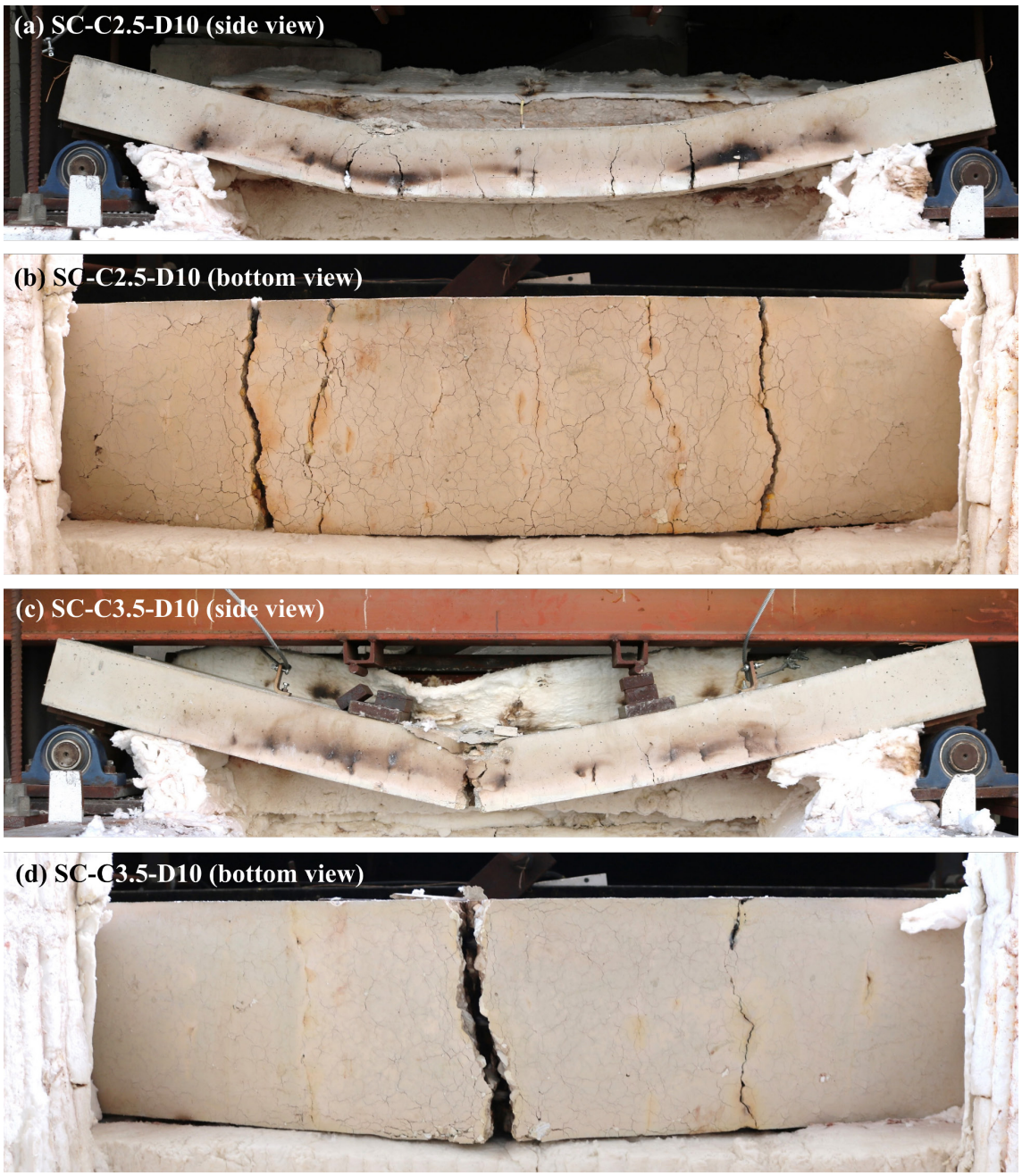

Figure 6.16. View of slab strips with SC continuous reinforcement after the fire resistance tests: (a, b) SC-C2.5-D10 and (c, d) SC-C3.5-D10 (concrete type II).

Figure 6.16 shows slabs SC-C2.5-D10 and SC-C3.5-D10 after collapse. After cooling, the concrete cover was removed in order to confirm the failure mode and assess the damage in the rebars and in the GFRP-concrete interface. Figure 6.17a illustrates a detail of a rebar in the central part of slab SC-C2.5-D10, showing that failure occurred due to tensile rupture of the longitudinal reinforcement (*i.e.*, of the glass rovings) which happened for temperatures well above the T_d (*cf.* Table 6.7). As presented in Figure 6.17a, the resin was completely decomposed and no signs of the sand coating was observed at the surface of the rebars in the fire exposed length of the reinforcement. The glass fibres were covered with a black carbon (char) layer and the wrapped rovings were either broken or loosen from the core. Aligned with the main cracks in the concrete, the fibres had turned into white, indicating the complete decomposition of the resin, including of the carbon black residue layer. Such evidence can be explained by the fact that when failure occurred, a very wide crack developed across the entire cross section depth, thus exposing the fibres directly to the thermal action of fire. The removal of the concrete cover at both extremities of the slabs confirmed that no rebar slippage took place in the anchorage zones, which remained practically undamaged due to the relatively low temperature range to which they were subjected (Figure 6.17b). In fact, as mentioned, the maximum temperature measured at the ends of the reinforcement was 69 ºC (*cf.* Table 6.7), *i.e.*, below the T_g. This confirms that the (cold) anchorages were responsible for ensuring the member's resistance once the T_g (and later the T_d) was reached at the span exposed to fire, where the bond between the GFRP reinforcement and the concrete was degraded and eventually lost.

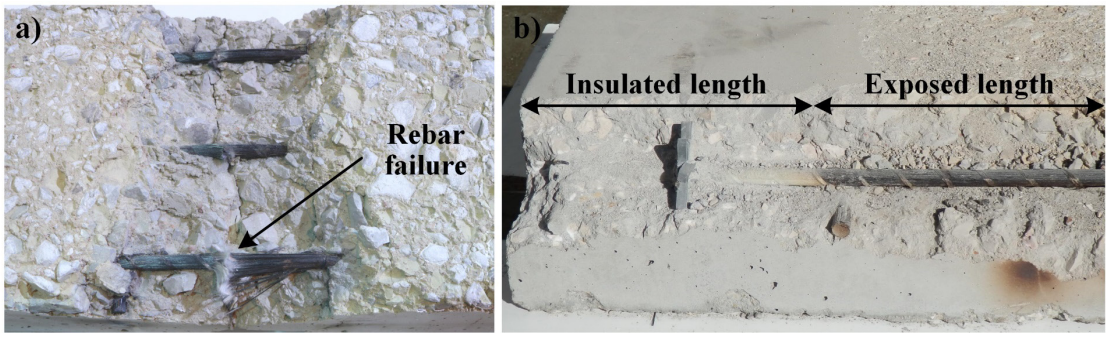

Figure 6.17. Slab SC-C2.5-D10 after the fire resistance test: (a) detail of rebar failure, and (b) damage in longitudinal reinforcement (bottom view).

The failure modes of slabs with lap-spliced reinforcement were very similar – failure occurred suddenly, with extensive cracking in the lap splice zones (Figure 6.18b and Figure 6.18c) and massive concrete spalling in slab SC-LS30(S)-D10 (Figure 6.18a and Figure 6.18b). The post-fire assessment showed that failure occurred due to slippage in the lap splice zones. Regarding slab SC-LS60(S)-D10, at least one rebar was broken in the transverse direction (illustrated in Figure 6.18d), possibly due to the sudden displacement increase when failure occurred. The rebars of slabs with overlap lengths of 60 cm and 65 cm were depleted of the sand coating, resulting from the softening of the bonding resin (as mentioned,

the maximum temperatures measured were above T_g), and some wrapped fibres also appeared to be broken; the level of damage of the rebars of slab SC-LS30(S)-D10 was less severe, with remains of resin and sand particles still adherent to the core of the rebars.

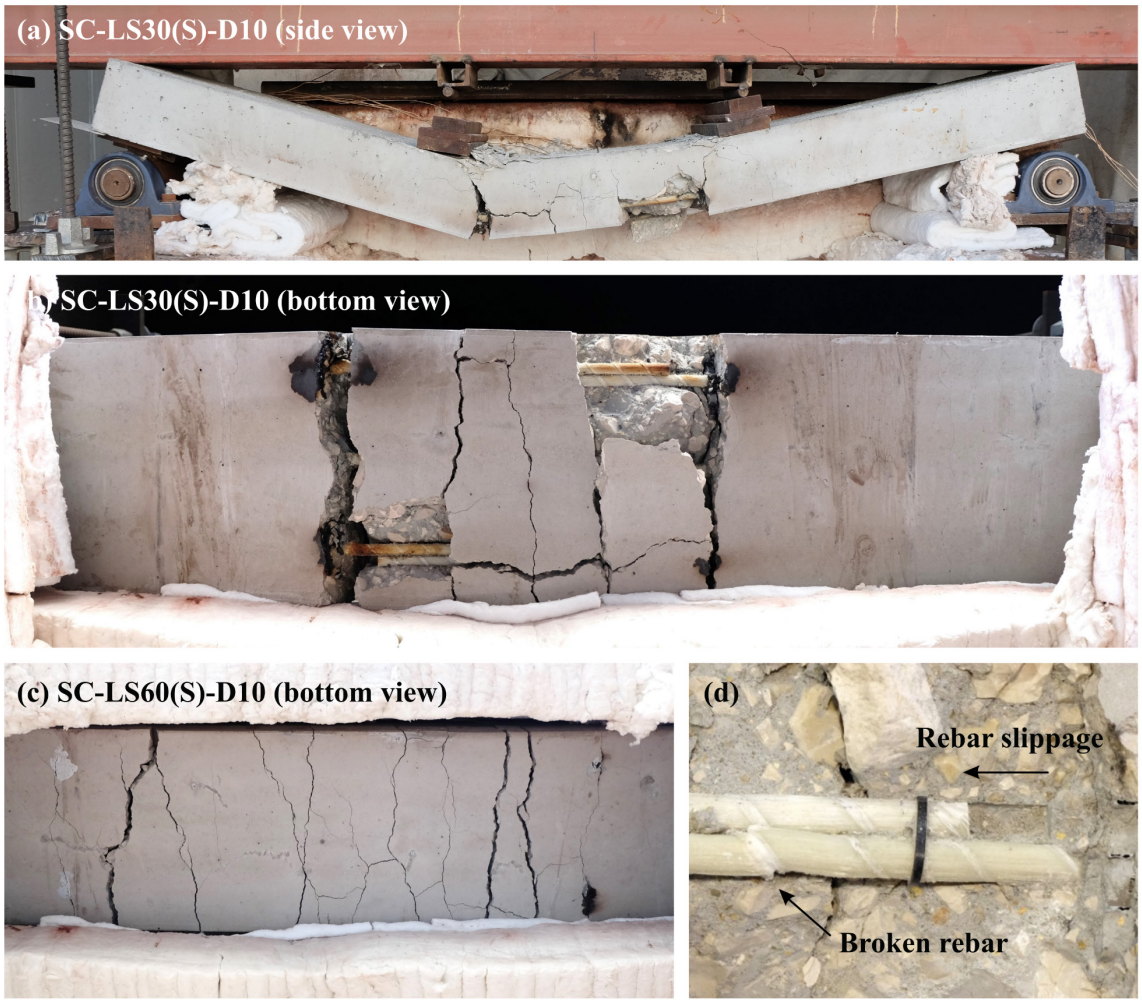

Figure 6.18. View of slab strips with lap-spliced reinforcement after the fire resistance tests: (a, b) SC-LS30(S)-D10, (c) SC-LS60(S)-D10, and (d) detail of broken rebar and rebar slippage on the lap splice.

Figure 6.19 presents the variation of the bond strength and tensile strength of the rebars, as a function of the time of fire exposure, in slabs SC-C2.5-D10 and SC-C3.5-D10; for this purpose, the degradation of the referred properties with temperature obtained in Section 3.4 was considered. A qualitative analysis of the tensile strength (Figure 6.20a) and bond strength retentions (Figure 6.20b) at different instants up to the time of failure and in different zones of the main reinforcement (midspan and anchorage zones) is presented for slab SC-C2.5-D10; Figure 6.20c shows the progression of the degradation of bond strength along the length of the slabs with lap-spliced reinforcement. It should be pointed out that the analysis presented herein should be taken as merely qualitative, as the following hypotheses/simplifications were assumed: (i) the degradation of tensile strength above 300 ºC was

considered equal to that obtained by Hajiloo and Green [107] (as the degradation of strength up to 300 ºC was similar in both studies), and (ii) the bond strength degradation in the splices was assumed to be equivalent to that of a single rebar embedded in concrete (*i.e.* as simulated in the pull-out tests). Moreover, an accurate estimate of the tensile strength of the rebars, and ultimately of the fire resistance of the slabs, would require assessing the stress variation in the rebars during the exposure to fire (the strains in the reinforcement were not measured).

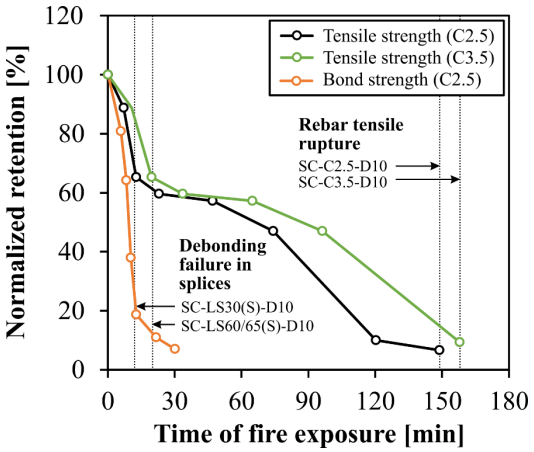

Figure 6.19. Variation of bond and tensile strengths in the main reinforcement (midspan section) during the fire tests performed in slabs from SC series (concrete type I).

According to Figure 6.20b and Figure 6.20c, the loss of bond progressed rapidly from the midspan section to the insulated zones of the slabs, especially within the first 10 min of exposure to fire. At this instant, the average temperature of the reinforcement in the heated span was around 60-74 ºC; based on the pull-out test results, the bond strength reduction for this temperature range was already between 36%-49% compared to that at ambient temperature. As shown in Figure 6.19, most of the GFRP-concrete bond in the exposed zone was lost in the first 20 min of fire exposure. The premature failures of the slabs with lap-spliced reinforcement occurred precisely in this early stage of the tests, when the temperature in the splices exceeded the T_g. These results agree with the pull-out test results, which showed that the T_g is the critical temperature for which most of the bond between these sand-coated GFRP rebars and the concrete is degraded; the estimated bond strength retention at this temperature was only 10%. This was however not determinant to the fire resistance of the slabs with continuous reinforcement since, as previously discussed, once bond was lost in the heated span, the load bearing capacity of the slabs was assured by sufficient anchoring of the rebars in the cooler extremities of the slabs. As illustrated in Figure 6.19 and Figure 6.20a, the rebars were able to retain a significantly high level of tensile strength in the early stages of the fire test. Similarly to the bond strength, the material tests had shown a significant reduction of the tensile strength up to the T_g; after that, the tensile strength was not affected by increasing temperatures (at least up to 300 ºC; for higher temperatures the strength was not measured). After 60 min of fire exposure, when the average temperature of the reinforcement

in the heated span varied between 288 ºC (in slabs with 2.5 cm cover) and 205 ºC (in slabs with 3.5 cm cover), the estimated tensile strength retention of the rebars was around 60%. Subsequently, the tensile strength further and gradually decreased with the temperature increase, eventually leading to failure of the glass rovings. The bond strength retention in the anchorages of slab SC-C2.5-D10 (Figure 6.20b) was around 70% at the time of failure (149 min), attesting that enough anchorage capacity was provided at the ends of the slabs to avoid slippage from occurring and to allow the full tensile capacity of the rebars (at that temperature) to be explored.

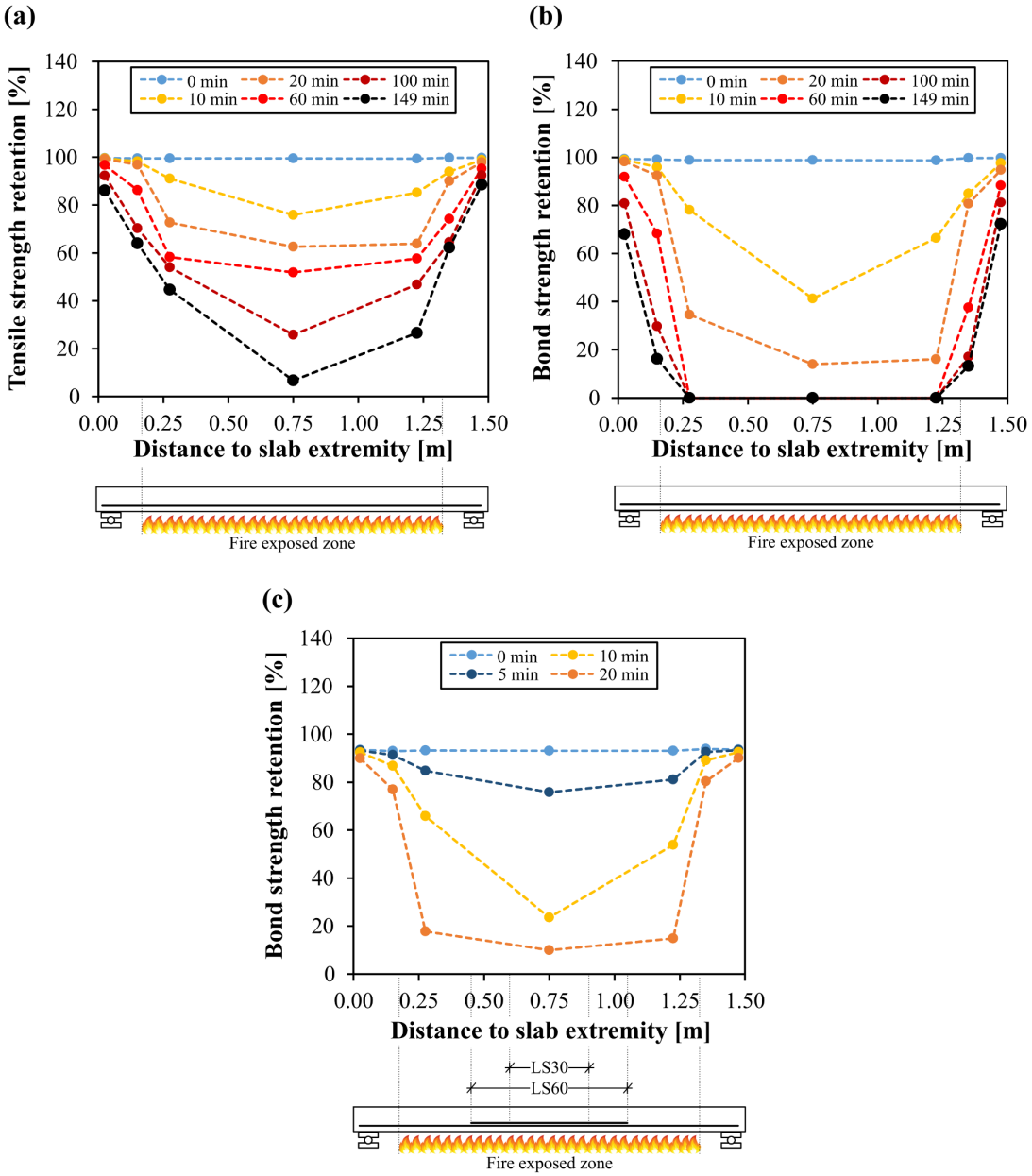

Figure 6.20. (a) Tensile strength and (b) bond strength retentions in the main reinforcement of slab SC-C2.5-D10, and (c) bond strength retention in the main reinforcement of slabs SC-LS30(S)-D10 and SC-LS60(S)-D10 (concrete type I).

6.5. Fire resistance tests of slabs with ribbed rebars – results and discussion

6.5.1. Thermal behaviour

The present and following subsection discuss the results obtained in the fire resistance tests performed in slabs with ribbed rebars (type RB and RBP) and in slab SR-C2.5-D10-III. Figure 6.21 presents the temperature *vs.* time curves of the steel-RC slab (Figure 6.21a) and of two GFRP-RC slabs with concrete cover thicknesses of 2.5 cm (RB-C2.5-D12, Figure 6.21b) and 3.5 cm (RB-C3.5-D12, Figure 6.21c), plotted together with the ISO 834 fire curve (which was followed closely by the furnace); these results are representative of the thermal distributions obtained on the remaining GFRP-RC slabs in which similar concrete covers were adopted. From the beginning of fire, the temperatures of the rebars increased at a significantly higher rate in the exposed span (T4, T5, T6, T10, T13) comparing to the zones farther from the exposed surface, namely the top bars (T3) and the insulated anchorage zones (T8, T9). It is worth noting that the overall temperatures registered in thermocouples located symmetrically along the longitudinal rebars (*e.g.* T9 and T12) were similar; yet, the small differences observed in some thermocouples (*e.g.* T10 and T13 in Figure 6.21b) likely stem from small differences in the placement of the thermocouples, including alignments/misalignments with cracks, and the heterogeneity of concrete.

When temperature approached ∼100 ºC, the heating rate decreased significantly due to moisture evaporation, increasing a few minutes later once the residual water was completely evaporated. Nevertheless, heat-induced concrete spalling was not observed after the tests (as discussed in Section 6.5.3, local spalling of the concrete cover was verified in three slabs, yet it was due to debonding in the splices). Large thermal gradients were observed throughout the slabs' thickness, with temperatures decreasing considerably from the exposed surfaces towards the unexposed surfaces. Taking slab RB-C2.5-D12 (Figure 6.21b) as an example, at the time of failure (165 min), the difference between the temperatures measured at midspan in the bottom (976 ºC in thermocouple T7) and top (153 ºC in thermocouple T2) surfaces of the slab was 823 ºC; accordingly, the temperature of the bottom bars (684 ºC in thermocouple T6) was much higher than that of the top rebars (296 ºC in thermocouple T3). Due to the low thermal conductivity of GFRP rebars, a high thermal gradient was also verified within their cross-section; for example, in slab RB-C2.5-D12 (Figure 6.21b), at failure, the temperatures measured in the top (T4'') and bottom (T4') sides of the rebars were 587 ºC and 758 ºC, respectively. In the case of steel rebars (Figure 6.21a), the distribution of temperature was more uniform within the rebars' cross-section, as attested by the readings of thermocouples T4' and T5.

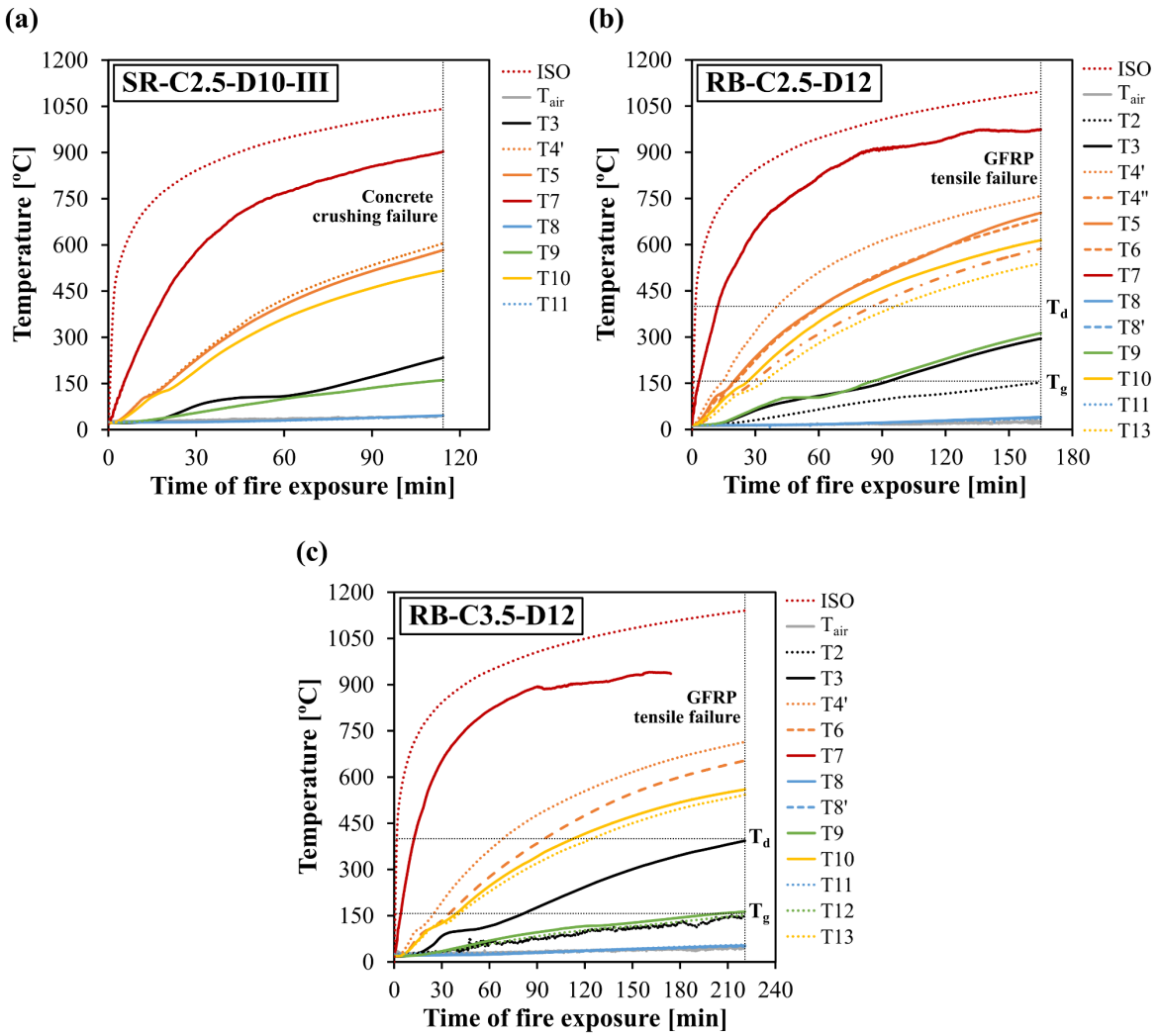

Figure 6.21. Temperature profiles obtained during fire resistance tests of slabs: (a) SR-C2.5-D10-III, (b) RB-C2.5-D12, and (c) RB-C3.5-D12 (vertical lines mark the instant of failure; horizontal lines mark the rebars' T_g and T_d).

Figure 6.22 illustrates the temperature distributions in the bottom reinforcement of various slabs for different periods of fire exposure. Considering, as an example, slab RBP-C2.5-D12 (Figure 6.22b), it can be seen that the temperature of the rebars in most of the exposed zone increased above the T_g (104 ºC) after 30 min of fire exposure, and that after 90 min the T_d (400 ºC) was approached and exceeded in the central zone of the slab. Based on the pull-out test results (*cf.* Figure 4.12 in Section 4.5.3.1 – page 117), these temperatures show that in less than 90 min, the GFRP-concrete bond was completely deteriorated in most of the fire exposed span. Thereafter, temperature continued to increase and, at the time of failure (181 min, due to rebars' rupture), the temperature of the bottom rebars in the exposed zone ranged between 576 ºC (near the transition zone between exposed and unexposed lengths, T10/T13, 0.275 m from the slab end) and 696 ºC (at midspan), thus well above T_d. Conversely, significantly lower temperatures were measured in the thermally insulated zones of the slabs (T8, T9 and T10), as depicted in detail in Figure 6.23; the measurements show that although the T_g was exceeded

in part of the insulated length, the rebars' extremity remained below that threshold temperature during the entire fire exposure. The maximum temperature measured in thermocouple T9 (located close to the transition zone) was 211 ºC, temperature at which the bond strength retention is very low compared to that at ambient temperature (*cf.* Figure 4.12 in Section 4.5.3.1 – page 117). However, the temperature at the rebars' extremity (T8) remained below 31 ºC (*i.e.*, close to ambient temperature), meaning that bond was mostly unaffected and therefore the bottom rebars were able to retain a sufficient anchorage capacity during the entire fire exposure.

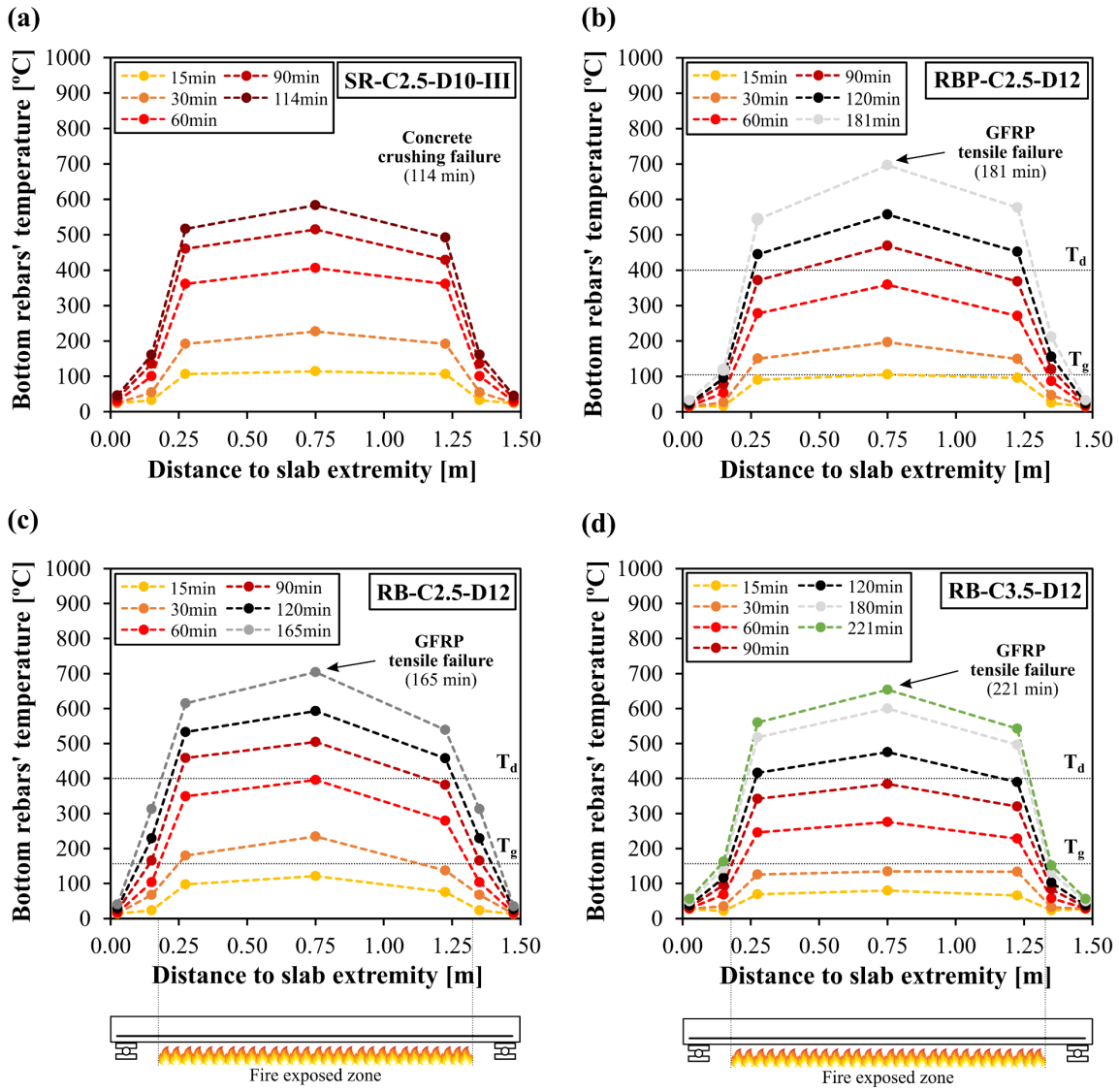

Figure 6.22. Temperature distribution along the length of the bottom longitudinal reinforcement of slabs: (a) SR-C2.5-D10-III, (b) RBP-C2.5-D12, (c) RB-C2.5-D12 and (d) RB-C3.5-D12 (horizontal lines mark the bars' T_g and T_d).

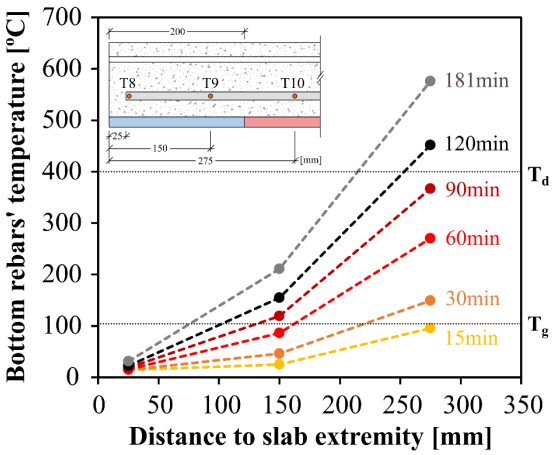

Figure 6.23. Temperature evolution in the bottom reinforcement along the anchorage zone of slab RBP-C2.5-D12-1 (failure after 181 min of fire exposure).

6.5.2. Deflection behaviour and fire resistance

Table 6.8 summarizes the results obtained with respect to the deflection behaviour of the slabs, regarding (i) the maximum deflection increase and deflection rate, both measured at midspan, (ii) the time until failure, (iii) the failure mode, and (iv) the time during which the load bearing criteria defined in EN 1363-1 [209] (Equations (6.1) and (6.2)) were met. In turn, Table 6.9 summarizes the results obtained in terms of the thermal behaviour of the slabs, specifically regarding the maximum temperatures registered in relevant locations of the bottom reinforcement and the time of fire exposure during which the insulation criterion was satisfied.

As shown in Table 6.9, the GFRP-RC slabs with continuous reinforcement fulfilled the load bearing criteria during at least 113 min (slab RBP-C2.5-D12-2) and 145 min (slab RB-C2.5-D12) of fire exposure. Since the slabs were only instrumented with one thermocouple (T2) at the unexposed surface, it was not possible to assess the insulation criterion; nevertheless, it was verified that the temperature increase limit of 180 ºC was always verified until the slabs' collapse (or until the deflection criterion ceased to be satisfied, as in the case of slab RBP-C2.5-D12-1). A comprehensive analysis of the deflection response and fire resistance of each slab is performed in the following sections.

Table 6.8. Summary of results obtained in fire resistance tests performed in slab SR-C2.5-D10-III and slabs from RB and RBP series – results in terms of the failure mode, maximum deflection increase (D_{max}) and deflection rate ($(dD/dt)_{max}$), time until failure ($t_{failure}$) and time during which the load bearing criteria of EN 1363-1 [209] are met (limiting deflection (D = 44.5 mm) and limiting deflection rate (dD/dt = 2 mm/min)).

Slab strip	**D_{max} [mm]**	**$\left(\frac{dD}{dt}\right)_{max}$ [mm/min]**	**$t_{failure}$ [min]**	**Time during which the load bearing criteria of EN 1363-1 are satisfied [min]**		**Failure mode (1)**
				Deflection (D)	**Deflection rate $\left(\frac{dD}{dt}\right)$**	
SR-C2.5-D10-III	77	3.2	114	104	104	CC
RB-C2.5-D12	61	0.6	165	145	165	TR
RB-C3.5-D12	84	0.5	221	158	221	TR
RB-LS32.5(S)-D12	9	0.3	24	24	24	SS
RB-LS65(S)-D12	16	0.5	39	39	39	SS / SP
RB-C2.5-D8	53	0.7	133	126	133	TR
RBP-C2.5-D12-1	81	0.6	181	122	181	TR
RBP-C2.5-D12-2	78	1.3	139	113	139	TR
RBP-LS32.5(S)-D12	13	1.9	20	20	20	SS
RBP-LS32.5(B)-D12	13	0.9	19	19	19	SS / SP
RBP-LS65(S)-D12	13	0.8	19	19	19	SS / SP
RBP-LS84.5(S)-D12	14	0.9	26	26	26	SS / SP
RBP-LS84.5(B)-D12	26	0.4	75	75	75	SS

(1) CC: concrete crushing; SP: local spalling of concrete cover of the spliced rebars; SS: slippage in the splices; TR: tensile rupture of reinforcement.

Table 6.9. Summary of results obtained in fire resistance tests performed in slab SR-C2.5-D10-III and slabs from RB and RBP series – results in terms of the time until failure ($t_{failure}$), maximum temperatures measured in the bottom reinforcement, maximum temperature increase in the unexposed surface of the slab and time during which the insulation criterion of EN 1363-1 [209] is satisfied.

Slab strip	$t_{failure}$ [min]	Maximum (average) temperature in the bottom reinforcement [ºC]					Maximum temperature increase in unexposed surface [ºC]	Time during which the insulation criterion of EN 1363-1 [30] is satisfied (ΔT ≤ 180ºC) [min]
		Midspan section	Splice end (1)	T10 / T13	T9 / T12	Anchor. end (T8, T11)		
SR-C2.5-D10	114	606	-	516	161	46	104	114
RB-C2.5-D12	165	684	-	615	-	40	137	165
RB-C3.5-D12	221	654	-	560	163	56	130	221
RB-LS32.5(S)-D12	24	189	-	171	28	16	20	24
RB-LS65(S)-D12	39	341	-	243	49	15	45	39
RB-C2.5-D8	133	691	-	554	144	34	173	133
RBP-C2.5-D12-1	181	696	-	576	211	32	212	148
RBP-C2.5-D12-2	139	713	-	573	139	45	155	139
RBP-LS32.5(S)-D12	20	122	-	114	31	18	10	20
RBP-LS32.5(B)-D12	19	139	15	147	111	19	10	19
RBP-LS65(S)-D12	19	135	-	108	28	15	8	19
RBP-LS84.5(S)-D12	26	208	110	105	35	20	-	-
RBP-LS84.5(B)-D12	75	544	100	322	76	25	78	75

(1) Temperature measured in thermocouple T18/T19 in straight-end splices and in thermocouples T14/T15 in bent-end splices.

6.5.2.1. Effect of using straight rebars in lap splices

Figure 6.24 compares the evolution of the midspan displacement as a function of the time of fire exposure of GFRP-RC slabs with continuous and spliced reinforcement from series RB (Figure 6.24a) and series RBP (Figure 6.24b). Instant $t = 0$ min corresponds to the onset of the heating stage and the displacements were set to zero after the fire load stabilization to display only the heat-induced deflection. The failure instant of each slab is marked in the displacement curves as a sudden large increase in

deflection. The limiting deflection criterion defined in EN 1363-1 [209] is also plotted with a horizontal dashed line, marking the fire resistance of the slabs.

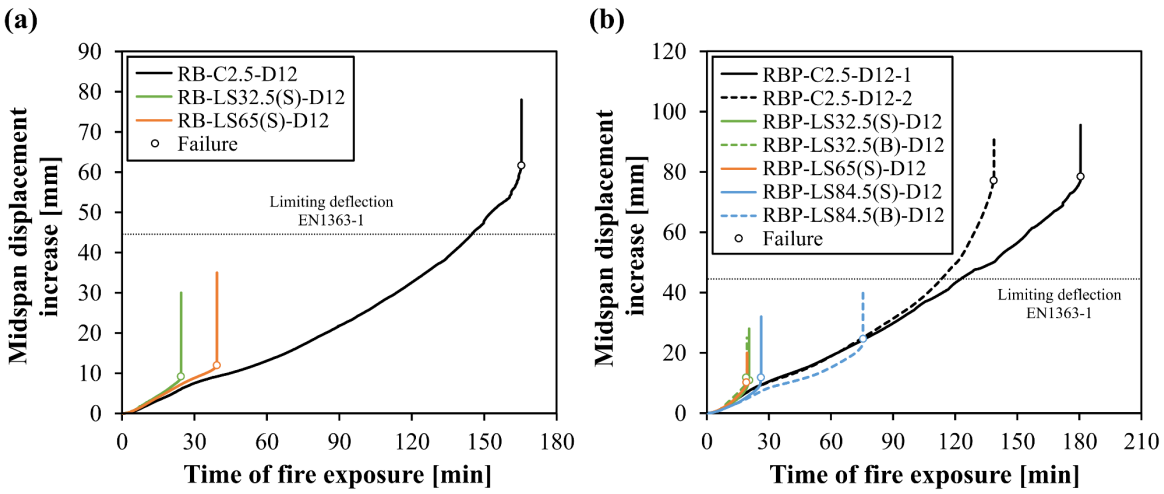

Figure 6.24. Midspan displacement increase during fire exposure – effect of splicing and bar geometry in slabs with (a) RB and (b) RBP rebars (slabs with straight rebars – continuous line; slabs with bent rebars – dashed line).

During the first 5 min of fire exposure, the slabs did not show a meaningful increase in deflection due to the very low temperature gradient installed in the concrete's cross-section. After that, they presented a non-linear variation in deflection up to failure, stemming from: (i) the thermal bowing, derived from the increasing temperature gradient within the slabs' cross-section, (ii) the concrete cracking, and (iii) the non-linear degradation of the concrete and rebars' mechanical properties, as well as of the GFRP-concrete bond, with the increase in temperature.

After approximately 30 min of fire exposure, the displacement increase rate of slabs with continuous bars changed, increasing gradually thereafter; as analysed next, this was mainly due to the severe loss of bond that occurred along the exposed length for this duration, *i.e.*, when the rebars' temperature exceeded the T_g (Figure 6.22b and Figure 6.22c). Figure 6.25 presents the quantitative variation of the tensile and bond strengths of the bottom reinforcement at the midspan section during fire exposure, exemplified for RBP rebars. In turn, Figure 6.26 plots the tensile and bond strength retention percentages for different times of fire exposure for slab RBP-C2.5-D12-1. In both figures, the tensile and bond strength retentions were computed using the temperatures measured at the bottom reinforcement at the midspan section together with the results of the tensile and pull-out tests.

Figure 6.25 and Figure 6.26b show that the GFRP-concrete bond at midspan presented a steep decrease in the first 30 min of fire exposure, much more severe than that undergone by the tensile strength of the rebars. Figure 6.26b shows that the loss of bond along the central zone of the slab was quite severe – after 30 min of fire exposure, the bond reduction was about 80% (towards the insulated anchorage zones,

this reduction of bond strength was less significant, because temperatures were lower). The displacement *vs.* time curves plotted in Figure 6.24b show that the failure of slabs with spliced RBP reinforcement and development lengths of 32.5 cm and 65 cm took place within this 20-30 min time frame. This occurred because when the rebars approached the T_g, the softening of the polymeric matrix severely compromised the stress transfer capacity between the concrete and the rebars (as well as between the resin and the fibres). The loss of bond in the heated span led to the deflection rate increase and cracking in all slabs and, in the case of slabs with lap splices, also to the premature debonding of the overlapped rebars.

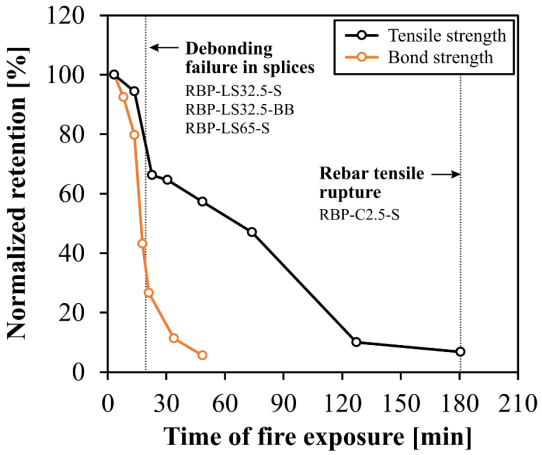

Figure 6.25. Variation of the tensile and bond strengths in the bottom RBP rebars (midspan section) during fire exposure.

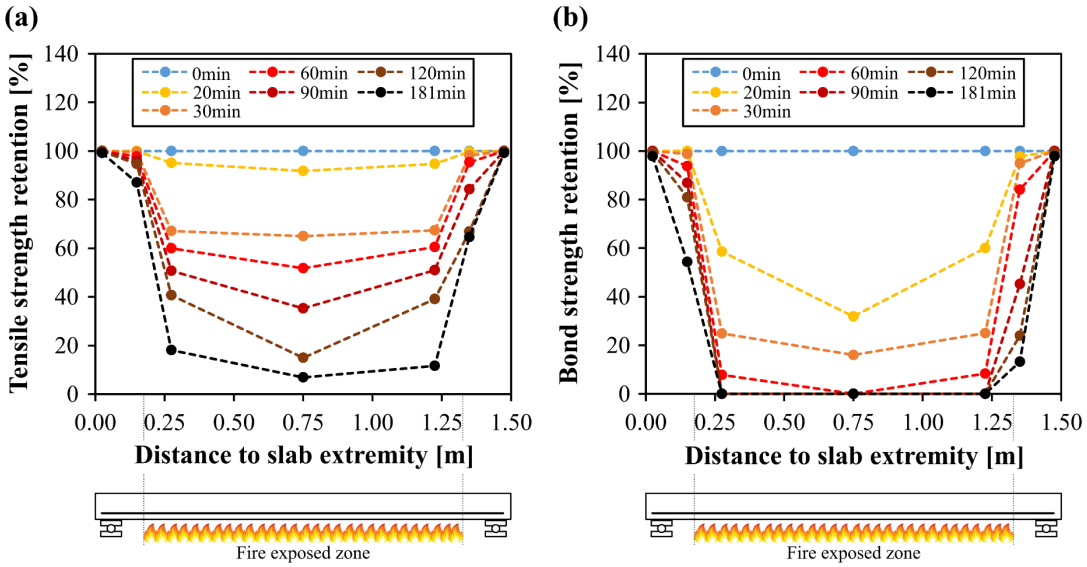

Figure 6.26. (a) Tensile strength and (b) bond strength retention in the bottom longitudinal reinforcement of slab RBP-C2.5-D12-1 for different times of fire exposure (the plots are also representative of the strength retentions estimated for slabs RBP-LS32.5(S)/(B)-D12 and RBP-LS65(S)-D12.

As shown in Figure 6.22b, after 90 min of fire exposure, the temperature of continuous RBP rebars along the exposed length approached and exceeded the T_d, reaching up to 371 ºC near the transition with the insulated zone (T10/T13) and up to 468 ºC at midspan. Therefore, the temperature of the rebars was high enough to cause the complete loss of bond (Figure 6.26b) and a significant reduction of the rebars' tensile capacity along the exposed length (~49-65%, as shown in Figure 6.25 and Figure 6.26a). Note that the reduction of tensile modulus for these temperatures was much lower (~8-14%, Figure 3.12 in Section 3.4.3.3 – page 85). However as shown in Figure 6.23, while temperatures in the heated length largely exceeded the T_d at the end of the tests, the extremities of the reinforcement were kept below the T_g, and therefore remained well-anchored in the concrete during the entire fire exposure. This means that once the GFRP-concrete bond was completely deteriorated along the fire exposed length, the behaviour of the continuous rebars changed to a cable (or tied arch) mechanism, anchored in the cold ends of the slabs. This mechanism was comprehensively analysed in the numerical simulations conducted in Chapter 7, where it was shown that when the bond is lost in the span, the tensile forces in the rebars are transferred to the cold anchoring zones, resulting in an increase in bond stresses in that region. For that reason, it is important to provide sufficiently long anchoring lengths, protected from fire, in order to prevent premature pull-out failures. These conditions were met in the present study, which enabled the slabs with continuous GFRP reinforcement to fail due to the tensile rupture of the fibre rovings at very high temperatures (above T_d) and to attain fire resistances significantly above 120 min. Moreover, as shown in Figure 6.24, the slabs with continuous reinforcement fulfilled the (load bearing) fire resistance requirements defined in the European regulation [209] during at least 113 min and up to 145 min of fire exposure (also *cf.* Table 6.8 in section 6.5.2).

Conversely, slabs with spliced reinforcement presented significantly lower fire resistance because the lap splices were directly exposed to fire, which triggered debonding failures when the ends of the overlapping bars approached the T_g. As shown in the pull-out tests (*cf.* Figure 4.12b in Section 4.5.3.1 – page 117), the bond strength of RB bars was less degraded than that of RBP bars for temperatures between 100 ºC and 300 ºC, due to the higher T_g of the former. This explains the difference in fire endurance of slabs with the same splice length but different types of straight-end rebars, RB-LS65(S)-D12 (Figure 6.24a) and RBP-LS65(S)-D12 (Figure 6.24b): 39 min for RB rebars (T_g of 157 ºC) and 19 min for RBP rebars (T_g of 104 ºC) when the temperature of the rebars at midspan attained, respectively 341 ºC and 135 ºC (it is likely that the former temperature was measured a section with a crack, hence the considerably higher value). These results also demonstrate that the overlapping length designed for ambient temperature conditions (65 cm) is insufficient to attain fire endurances above 60 min if the splices are directly exposed to heat and only 2.5 cm of concrete cover thickness are adopted.

Considering the RB series (Figure 6.24a), increasing the splice length from 32.5 cm to 65 cm enabled the debonding failure to occur at higher temperatures and enhanced the slabs' fire resistance by 15 min, from 24 min to 39 min, which is still very low; at failure, the temperature of the rebars at midspan was 189 ºC

in slab RB-LS32.5(S)-D12 (32 ºC above T_g) and 341 ºC in slab RB-LS65(S)-D12 (184 ºC above T_g). However, in the RBP series, the same increase in the splice length was insufficient to improve the slabs' fire endurance: slabs RBP-LS32.5(S)-D12 and RBP-LS65(S)-D12 (with straight-end splices) and also slab RBP-LS32.5(B)-D12 (with bent-end splices – further discussion is provided in the next section) collapsed during the first 20 min of fire when the temperature at midspan (T5/T6) increased slightly above the T_g (between 122 ºC and 139 ºC, *cf.* Table 6.9). The ineffectiveness of increasing the splice length from 32.5 cm to 65 cm in the RBP series can be explained, again, by the steeper reduction of the bond strength of these rebars for temperatures above 100ºC, when compared to that of the RB rebars (*cf.* Figure 4.12b in Section 4.5.3.1 – page 117). Increasing the overlap length to 84.5 cm in straight-end splices (slab RBP-LS84.5(S)-D12) only provided a minor increase in fire resistance (6 min), leading to attaining slightly higher temperatures in the midspan section before failure (208 ºC). The thermocouples installed in the extremities of the overlapping bars (T22 and T23) of this slab allowed to confirm that failure occurred when the extremities of the splices attained a temperature close to the T_g (more precisely, 110 ºC) and for which the bond had been steeply reduced.

6.5.2.2. Effect of using bent rebars in lap splices

As shown in Figure 6.24b, the use of 90º bent rebars was not effective in improving the bond behaviour of the splices of slab RBP-LS32.5(B)-D12 due to the following reasons: (i) the short splice length adopted (half the length recommended for design at ambient temperature), (ii) the short tail length after the bend, and (iii) the unfavourable location of the splices, located between the load application points, where load effects are more significant. However, a very significant improvement in fire endurance was obtained in slab RBP-LS84.5(B)-D12 when adopting bent extremities in splices with 84.5 cm of length. As shown in Figure 6.24b, this slab failed after 75 min, therefore presenting additional 49 min of fire resistance w.r.t. slab RBP-LS84.5(S)-D12 (with straight-end splices, which failed after 26 min). As discussed next, the use of 90º bent rebars allowed to exploit the high thermal gradient along the slabs' thickness and anchor the overlapping rebars in a cooler zone of the slab where the degradation of bond occurred at a slower rate.

The evolution of (i) temperature and (ii) bond strength retention with the time of fire exposure obtained in slab RBP-LS84.5(B)-D12 is presented in Figure 6.27a and Figure 6.27b (regarding the bottom reinforcement) and in Figure 6.27c and Figure 6.27d (regarding the bent extremity of the splices). The temperature peaks depicted in Figure 6.27a are indicative of the localized heating of the rebars in largely cracked sections (in this case, aligned with the thermocouples positioned at midspan and in a section distanced 1.20 m from the left extremity of the slab). It should also be pointed out that the bond strength retentions in the bend presented in Figure 6.27d were estimated considering that the bond degradation in the bent splices is equivalent to that of a single 90º bent bar embedded in concrete and exposed to a uniform temperature along its entire length (as measured in the pull-out tests); for this reason, since both the temperature distribution and loading conditions in the pull-out tests differed from those of the slabs,

the analysis presented here should be considered mostly from a qualitative point of view. Figure 6.27a and Figure 6.27c show that temperature in the span increased rapidly, approaching the T_g after only 15 min of fire exposure and exceeding the T_d after between 45 and 60 min. Consequently, as depicted in Figure 6.27b and Figure 6.27d, the bond along the straight development of the splices was strongly reduced within the first 30 min; indeed, the failure of slab RBP-LS84.5(S)-D12 (with straight-end splices) occurred in this time period, after 26 min of fire exposure. However, along the bent extremities of the splices, the temperature rise (Figure 6.27c) and thereby the bond degradation (Figure 6.27d) were much slower, especially in the zones farthest from the exposed surface of the slab, allowing the retention of bond in the splices' extremities over a longer period of time. As a result, slab RBP-LS84.5(B)-D12 failed after 75 min, when the extremity of the bend (T15) approached the T_g, which occurred long after that temperature was attained in the bottom section of the bend (T22) (around 60 min later).

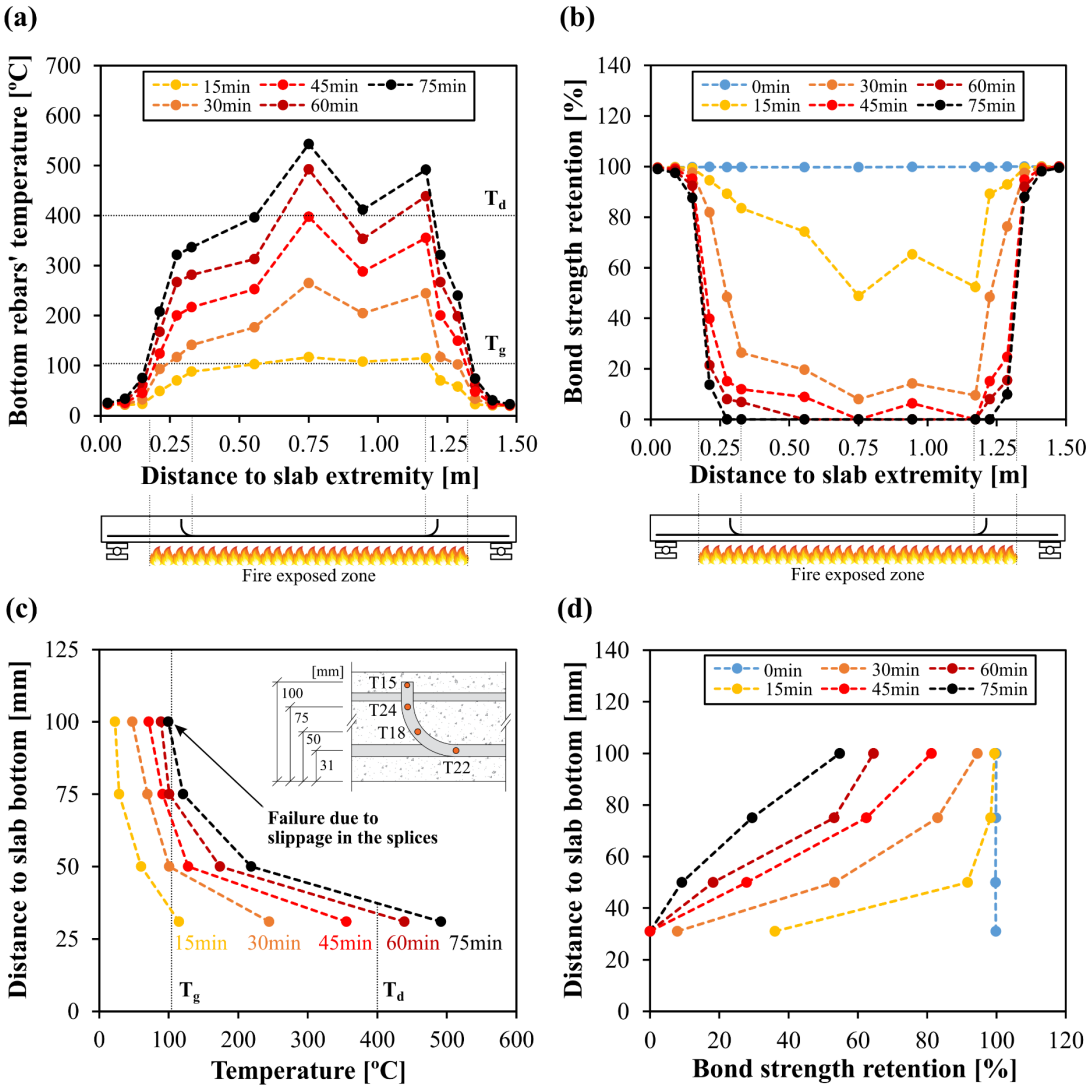

Figure 6.27. Evolution of (a,c) temperature and (b,d) bond strength retention of slab RBP-LS84.5(B)-D12 along: (a,b) the bottom longitudinal reinforcement (temperature peaks correspond to a crack location); and (c,d) the bent extremity of the splices.

These results suggest that the adoption of bent rebars in lap splices has even greater potential in thicker slabs (and in beams) than in the relatively thin slabs tested here, as such constructive detail enables increasing the tail length of the bar and take further advantage of the higher thermal gradient installed in the cross-section of those thicker members. The results presented here and in the previous section agree with the conclusions obtained in the parametric studies conducted in Section 5.4, where it was shown that significantly longer development lengths are required to anchor GFRP bars at elevated temperatures than those needed at ambient temperature. The design of tension lap splices should therefore consider the high vulnerability of GFRP bars to elevated temperatures when defining the required development lengths and the adoption of bent reinforcement should be considered as an option to improve the members' fire endurance. Nevertheless, these results demonstrate that splices cannot be directly exposed to fire and, in turn, their extremities should be extended over the supports (embedded in the beams).

6.5.2.3. Effect of reinforcement type and surface finish

The mechanical responses obtained in slabs with 2.5 cm of cover and different types of rebars – *i.e.*, materials (GFRP and steel) and surface finishes (ribbed and sand coated bars) – are compared in Figure 6.28; all GFRP-RC slabs respect to concrete type II. The results show that the GFRP-RC slabs with continuous reinforcement, which collapsed due to the tensile rupture of the bottom rebars, presented fire endurances above 120 min and up to 181 min (*cf.* slab RBP-C2.5-D12-1). The differences in deflection and time to failure obtained in the different slabs are mainly explained by the different degradation rates of the bond and tensile properties of SC, RB and RBP bars with increasing temperatures.

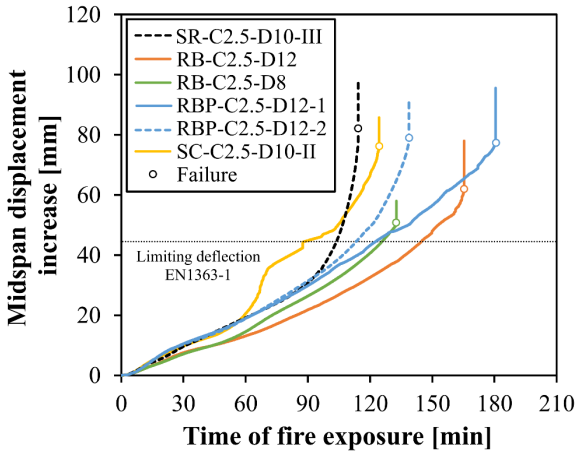

Figure 6.28. Midspan displacement increase during fire exposure of slabs with continuous steel and GFRP reinforcement (2.5 cm cover) – effect of reinforcement type.

For relatively low temperatures approaching the T_g, the softening of the resin reduces the load transmission capacity between the concrete and the GFRP reinforcement, resulting in an increase in crack width and deflection. Figure 6.28 shows that from the early stages of the fire, the heat-induced deflection of slabs with RBP bars was higher than that of slabs with RB bars, because the bond strength of RBP bars was more rapidly reduced with the increase in temperature than that of RB bars (due to the lower T_g of the former, *cf.* Figure 4.12a in Section 4.5.3.1 – page 117). As discussed in Section 6.5.2.1, this also explains the earlier collapses of slabs with RBP spliced rebars (Figure 6.24b) compared to those with RB rebars (Figure 6.24a). Likewise, the slabs with SC spliced rebars (similar T_g than RBP rebars) also presented lower fire resistance than slabs with RB rebars (*cf.* Table 6.6 in Section 6.4.3 – page 188). For instance, comparing the slabs with splice length of 65 cm, those with SC rebars (T_g of 98 ºC) and RBP rebars (T_g of 104 ºC) endured 19-20 min of fire exposure, while the slab with RB rebars (T_g of 157 ºC) failed after 39 min. As shown in Figure 4.12 (Section 4.5.3.1, page 117), SC rebars presented a steeper reduction of bond strength with temperature compared to the ribbed RB and RBP rebars, which explains the higher deflections measured in slab SC-C2.5-D10-II.

Since no pull-out failures were observed in the anchorage zones, the time to failure of slabs with continuous rebars was governed by the tensile strength of each rebar at very high temperatures. At failure, the temperatures measured in the rebars at midspan in slabs with RB rebars varied between 654 ºC and 691 ºC (between 696 ºC and 713 ºC in the case of RBP bars), which is greatly above their T_d. According to the tensile tests, the tensile strength retention of RB rebars at 715 ºC was indeed very low (around 4% of the strength at ambient temperature). In the case of the slabs with SC rebars, the tensile rupture of the reinforcement occurred sooner than in slabs with ribbed rebars and typically at lower temperatures, between 570 ºC and 651 ºC, also above the resin T_d (*cf.* Table 6.7 in Section 6.4.3 – page 189). This result is in agreement with the data obtained in the tensile tests (*cf.* Table 3.7 in Section 3.4.3.3 – page 84), which, although performed up to temperatures lower than those attained in the fire tests, showed that at 300 ºC the tensile strength of SC rebars (∼598 MPa) was already lower than that of RB-D12 and RBP rebars (∼661 MPa and ∼678 MPa, respectively).

Figure 6.29 presents the results of the test repetition of slab RBP-C2.5-D12, depicting the variation of displacement and temperature at midspan during fire exposure for slabs RBP-C2.5-D12-1 and RBP-C2.5-D12-2. It can be seen that although both slabs presented similar displacements at midspan and maximum temperatures in the reinforcement at failure (696 ºC and 713 ºC, respectively), they failed with a difference of 42 min: slab 1 collapsed after 181 min of fire exposure, while slab 2 failed after 139 min (both due to the rebars' tensile rupture at midspan). This difference is most likely due to the intrinsic variability of the cracking phenomenon at elevated temperatures which, in this case, led to more severe concrete cracking in slab 2, as evidenced by the faster temperature increase of the reinforcement at midspan depicted in Figure 6.29; as a result, the deterioration rate of the rebars' mechanical properties and bond in cracked sections increased more rapidly, triggering failure to occur sooner. As discussed in

Section 6.4.3 (regarding to the slabs reinforced with sand coated rebars), these results confirm that the severe cracking of concrete can adversely affect the fire endurance of FRP-RC structural members.

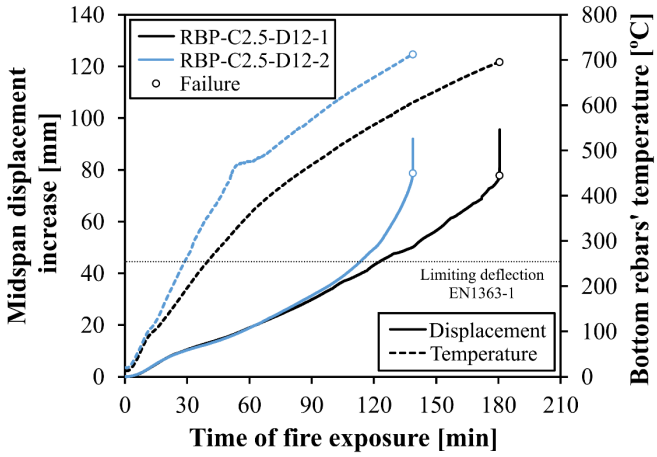

Figure 6.29. Variation of (i) midspan displacement increase (continuous lines) and (ii) bottom rebars' temperature at midspan (dashed lines) during fire exposure of slabs RBP-C2.5-1 and RBP-C2.5-2.

According to Figure 6.28, the steel-RC slab failed after 114 min of fire exposure, therefore prior to the failure of the GFRP-RC slabs – this result can be (at least partly) explained by the lower mechanical properties of the concrete used in the steel-RC slab (which failed due to concrete crushing). As mentioned, the failure times of the GFRP-RC slabs corresponding to the European fire performance criteria [209] ranged between 113 min (slab RBP-C2.5-D12-2) and 145 min (slab RB-C2.5- D12) (*i.e.* above 2 hours, *cf.* Table 6.8 in Section 6.5.2); in turn, the steel-RC slab fulfilled these criteria during 104 min.

Following the discussion of Section 6.5.2.1, these results further highlight the importance of protecting the anchorage zones of the rebars from the direct heat exposure. The insulated anchorage zones should be properly designed in order to provide sufficient embedment of the rebars in zones where temperature remains below the T_g during a fire event. In this study, the protected length of 175 mm was adequate to prevent premature pull-out failures, even when straight bars were adopted. Assuring cold anchoring zones can be easily implemented in real applications, since the extremities of the slabs' rebars are normally embedded in the beams (or in the columns, in the case of beam applications) or separated from the fire compartment through partition walls. Additionally, bearing in mind the good results obtained with the use of bent rebars in splicing zones, they can also be used in end anchorages to decrease the usually long development lengths required to anchor FRP bars, as already shown in [13,14,18].

6.5.2.4. Effect of bar diameter

Figure 6.30 compares the variation of the displacement increase and temperature of the bottom rebars (at midspan) obtained in the fire resistance tests of slabs RB-C2.5-D12 and RB-C2.5-D8. The results show that the fire resistance of the slab with larger rebars (RB-C2.5-D12) was 32 min higher than that of the slab with smaller rebars (RB-C2.5-D8) – with respect to the fire performance criteria [209], such difference was 19 min). This result can be (at least partly) explained by the slower propagation of heat through the bars' thickness in larger cross-sections, resulting in a slower degradation of the GFRP's tensile properties. Figure 6.30 shows that the rebars' temperature increased faster in the slab with smaller bars, though the reinforcement of both slabs ruptured at similar (average) temperatures (684-691 ºC).

Other reasons that might explain this result are related to the slightly higher tensile stresses installed in RB-D8 rebars at the onset of the fire test (*cf.* Table 6.4 in Section 6.2.5), the effect of the localized heating of the rebars in cracked sections, and/or the experimental variability associated with these tests (particularly with respect to the influence of cracking at elevated temperatures, as demonstrated in the test repetitions of slab RBP-C2.5-D12 – see Figure 6.29 in Section 6.5.2.3). Due to the lack of studies in the literature to corroborate/refute these results, additional investigations are required in order to draw more specific recommendations on this matter.

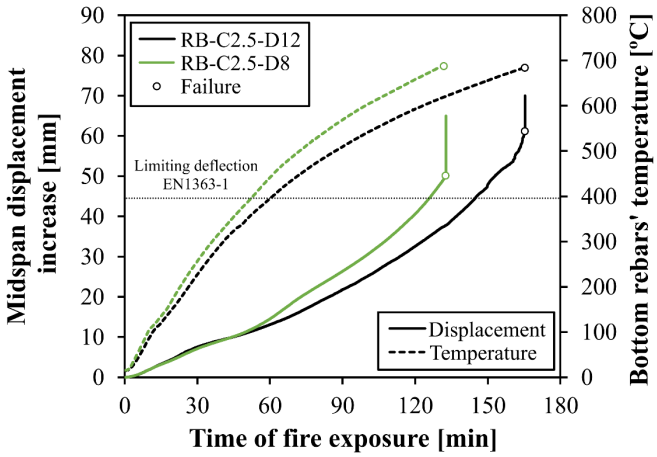

Figure 6.30. Variation of (i) midspan displacement increase (continuous lines) and (ii) bottom rebars' temperature at midspan (dashed lines) during fire exposure of slabs RB-C2.5-D8 and RB-C2.5-D12 – effect of bar diameter.

6.5.2.5. Effect of concrete cover thickness

Figure 6.31 compares the deflection behaviour and temperature of the bottom reinforcement (measured at midspan) of slabs with different cover thicknesses: slab RB-C2.5-D12 (2.5 cm of cover) failed after 165 min, while slab RB-C3.5-D12 (3.5 cm of cover) collapsed after 221 min (56 min later) – the slabs'

fire resistance according to the fire performance criteria [209] was 145 min and 158 min, respectively. These results demonstrate the significant increase in fire endurance of GFRP-RC slabs that can be provided with a small increase in the bar cover of 1 cm; as shown in Figure 6.31 and discussed in Section 6.5.2.1 (*cf.* Figure 6.22c and Figure 6.22d), the adoption of a thicker layer of concrete cover slowed down the temperature rise in the reinforcement and, in turn, allowed the retention of the rebars' mechanical properties and bond to concrete over a longer time span. It was not possible to corroborate these results with previous experimental studies from the literature in which the concrete cover thickness was also varied (*e.g.* [11,14,70,148]), because those studies were unable to properly assess the influence of this parameter on the fire resistance of FRP-RC members: in [11,148] some slabs failed prematurely in the anchorage zones, in [14] the fire resistance tests were interrupted before collapse, and in [70] the slabs were not mechanically loaded during fire exposure; nevertheless, the results obtained herein are in agreement with those numerically obtained in [165,166].

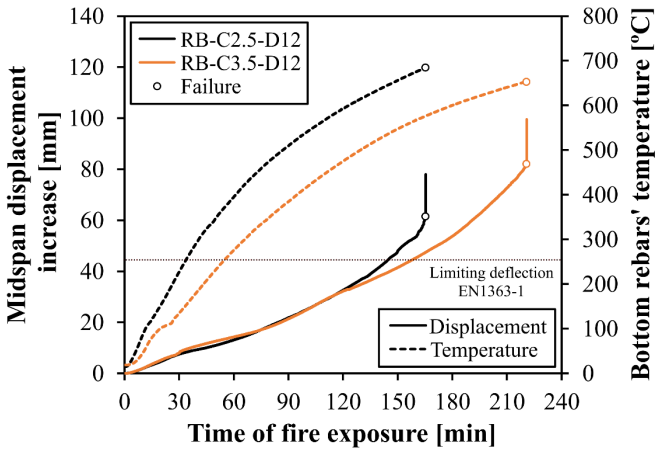

Figure 6.31. Midspan displacement increase during fire exposure of slabs RB-C2.5-D12 and RB-C3.5-D12 – effect of cover thickness.

Furthermore, these results prove that GFRP-RC slabs can achieve fire endurances above 180 min with relatively small concrete cover thicknesses (given that the bars remain well anchored in cool zones of the structure), thereby supporting the conclusions of [11,12] and those obtained in this study with respect to the slabs reinforced with sand coated bars, where it was shown that the cover recommendations specified in [8] are overly conservative. In fact, for the materials and slab geometry tested in the present study, that guide specifies a minimum cover of 60 mm for a 60 min fire resistance rating. Given that the high corrosion resistance of GFRP rebars enables the design of RC members with thinner concrete covers than those used for steel-RC, the results obtained in the present study thus confirm that current design recommendations can be improved, enabling a more economic and sustainable use of GFRP reinforcement [212].

6.5.3. Failure modes and post-fire assessment

The failure modes observed in the fire resistance tests were summarized in Table 6.8 (Section 6.5.2). A post-failure view of the slabs with continuous reinforcement is illustrated in Figure 6.32. As depicted in Figure 6.32a, the reference steel-RC slab presented bending failure due to concrete crushing between the load applications points. In turn, the GFRP-RC slabs with continuous reinforcement (Figure 6.32b) failed due to the tensile rupture of the bottom rebars in the central zone of the span for temperatures greatly above the T_d. As shown in Figure 6.33a and Figure 6.35a, in the slabs that presented longer fire endurance, the fibre rovings presented a char layer at the surface and no residue of resin was found in the rebars along the exposed span, evidencing matrix decomposition. The rupture of the rebars occurred along the maximum moment zone (at midspan or under the load application points), as indicated by the large crack depicted in Figure 6.32b and Figure 6.32c. In that cracked section, the reinforcement became directly exposed to fire, and the reinforcing fibres turned white (Figure 6.33a) as a result of the complete decomposition of the resin and char layer. Since a sufficient length of the bars' extremities were kept below the T_g during fire exposure, no slippage was observed in the end anchorage zones. Moreover, no passage of flames was detected through the slab's thickness during the tests and no heat-induced spalling was observed after the end of the tests.

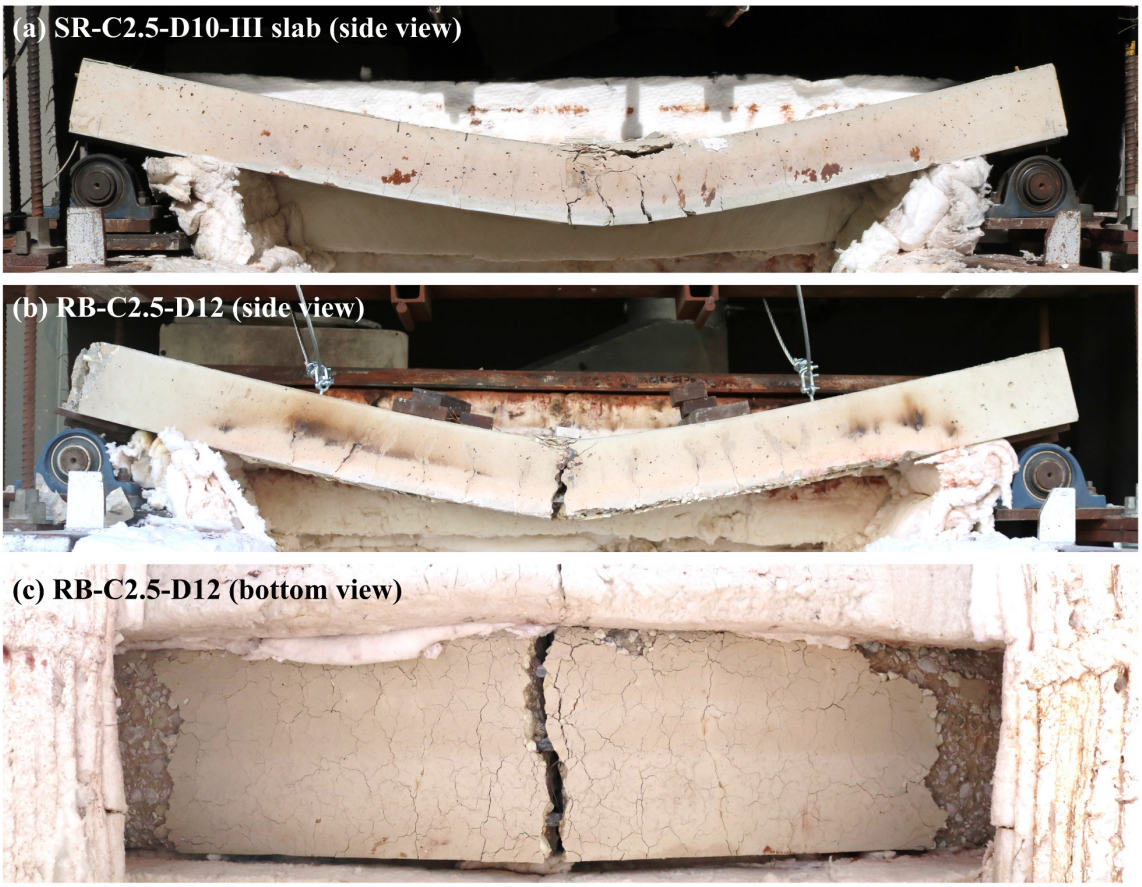

Figure 6.32. View of slabs with continuous reinforcement after failure: (a) SR-C2.5-D10-III and (b,c) RB-C2.5-D12-I.

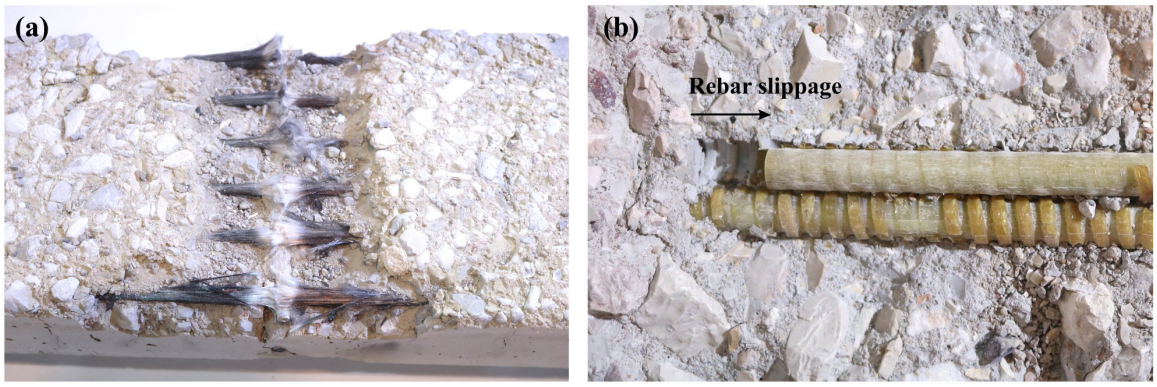

Figure 6.33. Typical failure modes of GFRP-RC slabs exposed to fire: (a) rebar tensile failure in slabs with continuous reinforcement (slab RB-C2.5-D8) and (b) rebar slippage in lap splices (slab RBP-LS65(S)-D12).

As shown in and Figure 6.34, all seven slabs with spliced reinforcement failed prematurely due to debonding of the overlapping rebars when the temperature at the extremities of the splices attained the T_g. As the slabs presented extensive cracking along the transverse direction at the location of the splices, and also longitudinal cracks in the lateral faces, aligned with the bottom reinforcement. In four of the mentioned slabs (*cf.* Table 6.8 in Section 6.5.2), two of them illustrated in Figure 6.34a and Figure 6.34b, the pull-out failure was also combined with local spalling of the concrete cover.

A detail of the rebars' slippage in the ends of straight and bent-end lap splices is presented, respectively, in Figure 6.33b and Figure 6.35b, after the removal of the concrete cover. In the first case (slab RBP-LS65(S)-D12), both the resin and the fibre rovings presented less severe damage compared to that observed in the slabs with continuous reinforcement: the rebars showed mild discolouration and a significant part of the ribs were sheared off, broken and detached from the rebars' core due to the softening of the resin. However, in slab RBP-LS84.5(B)-D12, depicted in Figure 6.35 as an illustrative example, higher temperatures were attained along the exposed span due to the longer exposure to heat, causing more severe deterioration of the materials; yet, as shown in Figure 6.35b, the bent extremities of the splices remained less damaged due to the high temperature gradient installed in the slabs' cross-section.

Figure 6.34. View of slabs with spliced reinforcement after failure: (a) RB-LS65(S)-D12, (b) RBP-LS84.5(S)-D12 and (c) RBP-LS84.5(B)-D12.

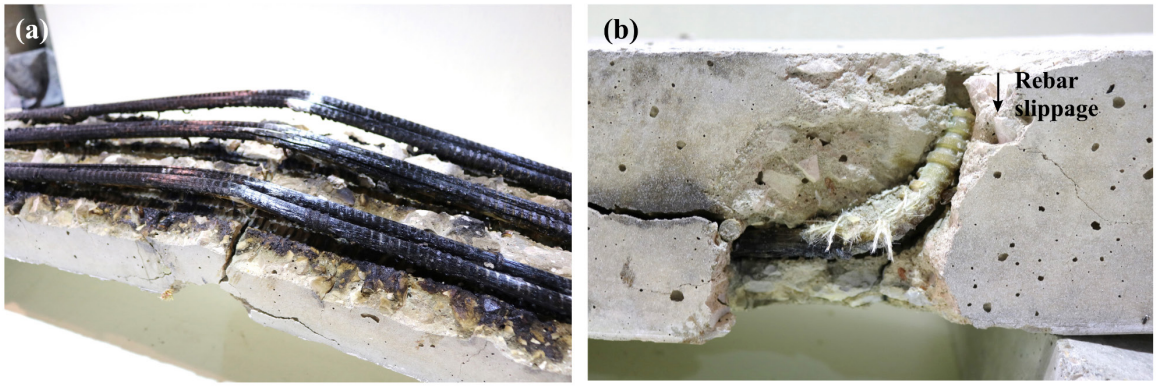

Figure 6.35. Detail of slab RBP-LS84.5(B)-D12 after failure and removal of the concrete cover: (a) longitudinal rebars after removal of concrete cover and (b) extremity of bent-end splices.

6.6. Concluding remarks

The experimental study presented in this chapter aimed to investigate the influence of several constructive details in the fire behaviour of concrete slabs reinforced with GFRP bars. The main conclusions from this study are summarized next.

The experiments confirmed that GFRP-RC slabs with continuous reinforcement can attain fire endurances above 180 min with considerably lower concrete cover thicknesses than those currently prescribed in the CAN/CSA S806 design code [8]. To that end, the anchorage zones of the reinforcement must be protected from direct thermal action in order to guarantee that their temperature remains below T_g, which should be considered as the critical temperature for the bond strength degradation. Even if the decomposition temperature is reached at the bottom reinforcement in the fire-exposed length (causing a significant level of degradation in the rebars and in the GFRP-concrete bond), the damaged rebars are still able to fulfil their load bearing function over longer periods of time, performing as cables securely anchored in the cold extremities of the RC member. As shown in the tests, the failure of FRP-RC slabs will likely be triggered by the tensile rupture of the rebars, as long as (i) continuous reinforcement is used and, (ii) the anchorage zones are well-anchored in cool zones of the member. In buildings, the connection zones to other structural members can fulfil this purpose, as the ends of the reinforcement used in slabs are usually embedded in the beams or separated from the heat source through partition walls; accordingly, in beam applications, the columns may guarantee this insulation function.

The results obtained confirm that the fire resistance of slabs with continuous GFRP reinforcement, besides depending on the thermally insulated anchorage zones, is also determined by the concrete cover thickness and, ultimately, the tensile strength of the GFRP rebars at very high temperatures. On one hand, it was verified that for the test conditions considered in this study (slabs geometry, loading and support conditions), increasing the concrete cover (from 2.5 cm to 3.5 cm) provided increases in fire endurance ranging between approximately 10 and 60 min. As mentioned, these cover thicknesses are significantly thinner than those currently recommended in [8], showing (as in [11,12]) that the design of FRP-RC flexural members can be more efficient than according to such code. On the other hand, the fire resistance of slabs comprising different types of GFRP rebars was governed by the different degradation rates of the rebars' tensile properties and of their bond to concrete with temperature; this justifies the need for compiling data regarding the thermophysical, mechanical and bond properties of different types of FRP reinforcement since, as shown in Chapter 3, they typically present large ranges of variation with temperature.

The experiments provided evidence that the severe cracking of concrete can adversely affect the slabs' fire endurance – slabs with higher concrete strength presented longer fire endurance comparing to those with lower concrete strength; in this regard, it was concluded that the fire performance of the slabs with lower concrete strength was conditioned by more extensive cracking, allowing temperature to (locally)

increase more rapidly and therefore triggering failure to occur sooner. The fire resistance of the slabs also showed some dependency of the bar diameter, however additional studies are needed to assess this aspect in further depth.

A very relevant result obtained was that, as expected, the presence of tension lap splices directly exposed to fire remarkably decreases the fire resistance of GFRP-RC slabs, due to the premature debonding of the overlapping rebars when temperature approaches and exceeds T_g. Indeed, even if the development lengths recommended in design guidelines are used (for design at ambient temperature), lap splices can remarkably reduce the fire resistance of GFRP-RC slabs (to less than 20 min), if they are located along the spans exposed to fire. In this study, slabs with straight-end splices failed before attaining 40 min of fire exposure, and their fire resistance was shown to be governed by the splice length, the type of surface finish and the T_g of the rebars. The adoption of 90º bent-end splices significantly improves the slabs' fire resistance by allowing to anchor the rebars in a cooler zone of the cross-section, where the degradation of bond occurs at a slower rate. These results, as well as those obtained in the parametric studies conducted in Section 5.4, confirm the possibility of using bent rebars to decrease the above-mentioned protected anchorage lengths (supporting the conclusions obtained in [14,18]). Nevertheless, whenever possible, one should avoid positioning the splices in cross-sections likely to be directly exposed to fire – they should be preferably extended towards the supports and their length and geometry should be defined according to optimal development and tail lengths defined as a function of temperature, such as those proposed in Section 5.4.

Chapter 7

Numerical modelling of the fire behaviour of GFRP-reinforced concrete slab strips

7.1. Introduction and objectives

The fire resistance tests presented in Chapter 6 showed that the fire design of tension lap splices and cold anchoring zones must necessarily consider the temperature-induced degradation of the bond between FRP bars and concrete and, for that purpose, such degradation has to be accurately considered in numerical simulations of the fire behaviour of FRP-RC members. Yet, due to the lack of temperature-dependent bond stress *vs.* slip laws for FRP bars, perfect bond has been often assumed in analytical and numerical simulations of FRP-RC structures exposed to fire (*e.g.* [117,119,167]), leading to unrealistic and inaccurate predictions of the structural performance, namely when failure is triggered by the loss of bond in the splices (*e.g.* [13,15]) or in the anchorage zones of the reinforcement (*e.g.* [11,12,14]).

In this context, this chapter presents numerical investigations of the fire performance of concrete slabs reinforced with sand-coated GFRP rebars, in which the main innovation with respect to the state-of-the-art is the following: (i) the explicit consideration in the numerical models of temperature-dependent GFRP-concrete bond *vs*. slip laws, and (ii) the simulation of lap splices on the reinforcement positioned at the fire-exposed span of the structural member. The objectives of this study (described in Section 7.2) were two-fold: (i) to describe in detail the development and validation of the numerical models, including the implementation of the above-mentioned interfacial laws (Section 7.3); and (ii) to conduct a numerical investigation of the structural fire behaviour of the GFRP-RC slabs (complementary to the experiments presented in Chapter 6), providing further insights about the effectiveness of the GFRP reinforcement under fire exposure, with particular focus on the efficacy of the anchorage zones and on the influence of lap splicing along the span on the fire resistance behaviour of the slabs (Section 7.4).

7.2. Description of the numerical models

7.2.1. Methodology

Table 7.1 presents the 5 slab strips that were modelled in the present study. The slabs were part of the SC series of fire resistance tests that were carried out in slabs with fibre-wrapped sand coated bars (*cf.* Section 6.4). Accordingly, the following parameters were numerically investigated: (i) the concrete cover (2.5 cm or 3.5 cm), (ii) the concrete strength (higher and lower strength, types I and II respectively), and (iii) the continuity of the reinforcement (continuous or lap spliced at midspan with an overlap length of 65 cm).

To investigate the thermomechanical behaviour of the slab strips under fire exposure, thermal and mechanical FE models were developed using *ABAQUS Standard* [198]; these two types of models were used, sequentially and in conjunction, by means of a sequentially coupled thermomechanical procedure (*ABAQUS* nomenclature). In other words, the evolution of temperatures with time was first determined in the thermal models, using as input the temperature-dependent thermophysical properties and thermal boundary conditions; next, the temperature outputs were used as imposed field inputs in the mechanical models (with the same geometry and FE mesh of the thermal models), which required the definition of temperature-dependent mechanical properties and kinematic boundary conditions.

Table 7.1. Details of the slab strips modelled in the numerical study.

Slab strip	Concrete type (*cf.* Table 6.2)	Concrete cover [cm]	Bar continuity	Fire load [kN]
SC-C2.5-D10-I	I	2.5	Continuous	16.9
SC-C2.5-D10-II	II			
SC-C3.5-D10-I	I	3.5	Continuous	13.6
SC-C3.5-D10-II	II			
SC-LS65(S)-D10-II	II	2.5	Spliced (65 cm overlap)	16.9

7.2.2. Geometry and finite elements mesh

Figure 7.1 shows the geometry and mesh of two (of three) of the 3D FE models developed to simulate the fire resistance tests performed in the slab strips with sand coated (SC) bars. The models consisted of three parts: concrete slab strip, GFRP reinforcing bars, and loading and bearing steel plates. Due to symmetry conditions, only 1/6 of the slabs with continuous reinforcement (right in the figure) and 1/3

of the slabs with lap splices (left in the figure) were modelled; the width of the models was 0.083 m. As detailed in Section 7.2.5, appropriate boundary conditions were defined accordingly.

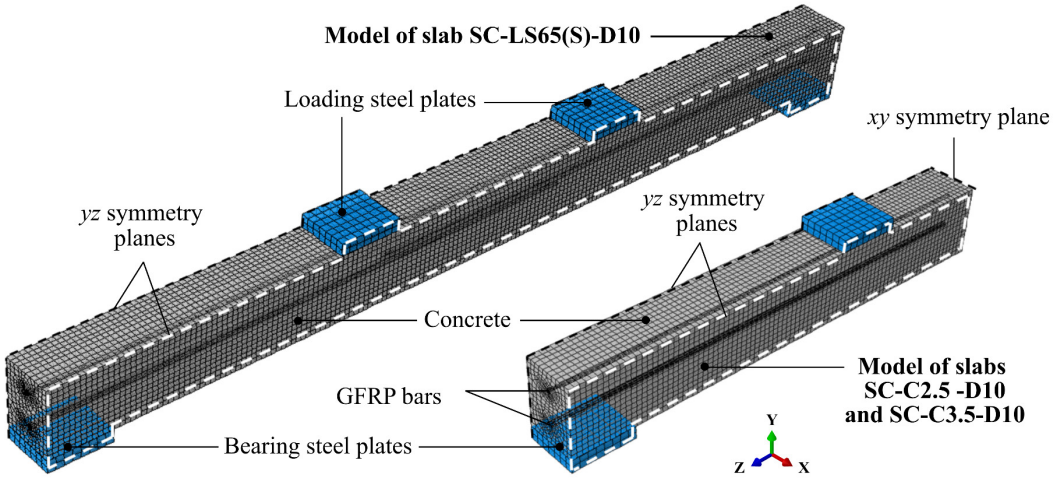

Figure 7.1. Geometry and mesh of models of SC-LS65(S)-D10 (left) and SC-2.5/C3.5-D10 (right) slab strips.

All the parts were modelled with 8-node solid finite elements: DC3D8 in the thermal models and C3D8 in the mechanical models, according to the *ABAQUS Standard* [198] designation. Regarding the FE dimensions in the concrete part, after performing a mesh sensitivity analysis, a maximum element size of 8.3 mm was adopted. For the longitudinal GFRP bars, the length of the FEs (along *z*-axis) was chosen to match that of the FEs of the concrete part, and their cross-sections were discretized with 10 FEs. The transverse reinforcement was not simulated given its negligible effect on the thermal and mechanical responses of the slabs. Finally, the steel plates were meshed with FEs with ~12 mm of size. In sum, the models with and without lap splices had, respectively, about 102,300 and 38,500 FEs.

7.2.3. Material properties

7.2.2.1. Thermophysical properties

The thermophysical properties of concrete, GFRP (bars) and steel (plates), namely the density (Figure 7.2a), specific heat (Figure 7.2b) and thermal conductivity (Figure 7.2c) were implemented in the models as a function of temperature. The variation with temperature of the properties of concrete and steel were defined in accordance with respectively EC 2 - Part 1-2 [79] and EC 3 – Part 1-2 [213], while those of GFRP were set according to Bai *et al.* [75]. Regarding the properties of concrete, the density at ambient temperature was taken as 2400 kg/m^3, the specific heat was computed assuming a (typical) moisture content of 1.5% of concrete weight and the thermal conductivity was defined as the average of the upper and lower limit values defined in [213]. Furthermore, the emissivity of concrete was taken as $\varepsilon_c = 0.7$

(temperature independent) according to [213]. It is worth mentioning that the thermophysical properties of the GFRP considered in the models are those reported for an inert environment, as the reinforcing bars are not in contact with oxygen/air and, therefore, combustion does not occur (with the exception of local sections where very wide cracks may develop in the concrete cover).

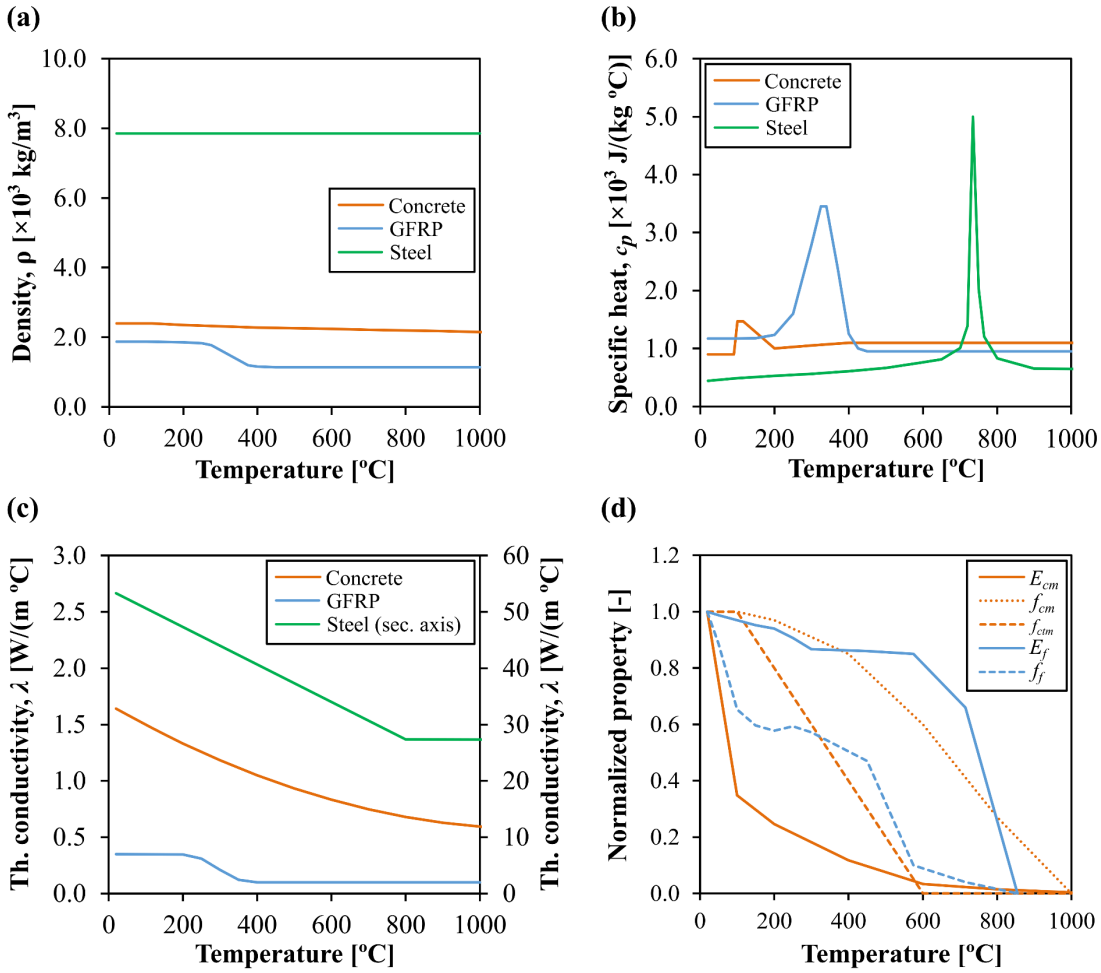

Figure 7.2. Material properties of all constituent materials as a function of temperature: (a) density, (b) specific heat and (c) thermal conductivity; (d) mechanical properties of concrete and GFRP bars as a function of temperature.

7.2.2.2. Thermomechanical properties

The CDP material model [198] was used to simulate the concrete's non-linear tensile and compressive inelastic behaviour. The following plastic flow parameters (previously designated in Section 5.3.2.2) were adopted: ψ = 36º (value suggested in *ABAQUS manual* [198] and within the range of values successfully used in the modelling of concrete elements [214–216]); $e = 0.1$; $f_{b0}/f_{c0} = 1.16$ (default value); $K_c = 2/3$, and $\mu = 1\times10^{-5}$ [203]. The constitutive relationships of concrete in compression and tension at ambient temperature were defined according to EC2 – Part 1-1 [192], considering the mechanical properties formerly presented in Table 6.2 (*cf.* Section 6.2.2 – page 168) determined at the time of the

fire resistance tests. Cube compressive strengths were converted into their equivalent cylinder values (f_{cm}) and the Young's moduli (E_{cm}) were estimated based on the compressive strengths according to EC2 – Part 1-1 [192]. Regarding the tensile behaviour, fracture energies (G_f) of 0.104 N/mm and 0.077 N/m were estimated according to Hilsdord and Brameshuber [205] for concrete types I and II, respectively. The variation of the mechanical properties (Figure 7.2d) and of the thermal expansion coefficient of concrete (α_c) with temperature was defined according to EC 2 – Part 1-2 [79], with the exception of the Poisson's ratio (υ_c = 0.2) and fracture energy ([217,218]), which were assumed constant with temperature.

The SC GFRP bars were modelled as linear elastic isotropic materials, considering the tensile properties at ambient temperature determined in the tensile tests (*cf.* Table 3.7 – page 84). The reductions of the tensile modulus (E_f) and tensile strength (f_f) of the bars with temperature, depicted in Figure 7.2d, were defined according to results of the tensile tests up to 300 ºC; for higher temperatures (up to 715 ºC), the results obtained in RB-D12 bars were considered. Due to the lack of test data for temperatures higher than 715 ºC, a reduction of 99% in both strength and modulus was considered at 855 ºC, since glass fibres (in this case, of type E-CR) begin to soften between 830 ˚C and 880 ˚C [57,219]. Tensile failure of the bars was simulated by defining an elastic limit stress (at each temperature) and adopting the *Plastic* material behaviour in *ABAQUS* [36] which considers the von Mises criterion and a plastic behaviour (plateau) beyond the elastic limit stress; this simplification, which is deemed acceptable at elevated temperatures (namely, above T_d, as shown in [105] and in Figure 3.9 from Section 3.4.3.1 – page 80), was adopted to allow identifying the tensile failure (initiation) of the bars and, therefore, allowing to easily detect failure of the slabs by a sudden slope increase on midspan *vs.* time curves. Hence, it is important to highlight that, given this approximation on the material model of the GFRP bars, the numerical results (shown ahead) beyond that sudden slope increase have no physical/mechanical meaning.

The Poisson's ratio of the bars ($\upsilon_{SC\ bar}$ = 0.26) was computed using the rule of mixtures and assumed constant with temperature. The thermal expansion coefficient of GFRP (α_f) was taken as 6.7×10^{-6} and assumed constant with temperature [220]. The steel of the loading plates was modelled adopting an elastic model and considering the following properties (constant with temperature): Young's modulus, E_s = 210 GPa, and Poisson's ratio, υ_s = 0.3.

7.2.4. Material interactions

The interaction between the (loading and bearing) steel plates and concrete was insured by applying the *TIE* constraint [198]. Regarding the bond behaviour between the GFRP rebars and concrete, cohesive interface surfaces were adopted using the *surface-to-surface small sliding* interaction [198]. To that end, the contact stiffness and the damage initiation and evolution of the bond properties along the tangential

direction were defined according to temperature-dependent local bond stress *vs.* slip laws calibrated for SC bars in Section 5.2; the bond laws are plotted in Figure 5.3 (*cf.* Section 5.2.2.1 – page 140).

Due to the lack of data for temperatures above 200 ºC (for which bond is drastically reduced), the bond stiffness (defined next) and maximum bond stress were considered to be nearly zero at 250 ºC. The tangential contact stiffness (K) for each temperature was taken as the slope of the line defined by the origin and the point corresponding to 90% of the maximum bond stress of the bond stress *vs*. slip law. The latter point also corresponded to the damage initiation of the bond property. As for damage evolution, bond stress *vs*. slip (τ-s) curves were converted into damage *vs*. plastic slip (D-s_{pl}) curves [198], with $D = 1 - \tau/(K \cdot s)$ and $s_{pl} = s - \tau/K$. For the direction normal to the GFRP-concrete surface, due to the lack of information in the literature and its reduced influence on the overall response of the slabs, a high contact stiffness (1000 MPa/mm, constant with temperature) was assumed.

7.2.5. Loading and boundary conditions

7.2.4.1. Thermal boundaries

In order to replicate the heating conditions of the fire tests and to provide accurate estimations of the temperature distributions along the exposed and unexposed regions of the slabs, the boundary conditions, schematized in Figure 7.3, were considered (some of the conditions are simplifications, defined by trial and error, following a similar approach to that adopted in [12,154]). Regarding the zone directly exposed to fire (central length of 950 mm between the furnace walls, Figure 6.11b in Section 6.2.5), the temperature of the bottom surface of the slabs was increased according to the ISO 834 standard fire curve [24], considering both radiation and convection heat transfer modes; a temperature independent convection coefficient h_c = 25 W/(m^2 ºC) was adopted, as suggested in [79].

The adjacent zone located above the furnace wall (corresponding to a length of 75 mm on each side of the slabs) was indirectly exposed to fire; here, only convection heat transfer was considered (radiation was disregarded) with 50% of the temperature defined in the ISO 834 curve (*i.e.*, lower than in the directly exposed zone). In the insulated zone located above the furnace wall (100 mm in length), heat transfer was considered by imposing a nodal temperature, equal to 10% of the values defined in the ISO 834 curve at the superficial nodes of the bottom surface of the slabs along that length. Adiabatic boundaries were considered on the lateral faces of the slab strips (in the experiments those surfaces were insulated with ceramic wool). For all remaining surfaces, both radiation and convection heat transfer modes were considered (also with h_c = 25 W/(m^2 ºC), constant with temperature). All nodes of both thermal and mechanical models were set to an initial temperature of 20 ˚C.

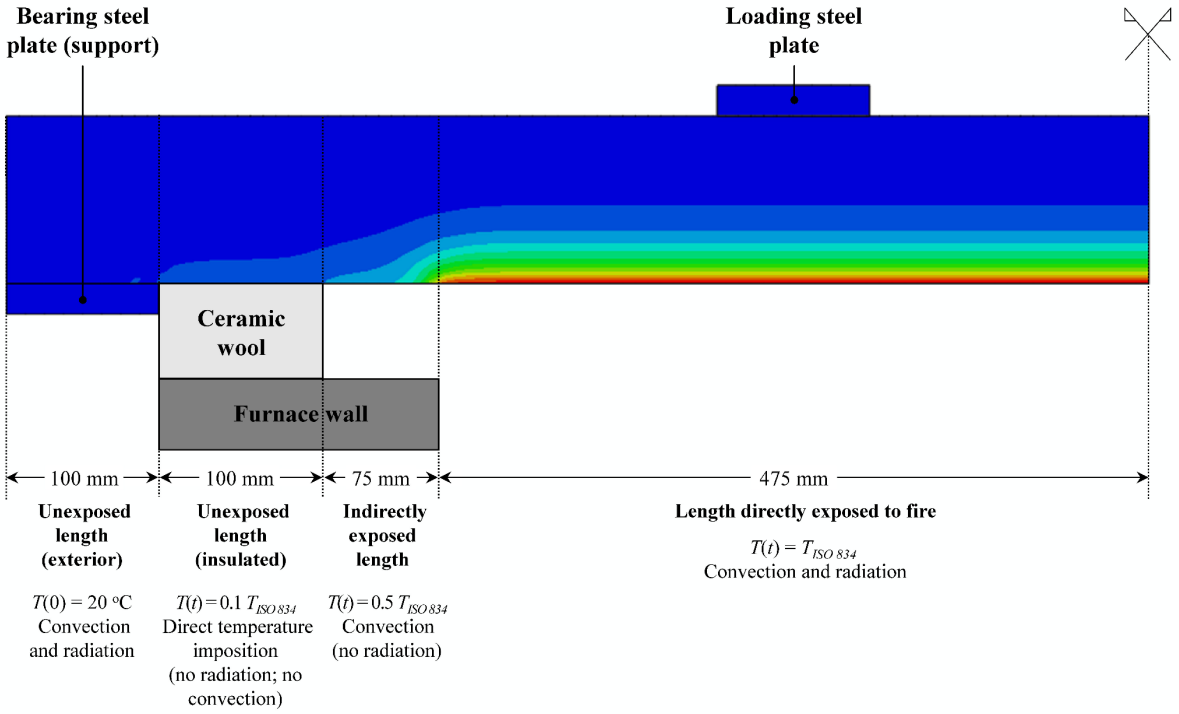

Figure 7.3. Thermal boundary conditions assumed along the length of the slab strips.

7.2.4.2. Kinematic boundaries and loading

As mentioned in Section 7.2.2, the model parts were simulated considering symmetry conditions. For this purpose, in the models with continuous reinforcement, (i) the nodes of the concrete located on the *yz* symmetry planes, and (ii) the nodes of the concrete and of the rebars located on the *xy* symmetry plane were prevented from displacing, respectively, along the *x*- and *z*-axes. To simulate the support conditions used in the experimental campaign, in the mechanical models, a row of nodes located at half-length of the lower face of the bearing steel plates were prevented from displacing along the *y*-axis (Figure 7.1). In the models of slab strips with lap splices, in one of the bearing steel plates, a row of nodes was also prevented from displacing along the *z*-axis. In the mechanical models, the sustained fire load (Table 7.1) was applied through nodal forces distributed in the loading steel plates.

7.2.6. Types of analyses

Two types of analyses were conducted: (i) transient heat-transfer analysis, using the thermal models; and (ii) physically non-linear and geometrically linear static general analysis, using the mechanical models. In the thermal and mechanical models, the maximum time steps varied between 3600 s and 10800 s depending on the fire exposure periods of each slab strip, and maximum time increments of 50 s were allowed. In the mechanical models, the fire load was applied in the first second of the simulations and then maintained constant up to the end of the analyses.

7.2.7. Summary of modelling assumptions

In summary, to model the complex thermomechanical behaviour of the GFRP bars and GFRP-RC slabs under fire exposure, the following assumptions and simplifying hypotheses were considered in the FE models:

(i) The thermal analysis of the slabs during fire exposure was uncoupled from the mechanical analysis.

(ii) The presence of the transverse reinforcement in the slabs was disregarded from the thermal and thermomechanical analyses due to its negligible influence.

(iii) The GFRP bars were modelled as isotropic materials and their tensile failure was numerically simulated, in a simplified way, by defining an elastic-plastic stress-strain relationship, in which an elastic limit stress was defined based on the tensile strength measured in the tensile tests, and the von Mises criterion was considered for the "inelastic behaviour".

(iv) The mechanical properties of the bars were defined as a function of temperature based on results obtained in tensile tests performed in steady-state conditions and in an oxidative environment.

(v) The variation with temperature of the bars' tensile strength and modulus at temperatures above 300 ºC (up to 715 ºC) was considered as obtained in Section 3.4.3.3 (for a different type of GFRP bar, but with very similar fibre content); the reduction of both properties at 855 ºC (not measured) was assumed to be 99% w.r.t. ambient temperature (considering the softening temperature of E-glass fibres).

(vi) The fracture energy of concrete, the thermal expansion coefficient of GFRP bars, as well as the Poisson's ratios of both concrete and GFRP bars were considered constant with temperature. Furthermore, in the material model of concrete (CDP) the value of the dilation angle and f_{b0}/f_{c0} ratio were considered as suggested in *ABAQUS* manual [198].

(vii) The GFRP-concrete interaction in the tangential direction was modelled as a function of temperature (up to 200 ºC) considering the bond stress-slip laws obtained (independently) from pull-out tests performed in steady-state conditions; the bond between the bars and the concrete was assumed to be completely deteriorated at 250 ºC. The effect of temperature in the GFRP-concrete interaction in the normal direction was neglected.

(viii) The interaction between the overlapped reinforcing bars, and between these and concrete, was considered equivalent to that of a single bar embedded in concrete (as simulated in the pull-out tests).

7.3. Comparison between experimental and numerical responses

7.3.1. Temperature distributions

This section compares the numerical and experimental thermal responses of the slabs. It is worth referring that the experimental thermal responses of the slabs did not show dependence on the concrete strength (however, as discussed ahead, locally, this may not have been always the case). Hence, for the thermal response under fire exposure shown hereafter, in the cases where both concrete types were studied for a given geometry, the results of slab strips with concrete type I are presented, since a wider collection of data could be obtained (due to the longer fire resistance). Figure 7.4 shows the numerical (N) and experimental (E) evolution of temperature with time in three thermocouples placed at different heights of the midspan section of slabs SC-C2.5-D10-I (Figure 7.4a), SC-C3.5-D10-I (Figure 7.4b) and SC-LS65(S)-D10-II (Figure 7.4c): T3 (top rebar), T4 (bottom rebar), and T7 (bottom concrete face). It can be seen that there is an overall good agreement between numerical and experimental temperatures (test data are shown until the instant corresponding to the numerical fire resistance or until experimental failure).

In all slabs, the curves depicted in Figure 7.4 reflect the expected temperature gradients across the sections depth, with significantly higher temperatures and rates of temperature increase closer to the fire-exposed (*i.e.*, bottom) surface, due to the relatively low thermal conductivity of concrete. The influence of concrete cover in the bottom rebars' temperature is shown in Figure 7.4d, which compares the results of slabs SC-C2.5-I, SC-LS65-II and SC-C3.5-I. As expected, for the same period of fire exposure, higher temperatures are attained in the slabs with lower concrete cover; for instance, after 50 min, the numerical temperature at the bottom reinforcement (T4) in the slabs with 2.5 cm of cover (SC-C2.5-I) is about 35% higher (20% if considering experimental data) than in slab with 3.5 cm of cover (SC-C3.5-I).

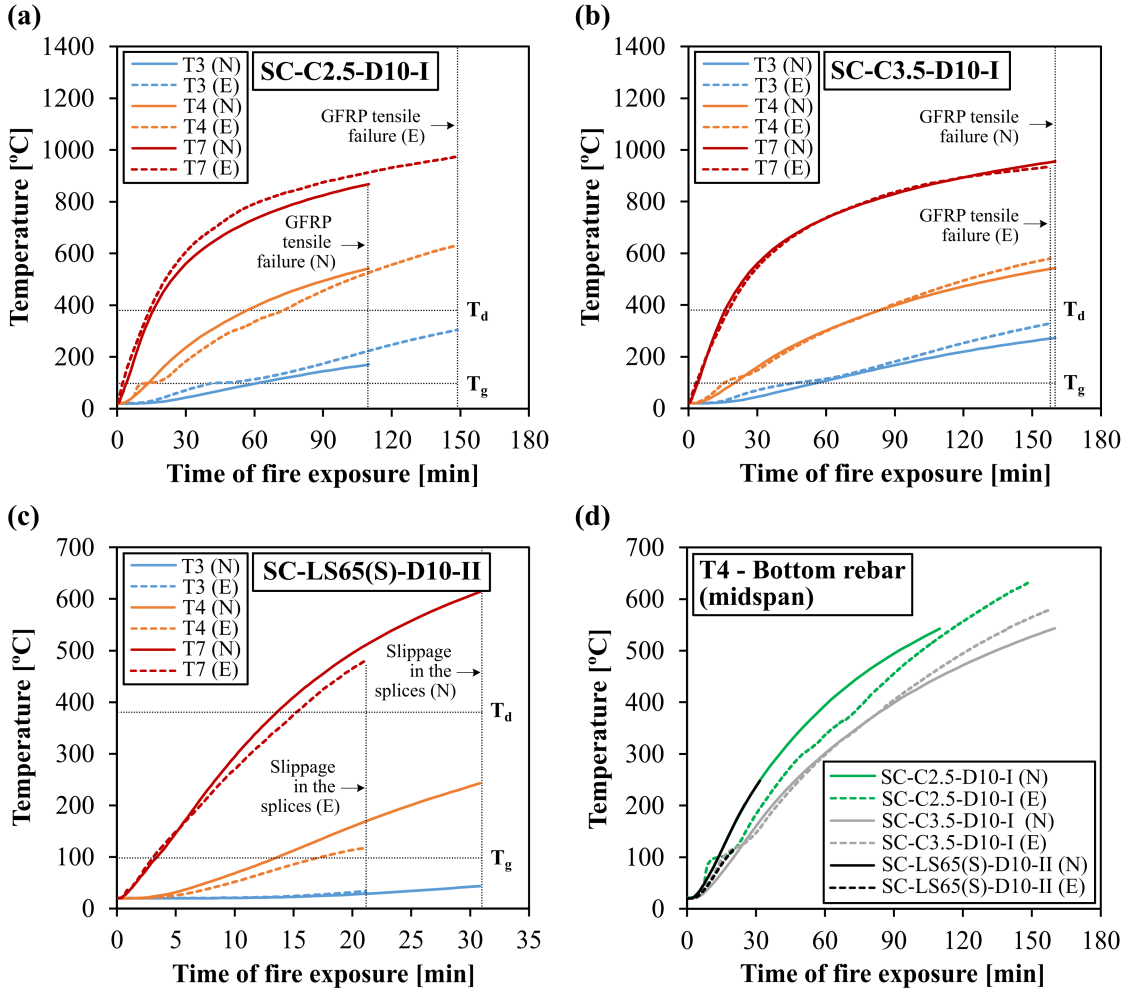

Figure 7.4. Numerical (continuous) and experimental (dashed) temperature *vs*. time curves of slabs: (a) SC-C2.5-D10-I, (b) SC-C3.5-D10-I and (c) SC-LS65(S)-D10-II, and (d) comparison of temperature curves obtained at the bottom reinforcement at midspan (thermocouple T4).

Figure 7.5a and Figure 7.5b show the good agreement between numerical and experimental temperature distributions obtained along the length of the bottom GFRP bars of slabs SC-C2.5-D10-I and SC-C3.5-D10-I, respectively, for different durations of fire exposure (30, 60, 90 and 120 min). The temperature profiles present a highly non-linear variation along the slabs' length, attaining higher values in the centre of the slabs that decrease towards the protected anchorage zones. The figures show that the T_g of the bottom rebars was exceeded during the first 30 min of fire exposure along the entire fire-exposed span of the slab. After a period of 90 min in slab SC-C2.5-D10-I (120 min in slab SC-C3.5-D10-I), the temperature along the heated span approached (and even exceeded) the T_d (374 ºC); at this temperature, bond is completely degraded (*cf.* Figure 5.3 – page 140) and the mechanical properties of the reinforcement, especially the tensile strength, are severely reduced due to the resin decomposition, but are not negligible (*cf.* Figure 7.2d).

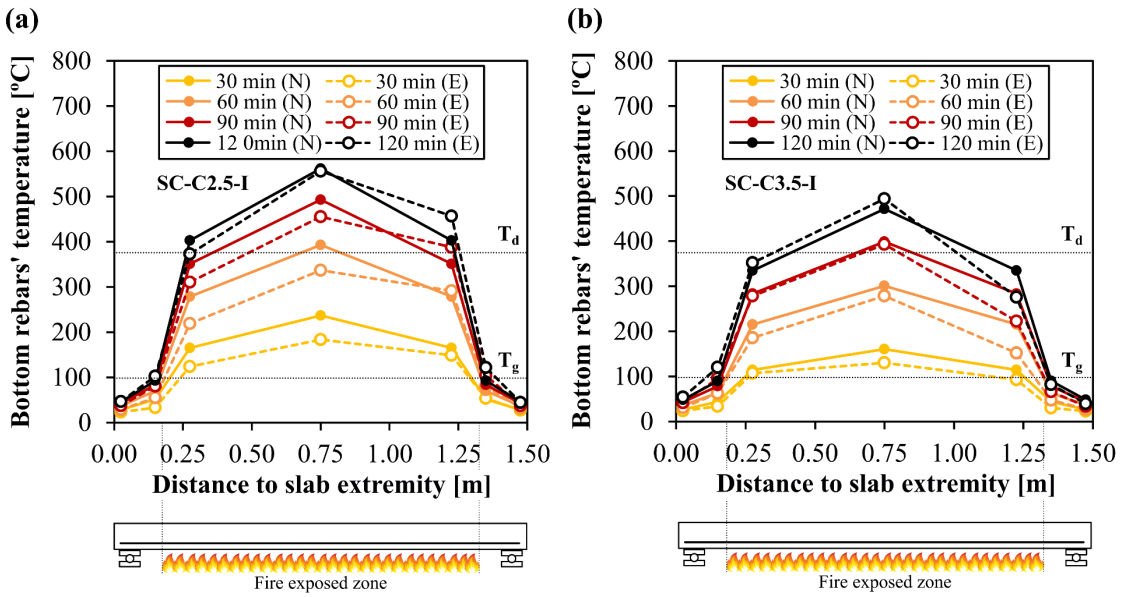

Figure 7.5. Numerical (continuous) and experimental (dashed) temperature evolution in the bottom reinforcement along the length of slabs for different times of fire exposure: (a) SC-C2.5-D10-I and (b) SC-C3.5-D10-I.

As for the insulated anchorage zones of the reinforcement, their temperature remained below T_g during most of the fire exposure period; yet, after 120 min, temperatures at 0.15 m from the slab extremity (thermocouples T9 and T12) approached very closely the T_g (in the experiments, the T_g was even slightly exceeded), indicating that bond was also significantly degraded within the protected anchorage zones. Nevertheless, as confirmed in the FE models, the remaining anchorage length of the bars remained below the T_g, which prevented premature pull-out failures from occurring and enabled the occurrence of tensile failure of the rebars at the fire-exposed span for temperatures considerably above their T_d. The good agreement between numerical and experimental thermal responses validated the temperature-dependent thermophysical properties of the materials adopted and showed that the thermal boundary conditions implemented in the models were appropriate.

7.3.2. Midspan displacement increase and failure modes

Figure 7.6 shows the midspan displacement increase *vs.* time of fire exposure (t) curves of slabs SC-C2.5-D10-I/II (Figure 7.6a), SC-C3.5-D10-I/II (Figure 7.6b) and SC-LS65(S)-D10-II (Figure 7.6c). Overall, there is reasonable agreement between numerical and experimental curves, with all pairs showing similar qualitative behaviour. Regarding the detailed analysis of the numerical curves, it can be seen that the thermomechanical response of the slabs with continuous rebars (SC-C2.5-D10 and SC-C3.5-D10) can be divided into three main development stages (denoted by I, II and III, defined as described next), whereas the slab with lap splices (SC-LS65(S) -D10) exhibits only the first two stages (failing at the beginning of stage II).

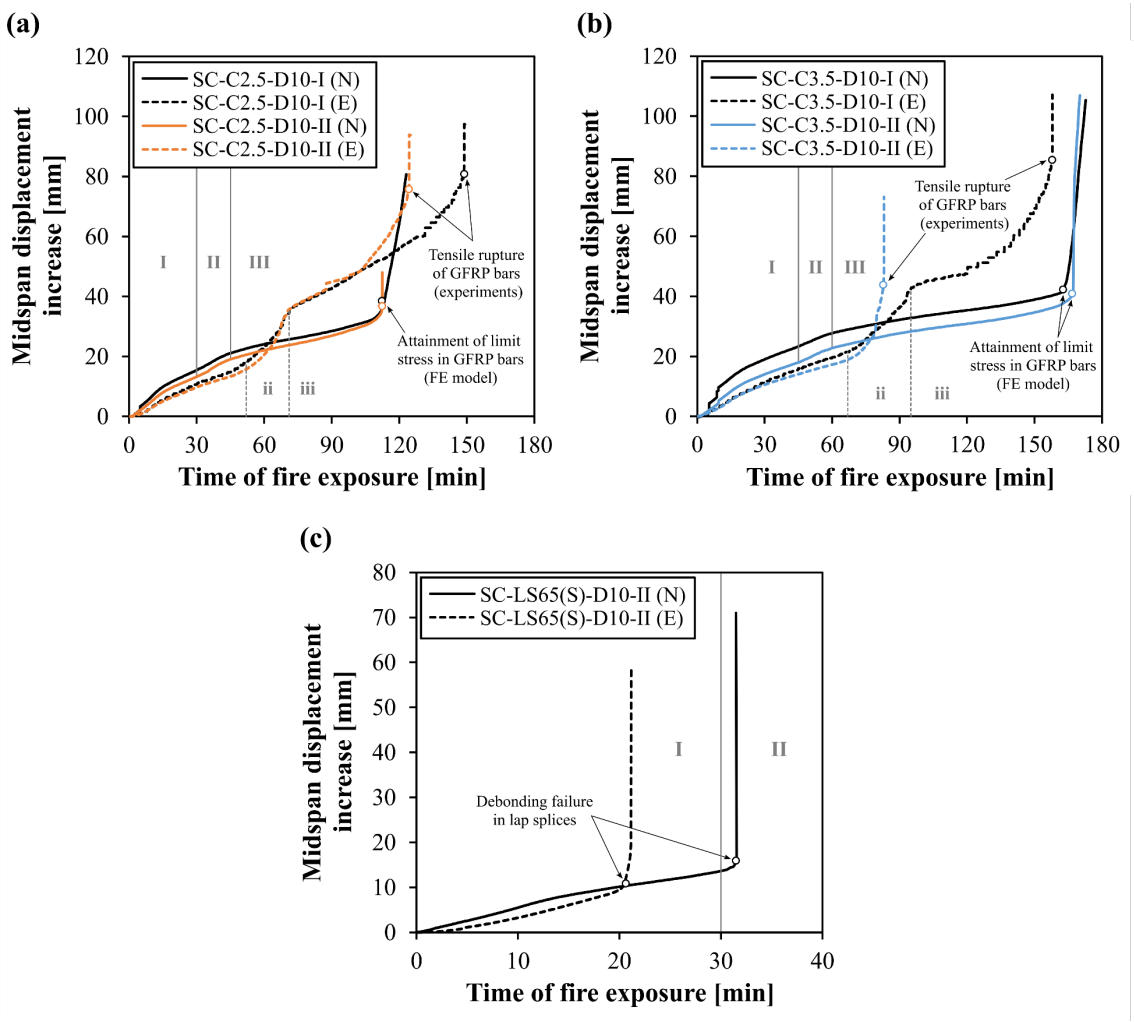

Figure 7.6. Numerical (continuous) and experimental (dashed) midspan displacement increase with time of fire exposure curves obtained in slabs (a) SC-C2.5-D10-I/II, (b) SC-C3.5-D10-I/II and (c) SC-LS65(S)-D10-II (stages I, II and III refer to numerical curves; stages ii and iii refer to experimental curves).

For all slabs, the first stage (stage I) of the numerical curves was defined from the beginning of fire exposure up to $t \approx 30$ min and $t \approx 45$ min, respectively, for the slabs with 2.5 cm and 3.5 cm of concrete cover, with the curves exhibiting a convex shape. During this first stage, the displacement increase is mainly attributed to: (i) the temperature gradient stemming from the fire exposure, which induces positive (downwards) bending (*i.e.*, thermal bowing); (ii) concrete cracking (and the resulting reduction of flexural stiffness); (iii) degradation of GFRP-concrete bond, and (iv) reduction of the GFRP tensile modulus along the heated length of the slabs. For $t \approx 30$ min (for slabs SC-C2.5-D10-I/II (N) and SC-LS65(S)-D10-II (N)) and 45 min (for slabs SC-C3.5-D10-I/II (N)), the average temperature of the bottom GFRP rebars was around 230 ºC, considerably above the T_g (Figure 7.4d), for which the GFRP-concrete bond properties are remarkably reduced. Indeed, this explains why slab SC-LS65(S)-D10-II (N) failed shortly after 30 min, at the beginning of stage II, for $t = 31$ min (*vs.* $t =$

20 min in the tests), as its load bearing capacity relies on the bond stress transfer capacity in the lap splice (positioned at midspan).

A second stage of the response (stage II) was identified in the numerical curves from $t \approx 30$ min (slabs SC-C2.5-D10-I/II (N)) and 45 min (slabs SC-C3.5-D10-I/II (N)), which lasted around 15 min. During this stage, an inflection of the curves occurred, now displaying a concave shape up to $t \approx 45$ min (slabs SC-C2.5-D10-I/II (N)) and 60 min (slabs SC-C3.5-D10-I/II (N)); at these instants, the average temperature of the bottom GFRP rebars along the fire-exposed span was around 300 ºC, for which the GFRP-concrete bond properties are virtually null (*cf.* Figure 5.3 – page 140), but their mechanical properties are still not negligible (Figure 7.2d) – this indicates that the GFRP rebars started behaving as cables anchored in the "cold" anchorage zones. A further assessment of this behaviour is provided in the next section. For the slabs with continuous reinforcement, the corresponding stage II in the experimental curves (denoted by stage *ii* in Figure 7.6), compared to the numerical curves, occurs about 15/20 min later, presents a slightly longer duration (30 min instead of 15 min), and exhibits a much more pronounced concave shape – these differences may be partially related to the uncertainties regarding the GFRP-concrete bond properties for temperatures above 200 ºC (resulting from the lack of experimental data at those temperatures); as mentioned in the Section 7.2.4, given the absence of bond-slip relations for higher temperatures, the GFRP-concrete interaction was assumed negligible for temperatures above 250 ºC. Moreover, these uncertainties might also be related to the differences between the actual bond behaviour of the bars when embedded in a RC member subjected to bending and that considered in the study (obtained from pull-out tested in bars embedded in concrete cylinders).

In the third stage of the thermomechanical response (stage III, from $t \approx 45$ min and 60 min of fire exposure, respectively in numerical curves of slabs SC-C2.5-D10-I/II (N) and SC-C3.5-D10-I/II (N)), the displacement increase rate was significantly reduced (as in the corresponding experimental curves – for these, the beginning of the corresponding stage is denoted by stage *iii* in Figure 7.6, maintaining an approximately linear increase up to failure, marked by a sharp displacement increase. During the initial part of stage III and up to $t \approx 105$ min in slabs SC-C2.5-D10-I/II (N) and ≈ 155 min in slabs SC-C3.5-D10-I/II (N), the temperature in the bottom GFRP rebars at midspan increase from 300 ºC to 530 ºC. For this temperature range, the GFRP stiffness reduction with temperature is small and almost linear (Figure 7.2d), which may explain why the displacement increase with time is approximately linear and presents a relatively small slope during most of stage III.

The gradual and severe reduction of the GFRP rebars' strength with increasing temperatures (especially above 500 ºC) led to their tensile rupture at temperatures (540 ºC) considerably above their T_d in the experiments. The fire resistance of slabs SC-C2.5-D10-I/II was estimated by the models as 109 min (149 and 124 min in the tests), while slab SC-C3.5-D10-I was predicted to fail after 160 min (158 min in the tests), and slab SC-C3.5-D10-II after 164 min (83 min in the tests). The deviations between predicted (numerical) and actual (experimental) thermomechanical responses, explained in greater detail

further ahead, may be attributed to two main reasons: (i) the use of a sequentially coupled thermomechanical analysis, and (ii) differences between the temperature-dependent material and bond properties of the GFRP bars considered in the models (obtained from independent experimental tests) and the actual ones. The reasons for the higher relative differences in fire resistance obtained for slab SC-C3.5-D10-II are discussed ahead.

Regarding the influence of the concrete cover thickness on the fire resistance of the slabs, by comparing the results of slab SC-C2.5-D10-I (N) with slab SC-C3.5-D10-I (N), and of slab SC-C2.5-D10-II (N) with slab SC-C3.5-D10-II (N), an average increase of fire resistances of circa 50% (*vs*. 30% in the tests, only for concrete I, as explained below) was obtained when the concrete cover was increased by 1 cm.

With respect to the influence of the concrete strength on the fire behaviour of the slabs, and contrary to what was observed in the experiments, this parameter did not affect the fire resistance (considered as the time to failure) predicted by the numerical models, as slabs with different concrete strengths (for a given concrete cover) failed after very similar periods of fire exposure. The influence of the concrete strength on the numerical midspan displacement *vs*. time curves can be seen essentially in the first instants of fire exposure (up to 5-10 min), during which slabs with concrete type I (higher strength) present more extensive cracking development (resulting in small but sharp increases of displacement, especially noticeable in slab SC-C3.5-D10-I, *cf.* Figure 7.6b); whereas in slabs with concrete type II (lower strength) a more significant part of the cracks developed at the load application stage (*i.e.*, prior to the fire exposure) and therefore the resulting higher midspan displacement is not visible in Figure 7.6. Indeed, the models of slabs with concrete type II began the fire exposure stage with further cracking and higher displacement due to the application of mechanical load (5.4 mm in slab SC-C2.5-D10-I (N) *vs*. 9.8 mm in slab SC-C2.5-D10-II (N), and 1.3 mm in slab SC-C3.5-D10-I (N) *vs*. 6.5 mm in slab SC-C3.5-D10-II (N) (the applied load was the same irrespectively of the concrete type).

Still regarding the influence of the concrete strength, the experimental results showed that lower concrete strength led to lower fire resistance – this expected conclusion can be explained by the higher proneness to cracking in slabs with lower strength concrete, resulting in higher deformations/stresses imposed to the bottom reinforcement (compared to those of less cracked slabs made of higher strength concrete). It is still worth referring that the thermal protection provided by the concrete cover to the GFRP rebars is locally reduced in cracked sections – as discussed next, this localized effect (not simulated in the numerical models) had a significant effect on the fire resistance of the tested slabs. In fact, the experimental results of slabs SC-C2.5-D10-I (E) and -II (E) confirm this observation and for slabs SC-C3.5-D10-I (E) and -II (E) this seems to have been amplified by the higher concrete cover, which, together with the relatively low strength of concrete, made slab SC-C3.5-D10-II (E) especially susceptible to cracking. This seems to be the reason why slab SC-C3.5-D10-II (E) had much lower fire resistance than expected *a priori* (namely, as predicted by the numerical model) and failed during the (experimental) corresponding stage II (stage *ii* in Figure 7.6a and Figure 7.6b). Once again, it is

emphasized that this localized behaviour is not captured by the FE models (a sequentially coupled modelling was used) nor it was by the thermocouples – in fact, the critical crack occurred in a section near (but not coincident with) the instrumented section at midspan; moreover, a wider crack also promotes an oxidative environment, in which glass fibres tend to present a faster and more significant degradation than in an inert environment [110]. The topic on the influence of the concrete strength and specially of the above-mentioned localized heating effects at cracked sections on the fire resistance of FRP-RC members should be investigated in further depth, namely using fully coupled thermomechanical numerical models (and additional instrumentation in experiments).

Finally, regarding the presence of lap splices, the numerical model of slab SC-LS65(S)-D10-II (N) confirms that their adoption in zones directly exposed to fire leads to a major reduction of fire resistance of about 70% (*vs*. circa 85% in the experiments) comparing to the slab with continuous rebars (slab SC-C2.5-D10-II (N)). As seen above and as discussed in more detail in the following section, slab SC-LS65(S)-D10-II (N) failed prematurely during the first 30 min of fire exposure (stage II) due to the loss of bond between the concrete and the overlapped GFRP rebars.

Figure 7.7 and Figure 7.8 present, for illustrative purposes, a comparison between the numerical and experimental failure modes of slabs SC-C2.5-D10-II and SC-LS65(S)-D10-II, respectively. Additionally, Figure 7.9 shows the numerical and experimental rebar slippage that triggered the failure of slab SC-LS65-II. The figures depict the good agreement between numerical and experimental failure modes: both slabs present significant downwards (positive) bending deformation, with formation of visible (wide) vertical cracks throughout the span due to concrete cracking and, in the case of SC-LS65(S)-D10-II, loss of bond between the rebars and concrete (Figure 7.9). It is worth noting that the large crack seen in Figure 7.8b was not simulated by the models, as it was mostly developed after the bond failure in the lap splices and, therefore, in a stage for which the (implicit) numerical models were no longer valid.

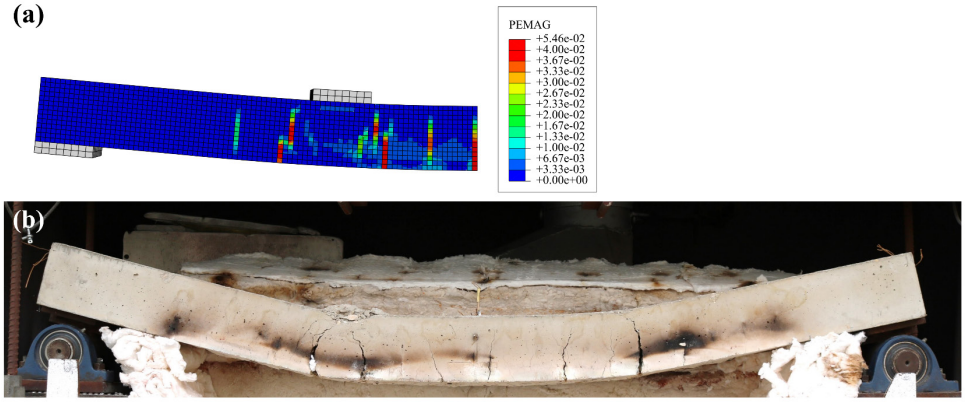

Figure 7.7. Side view of the (a) numerical (including the plastic strain magnitude field – PEMAG [-]) and (b) experimental failure modes of slab SC-C2.5-D10-II under thermomechanical loading.

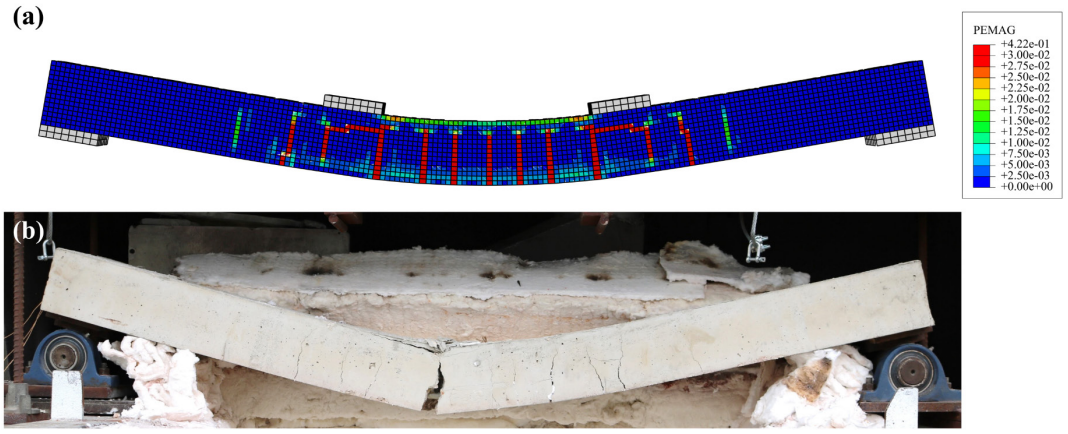

Figure 7.8. Side view of (a) numerical (including the plastic strain magnitude field – PEMAG [-]) and (b) experimental failure modes of slab SC-LS65(S)-D10-II under thermomechanical loading.

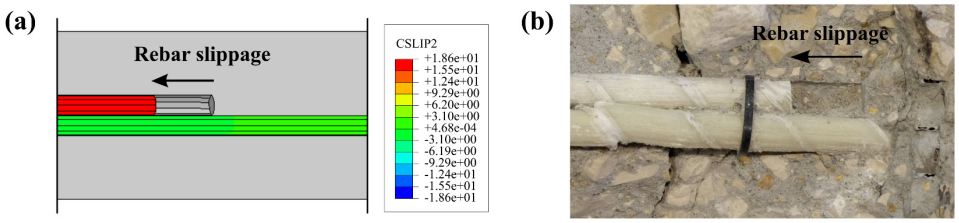

Figure 7.9. Bottom view of (a) numerical (including the longitudinal displacement field – U_3 [mm]) and (b) experimental rebar slippage of slab SC-LS65(S)-D10-II under thermomechanical loading.

Additionally, and not considering slab SC-C3.5-D10-II (for the reasons mentioned above) the average ratio between numerical and experimental times to failure is 1.05 (with a standard deviation of 0.31) and the maximum relative difference is ~55% for slab SC-LS65(S)-D10-II (although in this case corresponding to a difference of only 10 min).

Overall, considering the complexity of modelling the behaviour of FRP bars, FRP-concrete interfaces and FRP-RC structural members when subjected to elevated temperatures/fire, the models of slabs with continuous and spliced reinforcement were able to provide results with a reasonable degree of accuracy with respect to the experiments. The possible reasons for the deviations observed in Figure 7.6 regarding the deflection responses and time to failure of the slabs (described next) are mainly due to the simplifications and modelling assumptions that had to be considered in this study (*cf.* Section 7.2.7).

The first reason is that the sequentially coupled thermomechanical analysis adopted is not able to reproduce the localized combustion (in oxidative environment) and associated heating effects on the bottom reinforcing bars that occurred in the experiments, namely in sections where significant flexural cracks developed during fire exposure (namely, in more advanced stages of the tests). It is worth referring that the effect of concrete cracking on the thermal field and its influence on the fire endurance

of concrete members (which, in this study, was more relevant in slabs with lower concrete strength) has been object of recent investigations and consensual conclusions have not yet been reached, with some studies reporting that heat propagation tends to increase due to the presence of cracks (*e.g.* [158,159]), while others present contradictory results (*e.g.* [160–163]).

The second reason that explains the differences between experimental and numerical midspan displacement *vs*. time curves is that the tensile properties of the GFRP bars and the local bond stress-slip laws implemented in the models were independently determined from steady-state tests, hence under different heating and loading conditions than those experienced during the fire resistance tests of the slabs – these conditions are more accurately captured by means of transient-state tests [19,105,110,126]. Indeed, in the steady-state tests, the bars were loaded up to failure only after a certain target (constant) temperature was attained (in the pull-out tests, temperature was measured at the GFRP-concrete interface); however, in the fire tests, the bars were embedded in concrete and subjected to tension while exposed to increasing temperature (*i.e.*, transient-state conditions).

Regarding the mechanical properties, the following two additional aspects are worth being highlighted as possible reasons for the above-mentioned differences: (i) although the thermal decomposition of the bars in RC members takes place in an inert environment (except in largely cracked sections where decomposition due to oxidation may occur), the tensile properties considered in the models were determined in an oxidative environment, which, according to [110], leads to faster and more severe degradation of the glass fibres; and (ii) the tensile strength and modulus considered at temperatures between 300 ºC and 715 ºC were obtained for a different (but comparable) type of reinforcing bar than that used in the slabs, and, due to the lack of experimental data, it was assumed that these properties were fully degraded at 855 ºC. Due to the aforementioned reasons, the actual tensile properties of the GFRP bars may be slightly different from those considered in the models. With respect to the bond properties, is worth highlighting that the bond behaviour of the reinforcement at the tension lap splices was considered equivalent to that of the pull-out behaviour of a single bar embedded in a concrete cylinder; while differences are to be expected between those two cases, no experimental data are presently available about the bond behaviour of FRP reinforcement with lap splices. Furthermore, it was considered that the GFRP-concrete bond was fully degraded at 250 ºC; however, it was not possible to confirm this assumption by means of bond tests (performed only up to 200 ºC); these reasons can also explain the differences in the prediction of the fire endurance of slab SC-LS65(S)-D10-II (Figure 7.6c).

7.4. Structural effectiveness of GFRP reinforcement under fire exposure

In this section, the FE models were used to investigate in further depth the structural efficiency of the GFRP reinforcement during fire exposure, particularly to assess parameters that are not possible to measure at very high temperatures/fire conditions, namely the stresses in the GFRP reinforcement and

the bond stresses at the GFRP-concrete interface, as well as their evolution during fire exposure. The numerical results presented concern slabs with concrete type II, enabling the direct comparison between slabs with continuous and lap spliced reinforcement.

Figure 7.10 presents the evolution with time of fire exposure of: (i) the tensile stress in the bottom rebars (Figure 7.10a); (ii) the bond stress along the GFRP-concrete interface (Figure 7.10b), and (iii) the normalized tensile stress in the bottom rebars (Figure 7.10c), taken as the ratio between the tensile stress and corresponding strength at a given temperature. The results of these figures include numerical outputs in two relevant locations: (i) the anchorage length, denoted by (*A*), for which the results correspond to the average stresses obtained along the rebars' insulated length (*i.e.* 175 mm in length, *cf.* Figure 6.11b in Section 6.2.5); and (ii) the central length in the span, denoted by (*S*), for which the stress values were obtained in a section located between initial cracks (between loaded sections, position determined by peaks in the PEMAG output).

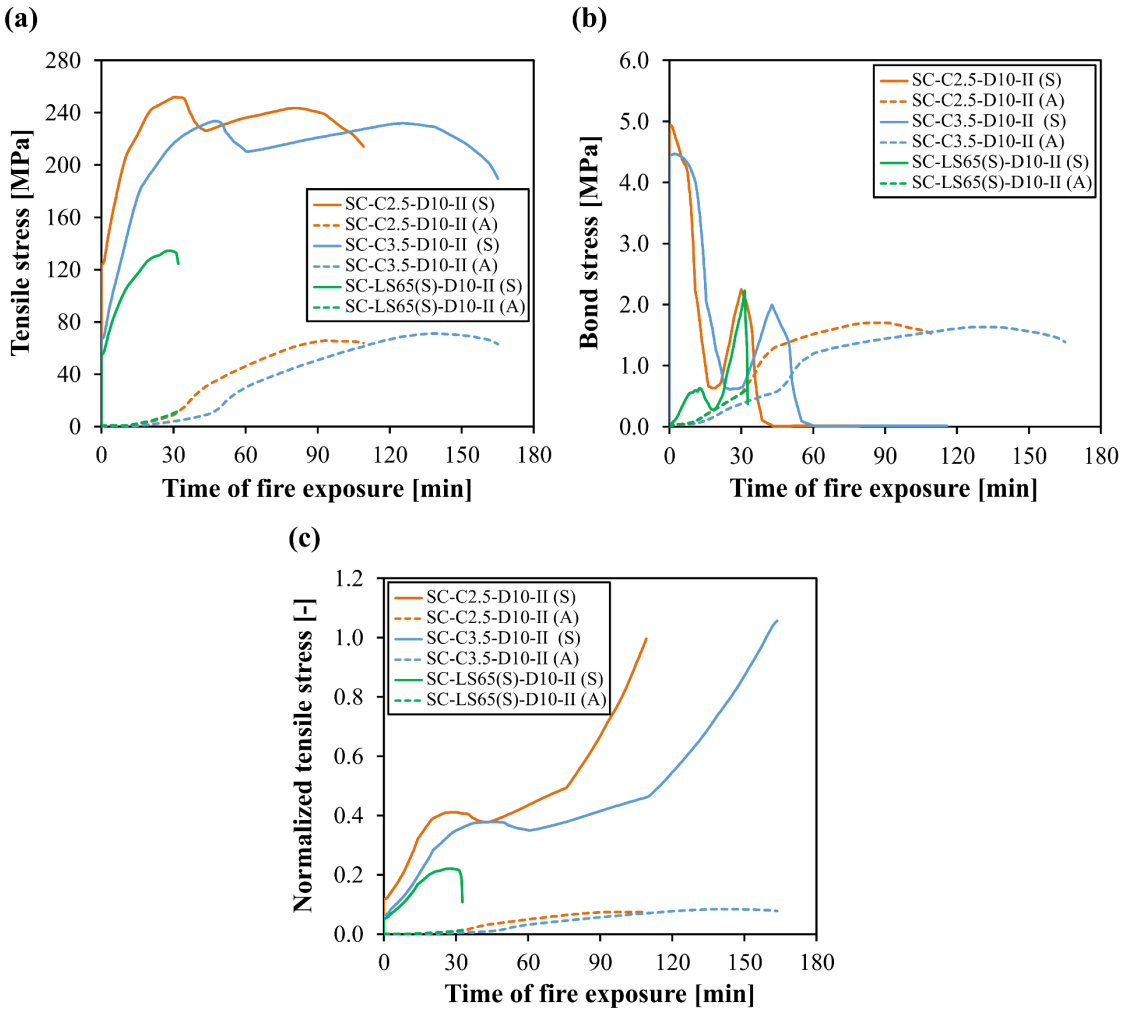

Figure 7.10. Evolution with time of fire exposure of: (a) tensile stress, (b) bond stress and (c) normalized tensile stress in bottom rebars of slabs SC-C2.5-D10-II, SC-C3.5-D10-II and SC-LS65(S)-D10-II (span (*S*) – continuous line; anchorage zone (*A*) – dashed line).

Figure 7.10a shows that, as expected, the initial average tensile stress in the rebars in the span of slab SC-LS65(S)-D10-II is much lower and about half of that in slab SC-C2.5-D10-II, as the former presents twice the number of effective bottom rebars than the latter (the overlap length was duly designed for ambient temperature conditions). It can also be observed that the tensile stress in the rebars of slab SC-C3.5-D10-II is lower than that on the rebars of slab SC-C2.5-D10-II: although the lever arm between the compressed concrete lamina and the tensioned rebars is lower in slab SC-C3.5-D10-II by circa 10% (which would increase the stress at the rebars for a given applied load), the applied load is 20% lower, thus counteracting (and exceeding) the previous effect.

In slabs SC-C2.5-D10-II and SC-LS65(S)-D10-II, during the first 30 min of fire exposure (45 min in slab SC-C3.5-D10-II), period corresponding to stage I in the midspan displacement *vs*. time curves (Figure 7.6), tensile stresses in the span and unexposed anchorage length increase due to thermal bowing (stemming from the high thermal gradient installed in the slabs' cross section) and also due to the stiffness reduction of concrete along the fire-exposed length of the slabs; due to the higher cover, slab SC-C3.5-D10-II exhibits a lower rate of stress increase. Furthermore, for slabs with continuous reinforcement, Figure 7.10b shows that the bond stresses in the span exhibit an overall reduction trend during this period, due to the degradation of the bond properties, leading to an increase in bond stresses in the anchorage zones. The increase of bond stress in the span for t ≈ 30 min in slabs SC-C2.5-D10-II and SC-LS65(S)-D10-II (45 min in slab SC-C3.5-II) shown in Figure 7.10b can be explained by the increase in bond stiffness of the local bond laws of the GFRP-concrete interaction (used as input) that occurs between 140 ºC and 200 ºC (*cf.* Figure 5.3 – page 140). In the particular case of slab SC-LS65(S)-D10-II, Figure 7.10b shows that the bond stresses in the span are null for $t = 0$ min – this result is related to the absence of initial cracks in-between loading sections – in this slab, the bond stresses (determined in-between two adjacent cracks that developed after the first instants of fire exposure) firstly increases with time as cracks develop and then decreases (as in the other slabs) as the bond properties in the span are degraded.

Figure 7.10a and Figure 7.10b show that between 30 min and 45 min in slab SC-C2.5-D10-II (between 45 min and 60 min in slab SC-C3.5-D10-II), *i.e.* during stage II (as identified in Figure 7.6a and Figure 7.6b), both tensile and bond stresses decrease in the span. Bond stresses decrease to zero because the bond properties become fully degraded. As for the tensile stresses, the results suggest that there is some internal redistribution of stresses, since the decrease of tensile stress in the span is accompanied by an increase of tensile stress (at a higher rate than previously) along the unexposed anchorage length. Figure 7.10c shows that during this stage, the normalized tensile stress of the rebars in the span is ~ 0.35-0.40 for both slabs with continuous reinforcement, explaining why they did not fail. With respect to slab SC-LS65(S)-D10-II, for $t > 30$ min, although the normalized tensile stress in the bottom rebars is very low (~ 0.20), the bond stress in the span presents a sharp decrease (*cf.* Figure 7.10b; note that the analysis

diverged before bond stresses reached zero) and the slab failed after 31 min, as its strength relied on the bond stress transfer capacity in the splices.

Between 45 min and 75 min (slab SC-C2.5-D10-II), and 60 min and 120 min (slab SC-C3.5-D10-II), the tensile stresses in the span and anchorage zones continue to increase, as shown in Figure 7.10a, likely due to thermal bowing; afterwards, for t > 75 min (slab SC-C2.5-D10-II) and t > 120 min (slab SC-C3.5-D10-II), these stresses begin to decrease until the slabs failed due to tensile rupture of the bottom rebars (further evidence of this failure mode is provided below). Figure 7.10c shows that for those time periods, in spite of the reduction of tensile stresses, the respective normalized tensile stresses increase. The numerical models reveal that the temperature for which the tensile stresses start to decrease is 460 ºC. For temperatures higher than 450 ºC (and up to 575 ºC), the estimated rate of GFRP tensile strength reduction with temperature was 3.1 MPa/ºC (Figure 7.2d); however, the estimated stress level reduction rate (Figure 7.10a) was 0.9 MPa/ºC; therefore, as the reduction of tensile strength exceeded that of the tensile stress installed in the rebars, the resulting normalized tensile stress presented a significant increase at the final stages of the fire exposure (Figure 7.10c). This rapid increase of normalized tensile stresses up to 1.0 (109 min in slab SC-C2.5-D10-II and 164 min in slab SC-C3.5-D10-II) provides further evidence that the failure of slabs with continuous reinforcement was due to tensile rupture of the bottom reinforcement.

Figure 7.11 illustrates the evolution of bond stresses on the bottom rebars of slab SC-C2.5-D10-II, along the length between the slab extremity and the loading section, for several instants of fire exposure and up to the failure instant (109 min), together with the rebars' temperature. The positions of the loading section, insulated length and initial cracks (formed due to load application, prior to fire exposure) are also marked. The analysis of this figure prompts the additional following remarks:

(i) For t = 0 min, bond stresses are nearly null at the insulated anchorage length and the rebars are anchored closer to the load application section. As time and temperature increase, the anchoring length migrates further away from the loading section moving towards the insulated length, as bond stresses decrease in the former zone and increase in the latter. After 45 min, bond is entirely lost along most of the exposed span (between 300 mm and 500 mm from the slab's end).

(ii) Even within the insulated anchorage length, there is some transfer of bond stresses: between 45 min and 109 min of fire exposure, the magnitude of the bond stresses decreases in sections subjected to higher temperature (closer to a length of 175 mm) and increases in sections at lower temperature (closer to the extremity). However, only for t > 45 min does the insulated anchorage length begin to display non-null bond stresses at the extremity.

(iii) The insulated anchorage zones were crucial to ensure long fire endurances in slabs with continuous reinforcement, significantly higher than the time span that corresponded to the

loss of GFRP-concrete bond interaction along the fire-exposed length; this resulted in tensile failure of rebars at temperatures considerably above the resin decomposition (in slab SC-C2.5-D10-II, the average temperature attained in the midspan section of the rebars – not shown in Figure 7.11 – was 540 ºC).

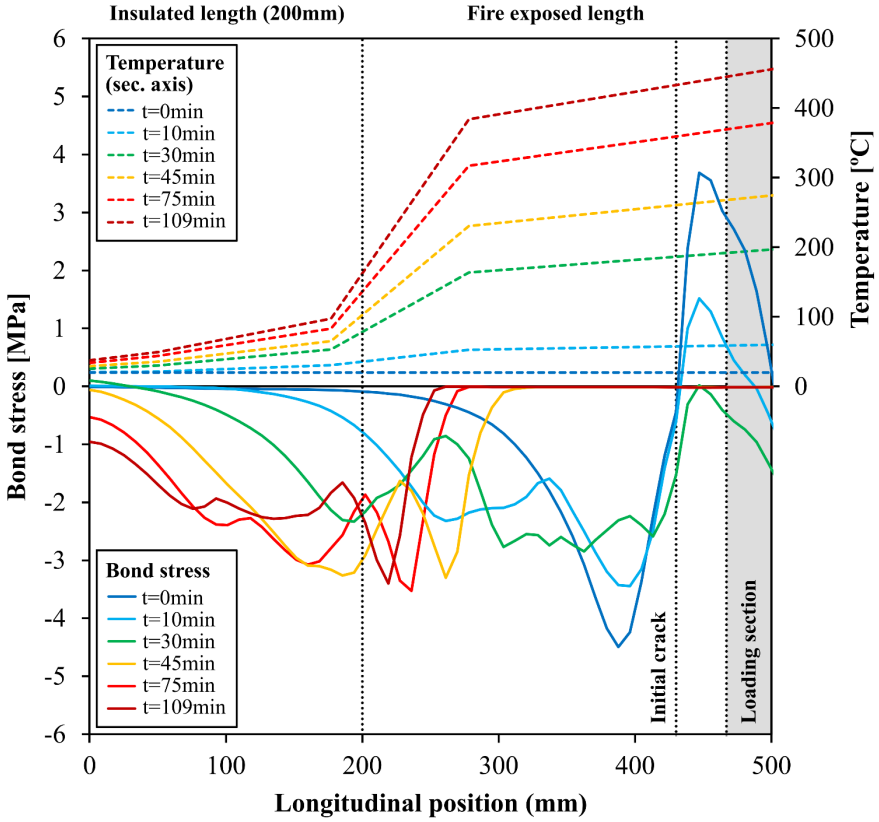

Figure 7.11. Variation of temperature (dashed line) and bond stress (continuous line) in the bottom GFRP rebars, for different fire exposure periods (up to failure), along the length of slab SC-C2.5-D10-II.

7.5. Concluding remarks

This chapter presented a numerical study about the thermomechanical behaviour of concrete slab strips reinforced with continuous or spliced GFRP rebars exposed to fire. The 3D solid FE models developed in this study were able simulate the thermal and thermomechanical responses of the slabs, providing fairly accurate predictions of temperature distributions, deflection behaviour, failure modes and fire resistance. Moreover, the numerical analysis provided an in-depth understanding of the evolution with time of fire exposure of the tensile and bond stresses of the main reinforcement along the slabs' length, particularly in the fire exposed span and insulated anchorage zones, showing the importance of guaranteeing proper cold anchorages for the rebars to extend the fire resistance of GFRP-RC members.

For the test conditions considered in the present study, the models allowed to verify that the protected anchorage length of the bottom reinforcement (175 mm in both ends of the slabs) was adequate to ensure fire resistances above 120 min in slabs with continuous reinforcement, enabling them to fail due to tensile rupture of the bottom reinforcement at temperatures considerably above the T_g and T_d of the GFRP material. The study also confirmed that the GFRP reinforcing bars were able to maintain their structural effectiveness, through an anchored cable mechanism, even after the GFRP-concrete bond was entirely lost along the heated span of the slabs; in fact, this cable behaviour was activated within the first 30-45 min of fire exposure (depending on the concrete cover), during which a large portion of the central length of the longitudinal reinforcing bars attained the T_g, and therefore experienced a severe loss of bond to concrete.

The explicit implementation in the models of the progressive degradation of bond with increasing temperatures allowed to predict the premature failure of the slab with spliced reinforcement (which would not be possible if the simplifying hypothesis of perfect bond had been considered instead). The results demonstrated that the design of splicing details comprising GFRP reinforcement must consider the severe degradation of bond that occurs along the heated span; this study showed that if unprotected from fire, the presence of lap splices directly exposed to heat can decrease the fire resistance by 70% compared to continuous reinforcement.

The thermal simulations confirmed that the increase in concrete cover thickness delays the temperature increase and therefore the degradation of the mechanical and bond properties of the GFRP bars. The numerical results showed that the increase in cover thickness from 2.5 cm to 3.5 cm has the potential to increase by 50% the fire resistance of slabs with continuous reinforcement (in the fire resistance tests, however, a lower increase of 30% was observed due to the occurrence of premature failure).

In the fire resistance tests, slabs with lower concrete strength presented lower fire resistances compared to those with higher concrete strength, as the former were more prone to extensive cracking and hence to a faster (local) temperature increase of the GFRP reinforcement in sections with wider cracks. In this study, since sequentially coupled thermomechanical analyses were performed (*i.e.*, the thermal analysis was uncoupled from mechanical analysis), the FE models were not able to simulate this localized phenomenon, and hence did not capture properly the influence of concrete strength on the fire resistance of the slabs; this effect, which seems to have played an important role in the experiments, should be object of future research.

Part V

Conclusions and future developments

Chapter 8

Conclusions and recommendations for future research

8.1. Conclusions

GFRP-reinforced concrete structures operating for several years in chemically aggressive environments have confirmed the good mechanical performance and durability of GFRP reinforcement. However, one of the main issues regarding the use of GFRP bars is that their mechanical properties and bond to concrete experience significant reductions at elevated temperatures. Although these issues are not usually relevant in the design of bridge decks and maritime structures (presently, the most frequent applications of FRP bars), they are of great concern in building applications, since the fire action has to be considered in design. Despite its relevance, the fire performance of GFRP materials and GFRP-RC structures is not comprehensively addressed in the literature, which explains why the fire design recommendations provided in existing FRP-RC codes are very limited and of (too) broad scope comparing to those available for steel-RC. The concerns and lack of knowledge about the fire behaviour of FRP-RC members are therefore hampering the development of further design guidelines and, consequently, the widespread use of FRP bars as internal reinforcement of concrete structures, namely those that need to be design for the accidental fire action.

The research developed in this thesis aimed at bridging relevant gaps in knowledge regarding the performance of GFRP-RC members under exposure to elevated temperatures/fire, particularly with respect to the following three domains:

- Thermophysical and mechanical behaviour of GFRP bars at elevated temperature;
- Bond behaviour of GFRP bars in concrete at elevated temperature;
- Fire behaviour of GFRP-reinforced concrete slabs.

The thesis comprised an extensive experimental campaign, complemented by analytical and numerical studies, which provided novel and relevant insights in all aforementioned domains. Besides delivering a wealth of new experimental data that was either scarce or unavailable in the literature, this study allowed the development of numerical tools that were able to simulate, with relatively good accuracy, the structural response of GFRP-RC flexural members under fire exposure. The conclusions obtained from this work allowed to confirm preliminary results obtained in recent studies –the use of GFRP bars

in buildings seems to be feasible, provided that some details about the GFRP reinforcement anchors and splices are ensured (*e.g.* [11,12]). Yet, the most meaningful and innovative contribution of this thesis is the fact that it provides results with practical relevance for the drafting of more detailed fire design recommendations about aspects that are presently not considered with due importance in existing codes. The main general conclusion drawn from the thesis is that GFRP-RC slabs can meet the building code requirements with significantly lower concrete covers than those presently recommended in the CAN/CSA-S806 guide [8], provided that (i) the rebars are well-anchored in cool zones of the structure and (ii) splicing is avoided in spans directly exposed to fire. Furthermore, it was also found that bent reinforcement can be adopted to effectively improve the anchorage strength in lap splices, as well as to decrease the length of "cold" anchorages. A more detailed description of the conclusions drawn in the thesis concerning the above-mentioned research domains is presented in the following sections.

8.1.1. Thermophysical and mechanical behaviour of GFRP bars at elevated temperature

The first domain of this thesis concerned the thermophysical and mechanical behaviour of GFRP bars at elevated temperatures. This work considered GFRP bars from different manufacturers, with the objective of being representative of the wide variety of bars that are now commercially available; indeed, even within the same manufacturer, the mechanical and thermophysical properties of the bars (namely, (the T_g and T_d) were found to vary considerably due to differences in manufacturing and curing procedures, as well as in the constituent materials.

The tensile tests presented in Chapter 3 provided a significant amount of data regarding the tensile strength and modulus degradation with temperature of four different GFRP bars. The results obtained at temperatures between 400 ºC and 715 ºC (*i.e.*, above decomposition) are mostly new in the literature and, therefore, when implemented in FE models (Chapter 7), allowed to significantly improve the accuracy of the simulations of the thermomechanical response of the GFRP-RC slab strips during fire exposure (described in Chapter 6). The experiments showed that the tensile strength is considerably more degraded with temperature than the tensile modulus, especially during the glass transition and after the decomposition of the polymeric resin. The tensile strength of the bars was reduced near the T_g between 6% and 35% with respect to ambient temperature, and about 50% up to 300 ºC; at the latter temperature the tensile modulus was only reduced between 3% and 23%. At 715 ºC, after full decomposition of the resin, the tensile strength decreased to 4% of the value at ambient temperature, while the remaining tensile modulus was still 66%.

Although the results obtained in this study fit within the (high) scatter of data available in the literature, the magnitude of such scatter clearly justifies the importance of characterizing the properties of different types of FRP bars at elevated temperatures in order to obtain accurate values of their reduction with

temperature that might be used for fire design purposes. The analytical models proposed to describe the variation of the tensile properties of GFRP bars with temperature can now be used in other studies where this information is unavailable; yet, it is important to mention that while these models were derived solely considering the exposure temperature, for fire design purposes, the bars' T_g, T_d and thermal exposure conditions also need to be incorporated as variables – to attain such goal, further data about these parameters is required (cf. Section 8.2.1).

8.1.2. Bond behaviour of GFRP bars at elevated temperature

The second research domain of the thesis comprised experimental, analytical and numerical studies about the bond behaviour of GFRP bars in concrete at moderately elevated temperatures.

The pull-out tests carried out in the first stage of the study (Chapter 4) delivered a large set of new data that complemented the limited database of results available to date in the literature. These data included the bond strength and stiffness degradation with temperature of the GFRP-concrete interface (up to 300 ºC) obtained in bars with different surface finishes (sand coated and different types of ribbed bars), embedment lengths in concrete, diameters and geometries (straight or 90º bent). Regardless of the type of GFRP bar, the following main conclusions were obtained: (i) the strength and stiffness of the GFRP-concrete interface are significantly reduced with the increase in temperature, especially when the bars' T_g is approached and exceeded, and (ii) the GFRP-concrete bond degradation with temperature is more severe than that experienced by the bars' tensile properties.

The experiments showed that the key parameters governing the bond of straight bars at elevated temperatures are their surface finish and T_g: ribbed bars (T_g of 104 ºC and 157 ºC) presented bond strength reductions of 34% at 100 ºC (with respect to ambient temperature), while in sand coated bars (T_g of 98 ºC) the reduction at the same temperature was significantly higher, around 80%. However, at 250 ºC, the bond strength of all bars was severely degraded (reductions of 80% to 90% were obtained) due to the advanced softening state of the resin. It was concluded that while most of the bond degradation of ribbed bars occurred for temperatures above their T_g, that of sand coated bars took place almost entirely below that reference temperature – this observation is consistent with the results available in the literature. Additionally, together, both sets of data were then successfully used to calibrate the parameters that define two empirical (relaxation) models to predict the GFRP-concrete bond strength reduction with temperature.

Contrarily to the surface finish and T_g, the influence of the embedment length, bar diameter and bar geometry (*i.e.* straight *vs.* bent) in the degradation rate of bond with temperature was not as meaningful, at least for the materials, procedure and temperatures considered in this study. However, the experiments revealed that the hook effect provided by the bent and tail lengths of 90º bent bars enabled bond strength increases of 30% to 90% compared to straight bars in the entire range of temperatures tested; these

results showed the potential beneficial effect of using bent reinforcement to improve the anchorage strength in RC members exposed to fire; in fact, this was then confirmed in the fire resistance tests performed in Chapter 6.

In the second stage of the study (Chapter 5, Section 5.2), local bond stress *vs*. slip laws for the GFRP-concrete interface were proposed for straight bars with different surface finishes and diameters and for temperatures up to 300 ºC; to that end, the defining parameters of these laws were calibrated through a numerical procedure and using the experimental data obtained from the pull-out tests. It is worth noting that up to the present date, local bond *vs.* slip laws such as those provided in this thesis (*i.e.*, describing both the peak- and post-peak bond stress *vs.* slip response at elevated temperature and considering the non-uniform distribution of stress along the bonded length) were not available in the literature. As mentioned ahead, the implementation of these temperature-dependent local bond *vs.* slip laws in numerical models of slab strips allowed to substantially improve the models' ability to simulate the bond behaviour of the GFRP bars during fire exposure, namely, to predict bond failures of overlapped rebars (Chapter 7).

In the third stage of the study about the bond behaviour (Section 5.3), the bond *vs.* slip laws (calibrated for straight bars) were successfully implemented in 3D solid FE models simulating the pull-out tests performed in: (i) sand coated and ribbed straight bars, at both ambient and elevated temperatures, and (ii) 90º bent ribbed bars at ambient temperature. Yet, in order to simulate the bond interaction along the bent length of the ribbed bars at elevated temperature, local bond *vs.* slip laws had to be calibrated specifically for the bent development, based on an inverse analysis; this procedure intended to implicitly consider the localized damage in the bars' ribs in the bent section and to simulate the differences in bond behaviour of the material along the bent and straight developments. These simulations highlighted the complexity in modelling the FRP-concrete interaction at elevated temperature, especially along bends of the reinforcement.

Lastly, design-oriented parametric studies were performed based on the calibrated FE models and, based on those models, optimal anchorage lengths for straight and bent GFRP bars were proposed as a function of temperature for beam and slab applications (Section 5.4). From these results, the following three main conclusions were drawn. First, the design of FRP anchorages should consider the combined influence of the bars' surface finish, its constituent materials and T_g, given that these are key parameters that affect the tensile properties and bond to concrete at elevated temperatures, and therefore the development length required to anchor the reinforcement in fire conditions (as confirmed in the fire resistance tests). Second, the adoption of 90º bent anchorages with appropriate tail lengths is an effective and practical approach to improve the bond strength of FRP bars at both ambient and elevated temperatures. Third, to mobilize the tensile strength of FRP bars at elevated temperatures, the development length of straight and bent bars designed for ambient temperature must be significantly increased to take into account the severe loss of bond occurring near the T_g. It is important to emphasize that these recommendations have

practical significance for the fire design of FRP-RC structures, especially for the detailing of end anchors and tension lap splice lengths.

8.1.3. Fire behaviour of GFRP-reinforced concrete slabs

The third research topic, the structural behaviour of GFRP-RC slabs exposed to fire, was firstly addressed by means of fire resistance tests on slab strips reinforced with different GFRP rebars and comprising different detailing configurations (Chapter 6). The tests allowed determining the slabs' thermal and thermomechanical responses during fire exposure, providing a wealth of data that were directly correlated with the knowledge acquired from the studies about the tensile and bond behaviour of the rebars at elevated temperatures. This comprehensive/combined analysis of results allowed to significantly improve the current understanding about the fire performance of GFRP-RC flexural members, as well as to deliver new insights and design recommendations with respect to relevant aspects not yet covered in sufficient detail (or not considered at all) in existing FRP-RC codes. These aspects included the anchoring conditions of the reinforcement in cool zones of the structure, the detailing of tension lap splices, and the influence of the material and surface finish of the rebars on the members' fire resistance.

As mentioned, one of most important conclusions obtained from the study was that RC slabs incorporating GFRP rebars can meet building code requirements regarding the fire resistance times (typically within 60-180 minutes), even endure over 180 min of fire exposure with considerably thinner concrete covers than those currently prescribed in the Canadian guide [8], provided that (i) continuous rebars are adopted between the supports, and (ii) the rebars are well-anchored in cool zones of the structure, where their temperature does not increase above the T_g. The experiments showed that when the aforementioned conditions were met, the GFRP rebars were able to maintain their structural effectiveness, through an anchored cable mechanism, even after the GFRP-concrete bond was entirely lost along the heated span of the slabs. The fire endurance was governed by the tensile rupture of the GFRP rebars along their central (heated) length. The GFRP-RC slabs with continuous reinforcement endured between 90 min and 220 min of standard fire exposure and the time to failure was shown to be dependent on the type of rebar and cover thickness adopted, resulting in different degradation rates of the tensile and bond properties of the reinforcement with temperature; the fire endurance also showed some dependency of the concrete strength and the bar diameter, as addressed ahead.

As shown in previous numerical studies ([166,221]), increasing the concrete cover thickness allowed reducing the degradation rate of the rebars' mechanical properties and bond to concrete, and thereby enhance the slabs' fire resistance – in this study, the increase in cover from 25 mm to 35 mm improved the slabs' fire endurance (*i.e.*, the time to failure) by approximately 10 min (in slabs with sand coated bars) and 60 min (in slabs with ribbed bars). On the other hand, as reported in [11,12], it was confirmed

that it is possible to revise the current design recommendations provided in the Canadian guide [8] (the only one that specifies cover values with respect to fire) to allow the adoption of thinner cover thicknesses (provided that the above-mentioned details regarding the end anchors are respected) and, in that way, contribute to more sustainable and economic applications of the FRP material. According to [8], for the slab geometry and materials considered in this study, the bars' critical temperature is between 200 ºC and 300 ºC (corresponding to a 50% retention of their tensile strength at ambient temperature) and, based on that value, the code stipulates a minimum cover of 60 mm for a 60 min fire resistance rating. However, the slabs tested in present thesis with "cold" FRP anchorages were able to endure much more than 60 min under fire exposure (as mentioned, up to 220 min) with covers of 25-35 mm, for which the maximum temperatures reached in the rebars were between 570 ºC and 713 ºC.

The experiments showed that the fire resistance of FRP-RC members may be reduced (i) when adopting smaller diameter rebars, and (ii) due to the occurrence of localized heating phenomena of the rebars in widely cracked zones, predominantly observed in slabs with lower concrete strength, which are more prone to extensive cracking (as also reported in [91]). However, due to the lack of studies to corroborate/refute these results, more thorough investigations are required in order to draw specific recommendations on this matter.

The performance of GFRP lap splices in a scenario where they are directly exposed to fire was comprehensively investigated in this thesis. It was shown that even if the development lengths recommended in current design guidelines are used (for design at ambient temperature), the presence of lap splices can remarkably reduce the fire resistance of GFRP-RC slabs to less than 20 min if these are located in spans directly exposed to fire – this was the case of slabs with straight-end splices, which failed prematurely due the rebars' debonding when the ends of the overlapped rebars approached T_g. It was concluded that extending the overlap length (for example, from 65 cm to 84.5 cm) provided minor increases in fire resistance (below 7 min) when straight bars were used, because the T_g was quickly attained along most of the heated span in the early stages of the fire. The bond behaviour of straight-end splices with different GFRP rebars (*i.e.*, different constituent materials and surface finishes) was compared and, as expected (according to the bond tests results), the spliced rebars with lower T_g failed sooner (and for lower temperatures) than those with higher T_g.

One of main innovations of the research developed in this thesis was the assessment of the use of bent rebars in the extremities of overlapping bars to improve their bond to concrete at elevated temperature. In this regard, it was demonstrated that the fire endurance of the slabs significantly improved from 26 min (using straight-end splices) up to 75 min with the adoption of 90º bent-end splices, as the latter allowed anchoring the reinforcement in a cooler zone of the member where bond is degraded at a slower rate and, therefore, remains less damaged during the fire exposure. In this respect, it is worth mentioning that the potential beneficial effect of using bent reinforcement to enhance the anchorage strength in the splices is expected to be even more beneficial in beam applications, where the increased height of the

member allows the adoption of longer tail lengths. These findings, together with those obtained about the bond behaviour at elevated temperature (namely, from the parametric studies conducted in Section 5.4), indicate that the use of bent reinforcement can be an effective fire design option to decrease the length of "cold" anchorages in FRP-RC members, as shown earlier in [14,18].

With respect to the numerical study, using the 3D solid FE models of the slabs (Chapter 7), were able reasonably accurate predictions of the thermal and thermomechanical responses under fire exposure of the GFRP-RC slab strips were obtained, including the simulation of: (i) the temperature distribution at different positions and constituent materials of the slabs; (ii) the evolution of the midspan deflection with the time of fire exposure; (iii) the GFRP tensile failure in slabs with continuous reinforcement; (iv) the bond failure of overlapping rebars in slabs with straight-end splices; and (v) the increase in fire resistance with the increase in concrete cover. This was only made possible due to the implementation in the models of the temperature-dependent thermophysical and mechanical properties of the concrete and GFRP rebars, and of the explicit modelling of the GFRP-concrete interaction by means of local bond stress *vs*. slip laws, calibrated for these specific rebars at different temperatures. The numerical simulations enabled tracing the evolution of both bond and tensile stresses during fire exposure along the "cold" anchorage zones and central heated span, thereby providing further insights about the cable behaviour of the GFRP reinforcement observed in the experiments.

The research carried out in this thesis highlighted the remarkable influence of the location and detailing of lap splices and anchorage zones on the fire resistance of FRP-RC members. In this regard, the following main general recommendations, deriving from this study, are noted. On the one hand, critical temperatures should be defined for different locations of the FRP reinforcement and based on both the tensile and bond strengths of FRP rebars at elevated temperatures; for continuous rebars located in zones likely to be subjected to fire, appropriate concrete covers should be defined with the purpose of preventing the tensile rupture of the reinforcement by maintaining its temperature below a certain temperature (defined based on the stress level installed on the rebars, together with the data determined in this thesis about its tensile strength as a function of temperature). On the other hand, FRP-concrete bond failures in the anchorage zones and lap splices of rebars should also be prevented by limiting the temperatures to a critical value defined by its T_g – to this end, these key points of the reinforcement should be protected from direct heat exposure, preferably locating them in cooler areas of the structure, such as in connection zones with beams, over partition walls and columns; nevertheless, their length and geometry (straight or, whenever possible, bent) should be designed in order to consider optimal development and tail lengths defined as a function of temperature (as those proposed in Section 5.4), which should take into the account the type of surface finish and T_g of the bars.

As final remarks, two aspects are worth noting. The first is that this thesis provided a wealth of important new data as well as improved numerical tools, which can now be used to deepen the knowledge about the behaviour of FRP-RC structural members under elevated temperature and fire conditions. The

second remark is that this newly acquired knowledge about the fire performance of FRP reinforcement, which is considered to be very relevant within the existing literature, may hopefully encourage the revision/improvement of the fire design provision for FRP-RC structural members, thus contributing to a widespread use of FRP materials in civil engineering applications.

8.2. Recommendations for future research

The experimental, analytical and numerical investigations performed in this thesis provided a comprehensive and better understanding of the fire performance of concrete structures reinforced with GFRP bars. The work delivered a wealth of experimental data, provided analytical and numerical tools to model the GFRP-concrete bond interaction at elevated temperatures, and also new insights on the fire behaviour of members with detailing configurations that had not yet been thoroughly addressed in the literature (nor considered in detail in existing FRP-RC design guidelines). However, the results obtained here (together with those from previous studies) are still unable to cover, in an exhaustive manner, the entire range of FRP bars currently available, neither the variety of parameters that are expected to affect the behaviour of FRP-RC members in a fire scenario, which justifies the need for further research. In this regard, the present section presents recommendations for future investigations in the domain of RC structures comprising FRP reinforcement subjected to elevated temperature and fire.

8.2.1. Thermophysical and mechanical behaviour of FRP bars at elevated temperature

The knowledge about the thermophysical and mechanical properties of FRP bars at elevated temperature needs to be further extended to address the following aspects:

- Experimental characterization of the temperature-dependent thermal and mechanical properties of FRP bars at elevated temperature which, despite being needed to accurately predict the fire response of FRP-RC members in fire conditions, are currently very scarce in the literature, namely the thermal conductivity, specific heat, density, and the longitudinal and transverse thermal expansion coefficients.
- Experimental characterization of the mechanical properties in both longitudinal and transverse directions of various types of FRP bars (*i.e.* resin, fibres and geometry), considering different testing procedures (steady-state and transient state conditions) and encompassing a broad temperature range that includes temperatures above T_d. These properties include: (i) the longitudinal tensile modulus (the information available in the literature for temperatures above 400 ºC remains very limited), (ii) the transverse tensile modulus, and (iii) the longitudinal and transverse shear moduli of FRP bars; it is worth noting that the properties in the transverse

direction are of particular relevance in bent FRP bars, and therefore should be property accounted for in thermomechanical analyses of FRP-RC members exposed to fire comprising this type of bar geometry.

- Evaluation of the effects of (i) duration of exposure to heat, (ii) post-curing process (due to exposure to moderate heat), and (iii) exposure environment (oxidative or inert) in the mechanical properties of FRP bars at elevated temperatures.
- Further investigation of the residual mechanical properties of FRP bars after exposure to fire (*e.g.* in the context of building applications) and during prolonged exposure to elevated service temperatures (*e.g.* in bridge decks operating in warm climates).
- Experimental characterization of the mechanical behaviour at elevated temperature and residual properties of bent FRP reinforcement, for which presently no information is available.
- Development of predictive models to describe the variation of the mechanical properties of FRP bars with temperature, in which the exposure temperature, as well as their thermophysical properties (T_g and T_d), the duration of heating and exposure environment are explicitly considered.

8.2.2. Bond behaviour of FRP bars at elevated temperature

In the context of the bond behaviour of FRP reinforcement at elevated temperature, the following subjects are worth being object of further research:

- To further investigate the bond behaviour of bent FRP reinforcement at elevated temperature, including the influence of different bar configurations (radius and angle of the bend, development and tail lengths), different types of bars (fibres, resins, surface finishes and diameters) and different confinement conditions (concrete strength and cover) – in addition to pull-out tests (easier to execute), the experiments should also comprise beam tests to allow simulating more realistic confinement, loading and heating conditions.
- To develop analytical formulae describing the variation of bond strength with temperature, considering as variables the relevant parameters, such as the surface finish and the T_g of the bars, as well as the concrete strength.
- To investigate the anchorage strength of straight (as in [122]) and bent FRP reinforcement under gradient temperature distributions, in order to simulate, in a more realistic manner, the bond behaviour in overlapping bars and cold anchorage zones of RC flexural members.
- To assess the variation with temperature of the FRP-concrete interface properties in the normal direction, which are needed to accurately model the bond behaviour of bent bars.

- To improve the limited knowledge available about the residual bond properties of FRP bars after exposure to fire and during prolonged exposure to moderately elevated temperatures.
- To calibrate temperature-dependent analytical bond *vs.* slip laws for different types of FRP bars available in the industry.
- To develop advanced numerical models (*e.g.* micro-modelling) capable of simulating the complex interaction between bent FRP bars and concrete at elevated temperature.

8.2.3. Fire behaviour of RC members comprising FRP reinforcement

In the domain of the fire performance of RC members incorporating FRP internal reinforcement, the following topics can be further investigated:

- To perform additional fire resistance tests on full-scale FRP-RC beams and slabs with different detailing configurations and covers where the axial restraint provided by adjacent structural elements is simulated; such experiments would also allow validating the adequacy of the fire design recommendations proposed in this study.
- To investigate in further depth, through both experimental and numerical studies, the influence of the following features in the fire endurance of FRP-RC structural members: (i) geometry of FRP hooks in insulated anchorage zones and lap splices, with respectively different bending angles (*e.g.* 90º, 180º) and tail lengths, (ii) location of splicing zones, (iii) bar diameter, (iv) axial restraint, (v) type of loading, and (vi) concrete strength.
- To investigate the efficacy of using bent FRP reinforcement in beams and thicker slabs than those tested in this study, since the potential improvement in fire endurance is expected to be even more significant than that obtained in the relatively thin slabs tested in the present study (due to the possibility of anchoring the rebars farthest from the fire exposed surface of the member).
- To develop 3D FE models capable of simulating the thermomechanical behaviour of slabs with bent FRP reinforcement exposed to fire, also assessing whether the numerical approach considered in Chapter 5 to model the GFRP-concrete interaction of bent rebars at elevated temperatures is suited to model the bond behaviour in lap splices and end anchors.
- To perform numerical simulations of the thermomechanical behaviour of FRP-RC structural members under realistic fire curves, including the modelling of connections zones with other structural elements (beam-slab and beam-column joints).
- To develop advanced 3D FE models to conduct fully coupled thermomechanical analyses, aiming to investigate in further depth the influence of the concrete strength on the fire performance of

FRP-RC members, specifically concerning the localized heating effects at cracked sections (which could not be assessed using sequentially coupled thermomechanical analyses, as shown in Chapter 7).

- To develop parametric studies to investigate the fire behaviour of FRP-RC members with arbitrary geometry, detailing and concrete cover, aiming to propose more detailed recommendations with respect to the design of: (i) thermally insulated anchorage zones of the rebars; (ii) length, geometry and positioning of lap splices; (iii) definition of critical temperatures for GFRP reinforcement, and (iv) minimum concrete cover thickness required for a given fire resistance rate.
- To investigate the fire performance of concrete members reinforced with basalt FRP rebars, for which very few research has been conducted so far (*cf.* [150,222,223]).
- To investigate the fire behaviour of RC members comprising heat-resistant FRP rebars, such as those incorporating phenolic resins (less flammable and with T_g typically between 220 ºC and 250 ºC [1]) which are expected to present improved performance at elevated temperature and under fire exposure [7].
- To comprehensively assess the residual (post-fire) behaviour of FRP-RC structural members ([112,113,150,151,222,223]), together with the data of the residual tensile and bond properties of FRP rebars, to investigate their remaining strength and assess the feasibility of repair after fire exposure.

Bibliography

[1] Bank L.C., "Composites for Construction - Structural Design with FRP Materials", Wiley, Hoboken, New Jersey, USA, 2006.

[2] Manalo A., Benmokrane B. and Park K., "Recent developments on FRP bars as internal reinforcement in concrete structures", *Concrete in Australia*, 40 (2), 46–56.

[3] Bakis C.E., Bank L.C., Brown V.L., Cosenza E., Davalos J.F., Lesko J.J., Machida A., Rizkalla S.H., Triantafillou T.C., "Fiber-reinforced polymer composites for construction — state-of-the-art review", *Journal of Composites for Construction*, 6 (2), 73–87, 2002.

[4] Zoghi M., "The international handbook of FRP composites in Civil Engineering", CRC Press, 2014.

[5] Hollaway L.C. and Teng J.G., "Strengthening and rehabilitation of civil infraestructures using fibre-reinforced polymer (FRP) composites", Woodhead Publishing Limited, 2018.

[6] ACI (American Concrete Institute), "Guide for the Design and Construction of Structural Concrete Reinforced with FRP Bars", ACI 440.1R-15, Farmington Hills, Michigan, USA, 2015.

[7] CNR (National Research Council), "Guide for the Design and Construction of Concrete Structures Reinforced with Fiber-Reinforced Polymer Bars", CNR-DT 203/2006, Rome, Italy, 2007.

[8] CSA (Canadian Standards Association), "Design and Construction of Building Structures with Fibre-Reinforced Polymers", CAN/CSA-S806-12, *Canadian Standards Association*, Rexdale, Ontario, Canada, 2017.

[9] FIB (International Federation for Structural Concrete), "Fib Model Code for Concrete Structures 2010", *International Federation for Structural Concrete*, Lausanne, Switzerland, 2013.

[10] FIB (International Federation for Structural Concrete), "Bulletin 40 - FRP Reinforcement for RC Structures", *International Federation for Structural Concrete*, Lausanne, Switzerland, 2007.

[11] Hajiloo H., Green M.F. and Noël M., "GFRP-Reinforced Concrete Slabs : Fire Resistance and Design Efficiency", *Journal of Composites for Construction*, 23 (2), 04019009, 2019.

[12] Hajiloo H., Green M.F., Noël M., Bénichou N. and Sultan M., "Fire tests on full-scale FRP reinforced concrete slabs", *Composite Structures*, 179, 705–719, 2017.

[13] Abbasi A. and Hogg P.J., "Fire testing of concrete beams with fibre reinforced plastic rebar",

Composites Part A: Applied Science and Manufacturing, 37 (8), 1142–1150, 2006.

[14] Nigro E., Bilotta A., Cefarelli G., Manfredi G. and Cosenza E., "Performance under fire situations of concrete members reinforced with FRP rods: bond models and design nomograms", *Journal of Composites for Construction*, 16 (4), 395–406, 2012.

[15] Weber A., "Fire-resistance tests on composite rebars", *4th International Conference of FRP Composites in Civil Engineering (CICE 2008)*, Zurich, Switzerland, 2008.

[16] Carvelli V., Pisani M.A. and Poggi C., "High temperature effects on concrete members reinforced with GFRP rebars", *Composites Part B: Engineering*, 54 (1), 125–132, 2013.

[17] Kiari M., Stratford T. and Bisby L.A., "New design of beam FRP reinforcement for fire performance", *5th International Workshop on Performance, Protection & Strengthening of Structures under Extreme Loading*, East Landing, MI, USA, 764–771, 2015.

[18] Kiari M., Stratford T.J. and Bisby L.A., "New approach to fire safe application of fibre-reinforced polymer reinforcement for concrete", *7th International Conference on Advanced Composite Materials in Bridges and Structures*, Vancouver, British Columbia, Canada, 2016.

[19] McIntyre E., "Fire performance of fibre reinforced polymer (FRP) bars in reinforced concrete: an experimental approach," *PhD thesis in Civil Engineering*, University of Edinburgh, United Kingdom, 2019.

[20] Nour O., Salem O. and Mostafa A., "Experimental fire testing of large-scale glass fibre-reinforced polymer-reinforced concrete beams with mid-span straight-end bar lap splices", *Fire and Materials*, 1–16, 2021.

[21] Gurung S. and Salem S., "Effects of load level on the structural fire behaviour of GFRP-reinforced concrete beams with straight-end bar lap splices", *8th International Conference on Advanced Composite Materials in Bridges and Structures*, Sherbrooke, Quebec, Canada, 2021.

[22] Gibson A.G., Wu Y.-S., Evans J.T. and Mouritz A.P., "Laminate theory analysis of composites under load in fire", *Journal of Composite Materials*, 40 (7), 639–658, 2006.

[23] Correia J.R., Gomes M.M., Pires J.M. and Branco F.A., "Mechanical behaviour of pultruded glass fibre reinforced polymer composites at elevated temperature: Experiments and model assessment", *Composite Structures*, 98, 303–313, 2013.

[24] ISO (International Organization for Standardization), "Fire Resistance Tests - Elements of Building Construction - Part 1: General Requirements", ISO 834-1, *International Organization for Standardization*, Geneve, Switzerland, 1999.

[25] Azevedo A.S., "Fire Behaviour of Reinforced Concrete Structures Strengthened with Advanced Carbon Fibre Reinforced Polymer (CFRP) Systems", *PhD thesis in Civil Engineering*, Instituto

Superior Técnico, University of Lisbon, Lisbon, Portugal (to be completed in 2022).

[26] Santos P., "Resistência ao fogo de lajes de betão armadas com varões em compósito de GFRP", *MSc dissertation in Civil Engineering*, Instituto Superior Técnico, University of Lisbon, Lisbon, Portugal, 2016.

[27] Granadeiro L., "Estudo experimental sobre o efeito da temperatura na aderência entre betão e varões em compósito de GFRP", *MSc dissertation in Civil Engineering*, Instituto Superior Técnico, University of Lisbon, Lisbon, Portugal, 2017.

[28] Mazzuca P., "Bond Behaviour between GFRP Rebars and Concrete at Elevated Temperature - Experimental and Analytical Investigation", *MSc dissertation in Civil Engineering,* Università della Calabria, Calabria, Italy, 2018.

[29] Carvalho R., "Varões em compósito de GFRP para estruturas de betão armado – Estudo da aderência betão-GFRP a temperatura elevada", *MSc dissertation in Civil Engineering*, Instituto Superior Técnico, University of Lisbon, Lisbon, Portugal, 2018.

[30] Bilotta A., Compagnone A., Esposito L. and Nigro E., "Structural behaviour of FRP reinforced concrete slabs in fire", *Engineering Structures*, 221, 111058, 2020.

[31] Rosa I.C., Granadeiro L., Firmo J.P., Correia J.R. and Azevedo A.S., "Effect of elevated temperatures on the bond behaviour of GFRP bars in concrete – pull-out tests", *3rd International Conference on Protection of Historical Constructions (PROHITECH'17)*, Lisbon, Portugal, 2017.

[32] Santos P., Rosa I.C., Firmo J.P., Correia J.R. and Azevedo A.S., "Behaviour under fire exposure of GFRP-reinforced concrete slabs", *3rd International Conference on Protection of Historical Constructions (PROHITECH'17)*, Lisbon, Portugal, 2017.

[33] Rosa I.C., Granadeiro L., Firmo J.P., Correia J.R. and Azevedo A.S., "Bond behaviour between GFRP bars and concrete at elevated temperature", *20th International Conference on Composite Structures (ICCS 20)*, Paris, France, 2017.

[34] Rosa I.C., Firmo J.P., Granadeiro L. and Correia J.R., "Effect of high temperatures on the bond performance of GFRP bars to concrete", *9th International Conference on Fibre-Reinforced Polymer (FRP) Composites in Civil Engineering (CICE 2018)*, Paris, France, 2018.

[35] Rosa I.C., Firmo J.P., Santos P., Arruda M.R.T. and Correia J.R., "Fire behaviour of GFRP-reinforced concrete slab strips: fire resistance tests and numerical modelling", *9th International Conference on Fibre-Reinforced Polymer (FRP) Composites in Civil Engineering (CICE 2018)*, Paris, France, 2018.

[36] Rosa I.C., Firmo J.P., Correia J.R. and Mazzuca P., "Influence of elevated temperatures on the

bond behaviour of ribbed GFRP bars in concrete", *IABSE Symposium 2019 Guimarães - Towards a Resilient Built Environment - Risk and Asset Management*, Guimarães, Portugal, 2019.

[37] Rosa I.C., Arruda M.R.T., Firmo J.P. and Correia J.R., "Influence of anchorage geometry on the bond behaviour of GFRP bars at elevated temperature: pull-out tests and numerical simulations", *Fib Symposium 2021*, Lisbon, Portugal, 2021.

[38] Rosa I.C., Firmo J.P., Correia J.R. and Mazzuca P., "Influence of elevated temperatures on the bond behaviour of sand-coated and ribbed GFRP rebars in concrete - pull-out tests and calibration of temperature-dependent bond stress vs. slip laws", *10th International Conference on FRP Composites in Civil Engineering (CICE 2020/2021), Lecture Notes in Civil Engineering*, 198, Springer, Cham., 774-787, 2022.

[39] Duarte A.P.C., Rosa I.C., Arruda M.R.T., Firmo J.P. and Correia J.R., "Fire behaviour of GFRP-reinforced concrete slab strips: fire resistance tests and numerical simulation", *10th International Conference on FRP Composites in Civil Engineering (CICE 2020/2021), Lecture Notes in Civil Engineering*, 198, Springer, Cham., 788-800, 2022.

[40] Rosa I.C., Duarte A.P.C., Arruda M.R.T., Firmo J.P. and Correia J.R., "Fire behaviour of concrete structures reinforced with GFRP bars: Experimental tests, numerical simulations and design", *25th International Conference on Composite Structures (ICCS 25)*, Porto, Portugal, 2022.

[41] Rosa I.C., Firmo J.P., Correia J.R. and Barros J.A., "Efeito da temperatura elevada na aderência entre betão e varões de GFRP com acabamento superficial em areia – Ensaios de arrancamento e determinação de leis tensão de aderência-deslizamento", *Encontro Nacional Betão Estrutural (BE 2018)*, Lisbon, Portugal, 2018.

[42] Rosa I.C., Firmo J.P. and Correia J.R., "Influência da temperatura elevada na aderência entre betão e varões em compósito de GFRP nervurados – ensaios de arrancamento", *Encontro Nacional Betão Estrutural (BE 2018)*, Lisbon, Portugal, 2018.

[43] Rosa I.C., Santos P., Firmo J.P. and Correia J.R., "Comportamento ao fogo de lajes de betão armadas com varões de GFRP: estudo experimental", *Encontro Nacional Betão Estrutural (BE 2018)*, Lisbon, Portugal, 2018.

[44] Rosa I.C., Firmo J.P. and Correia J.R., "Ensaios de resistência ao fogo em faixas de laje armadas com varões GFRP com acabamento em areia", *Encontro Nacional Reabilitar & Betão Estrutural (BE 2020)*, Lisbon, Portugal, 2021.

[45] Duarte A.P.C., Rosa I.C., Arruda M.R.T., Firmo J.P. and Correia J.R., "Modelação numérica do comportamento ao fogo de lajes de betão armado com varões de GFRP com acabamento em

areia", *Encontro Nacional Reabilitar & Betão Estrutural (BE 2020)*, Lisbon, Portugal, 2021.

[46] Rosa I.C., Arruda M.R.T., Firmo J.P. and Correia J.R., "Aderência de varões de GFRP retos e dobrados ao betão a temperatura elevada: ensaios de arrancamento e modelação numérica", *Jornadas Portuguesas de Engenharia de Estruturas (JPEE 2022)*, Lisbon, Portugal, 2022.

[47] Rosa I.C., Firmo J.P. and Correia J.R., "Comportamento ao fogo de lajes de betão armadas com varões de GFRP: efeito da geometria de ancoragem nas zonas de emenda", *Jornadas Portuguesas de Engenharia de Estruturas (JPEE 2022)*, Lisbon, Portugal, 2022.

[48] Correia J.R., "Fibre-Reinforced Polymer (FRP) Composites", Materials for Construction and Civil Engineering, Fernanda Margarido, Maria Clara Gonçalves (eds), Springer, Cham, 2015.

[49] Schöck, "Schöck ComBAR - Technical information," Technical datasheet, 2013.

[50] Benmokrane B., El-Salakawy E., Cherrak Z. and Wiseman A., "Fibre reinforced polymer composite bars for the structural concrete slabs of a Public Works and Government Services Canada parking garage", *Canadian Journal of Civil Engineering*, 31 (5), 732–748, 2004.

[51] Ahmed E.A., Benmokrane B. and Sansfaçon M., "Case Study: Design, Construction, and Performance of the La Chancelière Parking Garage's Concrete Flat Slabs Reinforced with GFRP Bars", *Journal of Composites for Construction*, 21 (1), 05016001, 2017.

[52] Schöck, Case studies - District Leimbach, https://www.schoeck.com/en/case-studies/district-leimbach.

[53] Bisby L. and Stratford T., "Design for fire of FRP strengthened or reinforced concrete elements: state-of-the-art and opportunities from performance based approaches", *Canadian Journal of Civil Engineering*, 40 (11), 1–39, 2013.

[54] Bisby L.A., Williams B.K., Kodur V.K.R., Green M. and Chowdhury E., "Fire performance of FRP systems for infrastructure: a state-of-the-art report", 2005.

[55] Bisby L.A., Green M.F. and Kodur V.K.R., "Response to fire of concrete structures that incorporate FRP", *Progress in Structural Engineering and Materials*, 7 (3), 136–149, 2005.

[56] Maraveas C., Miamis K. and Vrakas A.A., "Fiber-reinforced polymer-strengthened/reinforced concrete structures exposed to fire: a review", *Structural Engineering International*, 22 (4), 500–513, 2012.

[57] Mouritz A.P. and Gibson A.G., "Fire properties of polymer composite materials", Solid mechanics and its applications, Springer, Dordrecht, 2006.

[58] McIntyre E., Bisby L. and Stratford T., "Bond strength of FRP reinforcement in concrete at elevated temperature", *7th International Conference on FRP Composites in Civil Engineering (CICE 2014)*, Vancouver, Canada, 2014.

[59] Griffis C.A., Masumura R.A. and Chang C.I., “Thermal response of graphite epoxy composite subjected to rapid heating”, *Journal of Composite Materials*, 15 (5), 427–442, 1981.

[60] Fanucci J.P., “Thermal Response of Radiantly Heated Kevlar and Graphite/Epoxy Composites”, *Journal of Composite Materials*, 21 (2), 129–139, 1987.

[61] Bai Y. and Keller T., “Time dependence of material properties of FRP composites in fire”, *Journal of Composite Materials*, 43 (21), 2469–2484, 2009.

[62] Henderson J.B., Wiebelt J.A. and Tant M.R., “A Model for the Thermal Response of Polymer Composite Materials with Experimental Verification”, *Journal of Composite Materials*, 19 (6), 579–595, 1985.

[63] Robert M. and Benmokrane B., “Behaviour of GFRP reinforcing bars subjected to extreme temperatures”, *Journal of Composites for Construction*, 14 (4), 353–360, 2010.

[64] Sumida A. and Mutsuyoshi H., “Mechanical properties of newly developed heat-resistant FRP bars”, *Journal of Advanced Concrete Technology*, 6 (1), 157–170, 2008.

[65] Rosa I.C., Firmo J.P. and Correia J.R., “Experimental study of the tensile behaviour of GFRP reinforcing bars at elevated temperatures”, *Construction and Building Materials*, 324, 126676, 2022.

[66] Del Prete I., Bilotta A., Bisby L. and Nigro E., “Elevated temperature response of RC beams strengthened with NSM FRP bars bonded with cementitious grout”, *Composite Structures*, 258, 113182, 2021.

[67] Spagnuolo S., Meda A., Rinaldi Z. and Nanni A., “Residual behaviour of glass FRP bars subjected to high temperatures”, *Composite Structures*, 203, 886–893, 2018.

[68] Maluk C., Bisby L., Terrasi G. and Green M., “Bond strength degradation for CFRP and steel bars in concrete at elevated temperature”, *American Concrete Institute Special Publication on Advances in Fire Design of Concrete Structures (ACI SP-297)*, 2.1-2.36, 2011.

[69] Dimitrienko Y.I., “Thermomechanical behaviour of composite materials and structures under high temperatures: 1. Materials”, *Composites Part A: Applied Science and Manufacturing*, 28 (5), 453–461, 1997.

[70] Kodur V.K.R., Bisby L.A. and Foo S.H.-C., “Thermal behavior of fire-exposed concrete slabs reinforced with fiber-reinforced polymer bars”, *ACI Structural Journal*, 102 (6), 799–807, 2005.

[71] Nigro E., Cefarelli G., Bilotta A., Manfredi G. and Cosenza E., “Fire resistance of concrete slabs reinforced with FRP bars. Part II: Experimental results and numerical simulations on the thermal field”, *Composites Part B: Engineering*, 42 (6), 1751–1763, 2011.

[72] Scott E.P. and Beck J. V., “Estimation of thermal properties in epoxy matrix/carbon fiber

composite Materials", *Journal of Composite Materials*, 26 (1), 132–149, 1992.

[73] Miller J.R. and Weaver P.M., "Temperature profiles in composite plates subject to time-dependent complex boundary conditions", *Composite Structures*, 59 (2), 267–278, 2003.

[74] Sweeting R.D. and Liu X.L., "Measurement of thermal conductivity for fibre-reinforced composites", *Composites Part A: Applied Science and Manufacturing*, 35 (7–8), 933–938, 2004.

[75] Bai Y., Vallée T. and Keller T., "Modeling of thermo-physical properties for FRP composites under elevated and high temperature", *Composites Science and Technology*, 67 (15–16), 3098–3109, 2007.

[76] Gentry T.R. and Hudak C.E., "Thermal compatibility of plastic composite reinforcement and concrete", Advanced Composite Materials for Bridges and Structures, M. El-Badry (eds), Avantage Inc., Montreal, PQ, 1996.

[77] Chaallal O. and Benmokrane B., "Physical and mechanical performance of an innovative glass-fiber-reinforced plastic rod for concrete and grouted anchorages", *Canadian Journal of Civil Engineering*, 20 (2), 254–268, 1993.

[78] Kodur V., "Properties of concrete at elevated temperatures", *ISRN Civil Engineering*, 20142014.

[79] CEN (European Committee for Standardization), "Eurocode 2: Design of Concrete Structures - Part 1-2: General Rules - Structural Fire Design", EN 1992-1-2, Brussels, Belgium, 2010.

[80] Masmoudi R., Zaidi A. and Gérard P., "Transverse thermal expansion of FRP bars embedded in concrete", *Journal of Composites for Construction*, 9 (5), 377–387, 2005.

[81] Aiello M.A., Focacci F., Huang P.C. and Nanni A., "Cracking of concrete cover in FRP reinforced concrete elements under thermal loads", *Proceedings of 4th International Symposium on FRP for Reinforcement of Concrete Structures, FRPRCS4, Baltimore*, (January), 233–243, 1999.

[82] Matthys S., De Shutter G. and Taerwe L., "Influence of transverse thermal expansion of FRP reinforcement on the critical concrete cover", Advanced Composite Materials for Bridges and Structures, M. El-Badry (eds), Montreal, PQ, Canada, 1996.

[83] Silverman E.M., "Elevated temperature testing for comparison of glass/resin composites", *Polymer Composites*, 4 (4), 214–218, 1983.

[84] Aydin F., "Experimental investigation of thermal expansion and concrete strength effects on FRP bars behavior embedded in concrete", *Construction and Building Materials*, 163, 1–8, 2018.

[85] Aiello M.A., "Concrete cover failure in FRP reinforced beams under thermal loading", *Journal of Composites for Construction*, 3 (1), 46–52, 1999.

[86] Gentry T.R. and Husain M., "Thermal compatibility of concrete and composite reinforcements", *Journal of Composites for Construction*, 3 (2), 82–86, 1999.

[87] Zaidi A., Brahim M.M., Mouattah K. and Masmoudi R., "FRP properties effect on numerical deformations in FRP bars-reinforced concrete elements in hot zone", *Energy Procedia*, 139, 798–803, 2017.

[88] Zaidi A., Masmoudi R. and Bouhicha M., "Numerical analysis of thermal stress-deformation in concrete surrounding FRP bars in hot region", *Construction and Building Materials*, 38, 204–213, 2013.

[89] Bellakehal H., Zaidi A., Masmoudi R. and Bouhicha M., "Behavior of FRP bars-reinforced concrete slabs under temperature and sustained load effects", *Polymers*, 6, 873–889, 2014.

[90] Rosa I.C., Firmo J.P. and Correia J.R., "Fire behaviour of GFRP-reinforced concrete slab strips – effect of straight and 90º bent tension lap splices", *submitted to Engineering Structures*.

[91] Sadek A.W., El-Hawary M.M. and El-Deeb A.S., "Fire resistance testing of concrete beams reinforced by GFRP rebars", *Journal of Applied Fire Science*, 14 (2), 91–104, 2005.

[92] Özkal F.M., Polat M., Yağan M. and Öztürk M.O., "Mechanical properties and bond strength degradation of GFRP and steel rebars at elevated temperatures", *Construction and Building Materials*, 184, 45–57, 2018.

[93] Ashrafi H., Bazli M., Najafabadi E.P. and Vatani Oskouei A., "The effect of mechanical and thermal properties of FRP bars on their tensile performance under elevated temperatures", *Construction and Building Materials*, 157, 1001–1010, 2017.

[94] McIntyre E., Bilotta A., Bisby L. and Nigro E., "Mechanical properties of fibre reinforced polymer reinforcement for concrete at high temperature", *8th International Conference on Structures in Fire*, Shanghai, China, 2014.

[95] Wang X. and Zha X., "Experimental research on mechanical behavior of GFRP bars under high temperature", *Applied Mechanics and Materials*, 71–78, 3591–3594, 2011.

[96] Abbasi A. and Hogg P.J., "Temperature and environmental effects on glass fibre rebar: modulus, strength and interfacial bond strength with concrete", *Composites Part B: Engineering*, 36 (5), 394–404, 2005.

[97] Wang Y.C. and Kodur V., "Variation of strength and stiffness of fibre reinforced polymer reinforcing bars with temperature", *Cement and Concrete Composites*, 27 (9–10), 864–874, 2005.

[98] Dimitrienko Y.I., "Thermomechanics of composites under high temperatures", Klewer Academic Publishers, London, UK, 1999.

[99] Tanano H., Masuda Y., Kage T., Fukuyama H., Nishida I. and Hashimoto T., "Fire resistance of continuous fibre reinforced concrete", Non-metallic (FRP) Reinforcement for Concrete Structures, L. Taerwe (eds), E&FN Spon, London, United Kingdom, 1995.

[100] Clarke J., "Alternative Materials for Reinforcement and Prestressing of Concrete", Blackie Academic and Professional (eds), Glasgow, United Kingdom, 1993.

[101] Kumahara S., Masuda Y., Tanano H. and Shimizu A., "Tensile strength of continuous fibre bar under high temperature", *Fibre-Reinforced-Plastic Reinforcement for Concrete Structures: An International Symposium*, Nanni A. and Dolan C. W. (eds), American Concrete Institute, Detroit, Michigan, 731–742, 1993.

[102] Zhou C., Pan J., Zhang Z. and Zhu Y., "Comparative study on the tensile mechanical behavior of GFRP bars under and after high temperature exposure", *Case Studies in Construction Materials*, 16, e00905, 2022.

[103] Khaneghahi M.H., Najafabadi E.P., Shoaei P. and Oskouei A.V., "Effect of intumescent paint coating on mechanical properties of FRP bars at elevated temperature", *Polymer Testing*, 71 (August), 72–86, 2018.

[104] Rozsypalova I., Prokes J., Cairovic D., Girgle F., Danek P. and Stepanek P., "Research on the residual tensile strength of composite reinforcing bars exposed to elevated temperatures", *IOP Conference Series: Materials Science and Engineering*, 1205, 012011, 2021.

[105] Najafabadi E.P., Oskouei A.V., Khaneghahi M.H., Shoaei P. and Ozbakkaloglu T., "The tensile performance of FRP bars embedded in concrete under elevated temperatures", *Construction and Building Materials*, 211, 1138–1152, 2019.

[106] Ashrafi H., Bazli M., Vatani Oskouei A. and Bazli L., "Effect of Sequential Exposure to UV Radiation and Water Vapor Condensation and Extreme Temperatures on the Mechanical Properties of GFRP Bars", *Journal of Composites for Construction*, 22 (1), 04017047, 2018.

[107] Hajiloo H., Green M.F. and Gales J., "Mechanical properties of GFRP reinforcing bars at high temperatures", *Construction and Building Materials*, 162, 142–154, 2018.

[108] Alsayed S., Al-Salloum Y., Almusallam T., El-Gamal S. and Aqel M., "Performance of glass fiber reinforced polymer bars under elevated temperatures", *Composites Part B: Engineering*, 43 (5), 2265–2271, 2012.

[109] Ashrafi H., Bazli M., Jafari A. and Ozbakkaloglu T., "Tensile properties of GFRP laminates after exposure to elevated temperatures: Effect of fiber configuration, sample thickness, and time of exposure", *Composite Structures*, 238, 2020.

[110] Feih S., Boiocchi E., Mathys G., Mathys Z., Gibson A.G. and Mouritz A.P., "Mechanical

properties of thermally-treated and recycled glass fibres", *Composites Part B: Engineering*, 42 (3), 350–358, 2011.

[111] AlAjarmeh O., Manalo A., Benmokrane B., Schubel P., Zeng X., Ahmad A., Hassanli R. and Sorbello C.-D., "Compression behavior of GFRP bars under elevated in-service temperatures", *Construction and Building Materials*, 314 (part A), 125675, 2022.

[112] Gooranorimi O., Claure G., De Caso F., Suaris W. and Nanni A., "Post-fire behavior of GFRP bars and GFRP-RC slabs", *Journal of Materials in Civil Engineering*, 30 (3), 2018.

[113] Hajiloo H. and Green M.F., "Post-fire residual properties of GFRP reinforced concrete slabs: A holistic investigation", *Composite Structures*, 201, 398–413, 2018.

[114] Ellis D.S., Tabatabai H. and Nabizadeh A., "Residual tensile strength and bond properties of GFRP bars after exposure to elevated temperatures", *Materials*, 11 (3), 1–14, 2018.

[115] Bisby L.A., "Fire behaviour of fibre-reinforced polymer (FRP) reinforced or confined concrete," *PhD thesis in Civil Engineering*, Queen's University, Canada, 2003.

[116] Saafi M., "Effect of fire on FRP reinforced concrete members", *Composite Structures*, 58 (1), 11–20, 2002.

[117] Rafi M.M., Nadjai A. and Ali F., "Finite element modeling of carbon fiber-reinforced polymer reinforced concrete beams under elevated temperatures", *ACI Structural Journal*, 105 (6), 701–710, 2008.

[118] Nigro E., Cefarelli G., Bilotta A., Manfredi G. and Cosenza E., "Behavior of FRP reinforced concrete slabs in case of fire: theoretical models and experimental tests", *Advances in Structural Engineering*, 15 (4), 637–652, 2012.

[119] Rafi M.M. and Nadjai A., "Numerical modelling of carbon fibre-reinforced polymer and hybrid reinforced concrete beams in fire", *Fire and Materials*, 37, 374–390, 2013.

[120] Aslani F., "Residual bond between concrete and reinforcing GFRP rebars at elevated temperatures", *Proceedings of the Institution of Civil Engineers - Structures and Buildings*, 172 (2), 127–140, 2018.

[121] Rosa I.C., Arruda M.R.T., Firmo J.P. and Correia J.R., "Bond behaviour of straight and bent GFRP bars at elevated temperature: pull-out tests and numerical simulations", *Journal of Composites for Construction*, 26 (3), 04022028, 2022.

[122] Mousavi A., Hajiloo H. and Green M.F., "Bond Performance of GFRP Reinforcing Bars under Uniform or Gradient Temperature Distributions", *Journal of Composites for Construction*, 25 (6), 1–13, 2021.

[123] Rosa I.C., Firmo J.P., Correia J.R. and Mazzuca P., "Influence of elevated temperatures on the

bond behaviour of ribbed GFRP bars in concrete", *Cement and Concrete Composites*, 122, 104119, 2021.

[124] Solyom S., Di Benedetti M., Guadagnini M. and Balázs G.L., "Effect of temperature on the bond behaviour of GFRP bars in concrete", *Composites Part B*, 183, 107602, 2020.

[125] Rosa I.C., Firmo J.P., Correia J.R. and Barros J.A.O., "Bond behaviour of sand coated GFRP bars to concrete at elevated temperature – Definition of bond vs. slip relations", *Composites Part B: Engineering*, 160, 329–340, 2019.

[126] Hajiloo H. and Green M.F., "Bond strength of GFRP reinforcing bars at high temperatures with implications for performance in fire", *Journal of Composites for Construction*, 22 (6), 04018055, 2018.

[127] Alvarez A., Zaidi A. and Masmoudi R., "Bond-slip behaviour of FRP bars under low and high temperature - experimental and theoretical studies", *3rd International Conference on Durability & Field Applications of Fiber Reinforced Polymer (FRP) Composites for Construction*, 523–530, 2007.

[128] Katz A., Berman N. and Bank L.C., "Effect of high temperature on bond strength of FRP rebars", *Journal of Composites for Construction*, 3 (2), 73–81, 1999.

[129] Li C., Gao D., Wang Y. and Tang J., "Effect of high temperature on the bond performance between basalt fibre reinforced polymer (BFRP) bars and concrete", *Construction and Building Materials*, 141, 44–51, 2017.

[130] Hamad R., Johari M.A. and Haddad R., "Mechanical properties and bond characteristics of different fiber reinforced polymer rebars at elevated temperatures", *Construction and Building Materials*, 142, 521–535, 2017.

[131] El-Gamal S., "Bond strength of glass fiber-reinforced polymer bars in concrete after exposure to elevated temperatures", *Journal of Reinforced Plastics and Composites*, 33 (23), 2151–2163, 2014.

[132] Masmoudi A., Masmoudi R. and Ouezdou M. Ben, "Thermal effects on GFRP rebars: Experimental study and analytical analysis", *Materials and Structures/Materiaux et Constructions*, 43 (6), 775–788, 2010.

[133] Galati N., Nanni A., Dharani L.R., Focacci F. and Aiello M.A., "Thermal effects on bond between FRP rebars and concrete", *Composites Part A: Applied Science and Manufacturing*, 37 (8), 1223–1230, 2006.

[134] FIB, "Bond of reinforcement in concrete – state-of-the-art report", Bulletin 10, Lausanne, Switzerland, 2000.

[135] Masmoudi R., Masmoudi A., Ouezdou M. and Daoud A., "Long-term bond performance of GFRP bars in concrete under temperature ranging from 20 °C to 80 °C", *Construction and Building Materials*, 25, 486–493, 2011.

[136] Calvet V., Valcuende M., Benlloch J. and Cánoves J., "Influence of moderate temperatures on the bond between carbon fibre reinforced polymer bars (CFRP) and concrete", *Construction and Building Materials*, 94, 589–604, 2015.

[137] Kiari M., Triantafyllidou E., Grosu S., Stratford T. and Bisby L., "Design of an FRP-reinforced concrete beam system for fire performance", *Advanced Composites in Construction 2013 (ACIC 2013) – 6th International ACIC Conference*, Belfast, United Kingdom, 2013.

[138] Katz A. and Berman N., "Modeling the effect of high temperature on the bond of FRP reinforcing bars to concrete", *Cement and Concrete Composites*, 22 (6), 433–443, 2000.

[139] Eligehausen R., Popov E.P. and Bertero V. V., "Local bond stress-slip relationships of deformed bars under generalized excitations," Berkeley, USA, 1983.

[140] Cosenza E., Manfredi G. and Realfonzo R., "Bond characteristics and anchorage length of FRP rebars", *Proceedings of the 2nd International Conference on Advanced Composite Materials in Bridges and Structures*, Montreal, Canada, 1996.

[141] Cosenza E., Manfredi G. and Realfonzo R., "Analytical modelling of bond between FRP reinforcing bars and concrete", *2nd International RILEM Symposium (FRPRCS-2)*, Ghent, Belgium, 1995.

[142] Duan D., Ouyang L., Gao W., Xu Q., Liu W. and Yang J., "Fire performance of FRP-RC flexural members: a numerical study", *Polymers*, 14 (346)2022.

[143] Veljkovic A., Carvelli V., Solyom S., Balázs G.L. and Rezazadeh M., "Modelling the temperature effects at the interface between GFRP bar and concrete", *IABSE Symposium 2019 Guimarães – Towards a Resilient Built Environment - Risk and Asset Management*, Guimarães, Portugal, 1065–1072, 2019.

[144] Sena-Cruz J.M., "Strengthening of concrete structures with near-surface mounted CFRP laminate strips", *PhD thesis in Civil Engineering*, Universidade do Minho, Guimarães, Portugal, 2005.

[145] Stang H. and Aarre T., "Evaluation of crack width in FRC with conventional reinforcement", *Cement and Concrete Composites*, 14 (2), 143–154, 1992.

[146] Duarte A.P.C., Rosa I.C., Arruda M.R.T., Firmo J.P. and Correia J.R., "Three-dimensional finite element modelling of the thermomechanical response of GFRP-reinforced concrete slab strips subjected to fire", *Journal of Composites for Construction*, 26 (5), 04022044, 2022.

[147] Rosa I.C., Santos P., Firmo J.P. and Correia J.R., "Fire behaviour of concrete slab strips reinforced with sand-coated GFRP bars", *Composite Structures*, 244, 112270, 2020.

[148] Nigro E., Cefarelli G., Bilotta A., Manfredi G. and Cosenza E., "Fire resistance of concrete slabs reinforced with FRP bars. Part I: Experimental investigations on the mechanical behavior", *Composites Part B: Engineering*, 42, 1739–1750, 2011.

[149] Rafi M.M., Nadjai A., Ali F. and O'Hare P., "Evaluation of thermal resistance of FRP reinforced concrete beams in fire", *Journal of Structural Fire Engineering*, 2 (2), 91–107, 2011.

[150] Hamad R.J.A., Megat Johari M.A. and Haddad R.H., "Effects of bars slippage on the pre-and post-heating flexural behavior of FRP reinforced concrete beams: Experimental and theoretical investigations", *International Journal of Civil Engineering and Technology*, 10 (2), 574–602, 2019.

[151] Schmitt A., Carvelli V. and Pahn M., "Thermo-mechanical loading of GFRP reinforced thin concrete panels", *Composites Part B: Engineering*, 81, 35–43, 2015.

[152] Prokeš J., Rozsypalová I., Girgle F., Daněk P. and Štěpánek P., "Effects of elevated temperature on the behaviour of concrete beams reinforced with fiber reinforced polymers", *IOP Conference Series: Materials Science and Engineering*, 1039 (1), 2021.

[153] Kodur V.K.R. and Bisby L.A., "Evaluation of fire endurance of concrete slabs reinforced with fiber-reinforced polymer bars", *Journal of Structural Engineering*, 131 (1), 34–43, 2005.

[154] Hajiloo H. and Green M.F., "GFRP reinforced concrete slabs in fire: Finite element modelling", *Engineering Structures*, 183, 1109–1120, 2019.

[155] Rafi M.M. and Nadjai A., "Behavior of hybrid (steel-CFRP) and CFRP bar-reinforced concrete beams in fire", *Journal of Composite Materials*, 45 (15), 1573–1584, 2010.

[156] Rafi M.M., Nadjai A. and Ali F., "Fire resistance of carbon FRP reinforced-concrete beams", *Magazine of Concrete Research*, 59 (4), 245–255, 2007.

[157] Kodur V.K.R. and Sultan M.A., "Effect of temperature on thermal properties of high-strength concrete", *Journal of Materials in Civil Engineering*, 15 (2), 101–107, 2003.

[158] Ba G., Miao J., Zhang W. and Liu C., "Influence of cracking on heat propagation in reinforced concrete structures", *Journal of Structural Engineering*, 142 (7), 04016035, 2016.

[159] Ba G., Miao J., Zhang W. and Liu J., "Influence of reinforcement corrosion on fire performance of reinforced concrete beams", *Construction and Building Materials*, 213, 738–747, 2019.

[160] Vejmelková E., Padevět P. and Černý R., "Effect of cracks on hygric and thermal characteristics of concrete", *Bauphysik*, 30 (6), 438–444, 2008.

[161] Wu B., Xiong W. and Wen B., "Thermal fields of cracked concrete members in fire", *Fire Safety Journal*, 66, 15–24, 2014.

[162] Ervine A., Gillie M., Stratford T.J. and Pankaj P., "Thermal propagation through tensile cracks in reinforced concrete", *Journal of Materials in Civil Engineering*, 24 (5), 516–522, 2012.

[163] Zhang H.Y., Li Q.Y., Kodur V. and Lv H.R., "Effect of cracking and residual deformation on behavior of concrete beams with different scales under fire exposure", *Engineering Structures*, 245 (July 2020)2021.

[164] Kodur V.K.R. and Baingo D., "Fire resistance of FRP reinforced concrete slabs," Internal Report No. 758, Canada, 1998.

[165] Hawileh R.A. and Naser M.Z., "Thermal-stress analysis of RC beams reinforced with GFRP bars", *Composites Part B: Engineering*, 43 (5), 2135–2142, 2012.

[166] Yu B. and Kodur V.K.R., "Factors governing the fire response of concrete beams reinforced with FRP rebars", *Composite Structures*, 100, 257–269, 2013.

[167] Lin X. and Zhang Y.X., "Nonlinear finite element analyses of steel/FRP-reinforced concrete beams in fire conditions", *Composite Structures*, 97, 277–285, 2013.

[168] Veljkovic A., Carvelli V. and Rezazadeh M., "Modelling the bond of GFRP bar and concrete for the thermo-mechanical behaviour of RC slabs", 10th International Conference on FRP Composites in Civil Engineering (CICE 2021) – Lecture notes in Civil Engineering, Ilki A., Ispir M., Inci P. (eds), 198, Springer, Cham, 2022.

[169] Hajiloo H., "Glass Fibre Reinforced Polymer (GFRP) Internally Reinforced Concrete Slabs in Fire," *PhD Thesis in Civil Engineering*, Queen's University, Kingston, Ontario, Canada, 2017.

[170] Pagani R., Bocciarelli M., Carvelli V. and Pisani M.A., "Modelling high temperature effects on bridge slabs reinforced with GFRP rebars", *Engineering Structures*, 81, 318–326, 2014.

[171] Nigro E., Cefarelli G. and Billota A., "Comparison between results of numerical simulations and experimental tests on FRP RC slabs in fire situation", *7th International Conference on Structures in Fire*, Zurich, Switzerland, 2012.

[172] Adelzadeh M., Hajiloo H. and Green M., "Numerical study of FRP reinforced concrete slabs at elevated temperature", *Polymers*, 6, 408–422, 2014.

[173] Bisby L.A. and Kodur V.K.R., "Evaluating the fire endurance of concrete slabs reinforced with FRP bars: Considerations for a holistic approach", *Composites Part B: Engineering*, 38 (5–6), 547–558, 2007.

[174] Rafi M.M. and Nadjai A., "Parametric finite element analysis of FRP reinforced concrete beams in fire and design guidelines", *Fire and Materials*, 38, 293–311, 2014.

[175] JSCE (Japan Society of Civil Engineers), "Recommendations for Design and Construction of Concrete Structures using Continuous Fibre Reinforcing Materials", Tokyo, Japan, 1997.

[176] Intelligent Sensing for Innovative Structures Canada, "Reinforcing concrete structures with fibre-reinforced polymers", Design manual No. 3, Winnipeg, Manitoba, Canada, 2007.

[177] AASHTO (American Association of State Highway & Transportation Officials), "AASHTO LRFD Bridge Design Guide Specifications for GFRP- Reinforced Concrete Bridge Decks and Traffic Railings", Washington, USA, 2018.

[178] CSA (Canadian Standards Association), "Design and Construction of Building Components with Fibre-Reinforced Polymers", CAN/CSA-S806-02, Rexdale, Ontario, Canada, 2009.

[179] ACI (American Concrete Institute), "Guide for the Design and Construction of Concrete Reinforced with FRP Bars", ACI 440.1R-06, Farmington Hills, Michigan, USA, 2006.

[180] Lie T.T., "Calculation of the fire resistance of composite concrete floor and roof slabs", *Fire Technology*, 14 (1), 28–45, 1978.

[181] Fujisaki T., Nakatsuji T. and Sugita M., "Research and development of grid shaped FRP reinforcement", *Fibre-Reinforced-Plastic Reinforcement for Concrete Structures: An International Symposium*, Detroit, Michigan, USA, 177–192, 1993.

[182] Rahman A.H., Taylor D.A. and Kingsley C.Y., "Evaluation of FRP as reinforcement for concrete bridges", *Fibre-Reinforced-Plastic Reinforcement for Concrete Structures: An International Symposium*, Detroit, Michigan, USA, 71–86, 1993.

[183] Owens Corning, "Aslan 100 – Glass fiber reinforced polymer (GFRP) rebar for infrastructure solutionss", technical datasheet, 2018.

[184] ASTM (American Society for Testing and Materials), "Standard Test Method for Assignment of the Glass Transition Temperature By Dynamic Mechanical Analysis", ASTM E1640-09, West Conshohocken, Pennsylvania, USA, 2009.

[185] ISO (International Organization for Standardization), "Plastics - Differential scanning calorimetry (DSC) - Part 1: General principles", ISO 11357-1, Geneve, Switzerland, 2016.

[186] ISO (International Organization for Standardization), "Fibre-Reinforced Polymer (FRP) Reinforcement of Concrete - Test Methods - Part 1: FRP Bars and Grids", ISO 10406-1, Geneve, Switzerland, 2008.

[187] International Institute for FRP in Construction (IIFC), "Anchoring GFRP reinforcing bars and rods in metal pipe tabs for tensile testing (Practical Note No.1)", *FRP International*, 17 (1), 12–15, 2020.

[188] ASTM (American Society for Testing and Materials), "Standard Test Method for Bond Strength

of Fiber-Reinforced Polymer Matrix Composite Bars to Concrete by Pullout Testing", ASTM D7913/D7913M-14, West Conshohocken, Pennsylvania, USA, 2014.

[189] ACI (American Concrete Institute), "Guide Test Methods for Fiber-Reinforced Polymer (FRP) Composites for Reinforcing or Strengthening Concrete and Masonry Structures", ACI 440.3R-12, Farmington Hills, Michigan, USA, 2012.

[190] CEN (European Committee for Standardization), "Testing Hardened Concrete - Part 3: Compressive Strength of Test Specimens", EN 12390-3, Brussels, Belgium, 2009.

[191] CEN (European Committee for Standardization), "Testing Hardened Concrete - Part 6: Tensile Splitting Strength of Test Specimens", EN 12390-6, Brussels, Belgium, 2009.

[192] CEN (European Committee for Standardization), "Eurocode 2: Design of Concrete Structures - Part 1-1: General Rules and Rules for Buildings", EN 1992-1-1, Brussels, Belgium, 2010.

[193] Tighiouart B., Benmokrane B. and Gao D., "Investigation of bond in concrete member with fibre reinforced polymer (FRP) bars", *Construction and Building Materials*, 12 (8), 453–462, 1998.

[194] Baena M., Torres L., Turon A. and Barris C., "Experimental study of bond behaviour between concrete and FRP bars using a pull-out test", *Composites Part B: Engineering*, 40 (8), 784–797, 2009.

[195] Mesbah H.-A., Benzaid R. and Benmokrane B., "Evaluation of bond strength of FRP reinforcing rods in concrete and FE modelling", *International Journal of Civil Engineering and Construction Science*, 4 (3), 21–41, 2017.

[196] El-Nemr A., Ahmed E.A., El-Safty A. and Benmokrane B., "Evaluation of the flexural strength and serviceability of concrete beams reinforced with different types of GFRP bars", *Engineering Structures*, 173 (July), 606–619, 2018.

[197] Fava G., Carvelli V. and Pisani M.A., "Remarks on bond of GFRP rebars and concrete", *Composites Part B: Engineering*, 93, 210–220, 2016.

[198] Simulia, ABAQUS standard, User's manual, version 2018, Johnston, RI: Dassault Systèmes, 2018.

[199] Sena-Cruz J. and Barros J., "Modeling of bond between near-surface mounted CFRP laminate strips and concrete", *Computers and Structures*, 82 (17–19), 1513–1521, 2004.

[200] Azevedo A., Tiago C., Firmo J.P. and Correia J.R., "Development of a Matlab code for the numerical modelling of the bond between FRP composites and concrete", Report, University of Lisbon, Lisbon, Portugal, 2021.

[201] Eligehausen R., Popov E.P. and Bertero V. V., "Local bond stress-slip relationships of deformed bars under generalized excitations: experimental results and analytical model," Report No.

UCB/EERC-8, Earthquake Engineering Resarch Center, California, USA, 1983.

[202] Duarte A.P.C., Silva B.A., Silvestre N., de Brito J., Júlio E. and Castro J.M., "Finite element modelling of short steel tubes filled with rubberized concrete", *Composite Structures*, 150, 28–40, 2016.

[203] Lopes B., Arruda M.R.T., Almeida-Fernandes L., Castro L., Silvestre N. and Correia J.R., "Assessment of mesh dependency in the numerical simulation of compact tension tests for orthotropic materials", *Composites Part C: Open Access*, 1, 100006, 2020.

[204] Bažant Z.P. and Lin F., "Nonlocal smeared cracking model for concrete fracture", *Journal of Structural Engineering*, 114 (11), 2493–2510, 1988.

[205] Hilsdorf H.K. and Brameshuber W., "Code-type formulation of fracture mechanics concepts for concrete", *International Journal of Fracture*, 51 (1), 61–72, 1991.

[206] Rosa I.C., Morgado T., Correia J.R., Firmo J.P. and Silvestre N., "Shear behaviour of GFRP composite materials at elevated temperature", *Journal of Composites for Construction*, 22 (3), 04018010, 2018.

[207] Yuan J.S. and Hadi M.N.S., "Friction coefficient between FRP pultruded profiles and concrete", *Materials and Structures*, 51 (120), 1–10, 2018.

[208] ACI (American Concrete Institute), "Building Code Requirements for Structural Concrete", ACI 318-11, Farmington Hills, Michigan, USA, 2011.

[209] CEN (European Committee for Standardization), "Fire Resistance Tests - Part 1: General Requirements", EN 1363-1, Brussels, Belgium, 2012.

[210] Firmo J.P., Correia J.R. and França P., "Fire behaviour of reinforced concrete beams strengthened with CFRP laminates: Protection systems with insulation of the anchorage zones", *Composites Part B: Engineering*, 43 (3), 1545–1556, 2012.

[211] Firmo J.P. and Correia J.R., "Fire behaviour of thermally insulated RC beams strengthened with NSM-CFRP strips: Experimental study", *Composites Part B: Engineering*, 76, 112–121, 2015.

[212] Pacheco J., "Reliability analysis of ecoconcrete," *PhD thesis in Civil Engineering*, Instituto Superior Técnico, University of Lisbon, Lisbon, Portugal, 2020.

[213] CEN (European Committee for Standardization), "Eurocode 3: Design of Steel Structures - Part 1–2: General Rules - Structural Fire Design", EN 1993-1-2, Brussels, Belgium, 2010.

[214] Genikomsou A.S. and Polak M.A., "Finite element analysis of punching shear of concrete slabs using damaged plasticity model in ABAQUS", *Engineering Structures*, 98, 38–48, 2015.

[215] Tysmans T., Wozniak M., Remy O. and Vantomme J., "Finite element modelling of the biaxial

behaviour of high-performance fibre-reinforced cement composites (HPFRCC) using Concrete Damaged Plasticity", *Finite Elements in Analysis and Design*, 100, 47–53, 2015.

[216] Lee S.H., Abolmaali A., Shin K.J. and Lee H. Du, "ABAQUS modeling for post-tensioned reinforced concrete beams", *Journal of Building Engineering*, 30 (August 2019), 101273, 2020.

[217] Bamonte P. and Felicetti R., "High-temperature behaviour of concrete in tension", *Structural Engineering International*, 22 (4), 493–499, 2012.

[218] Nielsen C. V and Biéanić N., "Residual fracture energy of high-performance and normal concrete subject to high temperatures", *Materials and Structures*, 36 (8), 515–521, 2003.

[219] Wallenberger F.T., Watson J.C. and Li H., "Glass Fibers", *ASM Handbook*, 21, 27–34, 2001.

[220] Morgado T., Silvestre N. and Correia J.R., "Simulation of fire resistance behaviour of pultruded GFRP beams – Part I: Models description and kinematic issues", *Composite Structures*, 187, 269–280, 2018.

[221] Zhang Y.X. and Lin X., "Nonlinear finite element analyses of steel/FRP-reinforced concrete beams by using a novel composite beam element", *Advances in Structural Engineering*, 16 (2), 339–352, 2013.

[222] Protchenko K., Elżbieta S., Urbański M. and Garbacz A., "Mechanical performance of FRP-RC flexural members subjected to fire conditions", *Budownictwo i Architektura*, 19 (4), 017–030, 2020.

[223] Protchenko K. and Szmigiera E., "Post-fire characteristics of concrete beams reinforced with hybrid FRP bars", *Materials*, 13 (5)2020.

Appendix

Appendix A.

Individual results obtained in tensile tests on GFRP bars

This appendix presents the individual results of the tensile tests performed to the GFRP bars at ambient and elevated temperatures (the results were summarized in Table 3.7 in Section 3.4). Table A.1 to Table A.5 show the results obtained in each tested bar specimen in terms of: (i) the maximum load, (ii) the tensile strength and modulus (in absolute and normalized values in reference to ambient temperature), and (ii) the failure mode. The failure mode identified as "valid" concerns to the tensile rupture of the GFRP within the free length of the specimens, while that denoted as "invalid" respects to the premature rupture of the bars near the grip zones or to the bar's slippage inside the steel anchors.

Table A.1. Individual results of tensile tests performed in SC bars.

T [ºC]	Specimen	Maximum load [kN]	Tensile strength [MPa]	Normalized tensile strength [-]	Tensile modulus [GPa]	Normalized tensile modulus [-]	Failure mode
20 ± 2	1	73.8	1036	0.99	48.3	1.00	Valid
	2	-	-	-	48.6	1.01	Invalid
	3	75.0	1052	1.01	49.2	1.02	Valid
	4	74.6	1047	1.00	47.0	0.97	Valid
	5	-	-	-	48.0	1.00	Invalid
50 ± 2	1	65.4	918	0.88	47.5	0.98	Valid
	2	-	-		47.8	0.99	Invalid
	3	66.5	933	0.89	47.7	0.99	Valid
	4	66.4	931	0.89	47.5	0.99	Valid
100 ± 2	1	48.3	678	0.65	-	-	Valid
	2	49.8	699	0.67	44.9	0.931	Valid
	3	-	-	-	43.1	0.894	Invalid
	4	47.8	671	0.64	43.1	0.893	Valid
	5	-	-	-	45.3	0.940	Invalid
150 ± 2	1	42.4	595	0.57	-	-	Valid
	2	42.7	599	0.57	44.6	0.925	Valid
	3	45.7	642	0.61	47.2	0.979	Valid
	4	46.8	657	0.63	45.9	0.951	Valid
200 ± 2	1	43.8	615	0.59	-	-	Valid
	2	41.6	584	0.56	47.9	0.99	Valid
	3	43.9	616	0.59	44.0	0.91	Valid
	4	42.7	599	0.57	44.2	0.92	Valid
250 ± 2	1	44.7	627	0.60	39.6	0.82	Valid
	2	44.6	626	0.60	41.8	0.87	Valid
	3	43.0	603	0.58	46.1	0.96	Valid
	4	44.3	622	0.60	47.1	0.98	Valid
300 ± 2	1	-	-	-	43.5	0.90	Invalid
	2	41.2	577	0.55	41.2	0.86	Valid
	3	42.3	593	0.57	46.2	0.96	Valid
	4	44.4	624	0.60	36.5	0.76	Valid

Table A.2. Individual results of tensile tests performed in RB-D8 bars.

T [ºC]	Specimen	Maximum load [kN]	Tensile strength [MPa]	Normalized tensile strength [-]	Tensile modulus [GPa]	Normalized tensile modulus [-]	Failure mode
20 ± 2	1	76.8	1526	1.03	58.2	1.01	Valid
	2	72.9	1449	0.98	58.3	1.01	Valid
	3	73.9	1470	0.99	56.3	0.98	Valid
50 ± 2	1	-	-	-	56.8	0.99	Invalid
	2	-	-	-	53.3	0.93	Invalid
	3	-	-	-	56.3	0.98	Invalid
	4	-	-	-	57.0	0.99	Invalid
	5	74.5	1482	1.00	55.6	0.97	Valid
	6	72.7	1446	0.98	54.1	0.94	Valid
100 ± 2	1	-	-	-	53.7	0.93	Invalid
	2	-	-	-	52.0	0.90	Invalid
	3	-	-	-	53.5	0.93	Invalid
	4	-	-	-	53.8	0.93	Invalid
	5	-	-	-	53.4	0.93	Invalid
	6	-	-	-	58.2	1.01	Invalid
	7	65.4	1299	0.88	54.8	0.95	Valid
	8	-	-	-	57.8	1.00	Invalid
	9	65.0	1292	0.87	-	-	Valid
	10	-	-	-	57.1	1.00	Invalid
150 ± 2	1	58.6	1166	0.79	57.4	1.00	Valid
	2	59.7	1186	0.80	55.8	0.97	Valid
	3	55.0	1093	0.74	55.9	0.97	Valid
200 ± 2	1	33.5	666	0.45	54.4	0.94	Valid
	2	35.9	714	0.48	54.2	0.94	Valid
	3	35.2	699	0.47	53.0	0.92	Valid
250 ± 2	1	28.3	562	0.38	54.9	0.95	Valid
	2	30.2	601	0.41	49.9	0.87	Valid
	3	31.6	629	0.42	54.8	0.95	Valid
300 ± 2	1	29.2	581	0.39	54.7	0.95	Valid
	2	28.0	557	0.38	48.1	0.84	Valid
	3	31.1	618	0.42	47.4	0.82	Valid

Table A.3. Individual results of tensile tests performed in RB-D12 bars up to 300 ºC.

T [ºC]	Specimen	Maximum load [kN]	Tensile strength [MPa]	Normalized tensile strength [-]	Tensile modulus [GPa]	Normalized tensile modulus [-]	Failure mode (1)
20 ± 2	1	-	-	-	58.7	0.98	Invalid
	2	-	-	-	61.9	1.03	Invalid
	3	-	-	-	61.9	1.03	Invalid
	4	-	-	-	60.9	1.01	Invalid
	5	-	-	-	61.4	1.02	Invalid
	6	-	-	-	58.9	0.98	Invalid
	7	-	-	-	59.3	0.99	Invalid
	8	155.1	1373	0.99	57.8	0.96	Valid
	9	156.8	1388	1.01	59.3	0.99	Valid
150 ± 2	1	108.9	964	0.70	61.2	1.02	Valid
	2	117.1	1036	0.75	57.5	0.96	Valid
	3	112.5	996	0.72	58.1	0.97	Valid
	4	-	-	-	61.3	1.02	Valid
200 ± 2	1	73.6	651	0.47	59.1	0.98	Valid
	2	83.7	741	0.54	57.1	0.95	Valid
	3	74.8	662	0.48	53.7	0.89	Valid
	4	-	-	-	58.8	0.98	I
300 ± 2	1	74	655	0.47	50.8	0.85	Valid
	2	72.8	644	0.47	61.8	1.03	Valid
	3	77.3	684	0.50	60.2	1.00	Valid
	4	-	-	-	59.6	0.99	I

I: test interrupted before failure.

Table A.4. Individual results of tensile tests performed in RB-D12 bars above 300 ºC.

T [ºC]	Specimen	Maximum load [kN]	Tensile strength [MPa]	Normalized tensile strength [-]	Tensile modulus [GPa]	Normalized tensile modulus [-]	Failure mode (1)
450 ± 5	1	76.4	676	0.49	-	-	Valid
	2	70.3	622	0.45	-	-	Valid
	3	73.5	650	0.47	-	-	Valid
	4	-	-	-	56.8	0.95	I
	5	-	-	-	51.4	0.86	I
	6	-	-	-	47.4	0.79	I
575 ± 5	1	14.9	132	0.10	-	-	Valid
	2	17.2	152	0.11	-	-	Valid
	3	13.3	118	0.09	-	-	Valid
	4	-	-	-	57.4	0.96	I
	5	-	-	-	50.1	0.83	I
	6	-	-	-	47.4	0.79	I
	7	-	-	-	48.5	0.81	I
715 ± 5	1	5.9	52	0.04	-	-	Valid
	2	6.8	60	0.04	-	-	Valid
	3	4.2	37	0.03	-	-	Valid
	4	-	-	-	40.9	0.68	I
	5	-	-	-	37.3	0.62	I
	6	-	-	-	41.5	0.69	I

I: test interrupted before failure.

Table A.5. Individual results of tensile tests performed in RBP-S bars.

T [ºC]	Specimen	Maximum load [kN]	Tensile strength [MPa]	Normalized tensile strength [-]	Tensile modulus [GPa]	Normalized tensile modulus [-]	Failure mode
20 ± 2	1	122	1151	0.97	54.3	0.90	Valid
	2	131.9	1244	1.05	63.6	1.06	Valid
	3	122.7	1158	0.98	62.5	1.04	Valid
100 ± 2	1	129.2	1219	1.03	55.6	0.92	Valid
	2	118.7	1119	0.95	59.5	0.99	Valid
	3	107.6	1015	0.86	54.5	0.91	Valid
150 ± 2	1	91.5	864	0.73	47.6	0.79	Valid
	2	74.1	699	0.59	-	-	Valid
	3	88.5	835	0.71	-	-	Valid
	4	78.2	738	0.62	52.6	0.87	Valid
200 ± 2	1	71.3	673	0.57	46.2	0.77	Valid
	2	84.5	798	0.67	47.6	0.79	Valid
	3	87.6	827	0.70	52.7	0.88	Valid
300 ± 2	1	88.5	835	0.71	-	-	Valid
	2	68.2	644	0.54	-	-	Valid
	3	58.9	556	0.47	46.2	0.77	Valid

Appendix B.

Individual results obtained in pull-out tests on GFRP bars

This appendix presents the individual results of the pull-out tests performed to the GFRP bars at ambient and elevated temperatures (the results were summarized in Table 4.4 to Table 4.9 in Chapter 4). Table B.1 to Table B.6 list the results obtained in each tested specimen with respect to: (i) the maximum pull-out load, (ii) the average bond strength and (iii) the bond stiffness at the loaded end (in absolute and normalized values in reference to ambient temperature), and (iv) the failure mode. It is worth noting that the bond stiffness was computed based on the initial slope of the bond stress *vs.* slip curves ($K_{\tau\text{-}s}$), in the case of specimens with straight bars, and the load *vs.* slip curves ($K_{F\text{-}s}$), in the case of specimens with bent bars.

Table B.1. Individual results of pull-out tests performed in (unconfined) specimens with SC bars and embedment length of 5*D*.

T [ºC]	Specimen	Maximum pull-out load [kN]	Average bond strength [MPa]	Normalized bond strength [-]	Bond stiffness (loaded end) ($K_{\tau\text{-}s}$) [MPa/mm]	Normalized bond stiffness [-]	Failure mode [1]
20 ± 2	1	30.6	19.5	0.84	-	-	PO
	2	38.4	24.4	1.06	-	-	PO
	3	38.2	24.3	1.05	-	-	PO
	4	39.8	25.3	1.10	37.1	1.06	PO
	5	33.4	21.2	0.92	37.4	1.07	PO
	6	37.6	23.9	1.03	30.3	0.87	PO
40 ± 2	1	30.5	19.4	0.84	22.8	0.65	PO
	2	25.9	16.5	0.71	49.2	1.41	PO
	3	30.9	19.7	0.85	23.7	0.68	PO
	4	30.1	19.1	0.83	33.8	0.97	PO
60 ± 2	1	22.0	14.0	0.61	10.8	0.31	PO
	2	25.0	15.9	0.69	9.3	0.26	PO
	3	22.0	14.0	0.61	16.2	0.46	PO
	4	24.3	15.4	0.67	23.8	0.68	PO
80 ± 2	1	11.5	7.3	0.32	7.2	0.20	PO
	2	13.4	8.6	0.37	13.4	0.38	PO
	3	11.1	7.1	0.31	17.6	0.50	PO
	4	19.8	12.6	0.55	16.4	0.47	PO
	5	13.0	8.3	0.36	6.1	0.17	PO
100 ± 2	1	6.2	4.0	0.17	3.7	0.11	PO
	2	6.2	4.0	0.17	2.9	0.08	PO
	3	9.0	5.7	0.25	6.0	0.17	PO
	4	5.6	3.6	0.16	5.4	0.15	PO
140 ± 2	1	4.2	2.7	0.12	6.6	0.19	PO
	2	4.1	2.6	0.11	3.9	0.11	PO
	3	3.6	2.3	0.10	4.2	0.12	PO
200 ± 2	1	2.7	1.7	0.07	12.9	0.37	PO

[1] PO: pull-out.

Table B.2. Individual results of pull-out tests performed in specimens with SC bars and embedment length of 9*D* (*C-#* specimens were confined with steel clamps).

T [ºC]	Specimen	Maximum pull-out load [kN]	Average bond strength [MPa]	Normalized bond strength [-]	Bond stiffness (loaded end) ($K_{\tau-s}$) [MPa/mm]	Normalized bond stiffness [-]	Failure mode [1]
20 ± 2	1	56.4	20.0	1.04	17.1	1.16	PO
	2	54.9	19.4	1.00	-	-	PO
	3	51.7	18.3	0.95	14.7	1.00	PO
	4 [2]	55.7	19.7	1.02	-	-	SPT
	C-1	49.4	17.5	0.91	12.8	0.87	PO
	C-2	55.5	19.6	1.01	13.1	0.89	PO
	C-3	59.7	21.1	1.09	17.3	1.17	PO
	C-4	54.7	19.3	1.00	13.4	0.91	PO
40 ± 2	1	48.9	17.3	0.90	13.0	0.88	PO
	2	45.3	16.0	0.83	13.3	0.90	PO
	3	47.7	16.9	0.88	12.9	0.88	PO
	4	43.9	15.5	0.80	10.4	0.71	PO
60 ± 2	1	31.4	11.1	0.57	13.3	0.90	PO
	2	35.5	12.6	0.65	11.8	0.80	PO
	3	45.1	16.0	0.83	-	-	PO
	4	43.0	15.2	0.79	10.3	0.70	PO
80 ± 2	1	23.4	8.3	0.43	8.4	0.57	PO
	2	15.8	5.6	0.29	-	-	PO
	3	21.2	7.5	0.39	8.1	0.55	PO
100 ± 2	1	6.5	2.3	0.12	1.8	0.12	PO
	2	10.8	3.8	0.20	3.9	0.26	PO
	3	13.1	4.6	0.24	3.2	0.22	PO
140 ± 2	1	4.9	1.7	0.09	2.5	0.17	PO
	2	5.7	2.0	0.10	6.0	0.41	PO
	3	5.8	2.1	0.11	6.7	0.45	PO

[1] SPT: splitting of concrete; PO: pull-out.

[2] This specimen was not considered in the calculation of the average bond strength at 20 ºC.

Table B.3. Individual results of pull-out tests performed in (unconfined) specimens with RB-D8 bars.

T [ºC]	Specimen	Maximum pull-out load [kN]	Average bond strength [MPa]	Normalized bond strength [-]	Bond stiffness (loaded end) ($K_{\tau-s}$) [MPa/mm]	Normalized bond stiffness [-]	Failure mode [(1)]
20 ± 2	1	8.6	6.9	0.97	26.1	1.11	PO
	2	9.2	7.4	1.03	20.9	0.89	PO
60 ± 2	1	7.5	6.1	0.85	27.0	1.15	PO
	2	8.6	6.9	0.97	23.2	0.99	PO
	3	6.8	5.5	0.77	17.7	0.76	PO
100 ± 2	1	7.5	6.0	0.84	20.5	0.87	PO
	2	5.5	4.4	0.62	13.4	0.57	PO
140 ± 2	1	7.1	5.7	0.80	21.9	0.93	PO
	2	5.5	4.4	0.62	14.2	0.61	PO
	3	7.6	6.1	0.85	17.6	0.75	PO
200 ± 2	1	5.2	4.2	0.59	16.9	0.72	PO
	2	4.7	3.8	0.53	18.4	0.78	PO
250 ± 2	1	2.0	1.6	0.22	10.4	0.44	PO
	2	2.2	1.8	0.25	9.8	0.42	PO
	3	2.4	1.9	0.27	-	-	PO
300 ± 2	1	2.1	1.70	0.24	5.2	0.22	PO
	2	2.1	1.70	0.24	5.3	0.23	PO

(1) PO: pull-out.

Table B.4. Individual results of pull-out tests performed in (unconfined) specimens with RB-D12 bars.

T [ºC]	Specimen	Maximum pull-out load [kN]	Average bond strength [MPa]	Normalized bond strength [-]	Bond stiffness (loaded end) ($K_{\tau-s}$) [MPa/mm]	Normalized bond stiffness [-]	Failure mode [1]
20 ± 2	1	33.5	12.4	1.02	43.0	0.89	PO
	2	32.1	11.9	0.98	53.4	1.11	PO
60 ± 2	1	32.1	11.9	0.98	28.9	0.60	PO
	2	25.6	9.5	0.78	20.9	0.43	PO
100 ± 2	1	21.9	8.1	0.67	14.6	0.30	PO
	2	20.8	7.7	0.63	17.1	0.35	PO
140 ± 2	1	22.0	8.2	0.67	14.1	0.29	PO
	2	23.2	8.6	0.71	11.4	0.24	PO
170 ± 2	1	19.7	7.3	0.60	12.6	0.26	PO
	2	17.1	6.3	0.52	12.1	0.25	PO
	3	20.4	7.6	0.63	17.4	0.36	PO
200 ± 2	1	9.2	3.4	0.28	11.9	0.25	PO
	2	9.9	3.7	0.30	7.1	0.15	PO
	3	9.6	3.6	0.30	12.2	0.25	PO
250 ± 2	1	4.8	1.8	0.15	11.3	0.23	PO
	2	4.7	1.7	0.14	15.3	0.32	PO

[1] PO: pull-out.

Table B.5. Individual results of pull-out tests performed in (confined) specimens with RBP-S bars.

T [ºC]	Specimen	Maximum pull-out load [kN]	Average bond strength [MPa]	Normalized bond strength [-]	Bond stiffness (loaded end) ($K_{\tau-s}$) [MPa/mm]	Normalized bond stiffness [-]	Failure mode [1]
20 ± 2	1	51.9	18.7	0.98	67.2	1.40	PO
	2	53.8	19.3	1.02	29.1	0.60	PO
60 ± 2	1	43.8	15.8	0.83	25.1	0.52	PO
	2	55.3	19.9	1.05	33.6	0.70	PO
	3	47.2	17.0	0.89	42.1	0.87	PO
100 ± 2	1	44.5	16.0	0.84	11.5	0.24	SPT
	2	39.7	14.3	0.75	13.1	0.27	SPT
120 ± 2	1	19.9	7.2	0.38	7.7	0.16	PO
	2	25.7	9.2	0.48	6.6	0.14	PO
140 ± 2	1	15.8	5.7	0.30	9.0	0.19	PO
	2	12.3	4.4	0.23	8.0	0.17	PO
220 ± 2	1	6.4	2.3	0.12	12.5	0.26	PO
	2	5.6	2.0	0.11	16.0	0.33	PO
300 ± 2	1	3.2	1.1	0.06	7.5	0.16	PO
	2	2.7	1.0	0.05	2.5	0.05	PO

[1] SPT: splitting of concrete; PO: pull-out.

Table B.6. Individual results of pull-out tests performed in (confined) specimens with RBP-B bars.

T [ºC]	Specimen	Maximum pull-out load [kN]	Normalized maximum pull-out load [-]	Bond stiffness (K_{F-s}) kN/mm]	Normalized bond stiffness [-]	Failure mode [(1)]
20 ± 2	1	102.4	1.03	-	-	T
	2	109.9	1.10	59.5	1.04	SPL
	3	96.3	0.97	57.2	1.00	T
	4	90.5	0.91	55.3	0.96	SPT
60 ± 2	1	91.4	0.92	37.0	0.65	PO
	2	92.7	0.93	61.1	1.07	SPL
	3	91.5	0.92	67.0	1.17	PO
100 ± 2	1	56.6	0.57	24.2	0.42	PO
	2	45.3	0.45	15.7	0.27	PO
	3	60.7	0.61	21.5	0.38	PO
120 ± 2	1	31.4	0.31	21.8	0.38	PO
	2	28.2	0.28	29.0	0.51	PO
	3	30.1	0.30	14.6	0.25	PO
140 ± 2	1	24.3	0.24	22.6	0.39	PO
	2	25.1	0.25	43.4	0.76	PO
220 ± 2	1	8.9	0.09	49.1	0.86	PO
	2	9.8	0.10	13.4	0.23	PO
	3	8.7	0.09	42.3	0.74	PO
300 ± 2	1	4.5	0.05	14.1	0.25	PO
	2	5.2	0.05	15.3	0.27	PO
	3	5.0	0.05	11.6	0.20	PO

[(1)] T: tensile rupture of the bar; SPL: spalling of the concrete cover above the bend; SPT: splitting of concrete; PO: pull-out.